Mechanical properties and function of CHMP2B in the ESCRT membrane remodelling and scission pathway

Maryam Alqabandi

Thèse de Doctorat de Sorbonne Universités

Université Pierre et Marie Curie (UPMC)

Ecole doctorale Physique en Ile-de-France (ED PIF 564)

Spécialité: Biophysique

Présentée par

Maryam ALQABANDI

Pour obtenir le grade de Docteur de l'Université Pierre et Marie Curie (Parie 6)

Mechanical properties and function of CHMP2B in the ESCRT membrane remodelling and scission pathway

Dirigée par Mme. Stéphanie MANGENOT et Mme. Patricia BASSEREAU

Présentée et soutenue publiquement le 01 Février 2018

Devant un jury composé de :

Mr. Benoît-Claude FORGET	Président
Mme. Kheya SENGUPTA	Rapporteur
Mr. Arnaud ECHARD	Rapporteur
Mr. Frédéric PINCET	Examinateur
Mr. Wouter ROOS	Examinateur
Mr. Winfried WEISSENHORN	Invité

Dédicace

A ceux qui m'ont donné et appris la vie,

Noura et Youssef.

Cette thèse vous est dédiée.

Acknowledgments

Je tiens tout d'abord à remercier ma directrice de thèse Stéphanie Mangenot. Dès le début, j'ai été touchée par ta patience, ta bienveillance et ton dévouement. Ce projet n'a jamais été simple et grâce à tes encouragements je n'ai baissé les bras. Je te remercie pour tout le temps que tu as passé avec moi à essayer de résoudre tous les problèmes scientifiques et humains encourus. Je suis si fière, honorée et heureuse de t'avoir eu comme ma directrice de thèse et aussi comme amie.

Je tiens aussi à remercier Patricia Bassereau ma co-directrice de thèse et directrice de l'équipe. Je te remercie de m'avoir acceptée en stage dans ton équipe puis en thèse. J'ai été dès le premier cours de Master impressionnée par ton enthousiasme, ton dynamisme et ta passion pour la recherche scientifique. Grâce à toi j'ai acquis des outils indispensables qui me serviront tout au long de ma carrière. Je te remercie pour tous nos échanges scientifiques, pour ta disponibilité et de m'avoir permis de réaliser un rêve qu'est la thèse de Doctorat.

Une grande gratitude à Benoit Forget, Kheya Sengupta, Arnaud Echard, Frederic Pincet, Wouter Roos et bien évidemment Winfried Weissenhorn d'avoir accepté de composer mon Jury de thèse. Merci à Kheya et Arnaud pour leurs rapports de thèse, rédigés en un lapse de temps assez court. Je vous remercie d'avoir pu consacrer votre temps précieux à la lecture détaillée de mon manuscrit et pour vos retours très positifs. Merci à Benoît d'avoir présidé ma thèse et surtout d'avoir suivi mon parcours académique dès la première année de Licence à Paris Descartes et durant la thèse en étant mon tuteur externe. Tu as réussi à me transmettre ta passion pour la Physique et surtout à me guider tout au long de ces années. Merci à Wouter pour la belle collaboration et de m'avoir permis d'obtenir ces remarquables résultats de HS-AFM. Sans cette collaboration, je n'aurai pu voir la structure nanoscopique de mes protéines et étudier plus amplement leur mécanique. Je tiens particulièrement à remercier Winfried sans qui ce projet n'aurait pu être entamé. Tu as suivi et encouragé mon travail ces cinq dernières années et pour cela je t'en suis très reconnaissante. Je remercie également Julie Plastino ma tutrice à Curie.

Je remercie Nolwenn Miguet, Aurélie Bertin, Marta Bally, Sourav Maity et Mélissa Piontek pour nos remarquables collaborations. Merci Nolwenn pour ces cinq années de collaborations. La purification de ces protéines a été très fastidieuse et je te remercie pour ta persévérance, pour nos nombreux échanges et de t'être déplacée pour ma soutenance. Je te remercie Aurélie d'avoir cru en ce projet dès le début et d'avoir accepté depuis 2013 de collaborer avec moi. Grâce à toi, j'ai pu terminer cette thèse avec splendeur. Merci à Marta pour les semaines passées à Göteborg. Tu m'as permis de découvrir une nouvelle technique qu'est le QCM pour l'étude de mes protéines et aussi de déguster ta succulente cuisine. Je te remercie pour ton accueil, ta convivialité et ton amitié. Je remercie aussi Sourav et Mélissa avec qui j'ai collaboré durant ma dernière année de thèse. Travailler avec vous a été si agréable et surtout une preuve qu'une collaboration entre un Post-Doc et une Doctorante puisse fonctionner sans tensions, triches ou manipulations (une chance dont je n'ai pu malheureusement bénéficier sur mon projet).

Ces cinq années n'ont pas été faciles, voire très difficiles, et c'est grâce à mes collègues et amis de l'équipe que j'ai pu voir la lumière même durant les jours les plus sombres. Je remercie tout d'abord Aurore Levy. Nous avons traversé tant de difficultés, nous avons pleuré et ri de nos maladies et nous nous sommes battus ensemble ! Je remercie Thibaut, mon voisin de bureau. Je n'oublierai jamais ton soutien lorsque j'ai perdu ma grand-mère. Tu es une personne extraordinaire et un ami sur qui l'on peut toujours compter. Merci aussi pour ta bonne humeur quotidienne. Quelle joie de travailler à tes côtés !

Merci à Alexandre (dixit Licsou) pour ta patience et pour ta gentillesse. Je t'ai fait souffrir avec moi ces derniers mois et je te remercie d'avoir été à chaque fois disponible et à mon écoute. Je me souviens encore du jour où je t'ai demandé de t'installer à mes côtés au bureau car je paniquais et tu as accepté. Je remercie aussi Feng, Michael, Oleg, Johanna, Juju, Ajay et Kodjo pour leurs encouragements et aide tout au long de cette thèse. Je remercie aussi mes anciens collègues et amis Coline, Mijo, François, Senthil, Thomas et David. Vous avez tous été si gentils, si bienveillants et je vous en suis tous très reconnaissante.

Ces cinq années m'ont aussi permis de faire la connaissance de personnes extraordinaires et qui m'ont soutenu jusqu'au bout. Merci à Fahima, Tatiania, Marie, Guillaume, Maj, Su-Jin, Laura, Cynthia, Tanh, John, Jonathan, Joël, Kevin, Mathieu ainsi que toute l'UMR 168. Vous avez formé ensemble ma grande et seconde famille en France. Je remercie aussi du fond du cœur Karen, Laurence, Christelle, Agnès et Brigitte. Quelle chance de vous avoir eu à mes côtés ! Merci aussi à Eric pour toute ton aide technique et à Vincent et Lucie de la plateforme Nikon.

Enfin, je tiens à remercier ma famille et mes amis. En particulier mes parents à qui je dédie cette thèse ainsi que May et Hmoud mes deux bébés. Une grande pensée est aussi dédiée à ma grand-mère qui nous a quitté en 2015, c'était une femme forte et qui m'a toujours inspirée dans la vie.

Pour conclure je tiens à remercier mon Ahmed, mon mari, mon amour et le formidable père de notre petit ange Nora. La vie ne nous a pas fait que des cadeaux ces dernières années et pourtant ta main n'a jamais lâché la mienne. Tu n'as jamais cessé de croire en moi et j'ai toujours puisé ma force de toi. Cette thèse n'aurait jamais pu voir le jour sans toi. Je t'aime Habibi !

This work has been supported by:

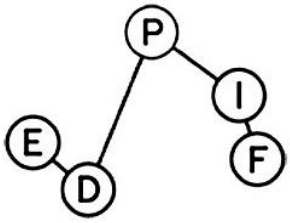

TABLE OF CONTENTS

TABLE OF ABBREVIATIONS

Aa, amino acids

AAA, ATPase associated with various cellular activities

ALIX, ALG-2 interacting protein X

AFM, atomic force microscopy

Bp, base paire

CEP, centrosomal protein

CHMP, charged multivesicular body protein

CHMP-FL, Full length CHMP protein

CHMP-WT, Wild-type CHMP protein

CHMP-ΔC, CHMP protein with a C-terminus truncation

CME, clathrin-mediated endocytosis

Cryo-EM, cryo-electron microscopy

C-ter, C-terminus

DEEM, deep-etch electron microscopy

DLS, Dynamic Light Scattering technique

Edissipation, energy dissipated

EM, electron microscopy

Env, envelope glycoprotein

ER, endoplasmic reticulum

ERES, ER exit sites

ESCRT, endosomal sorting complex required for transport

Estored, energy stored

FACS, fluorescence-activated cell sorting, applied in cell cytometry

FRAP, fluorescence recovery after photobleaching

FTD, fronto-temporal dementia neurodegenerative disease

FTD3, fronto-temporal dementia linked to chromosome 3 neurodegenerative disease

Gag, group-specific antigen

HIV, human immunodeficiency virus

ILV, intralumenal MVB vesicle

IST1, increased sodium tolerance 1 gene product

Ld, liquid disordered phase

L-domains, late domains

MIM, MIT interacting motif

MIT, microtubule-interacting and transport

MOP, Myopic accessory protein

MVB, multivesicular body

MVE, multivesicular endosome

NE, nuclear envelope

NPC, nuclear pore complex

PI, phosphatidylinositol

PIP, phosphatidylinositol phosphate derivate

PtdInsP, phosphatidylinositol phosphate derivate

PLW, platinum wires

PM, plasma membrane

PVA, polyvinyl hydrolyzed alcohol

QCM-D, quartz crystal microbalance with dissipation monitoring

ROI, region of interest

Snf, sucrose non-fermenting protein

Ub, ubiquitin

Vps, class E vacuolar protein sorting-associated protein

ΔD, Energy dissipation shift

ΔF, Frequency shift

Δm, Mass shift

TABLE OF FIGURES

CHAPTER 1. INTRODUCTION

Eukaryotic cells contain several compartments called organelles, which are specialized subunits within the cell (Figure 1-1). The cell and the organelles are delimited by membranes which form a physical barrier from the surrounding environment and preserve their integrity. The different organelles are not static isolated structures; they constantly communicate between each other by means of transport vesicles. Intracellular vesicular trafficking is mandatory for the cell survival and is achievable thanks to membranes deformability and shape modulation.

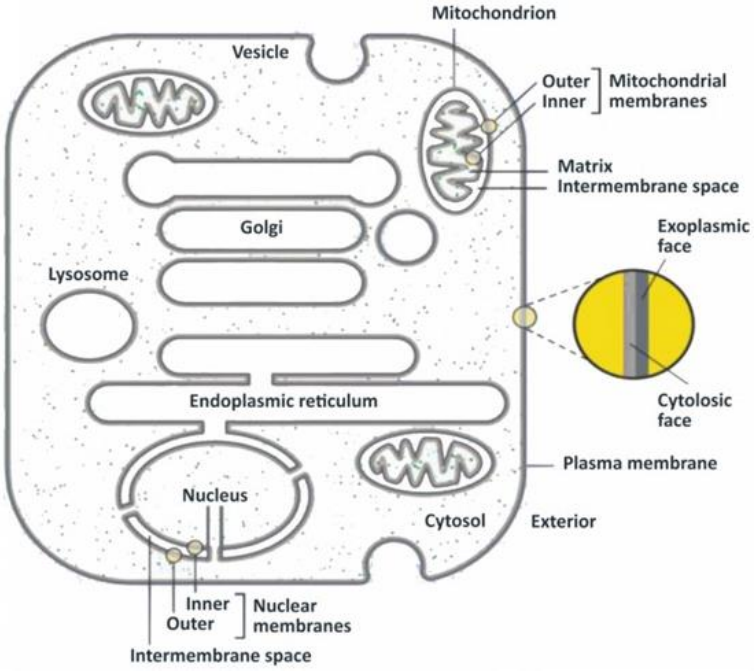

FIGURE 1-1: A EUKARYOTIC CELL INTERNAL ORGANIZATION. ADAPTED FROM (LODISH ET AL., 2003).

Different Intracellular trafficking pathways, critical for cell functioning, allow material exchange between the plasma membrane (PM), the Golgi apparatus, the endoplasmic reticulum (ER) and endosomes (Figure 1-2). These pathways are responsible for the transport of proteins and lipids within the cell, between and through the different organelles, while protecting their integrity. This communication of the cell with its environment is crucial for all tissue and organ function. The two major intracellular pathways, based on the direction of the exchanges, are the secretory pathway (or exocytic pathway) and the endocytic pathway. The secretory pathway which was the first communication pathway characterized in 1975 by George Palade, carries proteins and lipids from the endoplasmic reticulum through the Golgi apparatus to the plasma membrane (PM). It allows the cell to modify the molecules which are produced, in a series of steps, store them until needed, and then deliver them either to the plasma membrane (for receptors, adhesion proteins for instance) or to the exterior through exocytosis.

The endocytic pathway allows to internalize (through endocytosis) cargos from the cell external medium or the PM through a set of endosomes to the degradative cellular compartment, the lysosome. The two pathways are connected by bi-directional transport between the Golgi and endosomes. Both the secretory and endocytic intracellular trafficking pathways implicate the constant budding and transport of small vesicles or tubules enclosing the cargo (lipids or proteins) to be transported. These vesicles or tubules bud off from the donor compartment and shuttle through the cytoplasm along the cytoskeleton in general towards the targeted acceptor compartment where they fuse and release their content (Palade 1975; Bonifacino and Glick 2004; Takamori, Holt et al. 2006).

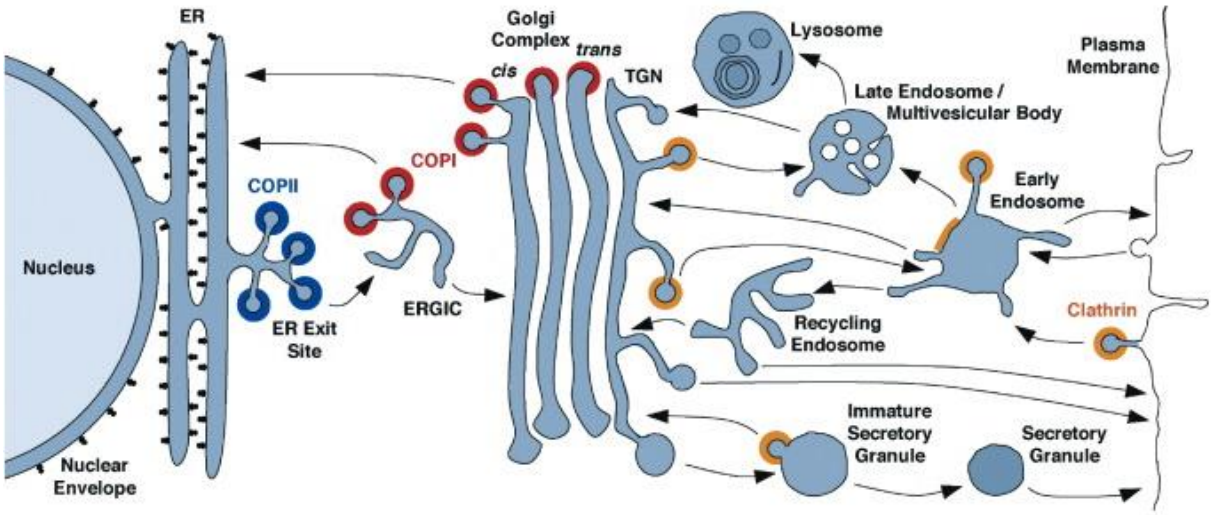

FIGURE 1-2: INTRACELLULAR TRANSPORT PATHWAYS (BONIFACINO AND GLICK 2004)
The secretory, lysosomal and endocytic pathways. The main types of coats are indicated by colored lines. Clathrin is involved in endocytosis and trafficking at the trans-Golgi network. COPII is involved in export from the ER, and COPI in retrograde transport from the Golgi complex.

Intracellular traffic can occur in the presence or in the absence of proteins on the cytosolic surface, which self-assemble on the membrane forming a protein coat (Doherty and McMahon 2009). There are three major coat proteins, which are implicated at various points during endocytosis and exocytosis: COPI and COPII, caveolae and clathrin, (Figure 1-2) (Hsu, Lee et al. ; Vassilieva and Nusrat 2008; McMahon and Boucrot 2011; Faini, Beck et al. 2013).

COPI and COPII coat proteins mediate the transport both ways between the ER and the Golgi apparatus (Figure 1-2). The proteins synthetized in the ER are exported to ER exit sites (ERES) where COPII coat proteins form the budding complex that will later go through the Golgi apparatus to be further glycosylated, processed or sorted before their release at the plasma membrane or out of the cell or returned to the ER through COPI-coated vesicles (Barlowe, Orci et al. 1994).

Clathrin coat proteins mediate endocytosis from the plasma membrane to endosomal compartments and the Golgi (Figure 1-2). The clathrin-mediated endocytosis pathway is involved in the regulation of the level of receptors, adhesion molecules at the plasma membrane and allows internalizing exterior substrates, etc. The incorporation of these materials is accomplished through deformation and invagination of the plasma membrane by the clathrin coat and associated proteins (Doherty and McMahon 2009). Clathrin assembles into a lattice-like cage on the plasma membrane with the assistance of adaptor proteins that directly bind lipids, cargo proteins, other adaptors, and clathrin itself. The clathrin multicomponent protein coat clusters cargo and bend the membrane by forming a scaffold that imposes its spontaneous positive curvature to the underlying membrane with dynamin, and in some cases with the help of adhering cytoskeleton. The clathrin-coated vesicles then pinch off from the plasma membrane by dynamin-mediated membrane scission before clathrin-uncoating and fusing with the specific targeted compartment (Figure 1-3).

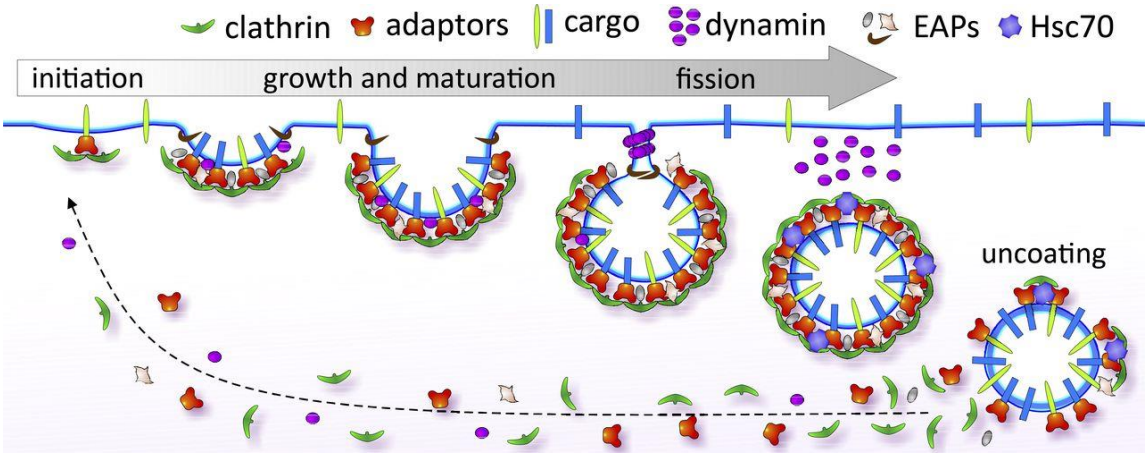

FIGURE 1-3: SCHEMATIC ILLUSTRATION OF CLATHRIN-MEDIATED ENDOCYTOSIS (CME) (SCHMID 2017).
CME is initiated when the coat-forming protein clathrin is recruited to the PM by the heterotetrameric adaptor proteins that also recognize cargo on the cytoplasmic domains of surface receptors. As clathrin assembles, cargo is concentrated into the inwardly growing clathrin-coated pit (CCP). With the help of numerous endocytic accessory proteins (EAPs), nascent CCPs undergo maturation until they are deeply invaginated but remain connected to the cell surface via a narrow neck. The large GTPase dynamin then assembles around these narrow necks forming collar-like structures and, with the help of curvature-generating EAPs, catalyzes membrane scission.

In all cases, once the coated-bud grows and is ready to detach, it has to be separated from the membrane of origin by fission of the membrane, without loss of cargo. Membrane fission requires specialized complexes: the GTPase dynamin in the context of clathrin-mediated endocytosis, the GTPase Sar1 in COP-II vesicle scission (Lee, Orci et al. 2005) or the endosomal sorting complex required for transport machinery (ESCRT) for driving the formation of intraluminal vesicles in the multivesicular body pathway (Peel, Macheboeuf et al. 2011; Guizetti and Gerlich 2012).

ESCRT complexes constitute an evolutionary conserved class of proteins that mediate a topologically unique mode of membrane remodelling and scission (Figure 1-4; Figure 1-5). In the multivesicular body pathway (MVB) (Henne, Stenmark et al. 2013), the ESCRT complexes catalyze membrane budding and fission processes, necessary for receptor sorting and down-regulation (Figure 1-5). In addition to the MVB generation, ESCRTs are involved in a variety of other cellular contexts such as in late steps of cytokinesis (Guizetti and Gerlich 2012; Agromayor and Martin-Serrano 2013), in plasma membrane repair (Jimenez, Maiuri et al. 2014), in exosome biogenesis (Juan and Furthauer 2017), in nuclear envelope assembly (Olmos and Carlton 2016; Christ, Raiborg et al. 2017), in neuron pruning and repair and in retroviral egress, etc. (Hurley 2015; Alonso, Migliano et al. 2016; Schoneberg, Lee et al. 2017) (Figure 1-4). Additionally, a dysfunction of these complexes could be partly associated with numerous pathologies like cancer or neurodegenerative diseases (Slagsvold, Pattni et al. 2006; Piper and Katzmann 2007; Saksena and Emr 2009).

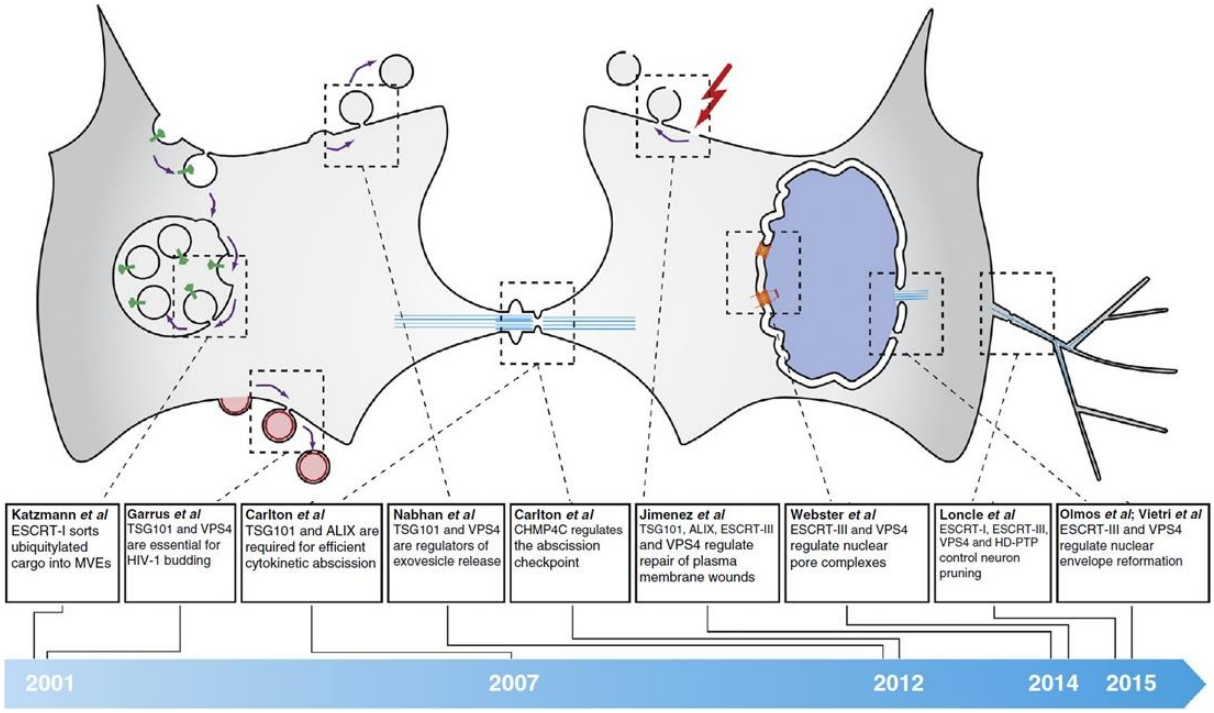

FIGURE 1-4: TIME-LINE OF DISCOVERY OF ESCRT-DEPENDENT PROCESSES (CAMPSTEIJN, VIETRI ET AL. 2016)
Overview of ESCRT functions described in a variety of cellular contexts since its identification in 2001.
The first study identifying each of the functionalities is indicated.

Interestingly, in all the ESCRT-dependent processes, the membrane-neck-directed mode of action of the machinery is preserved (Figure 1-5). The ESCRT complexes drive membrane scission of vesicles budding away from the cytosol, whether into internal compartments or out of the cell, (Figure 1-5).

In the case of the ESCRT-mediated membrane scission, budding happens from the inner surface of the membrane resulting in scission and vesicle formation away from the cytosol and towards the lumen of the endosome. Therefore, ESCRT complexes induce reverse-topology membrane scission events

compared to the membrane scission in CME (Figure 1-5). In contrast with dynamin-induced fission where the neck can be constricted without obstacle, ESCRT proteins are present inside the neck, thus, its direct thinning and self-fusion is hindered by the protein scaffold (Figure 1-5). Hence, the character of membrane deformation leading to scission driven by ESCRTs must differ essentially from that generated by dynamin in the CME context and the mechanics of the fission reaction must be dissimilar.

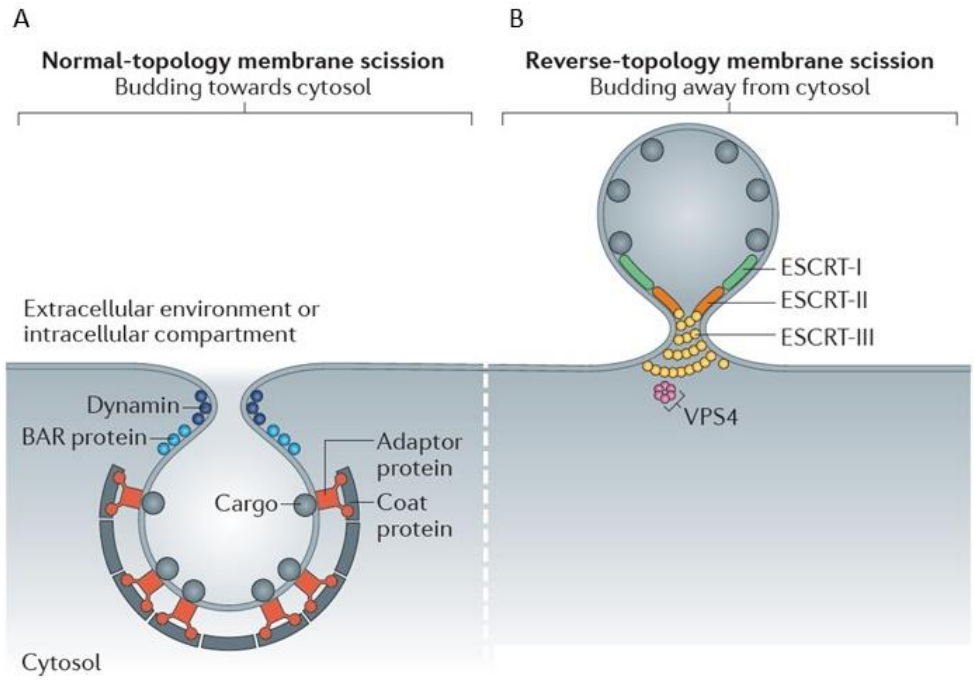

FIGURE 1-5: OPPOSITE MEMBRANE BUDDING TOPOLOGIES LEAD TO VESICLE FORMATION IN DIFFERENT DIRECTIONS (SCHONEBERG, LEE ET AL. 2017).
Normal-topology (left) and reverse-topology (right) membrane scission. Normal-topology scission occurs in the biogenesis of clathrin-, coat protein I (COPI) - and COPII-coated vesicles, where budding occurs towards the cytosol. Reverse-topology scission, carried out by the endosomal sorting complexes required for transport (ESCRTs), functions in vesicle budding away from the cytosol. Note that a fundamental mechanistic difference between normal-and reverse-topology scission arises from the fact that only the cytosolic side of the membrane neck is accessible for the protein scaffolding and scission machinery.

The ESCRT family comprises five different sub-complexes: ESCRT-0, ESCRT-I, ESCRT-II, ESCRT-III , the AAA-ATPase Vps4 (Vacuolar protein sorting 4) complex, and ESCRT-associated or accessory proteins such as ALIX (also known as BRO1) (Piper and Katzmann 2007). The ESCRT-accessory proteins play a key role in recruiting and stabilizing ESCRT subunits. The ESCRT complexes are recruited sequentially on the cytosolic side of the membrane as preformed complexes (ESCRT-0, I and II) or inactive monomers (ESCRT-III) and, together, contribute to specific steps in membrane budding and fission.

The ESCRT-0 complex is the first complex involved in the process as it recognizes and sequesters ubiquitynilated cargo proteins. In addition, ESCRT-0 triggers ESCRT-I (and ALIX) and ESCRT-II complexes which likewise contain ubiquitin-binding domains (Schmidt and Teis 2012) (Figure 1-6). This way,

ubiquitin tagged proteins are passed from one complex to the other, from ESCRT-0 to ESCRT-I and then to ESCRT-II, like on a conveyor belt.

ESCRT-I and ESCRT-II complexes mediate membrane deformation and invagination. But, acting alone, ESCRT-I and II can only generate the formation of membrane buds and are not able to induce membrane fission (Figure 1-6). This last step is performed by the hetero-oligomeric ESCRT-III complex, recruited either by ESCRT-II via ESCRT-I or by ALIX. The ESCRT-III complex is thus critical for accomplishing the last steps in membrane scission and, peculiarly, the ESCRT-III subunits are not internalized in the formed vesicle. Finally, ESCRT-III proteins are recycled into the cytoplasm by the Vps4 complex in an ATP-consuming reaction (Figure 1-6). Additionally to disassembling the ESCRT complex, recent studies indicate that Vps4 could also play an important role in the machinery regulation (Adell, Migliano et al. 2017; Mierzwa, Chiaruttini et al. 2017).

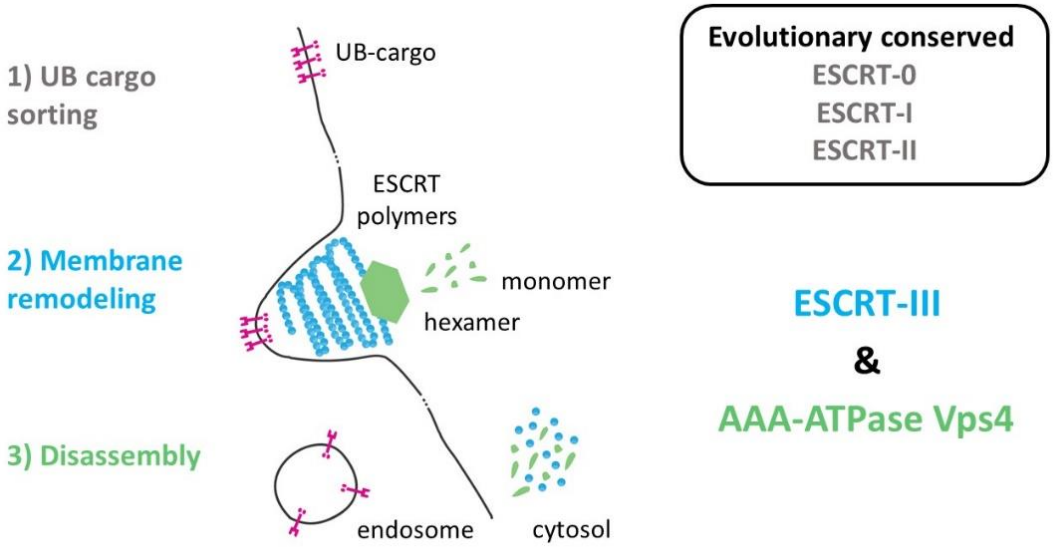

FIGURE 1-6: THE ESCRT MACHINERY
Schema of the different steps of membrane remodelling by ESCRTs. First, the ESCRT evolutionary conserved complexes ESCRT-0, -I, -II sort ubiquitynilated cargoes and initiate membrane deformation. Second, the ESCRT-III complex induces membrane budding and scission. Third, the AAA-ATPase Vps4 regulates the ESCRT-III components and prior to membrane scission, it disassembles and recycles back to the cytosol the ESCRT-III components. ESCRT-III subunits are not internalized in the formed vesicle.

The ESCRT-III complex differs from all other ESCRT machinery since it exists only transiently and contains both essential and non-essential components. The ESCRT-III subunits cycle between an inactive cytosolic state (Muziol, Pineda-Molina et al. 2006; Bajorek, Schubert et al. 2009; Xiao, Chen et al. 2009) and an active state when bound to the membrane (Zamborlini, Usami et al. 2006; Shim, Kimpler et al. 2007; Lata, Roessle et al. 2008). The latter state includes recruitment by adaptor proteins leading to

membrane binding and transient assembly of ESCRT-III subunits as a heteropolymer that ultimately lead to membrane fission.

The yeast ESCRT-III protein complex comprises four core subunits: Vps20, Vps24, Vps2 and Snf7 (vacuolar sorting proteins 20, 24, 2 and sucrose non-fermenting protein 7). In Homo sapiens, 32 proteins form the five different complexes ESCRT-0, -I, -II, -III and the ATPase Vps4 complex and up to 12 proteins exist for the ESCRT-III complex, called Charged Multivesicular Body Protein (CHMP 1-7) and IST1 (Increased Sodium tolerance 1 gene product). The increased number of ESCRT-III subunits in Homo sapiens is paralleled by the functional diversification of the complex in higher organisms. CHMPs proteins involve a set of closely related core components with their yeast homologues: Vps20 and Vps24 Homo sapiens homologous are respectively CHMP6 and CHMP3. Snf7 is present in three isoforms, namely CHMP4A, B and C. And, there are two subunits sharing a relative high sequence homology with Vps2, called CHMP2A and CHMP2B.Previous studies suggest that CHMP4B and CHMP2A are respectively the functional homologues of Snf7 and Vps2 according to their essential role in the MVB pathway (Henne, Stenmark et al. 2013). The role of the remaining ESCRT-III proteins (CHMP1A, B, CHMP5, CHMP7 and IST1) is less defined.

Although, the principal biochemical function of the ESCRT-III proteins is to induce membrane scission by constricting and narrowing membrane necks, the individual functions of the different respective human isoforms are not well conclusively proved and the minimal machinery necessary to induce membrane scission and its biophysical mechanism and regulation remain unknown. Several models have been proposed to explain how ESCRTs are spatially arranged to accomplish scission but the biochemical conditions for ESCRT-III interactions with the membrane, the role of the shape of the neck, the membrane curvature as well as the mechanical properties of ESCRT-III polymers, have been less investigated.

The aim of this thesis is to characterize the mechanical properties of CHMP2B protein in comparison with the other ESCRT-III subunits. And, additionally, we look forward in this study to present a biological function for CHMP2B within the other ESCRT-III core components in the membrane scission context. We have used biomimetic model systems to study in vitro CHMP protein affinity and effects on membrane by several techniques (confocal microscopy, FACS, FRAP, and EM and AFM with collaborators). We focused our work on CHMP2B protein, the less studied ESCRT-III subunit. We have determined and precisely quantified the interaction of CHMP2B protein with synthetic membranes of different lipid compositions. We established that CHMP2B binding is enhanced in the presence of PI(4,5)P2 lipids, whereas the other human core components (CHMP4, CHMP2A and CHMP3) have no lipid specificity besides their negative charge. In addition, we revealed for the first time the

supramolecular organization of CHMP2B proteins on membranes. We found that CHMP2B proteins form at the macroscopic scale a reticular-like structure on the surface of giant vesicles that was never observed before. At a smaller scale and high resolution, we observed by EM and AFM that CHMP2B proteins form a “honeycomb”-like pattern. Furthermore, we also characterized for the first time the mechanical properties of CHMP2B polymers, showing a strong membrane stiffening induced by CHMP2B in contrast with the other CHMPs subunits. These results provide strong experimental evidence that modulation of membrane elasticity is an important function of CHMP polymers. This property might play an important role in the context of membrane scission. With our collaborators (Aurélie Bertin at the UMR168 and W. Roos (Zernike Instituut, Groningen) using cryo-electron microscopy and high-speed AFM, we also studied how these protein complexes deform membranes. Our results show that in contrast with the actual prominent hypothesis, CHMP4 alone does not deform membranes, but when complexed with the other CHMP subunits (CHMP2A + CHMP3 or CHMP2B), it forms tubular helical structures that were never reported before. These observations provide a novel basis for proposing possible mechanism for membrane constriction in the presence of the ATPase Vps4.

The physics of biomembranes will be presented in Chapter 2. The ESCRT machinery in Yeast and Homo sapiens and the thesis objectives are detailed in Chapter 3. In Chapter 4, we will describe the different techniques used to study CHMP2B in comparison with the other ESCRT-III human core components: CHMP4, CHMP2A and CHMP3. And in Chapter 5, we will present our results. Finally, the conclusion and perspectives will be presented in Chapter 6.

CHAPTER 2. PHYSICS OF BIOMEMBRANES

2.1 STRUCTURE OF LIPIDS

The building block of a cellular membrane is lipids. The cellular membrane mainly consists of a double layer of lipids of 3 nm thickness each and with an area per lipid molecules about 0.7 nm^2 (Lipowsky 1995). It is an asymmetric structure with different lipid compositions on each leaflet.

Lipids are amphiphilic molecules with a hydrophilic head group and hydrophobic tails. The hydrophilic head group varies depending on the lipid type and can be neutral or negatively charged. The hydrophobic tail group is made of a variable number of hydrocarbon chains (from 1 up to 4) of various lengths and degrees of unsaturation. Their amphiphilic property is a chemical property that enables cells to segregate their internal constituents from the external environment. Lipids are highly soluble in organic solvents. When solubilized in water and when their concentration exceeds the critical micellar concentration (CMC) (of the order of µM for lysolipids (1 chain) in C16, C18 and of the order of nM for phospholipids (2 chains) in C16, C18) (Kuhl, Leckband et al. 1994), the amphiphilic property of lipids causes them to self-assemble spontaneously into various structures. The hydrophilic heads face the water and protect the hydrophobic tails from contact with water. The optimal arrangement of lipids in water results from the competition between two forces: the hydrophobic attraction force which tends to aggregate the molecules together, in other words to reduce the interfacial area, and the repulsion force of the head groups which tends to increase the interfacial area. The hydrophobic attraction is not a real interaction between hydrophobic molecules; rather, it is an effective interaction. It results from the so-called hydrophobic effect: when a non-polar molecule is introduced in water, it perturbs the arrangement of water molecules. These molecules reorient to minimize the disruption of hydrogen bonds. However, the arrangement of water molecules around non-polar solute is more ordered, and therefore entropically unfavorable. By aggregation, hydrophobic molecules minimize the entropic cost associated with the rearrangement of water molecules. The competition between hydrophobic attraction and head group repulsion forces results in a constant (equilibrium) area per lipid. Thus, the shape of the self-assembled or aggregated lipid structures depends on this parameter as well as on the geometrical shape of the lipids (Helm, Israelachvili et al. 1992). Lipids assembly can form for instance a globally flat structure, namely a lipid bilayer in which the lipid tails are arranged parallel to each other being sandwiched by the head groups or spherical shape structures such micelles (Figure 2-1). Micelles are globular structures with the lipid head groups at the water interface covering the lipid tails (Figure 2-1). This micelle structure is practically only found for one-chain lipids (lysolipids) at accessible concentrations.

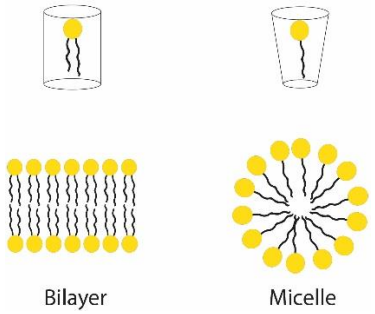

FIGURE 2-1: MOST COMMON LIPID SELF-ASSEMBLIES IN WATER DEPENDING ON THE INDIVIDUAL LIPID UNIT SHAPE
(Left) Lipid bilayer with cylindrical-shaped individual unit. The cross section of the lipid head equal that of the side chain.
(Right) Micelles with wedge-shaped individual unit. The cross section of the lipid head is greater than that of the side chain.

Besides being a protective barrier for the different organelles in cells, with a low permeability to most water-soluble molecules and ions, lipid membranes behave as highly dynamic two-dimensional fluid structures (Lipowsky 1995). Lipids continuously diffuse laterally within each leaflet of the bilayer (Figure 2-2 / A). This lateral diffusion is considered as a relatively fast phenomenon with a diffusion coefficient ranging from 1 to 10 $\mu m^2.s^{-1}$ in reconstituted membrane systems. Lipids can also flip in the bilayer between the inner and outer leaflets (Figure 2-2 / B). The passive transversal diffusion or flip-flop occurs less frequently and is very slow in the absence of protein involved in active transport such as flippase, floppase or scramblase (Figure 2-2 / C).

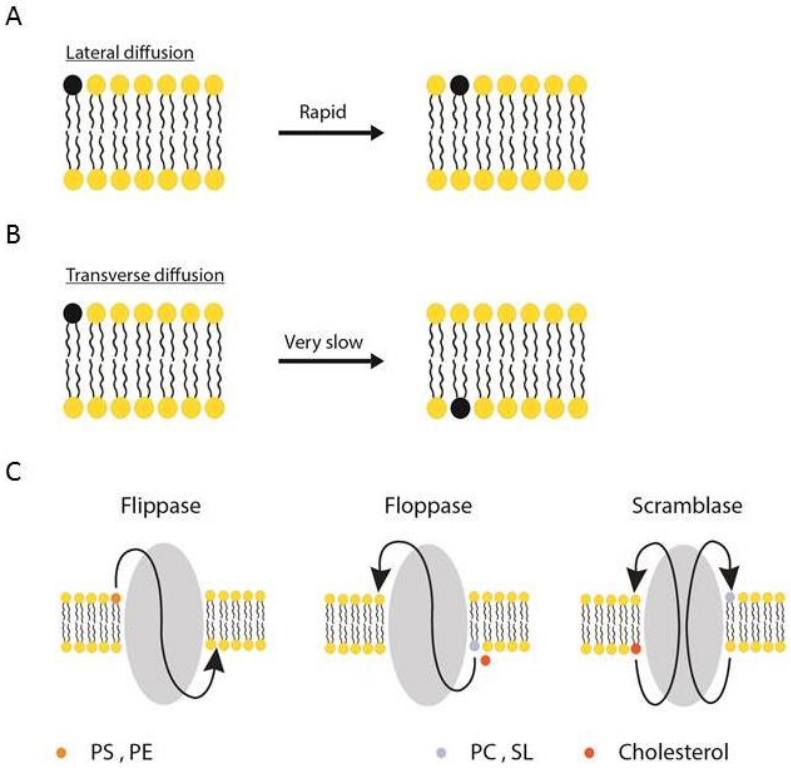

FIGURE 2-2: LIPID DIFFUSION IN A BILAYER: LATERAL VS. TRANSVERSE (FLIP-FLOP)
(A) Lipid lateral diffusion.
(B) Lipid Transverse diffusion or lipid Flip-Flop.
(C) Lipid transverse diffusion in the presence of proteins: Flippase, Floppase and Scramblase.

Lipids can be divided into two classes: structural lipids and signaling lipids. Structural lipids are responsible for the physical barrier function of the membrane and are the most abundant lipids in the membrane. Signaling lipids are present in smaller quantities. They are highly regulated and play a major role in defining organelles and recruitment of target proteins to the membrane (Sprong, van der Sluijs et al. 2001; van Meer, Voelker et al. 2008).

The most abundant structural lipids found in cell membranes are phospholipids (Figure 2-3). Phospholipids have in general one or two fatty acid hydrocarbon tails (providing the hydrophobic barrier) linked together to a platform, a phosphate group and additionally to that, they have a polar group (headgroup) defining their function. Depending on the headgroup, the distribution of phospholipids varies among the different organelles. The two major sub-types of phospholipids are glycerophospholipids, if the hydrophobic platform on which phospholipids are built is diacylglycerol (Figure 2-3 / A) and sphingolipids, if the platform on which phospholipids are built is ceramide (Figure 2-3 / B).

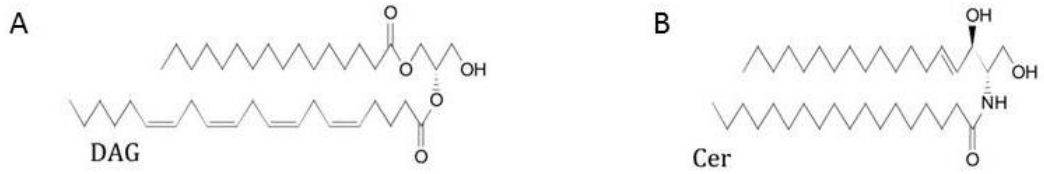

FIGURE 2-3: PRECURSORS OF PHOSPHOLIPIDS
They define the two major sub-types of phospholipids.
(A) Diacylglycerol (DAG) backbone, at the base of the glycerophospholipids.
(B) The ceramide backbone for the sphingolipids.

2.1.1 PHOSPHOLIPIDS

The main phospholipids found in biological membranes are glycerophospholipids that represent 40 to 60 mol % of the total lipid fraction. Glycerophospholipids have a diacyl hydrophobic backbone composed of two saturated or *cis*-unsaturated fatty acid chains of varying lengths (and various possible unsaturated levels) covalently linked to a glycerol molecule (Figure 2-4). The *cis*-unsaturations create kinks in the hydrocarbon chain. The presence of these kinks effectively reduces the surface area accessible to other fatty acid chains, weakening Van der Waals interactions. They form less dense irregular packing of individual lipid molecules as for saturated chains or in other terms a disordered organization of the membrane called the liquid disordered phase (Ld). The Ld phase corresponds to a highly fluid state in which individual lipids can move laterally across the surface of the membrane with a high diffusion constant. Note that glycerophospholipids with saturated chains can also form Ld phase above the gel-transition temperature (Tg), but their T_g is higher than their counterparts containing one or more unsaturations.

In glycerophospholipids, the diacylglycerol part is connected to the head group via a phosphate group. The most abundant glycerophospholipid in mammalian cells, with a ratio superior to 50% of the phospholipids, is phosphatidylcholine (PC) (Figure 2-4). Phosphatidylcholines have a cylindrical shape and mostly all of natural ones have one *cis*-unsaturated fatty acid chain making them fluid at room temperature. Phosphatidylcholine is zwitterionic as it has both a positive and a negative charge at physiological conditions, making in principle PC with a net neutral charge at neutral pH. Other dominant phospholipids in cells are phosphatidylserine (PS) and phosphatidylethanolamine (PE) (Figure 2-4). Phosphatidylserine, a cylindrical shaped lipid, is a negatively charged phospholipid highly concentrated on the cytosolic leaflet of the plasma membrane while phosphatidylethanolamine is zwitterionic. PE exhibits a conical molecular geometry because of its small-sized polar headgroup as compared to the chain. Phosphatidylinositol lipids (PI) are an example of signaling lipids (Figure 2-4). They are present in smaller quantities and have likewise PS a negative charge and a cylindrical shape. PI lipids will be described in detail below (in section 2.1.3).

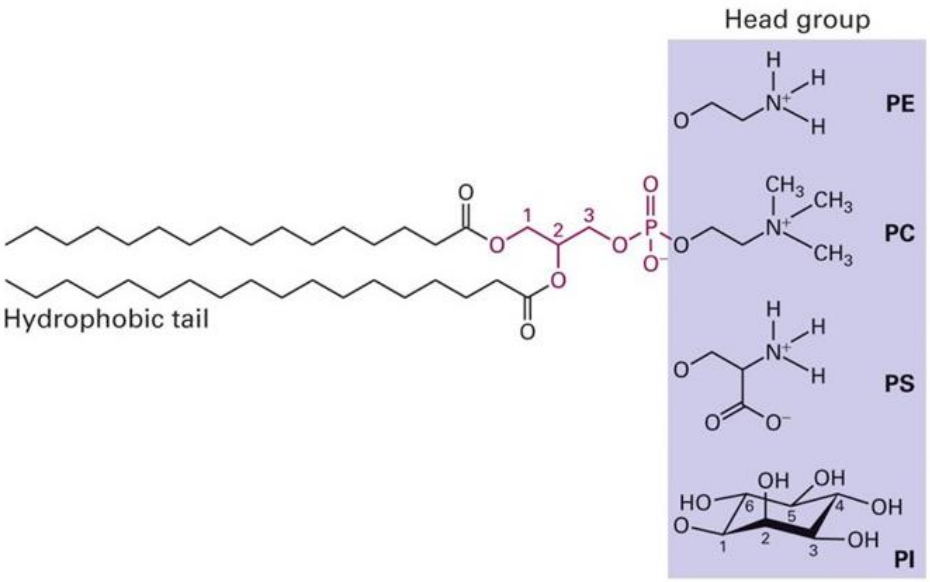

FIGURE 2-4: STRUCTURE OF MAJOR GLYCEROPHOSPHOLIPIDS
Examples of major glycerophospholipids in cells. Abbreviations: phosphatidylethanolamine (PE), phosphatidylcholine (PC), phosphatidylserine (PS) and phosphatidylinositol lipids (PI). The glycerophosphate part is shown in purple.

Sphingolipids have hydrophobic backbone composed of a sphingosine and a fatty acid. Sphingolipids have long and saturated hydrophobic tails. Hence, sphingolipids are more packed in comparison with glycerophospholipids with a *cis*-saturation, and form solid-like phases at usual temperatures. The major sphingolipids in mammalian cells are sphingomyelin (SM) and glycosphingolipids (GSL) (Neumann and van Meer 2008).

2.1.2 STEROLS

Sterols are lipids with an extremely small polar head group (hydroxyl OH group) and a bulky chain composed of a few carbon cycles and a short hydrocarbon chain. Similarly to phospholipids, sterols are considered as structural lipids and are not homogeneously distributed throughout the cells organelles. They are more abundant at the plasma membrane and almost absent from the ER (van Meer, Voelker et al. 2008). The most abundant sterol species in eukaryotic cells is cholesterol (Figure 2-5) that contains a tetracyclic ring, which confers a planar rigid conformation to the molecule. The addition of sufficiently high cholesterol concentration to lipids organized in a Ld phase leads to tighter packing of the membrane. The result is the emergence of another phase called the liquid ordered (Lo) phase (Figure 2-5). The Lo phase has intermediate properties, between solid and liquid, namely a higher conformational order and a lower diffusion than the Ld phase, but nevertheless a relatively high lateral diffusion of the lipids as compared to the solid phase (Figure 2-5) (Garcia-Saez and Schwille 2010). When added to solid-like phases of sphingolipids the opposite effect occurs, from the solid-like phase to the Lo fluid phase. Moreover, addition of cholesterol reduces the overall permeability of lipid bilayers to water (Rawicz, Smith et al. 2008).

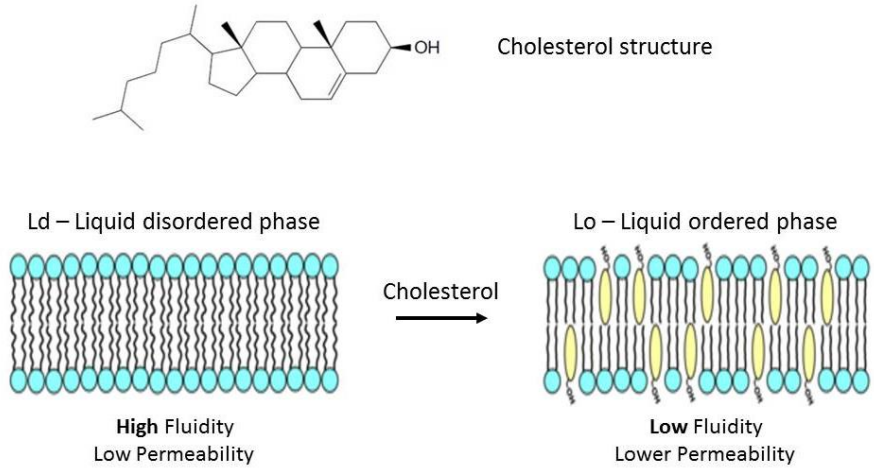

FIGURE 2-5: LIPID LIQUID DISORDERED (LD) PHASE VS. LIQUID ORDERED (LO) PHASE
Top: Structure of the cholesterol molecule. Bottom: effect of cholesterol addition in a lipid bilayer. Cholesterol induces changes in the bilayer organization: from liquid disordered with high membrane fluidity to liquid ordered phase with lower membrane fluidity and even lower organization. It also reduces membrane permeability.

2.1.3 PHOSPHOINOSITIDES

Phosphatidylinositol is synthetized in the endoplasmic reticulum by a PI synthase enzyme. Like other phospholipids, PI has a glycerol backbone esterified to two fatty acid chains, a phosphate and linked to a cyclic polyol *myo*-inositol headgroup that extends into the cytoplasm (Figure 2-4). The synthetized PI is then transported from the ER by PI transfer proteins and possibly vesicular trafficking to different

cellular membranes (Cockcroft and Carvou 2007). Once PI is distributed, it can be reversibly phosphorylated at different positions of the inositol ring, on the 3, 4 and/or 5 free hydroxyl group by cytoplasmic lipid kinases, yielding seven different phosphorylated derivatives of PI (Figure 2-6): PI(3)P, PI(4)P, PI(5)P, $PI(3,4)P_2$, $PI(3,5)P_2$, $PI(4,5)P_2$ and $PI(3,4,5)P_3$.

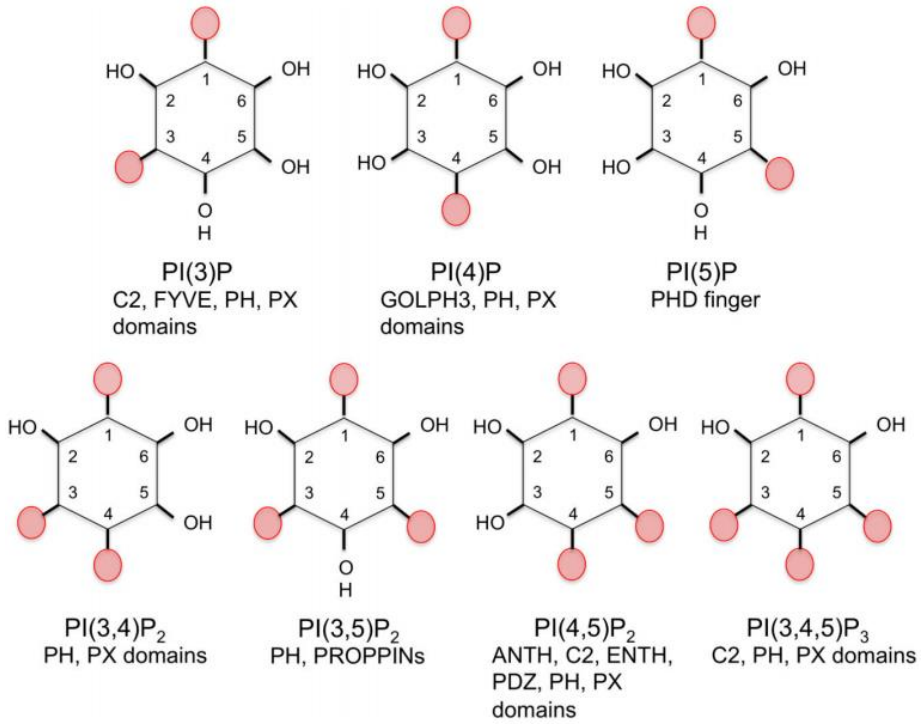

FIGURE 2-6: PHOSPHATIDYLINOSITOL DERIVATIVES (STAHELIN, SCOTT ET AL. 2014)
Examples of the seven phosphatidylinositol lipid derivatives corresponding to phosphorylation of the different positions 3,4 and 5. Abbreviations: phosphatidylinositol-3-phosphate PI(3)P, phosphatidylinositol-4-phosphate PI(4)P, phosphatidylinositol-5-phosphate PI(5)P, phosphatidylinositol-3,4-bisphosphate $PI(3,4)P_2$, phosphatidylinositol-3,5-bisphosphate $PI(3,5)P_2$, phosphatidylinositol-4,5-bisphosphate $PI(4,5)P_2$ and phosphatidylinositol-3,4,5-trisphosphate $PI(3,4,5)P_3$.

Phosphoinositides constitute a minority of the phospholipids family with a concentration lower than 1% in cell membranes. However, PI lipids play an important signaling role in cells. Each cellular membrane compartment uses a characteristic species of phosphoinositide (Figure 2-7). Each distinct phosphoinositide plays a specific role in cell signaling as it attracts phosphoinositide-specific and functionally important proteins to the membranes (Stahelin, Scott et al. 2014). Thus, by playing an instructional role in specific cytosolic protein recruitment to the different cell membranes, phosphorylated derivatives are involved in several cellular processes where they regulate membrane trafficking, cell growth and survival, cytoskeletal dynamics, etc. (Di Paolo, Moskowitz et al. 2004; Roth 2004). Phosphoinositides are thus considered as spatial landmarks.

$PI(4,5)P_2$ and PI(4)P are the most abundant of the PIP lipids. PI(4)P is enriched at the trans-Golgi network and $PI(4,5)P_2$ at the plasma membrane (Figure 2-7), in the range of approximately 5,000-20,000

molecules.μm^{-2} of the plasma membrane cytosolic leaflet (Falkenburger, Jensen et al. 2010). PI(4,5)P_2 plays a major role in signaling and membrane targeting. For instance, PI(4,5)P_2 present at the inner plasma membrane leaflet attract proteins that regulate the actin cytoskeleton. In addition, they act during endocytosis allowing membranes to recruit specific proteins that are involved in vesicle trafficking such as phospholipase C, protein kinase C which are implicated in membrane budding and fusion (Neumann and van Meer 2008; Stahelin, Scott et al. 2014).

PI(3)P and PI(3,5)P2 are present in smaller concentration, in early endosomes and late endosomes respectively (De Craene, Bertazzi et al. 2017) (Figure 2-7).

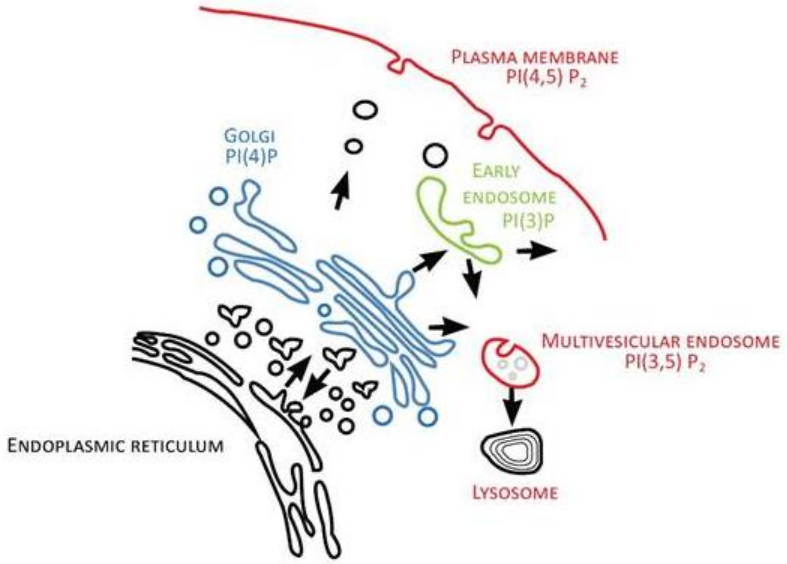

FIGURE 2-7: CELLULAR HETEROGENOUS DISTRIBUTION OF PI PHOSPHORYLATED DERIVATIVES IN THE DIFFERENT CELLULAR ORGANELLES (ROTH 2004)
The major phosphoinositide species are concentrated at distinct sites in intracellular membrane traffic pathways and may serve as organelle markers. The major concentration of phosphatidylinositol 4-phosphate P(4)P (blue) is at the Golgi complex, and very little free P(4)P is detected at the plasma membrane or on endosomes. P(3)P (green) is concentrated on early endosomes. The majority of phosphatidylinositol 4,5-bisphosphate P(4,5)P_2 (red) is at the plasma membrane at steady state. P(3,5)P_2 (orange) is found on multivesicular endosomes and lysosomes. Some phosphoinositides are found in the endoplasmic reticulum and in the nucleus, but probably do not play major roles in membrane traffic.

2.2 MEMBRANE MECHANICS

Because cellular membranes achieve essential biological functions by modulating their shapes, such as membrane trafficking and signaling, it is important to theoretically describe membrane mechanical properties, which represents a governing principle of cellular biological function.

In the 1970's, W. Helfrich and P. Canham proposed a theory on membrane elasticity. This theory embodies the idea that the elastic energy of a membrane is linked to its shape. Membranes are modeled as homogeneous two-dimensional fluid sheets, characterized by their surface tension σ, the mean and

Gaussian curvature moduli κ and κ_G, respectively. In most cases, their thickness about a few nanometers is considered to be negligible as compared to the length scale of their surface of about the micrometer order scale. If this approximation is satisfied then any membrane deformation can be decomposed into three main classes of membrane deformations, which are: stretching (changing the membrane area), bending, and shearing at constant area (Figure 2-8). The Canham-Helfrich Hamiltonian is derived by summing the three membrane deformation energies (stretching, bending and shearing, described below).

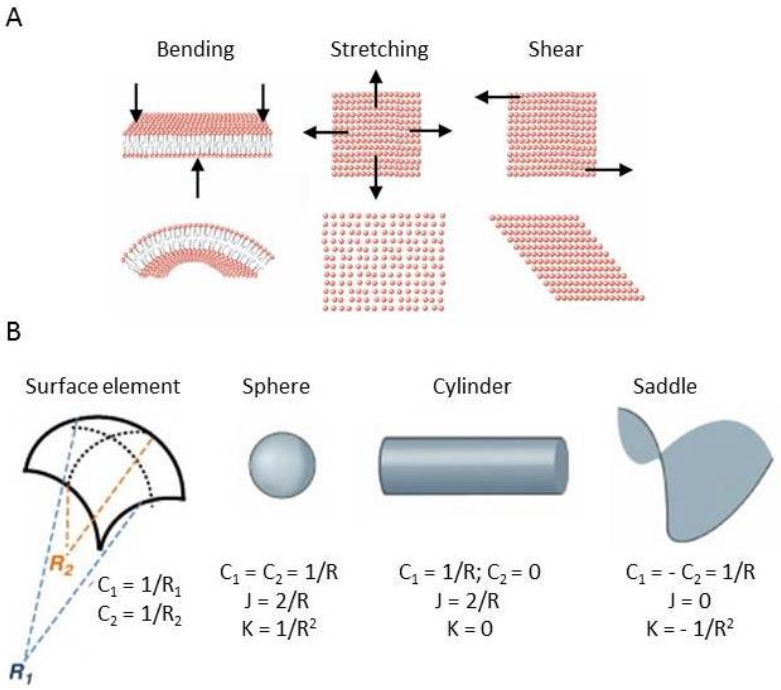

FIGURE 2-8: ELASTIC DEFORMATIONS OF A LIPID MEMBRANE
(A) Schematic representation of the three main membrane deformations. The arrows represent the direction of the deformation or stress, resulting in different strain responses: bending, stretching (or extension), and shear (Mijo Simunovic, PhD thesis, 2015).
(B) Examples of mean curvatures (J) and Gaussian curvatures (K) (Kozlovsky and Kozlov 2003).

2.2.1.1 STRETCHING A MEMBRANE

Stretching (or Extension and/or compression) are deformations involving a change in the membrane area (Figure 2-8). They correspond to the variation of the area in the membrane plane ΔA. If the original state of the membrane corresponds to its equilibrium state, stretching will be opposed by the internal stress in the membrane. The density of energy cost ($H_{stretching}$) of stretching a membrane is given following Hooke's law and can be expressed as a quadratic function of the relative deformation $\Delta A/A$:

$$H_{\text{stretching}} = \left(\frac{1}{2}\right)\chi\left(\frac{\Delta A}{A}\right)^2 \qquad (2\text{-}1)$$

Where χ is the stretching or the elastic area compressibility modulus and $\frac{\Delta A}{A}$ is the relative area variation. This parameter varies weakly with chain unsaturation or length and is of the order of 250 $mN.m^{-1}$ (Rawicz, Olbrich et al. 2000). However, it increases in the presence of sterols (Rawicz, Smith et al. 2008). The maximum stretching deformation on a bilayer does not usually exceed ~ 1-3 % in lipid bilayer, above which lysis by pore opening is observed. The order of magnitude of lysis tension is about the order of 10^{-3} $N.m^{-1}$ depending on the lipid composition of the membrane, (Sandre, Moreaux et al. 1999; Rawicz, Olbrich et al. 2000; Evans, Heinrich et al. 2003; Rawicz, Smith et al. 2008).

2.2.1.2 SHEARING A MEMBRANE

Shear is the stress involving a deformation of the material in two parallel opposite directions at constant surface area (Figure 2-8). A membrane resists such a deformation only if the relative positions of its constituent molecules are fixed by some lattice structure. Thus, fluid membranes are, by definition, unable to sustain shear deformations (Zeman, Engelhard et al. 1990). But shear deformations can become relevant in the case of gel-phase bilayers or if the membrane is coupled to an external lattice structure such as the cytoskeleton. Areal density of energy (H_{shear}) associated to shear stress can be deduced from Hook's law:

$$H_{\text{Shear}} = \left(\frac{1}{2}\right) \mu \left(\lambda^2 + \lambda^{-2} - 2\right) \qquad (2\text{-}2)$$

Where $\lambda = (L_0 + \Delta L)/L_0$ is the lateral extension rate, μ the shear modulus (expressed in $J.m^{-2}$). In the case of fluid membranes, shearing deformations are negligible compared to stretching and bending and is ignored.

2.2.1.3 BENDING A MEMBRANE

Membrane bending is the dominant deformation for fluid lipid bilayers. To describe membrane bending, one must relate to the notion of membrane curvature, which corresponds to any deformation out of the membrane plane (Figure 2-8). The bending energy derives from the curvature of the membrane: at a given point of the surface, one can define two perpendicular radii of curvature R_1 and R_2. The two principal curvatures are then defined as the inverse of these radii, with a positive or negative sign, which corresponds to the 2 radii oriented in the same or opposite direction relative to the surface, respectively. The two principal curvatures are thus $C_1 = 1/R_1$ and $C_2 = 1/R_2$. Thus, if the radius is very large (i.e., the membrane is nearly flat), the curvature is small, and vice versa. The sum of the principal curvatures C1 and C2 is the mean curvature $J = C_1 + C_2$. And, the product of the principal curvatures is the Gaussian Curvature $K = C_1 \times C_2$. The mean curvature J and the Gaussian Curvature K are local parameters that describe the membrane shape.

For example, for a sphere of radius R, the mean curvature is 2/R and the Gaussian curvature is $1/R^2$, whereas for an infinite cylinder of radius R, the mean curvature is 1/R and the Gaussian curvature is equal to zero at every point of the cylinder surface. Finally, a saddle point has the particularity of having two curvatures of opposite signs, a positive and a negative curvature. Thus a saddle point has a negative Gaussian curvature (Figure 2-8).

To define the capacity of a membrane to bend, two intrinsic parameters must be considered: κ, the bending rigidity modulus (or bending stiffness of the membrane) ranging from 10 to 100 k_BT and κ_G, the Gaussian bending rigidity modulus (or Gaussian Curvature modulus). Both depend on the membrane composition and they represent the energetic cost to generate principal curvature (by increasing J) and Gaussian curvature (by increasing K). The bending modulus depends on the aliphatic chain length and degree of unsaturation (Evans and Rawicz 1990; Rawicz, Olbrich et al. 2000; Marsh 2006; Rawicz, Smith et al. 2008), for instance it increases from 13 to 30 k_BT when the PC lipid chains contain 22 carbon atoms instead of 13 and decreases to 10 k_BT for cis-polyunsaturated PC lipid (Rawicz, Olbrich et al. 2000). The corresponding areal density of energy ($H_{curvature}$) is given by:

$$H_{\text{curvature}} = \left(\frac{1}{2}\right)\kappa\,(J - C_0)^2 + \kappa_G\,C_1\,C_2 \qquad (2\text{-}3)$$

Where $C_1 = 1/R_1$ and $C_2 = 1/R_2$ are the two principal local membrane curvatures describing the shape of the membrane at a given point, C_0 is the spontaneous curvature (i.e. the curvature of the membrane in the absence of any external stress). κ is the bending rigidity modulus (expressed in J or in k_BT unit) and κ_G is the Gaussian bending rigidity modulus (expressed in J or in k_BT unit).

The bending and the stretching moduli are related through membrane thickness (h) according to the following relation (Rawicz, Olbrich et al. 2000):

$$\kappa = \frac{\chi\,h^2}{24} \qquad (2\text{-}4)$$

Symmetrical membrane lipid bilayers are expected to be flat in the absence of external stress. Non-symmetrical bilayers adopt a particular curvature in the same condition namely the spontaneous curvature C_0. The spontaneous curvature C_0 is another intrinsic mechanical measure of the membrane and represents the curvature that the membrane would adopt when free of external constraints, i.e. the membrane mean resting curvature. For example, a symmetrical membrane, made of two identical lipid bilayers, would have in the absence of external stress a zero-spontaneous curvature. Whereas, a non-zero-spontaneous curvature occurs when the membrane has a variable composition of lipids incorporated in the two leaflets and the sum of the spontaneous curvatures of both leaflets is not equal to zero (Zimmerberg and Kozlov 2006). Other ways leading to a non-zero-spontaneous membrane

curvature are: (i) by introducing asymmetrical shaped objects into the membrane such as trans-membrane proteins (McMahon and Gallop 2005; Zimmerberg and Kozlov 2006; Campelo, McMahon et al. 2008) or (ii) by exposing the lipid bilayer leaflets to solutions containing different compositions of ions, particles or proteins (Lipowsky 1995).

According to the Gauss-Bonnet theorem, Gaussian curvature is conserved if the membrane bends without a change in its topology (topological invariant). Consequently, as long a membrane is not submitted to fusion of fission, the membrane bending energy per unit area can be expressed only using the mean curvature:

$$H_{\text{curvature}} = \left(\frac{1}{2}\right)\kappa\,(J - C_0)^2 \tag{2-5}$$

Measurements of the bending rigidity of lipid bilayers can for instance be achieved by micropipette aspiration of Giant Unilamellar Vesicles (GUVs) (described in chapter 0) with typical resulting values of the order of $\kappa \approx 20$ kBT.

By including, over the surface of the fluid membrane, the contributions of the deformation energies of stretching and bending (described above) we derive the Canham-Helfrich Hamiltonian:

$$H = \int_A ds \left(\left(\frac{1}{2}\right)\kappa\,(J - C_0)^2 + \kappa_G K + \sigma\right) \tag{2-6}$$

This formula represents the free energy of a membrane with a surface area A, a bending modulus κ, a Gaussian bending rigidity modulus κ_G and a tension σ (described below).
This formula represents the free energy of a membrane with a surface area A, a bending modulus κ, a Gaussian bending rigidity modulus κ_G and a tension σ (described below).

2.3 MEMBRANE TENSION

Another important parameter to describe membranes that can be added to Canham-Helfrich Hamiltonian is the one due to membrane lateral tension (σ), the stress associated to change in membrane area. Membrane tension is linked to the stretching energy of the membrane.
$\sigma = H$Another important parameter to describe membranes that can be added to Canham-Helfrich Hamiltonian is the one due to membrane lateral tension (σ), the stress associated to change in membrane area. Membrane tension is linked to the stretching energy of the membrane.

$$\sigma = \frac{\partial H_{\text{stretching}}}{\partial A} \tag{2-7}$$

Due to their low bending modulus, membrane deformation modes can be excited by thermal motion. Membrane fluctuations were first recognized at the origin of the flickering of red blood cells (Brochard

and Lennon 1975). At very low tensions, membrane fluctuations can be optically detected since they can have amplitudes up to a few microns (Pecreaux, Dobereiner et al. 2004). Stretching a fluctuating membrane tends to flatten its surface. Once the surface is fully flattened, further stretching pulls the lipids apart, further increasing the tension of the membrane. With these intuitive observations, we easily see that two regimes have to be considered to describe the stretching deformations: (i) the entropic regime at low tensions where the membrane is fluctuating and (ii) the enthalpic regime at higher membrane tensions where the membrane has a purely elastic behavior.

i. The entropic regime

When a membrane is stretched, the resulting change in membrane area is first due to the excess area stored in the thermal fluctuations of the membrane. The maximum amplitude of these fluctuations U_{max} can be derived from the theorem of energy equipartition and the Canham-Helfrich Hamiltonian:

$$U_{max} \propto \sqrt{\left(\frac{k_B T}{\sigma}\right) \ln \frac{L}{a}} \tag{2-8}$$

Where *L* is the macroscopic length scale of the membrane (typically about 10 µm), *a* the membrane microscopic length scale (typically about 0.5 nm), k_B is the Boltzmann constant and *T* the temperature. Note that in a system at a temperature T, each microscopic degree of freedom has a thermal energy on the order of $(\frac{k_B T}{2})$, with $k_B T = 4 \times 10^{-21}$ J at room temperature. It thus clearly appears in this formula that membrane tension tends to reduce the amplitude of fluctuations. More precisely the relationship between the relative membrane area variation $\alpha = \frac{\Delta A}{A}$ and membrane tension can be calculated from fluctuations spectrum analysis (Evans and Rawicz 1990):

$$\frac{\Delta A}{A} = \frac{k_B T}{8\pi\kappa} \ln \frac{\frac{\pi^2}{a^2} + \frac{\sigma}{\kappa}}{\pi^2 L^2 + \frac{\sigma}{\kappa}} \tag{2-9}$$

For low tensions, when the condition $\frac{\kappa\pi^2}{L^2} \ll \sigma \ll \frac{\kappa\pi^2}{a^2}$ is satisfied, the relationship simplifies:

$$\frac{\Delta A}{A} = \frac{k_B T}{8\pi\kappa} \ln \frac{\pi\kappa}{\sigma a^2} \tag{2-10}$$

If we consider a reference state (σ_0, A_0) and a final state (σ, A) with a variation of the excess area $\Delta\alpha$, membrane tension is related to $\Delta\alpha = \alpha - \alpha_0$ by:

$$\sigma = \sigma e^{\left(\frac{8\pi\kappa}{k_B T}\Delta\alpha\right)} \tag{2-11}$$

ii. The enthalpic regime

When all the excess area stored in the fluctuations of the membrane has been unfolded, the stretching energy is then mainly due to variation in membrane tension $\boldsymbol{\sigma}$ (Helfrich and Servuss 1984; Evans and Rawicz 1990).

With $\sigma = \frac{\partial H_{\text{stretching}}}{\partial A}$ and the stretching energy per unit area $H_{\text{stretching}} = \left(\frac{1}{2}\right) \kappa_{\text{A}} \left(\frac{\Delta A}{A}\right)^2$, tension in this enthalpic regime is given by:

$$\sigma = K_{\text{a}} \left(\frac{\Delta A}{A}\right) \tag{2-12}$$

Indicating that in the enthalpic regime the variation in area is linear with membrane tension.

Finally the relative change in area due to stretching is the sum of both contributions: the entropic regime (non-linear with tension) and the enthalpic regime (linear with tension) (Evans and Rawicz 1990):

$$\alpha \approx \frac{kT}{8\pi\kappa} \ln(1 + cA\sigma) + \frac{\sigma}{\chi} \tag{2-13}$$

The constant c can be calculated exactly if we consider the membrane being plane ($c = 1/\pi^2$) or taking into account its spherical shape ($c = 1/24\pi$) (Evans and Rawicz 1990). This expression was confirmed with a renormalization approach integrating the fluctuations at all scales (Fournier, Ajdari et al. 2001).

2.4 MEMBRANE FISSION

As described previously, cellular membranes undergo continuous rearrangements. Many cellular processes such as vesicular trafficking, exocytosis, endocytosis, cell division, entry and release of enveloped virus, etc., involve membrane budding and fission events. Intracellular vesicular trafficking is used to transfer cargoes between membranes in the secretory and the endocytic pathways. The generation of these vesicles occurs in three steps: cargo sorting from the donor compartment, membrane budding (or tubulation) and finally membrane separation from the donor compartment by a fission event. Membrane fission was first studied and discussed in the context of dynamin-induced membrane fission on clathrin-coated vesicles at the plasma membrane. But, there are many scission processes at the surface of organelles that are dynamin-independent. This is the case for the scission of COPI and COPII coated-vesicles at the Golgi apparatus and the ER, respectively, and of course, of the scission of vesicles in MVBs by the ESCRT complexes.

When a bud is formed at the surface of a membrane, fission reaction proceeds as follows: (i) constriction of the budding vesicle with formation of a highly curved neck (Figure 2-9 / A and B), which can be mediated by different means (ii) merge of the contacting monolayers in a stalk intermediate

(hemifission) (Figure 2-9 / C) and (iii) disappearance of the fission stalk and completion of the reaction (Figure 2-9 / D). Hemifission (similarly to the hemifusion-like pathway) is an intermediate stage of the fission reaction, where the opposing internal leaflets of the neck are fused, but not the external ones; it requires a transient membrane disruption which is opposed by the hydrophobic forces preserving the integrity and continuity of the lipid assembly (Chernomordik and Kozlov 2003; Kozlovsky and Kozlov 2003; Chernomordik and Kozlov 2005; Kozlov, McMahon et al. 2010). The formation of this hemifission state allows the accomplishment of membrane fission without compromising the integrity of the bilayer by exposure of the content to the external milieu or even content leakage (Matsuoka, Orci et al. 1998; Takahashi, Kishimoto et al. 2002; Frolov, Dunina-Barkovskaya et al. 2003).

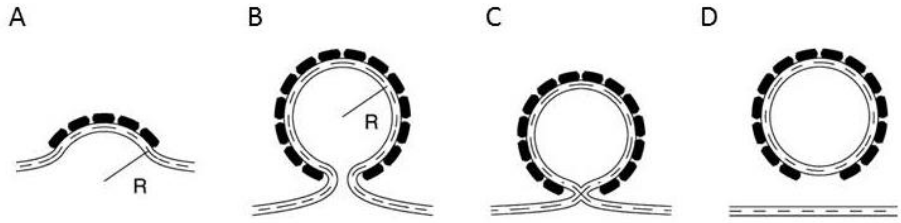

FIGURE 2-9: THE DIFFERENT INTERMEDIATE STEPS LEADING TO MEMBRANE FISSION (KOZLOVSKY AND KOZLOV 2003)
(A) The coated bud at an initial stage of the coat protein self-assembly.
(B) Constricted neck.
(C) Hemifission intermediate.
(D) Separated coated vesicle.

Because the different intermediate steps leading to membrane fission involve strong local bending and eventually changes in topology, a low bending modulus κ and forces leading to membrane constriction promote membrane fission. However, membrane fission is energetically unfavorable due to membrane self-sealing properties, and there is an energy barrier to overcome for the membrane to undergo scission. Yonathan Kozlovsky and Michael M. Kozlov presented in 2003 the first complete theoretical analysis for membrane fission (Kozlovsky and Kozlov 2003). This fission model is based on the elastic energy of the membrane. The initial state corresponds to a flat membrane with an area A and the final post-fission state to a vesicle of radius R + a flat membrane with an area A - $4\pi R^2$. The fission energy (minimal bending energy to form a vesicle) is the sum of the energies of the initial and final state (post-fission state) and can be deduced using the Canham-Helfrich Hamiltonian:

$$\int_{vesicle} ds \left(\frac{1}{2}\kappa\left(\frac{1}{2R}\right)^2 + \frac{\kappa_G}{R^2} + \sigma_{\text{vesicle}}\right) + \int_{flat\ membrane} ds\ (\sigma_{\text{flat}}) \tag{2-14}$$

$$= 4\pi\left(\frac{\kappa}{8} + \kappa_G\right) + \sigma_{\text{vesicle}} 4\pi R^2 + \sigma_{\text{flat}}(A - 4\pi R^2) \tag{2-15}$$

Because of the topological change upon scission, the Gaussian curvature term must be kept in the Hamiltonian. The Gaussian energy is given by the equation: $E = 2\pi\kappa_G\chi$, with χ being the Euler characteristic. X is defined as twice the number of independent compartments (N) minus the number of handles or holes in the membrane (g) : $\chi = 2\,(N - g)$. Before fission, χ=2 and after fission χ=4 making the energy of the Gaussian curvature equal to: $E = 4\pi\kappa_G$. If the tension remains constant during the fission process ($\sigma = \sigma_{vesicle} = \sigma_{flat}$) then the fission energy is equal to $4\pi\left(\frac{\kappa}{8} + \kappa_G\right)$. Thus this energy only depends on the bending rigidity modulus κ and on the Gaussian bending rigidity modulus κ_G which has been suggested to be negative and of the order of $\kappa_G \approx -15 k_B T$ (Siegel and Kozlov 2004). For membrane fission to occur, the energy of the final state must be lower than the energy of the initial state; i.e. a negative term for the fission energy, which is the case if we consider $\kappa = -0.8\,\kappa_G$. Thus, the fact that the Gaussian bending rigidity modulus κ_G is negative implies that the Gaussian energy favours spontaneous fission, regardless of the membrane shape. Indeed, the energy of Gaussian curvature is only dependent on the topology of the membrane.

Additionally, even if the post fission state is energetically favourable with respect to the pre-fission state, a large energy barrier could arrest the system kinetically in a bud configuration. Kozlovsky and Kozlov predicted that hemi-fission occurs when the constriction limits bud neck to a radius of the order 2.7-2.9 nm, thus to a lumen radius of the order of 1 nm.The hemifission intermediate involving rearrangements of the lipid bilayers, is the energy barrier as it that has to be surpassed by thermal fluctuations on the membrane to spontaneously lead to kinetically feasible fission (Kozlovsky and Kozlov 2003) and is about 40 $k_B T$ (Kuzmin, Zimmerberg et al. 2001; Campelo and Malhotra 2012). Indeed, when hemi-fission is reached, fission should spontaneously occur.

This theoretical modeling of membrane fission has been tested for dynamin-driven scission. This protein was discovered in 1989 (Shpetner and Vallee 1989); Dynamin is a 100 kDa GTPase that self-oligomerizes into contractile helical polymers (Hinshaw and Schmid 1995) wrapping around the neck of budding endocytic vesicles in plant and animal cells (Hinshaw and Schmid 1995; Sweitzer and Hinshaw 1998; Schmid and Frolov 2011; Ferguson and De Camilli 2012). Dynamin converts the energy of GTP hydrolysis into progressive severing of the lipid bilayer neck leading to membrane fission (Chappie, Mears et al. 2011; Morlot, Galli et al. 2012). Dynamin-mediated fission proceeds through a hemi-fission state according to different authors (Bashkirov, Akimov et al. 2008; Morlot, Galli et al. 2012; Shnyrova, Bashkirov et al. 2013; Mattila, Shnyrova et al. 2015), but the debate on the scission mechanism still exists today (for a recent state-of-the-art of the question, see (Antonny, Burd et al. 2016).

Dynamin-mediated scission has been reconstituted *in vitro* using the nanotube pulling assay (Morlot, Galli et al. 2012). Using purified dynamin and GTP, it was possible to measure the characteristic time

before scission, and from this, to estimate the reduction of the energy barrier upon GTP-mediated constriction. Morlot et al could not directly evidence the hemi-fission state leading to scission but nevertheless showed that the characteristic fission time is increased when the membrane bending rigidity is increased and decreased when membrane tension increases, as expected from the theoretical model.

CHAPTER 3. THE ESCRT-DEPENDENT MEMBRANE REMODELLING PROCESSES

3.1 ESCRT MACHINERY IN SACCHAROMYCES CEREVISIAE

The endosomal sorting complex required for transport (ESCRT) complexes were discovered and named, in 2001 by Scott Emr's group, for their main role in ubiquitin-dependent sorting from endosomes to lysosomes in the multivesicular body biogenesis (MVB) (Figure 3-1) (Katzmann, Babst et al. 2001).

The machinery was first identified in yeast by means of genetic isolation of mutants that cause defective protein sorting to the vacuole, the functional yeast equivalent of the lysosome (Bankaitis, Johnson et al. 1986; Rothman, Howald et al. 1989). These mutants, called "class E vps (Vacuolar Protein Sorting) mutants", caused a major morphological change of the vacuole (Raymond, Howald-Stevenson et al. 1992). Most of the class E vps genes were later found to act in succession to concentrate trafficking cargoes and include them in forming late endosomes, also termed multivesicular bodies (MVB). The latter, also called multivesicular endosomes (MVE), are specialized compartments within endosomes that are delivered into lysosomes for protein degradation (Katzmann, Babst et al. 2001). They consist of a limiting membrane and small intraluminal vesicles (ILVs).

Like all vesicle budding reactions, the formation of intraluminal MVB vesicles requires three successive steps, respectively, cargo recognition and sorting, membrane budding and, vesicle separation from a donor membrane which in this case is the endosome (Adell and Teis 2011).

In opposition to the formation of secretory and endocytic vesicles, where membrane budding and fission occur into the cytosol, the MVB formation requires budding away from the cytosol (Katzmann, Babst et al. 2001).

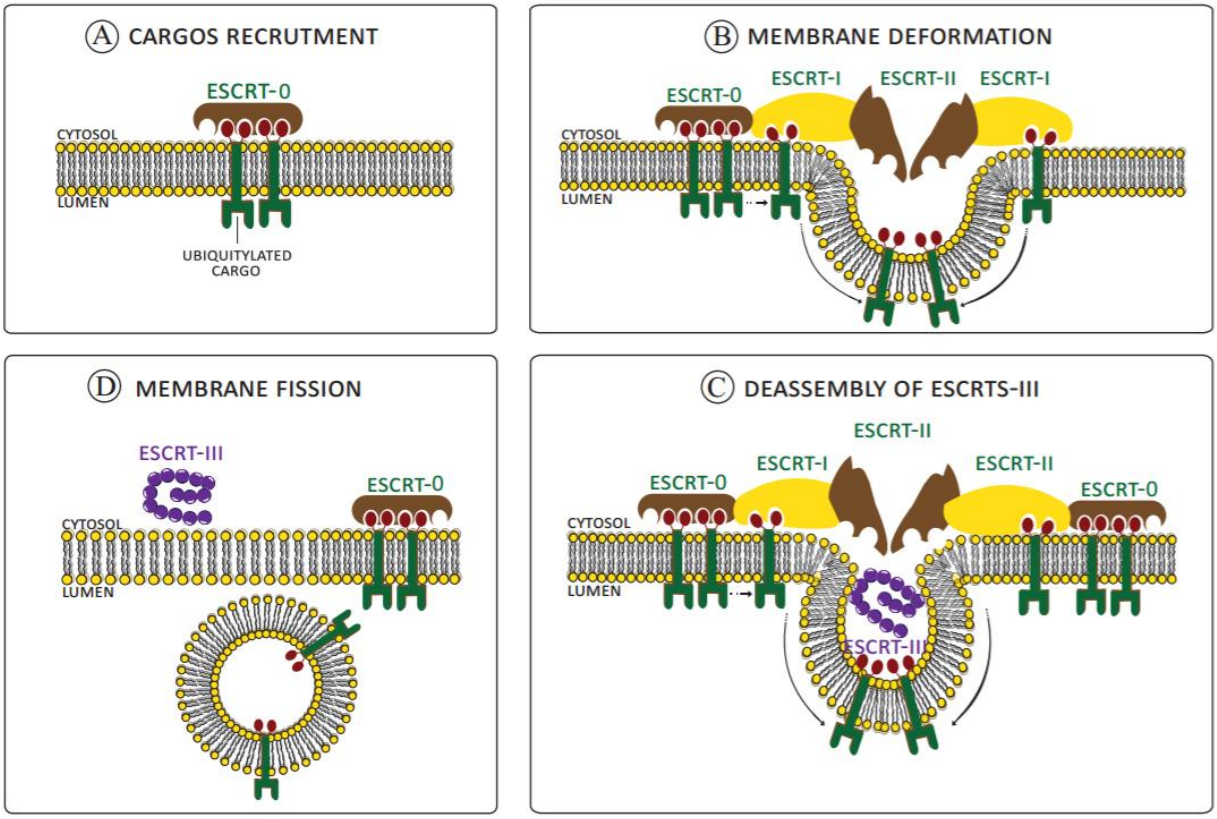

FIGURE 3-1: THE ESCRT COMPLEXES

Schematic illustration of the ESCRT machinery leading to membrane fission. ESCRT-0, -I and -II are responsible for cargo recruitment and membrane deformation (A) (B). ESCRT-III is then recruited to constrict at the membrane neck and induce membrane scission (C). The ESCRT-III subunits are disassembled before vesicle release and recycled back to the cytoplasm (D).

The different ESCRT complexes assemble sequentially on the cytosolic side of the endosomal membrane to sort and concentrate ubiquitinated membrane proteins into vesicles, which accumulate inside endosomes (Figure 3-2) (Teis, Saksena et al. 2008; Saksena, Wahlman et al. 2009; Hurley and Hanson 2010; Henne, Buchkovich et al. 2011). The ESCRT complexes are therefore crucial for membrane protein turnover and cell regulation.

ESCRT complex	Proposed Function	Evolutionary origin	Yeast	Human
ESCRT-0	**Ubiquitinated cargo recognition** Membrane binding through PI(3)P lipids	Opisthokonta	Vps27 Hse1	HRS STAM1, STAM2
ESCRT-I	**Upstream adapter** Binds ESCRT-0, -II and ubiquitinated cargo	Eukaryotes	Vps23 Vps28 Vps37 Mvb12	TSG101 Vps28 Vps37A, B, C, D Mvb12A, B
ESCRT-II	**Bridging adapter** Binds ESCRT-I and nucleates ESCRT-III Binds ubiquitinated cargo and PI(3)P		Vps22 Vps25 Vps36	EAP30 EAP20 EAP45
ESCRT-III	**Membrane sculpting** (Bud constriction and membrane scission)	Archaea	Vps20 Snf7 Vps24 Vps2	CHMP6 CHMP4A, B, C CHMP3 CHMP2A, B
Vps4 - Vta1	**ESCRT-III disassembly** (Membrane remodelling?)		Vps4 Vta1	Vps4A, B Vta1 (LIP5)

FIGURE 3-2: COMPOSITION OF THE ESCRT COMPLEXES IN THE MVB PATHWAY
Yeast proteins names and their Homo sapiens homologues are detailed for each ESCRT complex, as well as their proposed function and recruitment order in the ESCRT pathway.

The previously described genetic analysis in the yeast *Saccharomyces cerevisiae* identified precisely 17 class E genes that form the core of the ESCRT machinery. The ESCRT-0, -I and -II function early in the MVB pathway and are sequentially recruited as stable soluble hetero-oligomers preformed in the cytosol to cargo-laden endosomes (Saksena, Sun et al. 2007; Williams and Urbe 2007). ESCRT-0 is a 1:1 heterodimer composed of Vps27and Hse1 proteins that interact together via long coiled-coil GAT domains. Vps27 binds to PI(3)P lipids enriched at endosomes, thus directing the entire ESCRT-0 complex to endosomes (Figure 3-3). Together with Hse1, Vps27 binds to ubiquitin-tagged membrane proteins destined for degradation. The ESCRT-0 complex can bind up to five different ubiquitynilated cargo proteins or multiple ubiquitin moieties of poly-ubiquitinated cargos. So, by binding ubiquitinated cargos, PI(3)P membrane lipids and by recruiting the ESCRT-I complex through the direct binding with the ESCRT-I protein Vps23, Vps27 appears to be fundamental for the initiation of the MVB pathway.

ESCRT-I is a soluble hetero-tetramer consisting of Vps23, Vps28, Vps37 and Mvb12 proteins and forms a rod-like shaped complex. ESCRT-II, on the other hand, is a hetero-tetrameric protein complex consisting of Vps36, Vps22 and two Vps25 subunits (Figure 3-3). ESCRT-II complex adopts a Y-shaped structure with the two Vps25 subunits forming the arms of the Y-shaped heterotetramer. ESCRT-I and ESCRT-II complexes interact together through the binding of Vps28 with Vps36, and assemble in solution into a 1:1 supercomplex. In addition to binding simultaneously to PI(3)P, to ubiquitin and accordingly sorting cargo, in vitro studies have shown that ESCRT-I and ESCRT-II induce the formation of intraluminal

vesicle budding of 20 - 40 nm diameter (Murk, Humbel et al. 2003; Hurley and Hanson 2010; Wollert and Hurley 2010) (Figure 3-3). Thus, ESCRT-0, -I, and -II are responsible for cargo binding, early membrane bending and are therefore considered as the generators of membrane necks that can then serve as substrates for ESCRT-III-mediated fission (Figure 3-4).

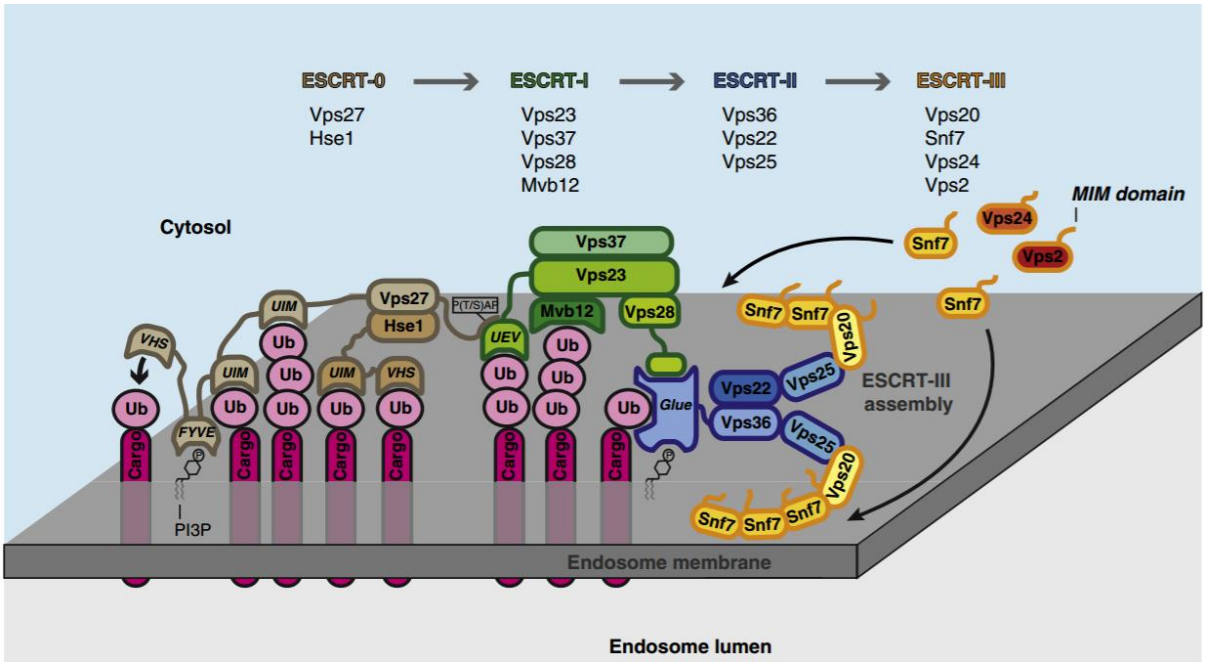

FIGURE 3-3: MODEL FOR CARGO CLUSTERING AND SEQUENTIAL ASSEMBLY OF THE ESCRT COMPLEXES (SCHMIDT AND TEIS 2012).
ESCRT-0 (brown) initiates the MVB pathway. ESCRT-0 binds to PI3P and clusters ubiquitinated membrane proteins via multiple ubiquitin-binding domains. ESCRT-I (green) is recruited by ESCRT-0 (Vps27) and binds to ubiquitinated cargo. ESCRT-II (blue) interacts via the Glue domain of Vps36 with ESCRT-I, PI3P and cargo. The ESCRT-II subunit Vps25 serves as a nucleation point for stepwise assembly of the filamentous ESCRT-III complex (yellow–orange), which leads to membrane scission.

In yeast, ESCRT-III complex consists of four core components Vps20, Snf7, Vps24 and Vps2 and three accessory components Did2, Vps60 and Ist1. The ESCRT-III core components remain monomeric in the cytosol and only assemble into two sub-complexes, formed by Vps20+Snf7 and Vps2+Vps24, upon activation and membrane binding. ESCRT-II complex has two binding sites to the ESCRT-III complex and serves as the adaptor that initiates ESCRT-III assembly. Both Vps25 subunits could recruit and activate the ESCRT-III subunit Vps20 (Teo, Perisic et al. 2004). Once recruited and activated, Vps20 initiates ESCRT-III filament assembly by recruiting Snf7, the most abundant ESCRT-III subunit present with at least 50% of the total complex components (Teis, Saksena et al. 2008; Henne, Buchkovich et al. 2012). By inducing conformational changes within Snf7, Vps20 promotes the movement of the inhibitory helix away from the core, thereby exposing and enabling the Snf7 core regions to interact with other ESCRT-III subunits. Snf7 builds then the main polymer scaffold and associates with Vps24 (Teis, Saksena et al. 2008). This latter recruits the last ESCRT-III core component Vps2 and stops Snf7 oligomerization (Figure 3-4). The growing ESCRT-III protein lattice recruits deubiquitinases, which mediate cargo

deubiquitylation and ubiquitin recycling prior to vesicle formation (Schmidt and Teis 2012). Once assembled, the ESCRT-III proteins induce membrane constriction at the neck and induce membrane scission and fusion of MVBs with lysosomes releases ILVs into the lumen of the lysosome where they are degraded together with their contents (Adell, Vogel et al. 2014) (Figure 3-4). Vps2 controls the complex disassembly by direct interaction to the MIT domain of Vps4 via its carboxyl-terminus MIM1 domain (Babst, Katzmann et al. 2002; Obita, Saksena et al. 2007; Teis, Saksena et al. 2008). Recent studies suggest that Vps4 takes part actively to the scission process by favoring the dynamical remodeling of the complex (Adell, Migliano et al. 2017; Mierzwa, Chiaruttini et al. 2017). Quantitative fluorescence lattice light-sheet experiments have shown that ESCRT-III subunits polymerize rapidly on yeast endosomes, together with the recruitment of at least two Vps4 hexamers and that productive budding events required at least two additional Vps4 hexamers (Christ, Wenzel et al. 2016). These experiments have also shown that membrane budding was associated with continuous, stochastic exchange of Vps4 and ESCRT-III components, rather than steady growth of fixed assemblies, and depended on Vps4 ATPase activity (Christ, Wenzel et al. 2016). Moreover, tomographic electron microscopy demonstrated that acute disruption of Vps4 recruitment stalled membrane budding (Christ, Wenzel et al. 2016).

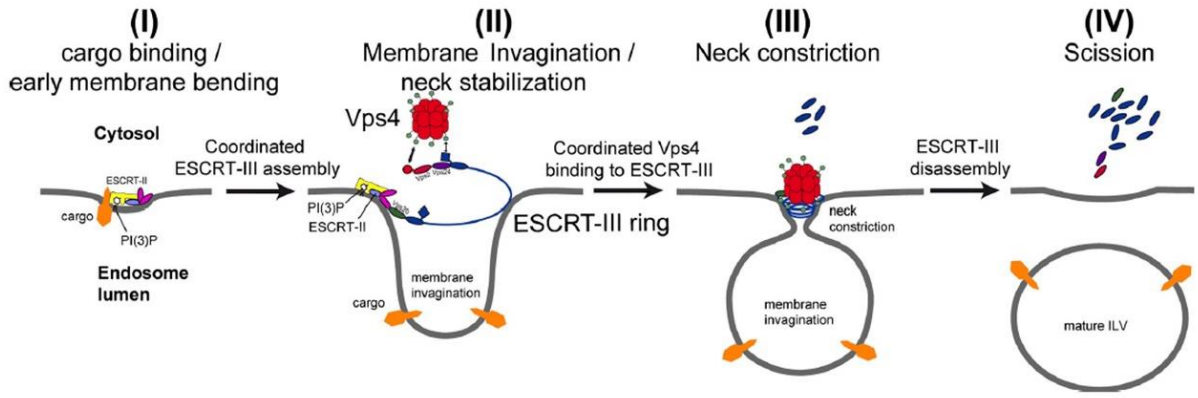

FIGURE 3-4: PROPOSED MODEL FOR THE MVB VESICLE FORMATION BY THE ESCRT-III COMPLEX (ADELL, VOGEL ET AL. 2014).
First, the ESCRT-0, -I and -II complexes are responsible for ubiquitinated cargo clustering and early membrane bending/deformation (I). Second, the ESCRT-III complex is recruited to induce further membrane invagination/budding leading to neck constriction (II) (III). This step is coordinated with the AAA-ATPase Vps4 binding to ESCRT-III (III). Third, just before achieving membrane scission and vesicle release, the ESCRT-III complex is disassembled by the action of Vps4 (IV).

3.2 ESCRT MACHINERY IN HOMO SAPIENS

In yeast, the ESCRT complexes are only involved in receptor trafficking regulation through endosomes (MVB pathway), while in *Homo Sapiens*, there is a large diversification of the processes as they play multiple roles in topologically equivalent membrane scission events such as in MVB formation (Babst, Davies et al. 2011), budding and release of some enveloped viruses from the plasma membrane of

infected cells (Morita, Sandrin et al. 2011), abscission in late step of cytokinesis (Morita, Sandrin et al. 2007), biogenesis of microvesicles and exosomes, plasma membrane wound repair (Scheffer, Sreetama et al. 2014), neuron pruning (Loncle, Agromayor et al. 2015), dendritic spine formation, nuclear envelope repair, nuclear envelope sealing during telophase (Olmos, Hodgson et al. 2015; Vietri, Schink et al. 2015) (Figure 3-5).

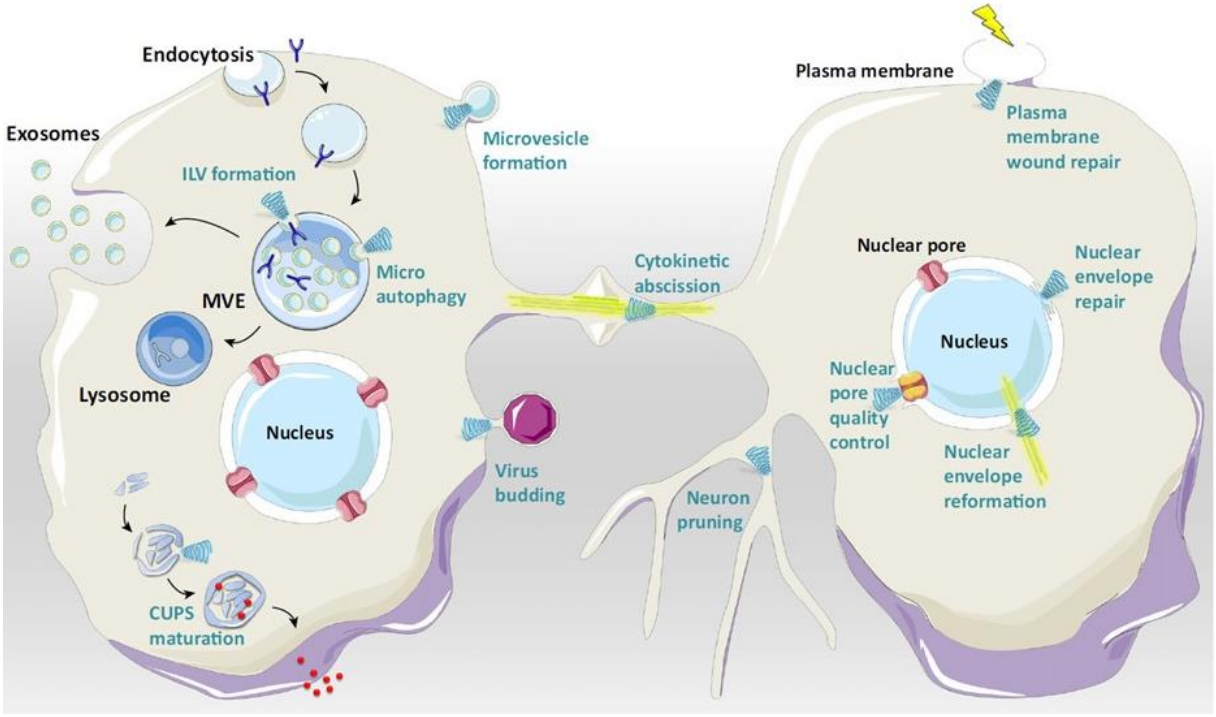

FIGURE 3-5: OVERVIEW OF ESCRT-DEPENDENT PROCESSES (CHRIST, RAIBORG ET AL. 2017)
Overview of the cellular membrane scission processes mediated by ESCRT-III that include biogenesis of multivesicular endosomes, budding of enveloped viruses, cytokinetic abscission, neuron pruning, plasma membrane wound repair, nuclear pore quality control, nuclear envelope reformation, and nuclear envelope repair.

3.2.1 ESCRT ROLE IN TERMINAL STAGES OF CYTOKINESIS

Cytokinesis, the last step of cell division, involves large-scale cleavage of the plasma membrane. This process is characterized by the constriction of an acto–myosin contractile ring leading to the ingression of the plasma membrane at the cell equator, which partitions two cytoplasmic domains of emerging sister cells that remain connected by a membrane tube about 1 µm wide, called the intercellular bridge (Figure 3-6) (Eggert, Mitchison et al. 2006; Steigemann and Gerlich 2009; Guizetti and Gerlich 2010; Green, Paluch et al. 2012). This process divides the organelles and most of the cytoplasm equally between the two daughter cells, but the microtubules forming the spindle remain in the intercellular bridge. To separate the daughter cells and finalize the cellular division process, the microtubules, mostly enriched at the center of the intercellular bridge, in a dark zone region named the “midbody”, must be

severed and the plasma membrane must be sealed (Figure 3-6). Furthermore, Cryo-EM measurements showed that cell separation does not take place at the midbody site itself but rather at two peripheral sites located about 1 µm away from the midbody center (Elia, Sougrat et al. 2011; Guizetti, Schermelleh et al. 2011).

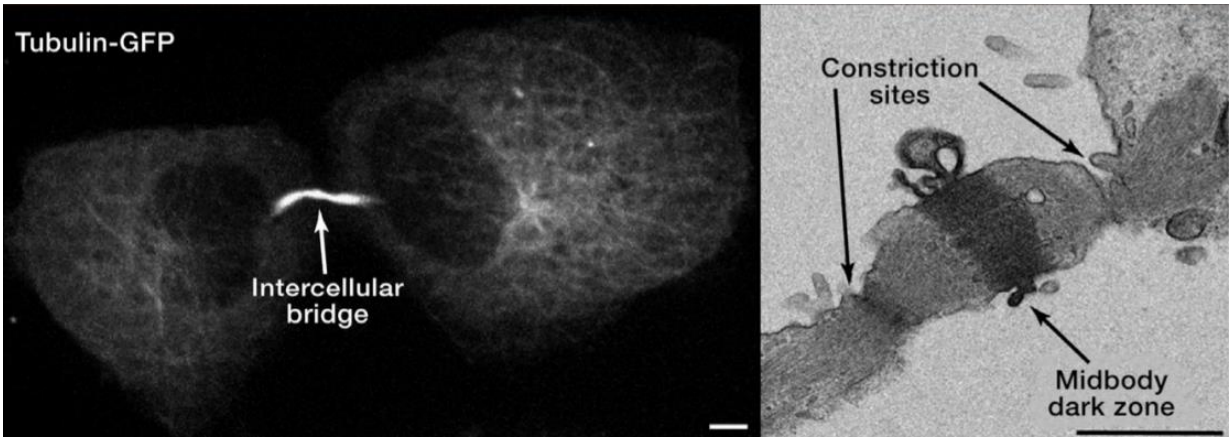

FIGURE 3-6: ABSCISSION OF THE INTERCELLULAR BRIDGE (ELIA, SOUGRAT ET AL. 2011)
The intercellular bridge connecting two daughter cells must be resolved to complete cytokinesis. The microtubules in the intercellular bridge are visible using both confocal microscopy and TEM. Shown here are live MDCK cells expressing tubulin GFP (left) and fixed MDCK cells imaged by TEM (right) (Elia, Sougrat et al. 2011; Elia, Ott et al. 2013). The bridge can be severed on either or both sides of the dark zone. Scale bars: (left) 5 µm, (right) 1 µm.

Cytokinesis abscission requires the function of the ESCRT complexes, ESCRT-I, ESCRT-II and ESCRT-III, and ALIX, an ESCRT-associated protein. ESCRT-III subunits are recruited to the midbody via ALIX or via ESCRT-I – ESCRT-II complexes (Christ, Wenzel et al. 2016).

ALIX consists of a BRO1 domain, a V domain (Fisher, Chung et al. 2007) and a Pro-rich domain (PRD), and functions as a homodimer (Figure 3-7). The main function of the curved BRO1 domain is to bind to the C-terminal helix of the ESCRT-III protein CHMP4 (Figure 3-7). The BRO1 domain can interact with all CHMP4 isoforms (McCullough, Fisher et al. 2008). The central V domain binds to viral L-domains (late domains) (Fisher, Chung et al. 2007; Lee, Joshi et al. 2007) and cargo sequences and to ubiquitin (Dowlatshahi, Sandrin et al.). The C-terminal PRD binds to upstream elements and other ESCRT proteins such as Tsg101 of the ESCRT-I complex (Chatellard-Causse, Blot et al. 2002). Additionally, the PRD domain auto inhibits the V domain and keeps ALIX in an inactive state. Once activated via its V domain, ALIX forms a banana-shaped dimer in solution that resembles ESCRT-II with two CHMP4 binding sites (Figure 3-7) (Pires, Hartlieb et al. 2009).

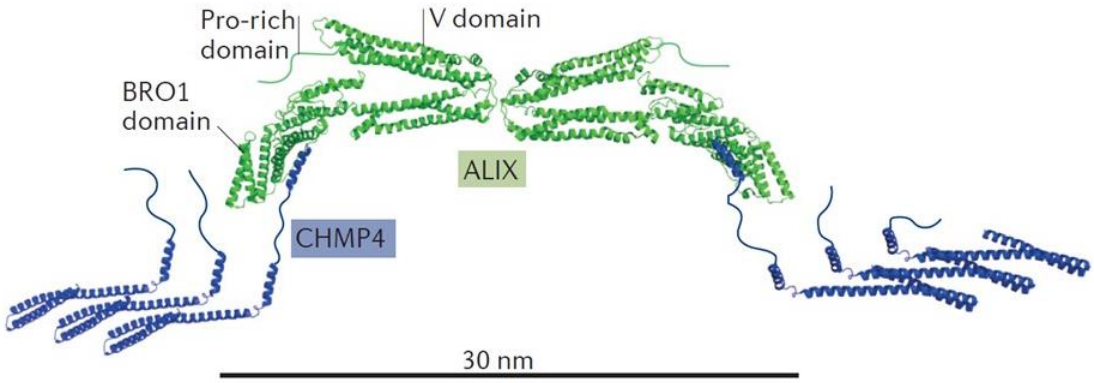

FIGURE 3-7: ALIX BRANCHES OF THE UPSTREAM ESCRTS (SCHONEBERG, LEE ET AL. 2017)
This figure shows how the upstream element ALIX organizes ESCRT-III subunit CHMP4 at the atomic scale. A dimer of ALIX initiates the formation of two CHMP4 filaments via direct interactions with the carboxyl terminus of CHMP4.

While much of mitosis proceeds rapidly (less than 30 min from metaphase to telophase), the intercellular bridge usually persists for over an hour prior to the final cleavage event (Elia, Sougrat et al. 2011; Guizetti, Schermelleh et al. 2011). The bridge constriction occurs acutely 20 min prior to final cleavage. ESCRT-I (TSG101) and ESCRT-III (CHMP4 and Vps4) components are recruited to the intercellular bridge at different times prior to abscission (time 0) by spastin, an AAA-ATPase which severs microtubules by inducing lesions in the microtubule lattice (Roll-Mecak and Vale 2008), and CEP55 (centrosomal and microtubule protein 55), which is a specific adaptor for ESCRTs in mammalian cytokinesis (Figure 3-8). In fact, CEP55 recruits ESCRT-I and ALIX, which subsequently targets ESCRT-III to the midbody.

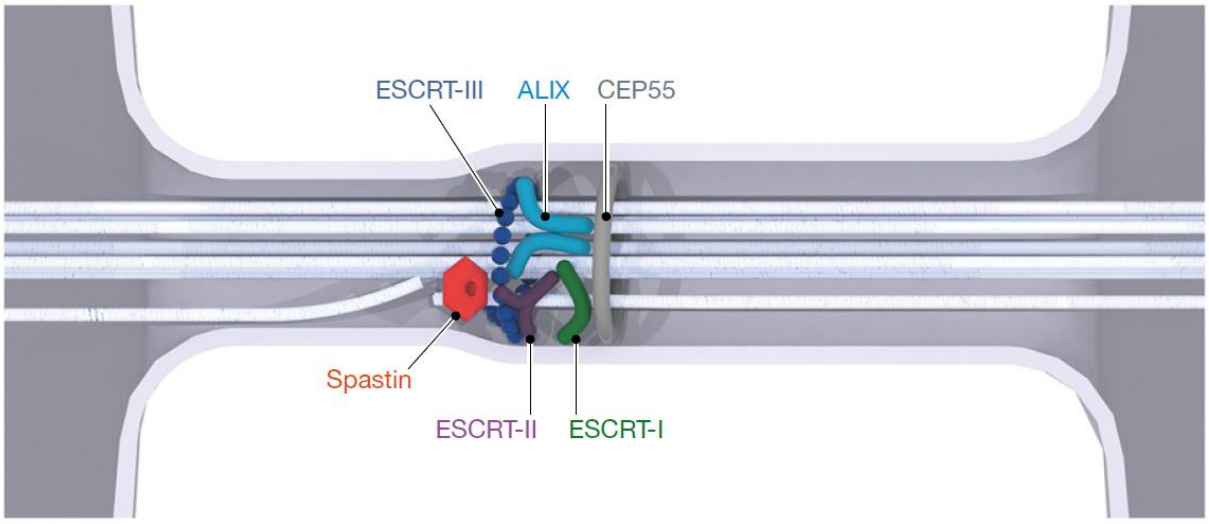

FIGURE 3-8: MEMBRANE NECK SCISSION BY ESCRTS IN CELL DIVISION (HURLEY 2015)
This figure shows the classical cytokinetic function of both the ESCRT-I/ESCRT-II and ALIX branches in membrane abscission by the ESCRT-III complex and coordination with microtubule severing by spastin.

Timing for the recruitment of the different components of the abscission complex was obtained using high-speed quantitative fluorescence imaging (Figure 3-9). While the relative fluorescence intensity values of CEP55 increase early, the levels of ESCRT-I and ESCRT-III increase later in abscission (Figure 3-9). An acute increase of fluorescence levels of ESCRT-III proteins was observed at the intercellular bridge approximately 20 min prior to cell separation, thus correlating with the time of constriction of the microtubule bridge (Figure 3-9) (Carlton and Martin-Serrano 2007; Lee, Elia et al. 2008; Yang, Rismanchi et al. 2008; Morita, Colf et al. 2010; Elia, Sougrat et al. 2011; Guizetti, Schermelleh et al. 2011). And, unexpectedly, recent Fluorescence Recovery After Photobleaching (FRAP) experiments have shown that ESCRT-III at the midbody rapidly turns over subunits with cytoplasmic pools while gradually forming larger assemblies. And that, ESCRT-III turnover depended on the ATPase VPS4, which accumulated at the midbody simultaneously with ESCRT-III subunits, and was required for assembly of functional ESCRT-III structures (Mierzwa, Chiaruttini et al. 2017).

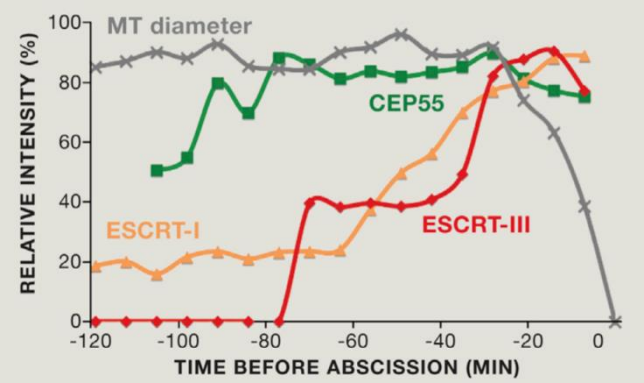

FIGURE 3-9: KINETICS OF CYTOKINETIC ABSCISSION ASSESSED USING HIGH-SPEED QUANTITATIVE FLUORESCENCE IMAGING (ELIA, SOUGRAT ET AL. 2011)
ESCRT components are recruited to the intercellular bridge at different times prior to abscission (time 0). As shown in the graph, the relative intensity values CEP55 increases early. ESCRT-I and ESCRT-III levels increase later in abscission. An acute increase in ESCRT-III level correlates with a decrease in the diameter of the intercellular bridge.

Importantly, both ESCRT-I and ESCRT-III proteins were found to organize in well-defined cortical rings of approximately 1 µm diameter indicating that the ESCRT-III complex can assemble into large diameter structures and is not restricted to small diameters complexes such as in MVBs buds (Figure 3-10). Furthermore, structured Illumination microscopy data revealed that a portion of the ESCRT-III proteins, assembled initially at the dark zone, polymerize and then migrate to the abscission site as the diameter of the microtubule bundle diminishes (Elia, Sougrat et al. 2011; Guizetti, Schermelleh et al. 2011).

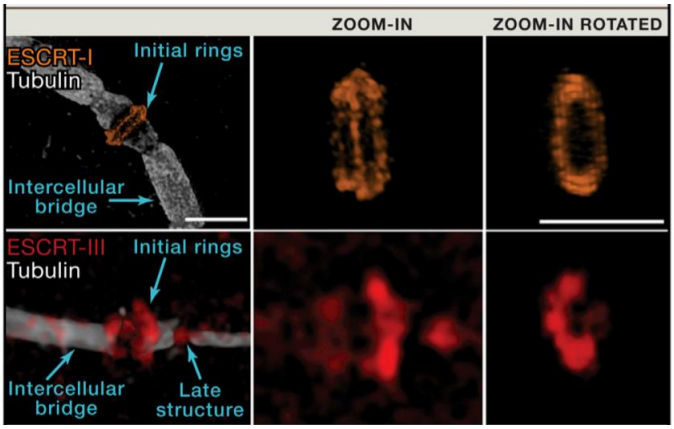

FIGURE 3-10: STRUCTURAL ORGANIZATION OF ESCRT COMPLEX AT THE INTERCELLULAR BRIDGE REVEALED BY SIM (ELIA, SOUGRAT ET AL. 2011; GUIZETTI, SCHERMELLEH ET AL. 2011).
The ESCRT-I protein TSG101 (top) localizes to ring structures on either side of the dark zone. The ESCRT-III protein CHMP4B (bottom) is visible both in rings adjacent to the dark zone and at a late structure closer to the cell body. Scale bar, 2 µm.

In addition, spinning-disk confocal microscopy studies revealed that release of membrane tension by ablation on one side of the dark zone promoted the abscission progression by accumulation of the ESCRT-III complex at the opposite constriction site (Figure 3-11) (Lafaurie-Janvore, Maiuri et al. 2013) pointing to the important inhibition role of membrane tension on the scission process.

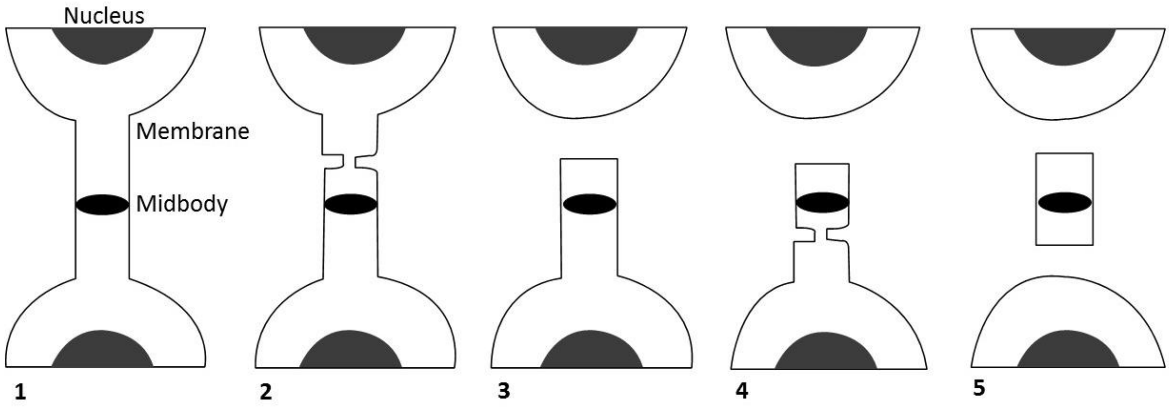

FIGURE 3-11: A SCHEME OF MAMMALIAN CYTOKINETIC ABSCISSION. NUMBERS INDICATE SUCCEEDING STAGES OF ABSCISSION (LEFT TO RIGHT; EARLY TO LATE, RESPECTIVELY)(ADAPTED FROM (SHERMAN, KIRCHENBUECHLER ET AL. 2016).
Schematic representation of cytokinetic abscission. This process is characterized by two consecutive events of membrane constriction (2, 4) and fission (3, 5), which occur at the abscission sites residing about 1 µm away, on each side, from the center of the bridge. The so-called midbody dark zone (black) positioned at the center of the bridge, plays a central role in coordinating abscission.

From all these data, a working model of cytokinetic abscission driven by ESCRTs was suggested. Early in cytokinesis, CEP55 localization to the dark zone appears to facilitate sequential recruitment of ESCRT-I and ESCRT-III proteins (CHMP4, CHMP3 and CHMP2). Abscission could then be driven by polymerization of the central ESCRT-III ring near the midbody (Figure 3-12). To reach the energetically preferred diameter for fission, the filaments constrict the bridge membrane. At the same time, microtubules are

severed in the constricted area and actin is removed from the bridge. Vps4 could mediate ESCRT-III helix remodelling during this process, which includes breaking the helix into two rings—one that remains associated with the dark zone, and a second that may slide outward, constricting the membrane further and forming an ESCRT-III fission complex (Mierzwa, Chiaruttini et al. 2017).

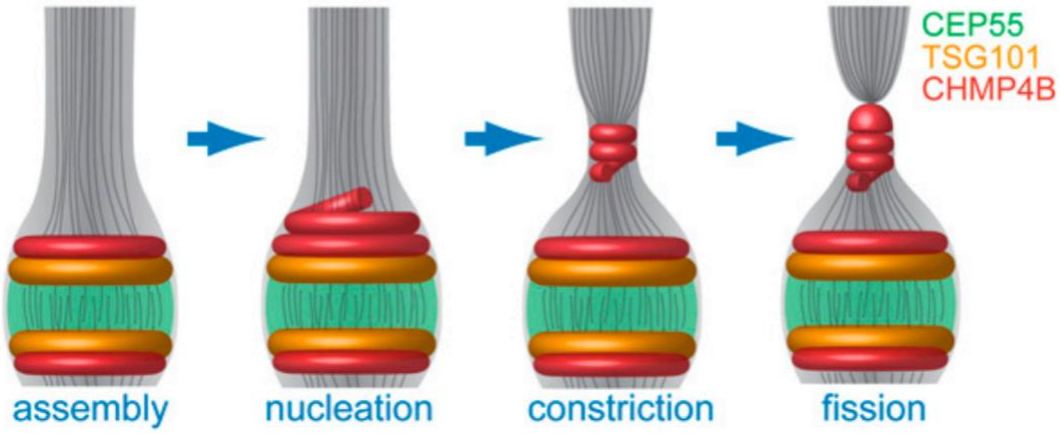

FIGURE 3-12: HYPOTHETIC MECHANISTIC MODEL FOR ESCRT-MEDIATED ABSCISSION (ELIA, SOUGRAT ET AL. 2011).
Suggested mechanistic model for ESCRT-driven cytokinetic abscission based on high-resolution microscopy data and computational modelling(Elia, Sougrat et al. 2011). Cytokinetic abscission begins with the assembly of early (ESCRT-I subunit Tsg101) and late (ESCRT-III subunit CHMP4) ESCRT proteins into a series of partially overlapping cortical rings located at the center of the intercellular bridge. Ring formation is followed by ESCRT-III polymerization and remodelling into 3D helical spirals. Breakage and sliding of the membrane-associated ESCRT-III spiral away from the dark zone, results in acute constriction of the cytokinetic tube. This continues until the ESCRT-III spiral reaches an equilibrium distance where it relaxes to a spontaneous diameter of 50 nm. At this point fission of the 50-nm diameter constricted membrane tube occurs, mediated by a dome-like end-cap structure, finalizing cell separation. Similar events occur on the other side of the bridge (not Illustrated).

3.2.2 ESCRT ROLE IN HIV-1 BUDDING

Many enveloped viruses, such as HIV, hijack the cellular ESCRT machinery to the cytoplasmic leaflet to promote their own egress from infected host cells (Morita and Sundquist 2004; Martin-Serrano and Neil 2011). Retroviruses such as HIV replicate and leave the cell through a process called budding. This means that the virus uses part of the host cell plasma membrane to enclose itself and bud out of the cell before proceeding to a new host. The complete process can be divided into a series of steps.

For the budding to be more efficient, it is also desirable to gather the viral proteins into defined budding spots. This is thought to be defined by specific lipid domains in the cell membrane called lipid rafts, where the lipids are arranged in a more ordered state. Following the assembly of the viral proteins at the budding sites, the budding is initiated by locally deforming the cell membrane. The membrane is then further deformed, making the buds grow to a usually defined size after which they are finally cut from the cell membrane allowing the now fully enveloped virus to exit the cell. In many enveloped

viruses that replicate through budding, scission is performed by the host cell machinery, the most common being the ESCRT complexes.

HIV assembly and budding require the clustering of viral Gag proteins at the plasma membrane. Gag proteins are the major structural proteins of retroviruses (Ganser-Pornillos, Yeager et al. 2008), and fluorescence microscopy experiments have shown that the HIV virions are fully assembled when the recruitment of Gag molecules stops (Jouvenet, Bieniasz et al. 2008). The resulting virus bud is connected to the plasma membrane by a narrow membrane neck; HIV buds have typically diameters ranging from 100 nm to 200 nm (von Schwedler, Stuchell et al. 2003; Morita, Sandrin et al. 2011). Thus, formation of the cell membrane-attached HIV bud occurs independently of ESCRT proteins. However, its detachment from the PM of the cell necessitates the ESCRT complexes to achieve the membrane scission step (Figure 3-13).

Studies have found that ESCRT-III filaments surround Gag assemblies at the PM in Vps4 depleted cells (Hanson, Roth et al. 2008). More recent super-resolution studies detect endogenous ESCRT proteins or low expression HA-tagged ESCRT components in clusters (diameter 60 – 100 nm) at the base of or inside viral necks, but not inside the viral particle (Van Engelenburg, Shtengel et al. 2014). This suggests that membrane scission by ESCRT-III filaments and Vps4 occurs within the bud neck, which is consistent with their role in other biological processes.

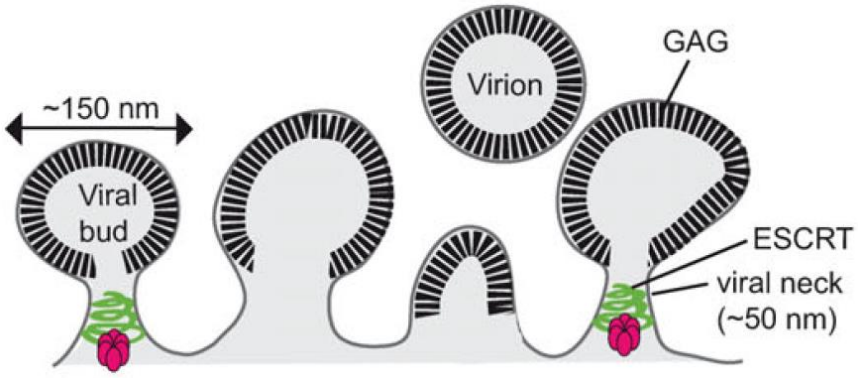

FIGURE 3-13: THE ROLE OF THE ESCRT MACHINERY IN HIV RELEASE (ALONSO, MIGLIANO ET AL. 2016)

The ESCRT machinery is recruited by Gag, which in addition to inducing plasma membrane negative curvature, also functions as an adaptor to ESCRTs. The ESCRT complexes are recruited by direct interactions with specific sequences called L-domains (late domains) contained in Gag. Gag proteins contain two L-domains, PTAP and LxxLF, with PTAP being the functionally more important motif and recruiting the ESCRT complex via a direct interaction with the ESCRT-I proteins (Tsg101) (Martin-

Serrano, Zang et al. 2001). The second L-domain, LxxLF, interacts with ALIX (Fisher, Chung et al. 2007), and in turn, ALIX is shown to be the alternative pathway to ESCRT-I – ESCRT-II complexes for the recruitment of the ESCRT-III subunit CHMP4 and Vps4.

The dynamics of recruitment of CHMP4 and Vps4A is coordinated with the completion of the recruitment of Gag. CHMP4 and Vps4A are recruited transiently, most often in a single pulse, with a typical residence time of few minutes, and appear to be tightly coupled temporally in their appearance at and disappearance from the membrane (Jouvenet, Zhadina et al. 2011). A siRNA-based knockdown screen of ESCRT-III showed that only CHMP4 and CHMP2A/B are essential for HIV-1 release, while depletion of all other ESCRT-III proteins induce minor HIV-1 budding and release defects. Cell depletion of CHMP4B reduces virion release and infectivity 12-fold without altering Gag protein levels. Depletion of CHMP2A, CHMP2B, and CHMP1A individually causes modest reduction of virus release and infectivity (4-, 2- and 2-fold reductions, respectively). But, co-depletion of CHMP2A and CHMP2B or CHMP4A, CHMP4B and CHMP4C resulted in dramatic reductions in HIV-1 release and infectivity (95- and 166-fold, respectively). These data imply that individual CHMP2 and CHMP4 family members can function redundantly (Morita, Sandrin et al. 2011). For individual CHMP4 family members, the relative functional importance (4B > 4A > 4C) parallels their reported cellular abundance (4B > 4A > 4C) (Katoh, Shibata et al. 2004).

Observations of CHMP4 binding in a context of CHMP2-deficient cells show a CHMP4 collar-like structure within the bud neck of virions that fails to pinch off; thus CHMP2 is required for the final cut (Morita, Sandrin et al. 2011). However, combinatorial siRNA knock-down screening demonstrated further that CHMP3 exerts a significant synergistic effect on budding together with CHMP2A and to a much lesser extent with CHMP2B (Effantin, Dordor et al. 2013), suggesting an important role for CHMP3 in HIV-1 budding.

Thus, the expected core of the ESCRT-III machinery for HIV release is CHMP4, CHMP2 (A / B) and CHMP3 (+ Alix) binding to the budding site and promoting scission of HIV particles off the plasma membrane (von Schwedler, Stuchell et al. 2003; Baumgartel, Ivanchenko et al. 2011; Jouvenet, Zhadina et al. 2011).

3.2.3 ESCRT ROLE IN NEURONAL PRUNING

Neuronal pruning is critical for maturation of the nervous system and implies large scale pruning of relatively long neuronal branches, that are no longer needed, from their parent neuron (Loncle, Agromayor et al. 2015). Large-scale pruning occurs as a local degeneration involving ESCRTs for the severing of the nerve cell membrane of axons and dendrites (Figure 3-14) (Zhang, Wang et al. 2014; Loncle, Agromayor et al. 2015). The latter participate actively in neuronal function, both as an apparatus for processing neuronal signals and as major sites of synaptic plasticity.

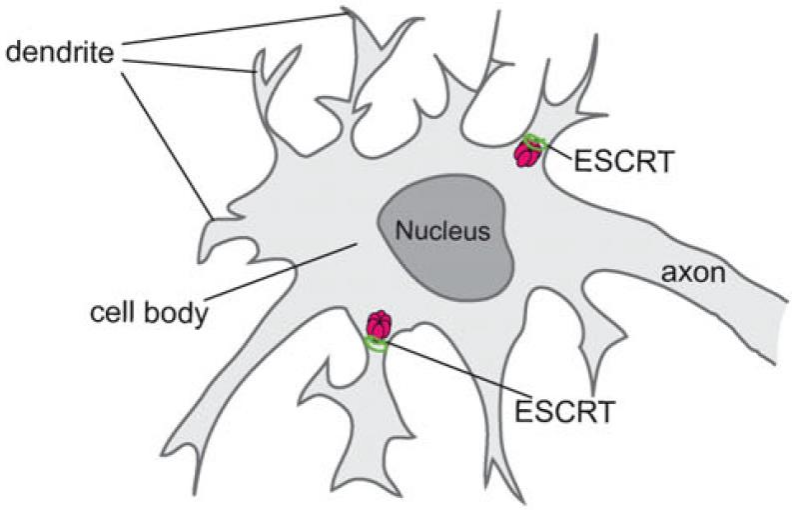

FIGURE 3-14: THE ROLE OF THE ESCRT MACHINERY IN NEURAL PRUNING (ALONSO, MIGLIANO ET AL. 2016)

A siRNAi-based knockdown screen of all ESCRT complexes showed that neuronal pruning is specifically dependent on ESCRT-I and ESCRT-III complexes and presumably independent of ESCRT-0 or ESCRT-II like in cytokinesis and HIV budding (Figure 3-15; Figure 3-16). Moreover, this screen showed that loss of activity of Tsg101 (ESCRT-I) and Shrub, the fly homologue of the human ESCRT-III subunit CHMP4B, and Vps4 leads to severe disruptions and defects in dendrites pruning (Figure 3-15) (Sweeney, Brenman et al. 2006; Loncle, Agromayor et al. 2015).

In addition, it appeared that similarly to cytokinesis and HIV budding, a direct interaction with an ESCRT-associated protein is necessary. Here, the Myopic accessory protein (Mop) is required for the recruitment of Shrub (CHMP4B) in the fly neuronal membrane remodelling process. Mop is the homolog of the human gene HD-PTP. HD-PTP is an ALIX-like protein (another Bro-domain protein) which replaces ALIX in recruiting CHMP4 in the neuronal pruning process (Doyotte, Mironov et al. 2008; Miura, Roignant et al. 2008).

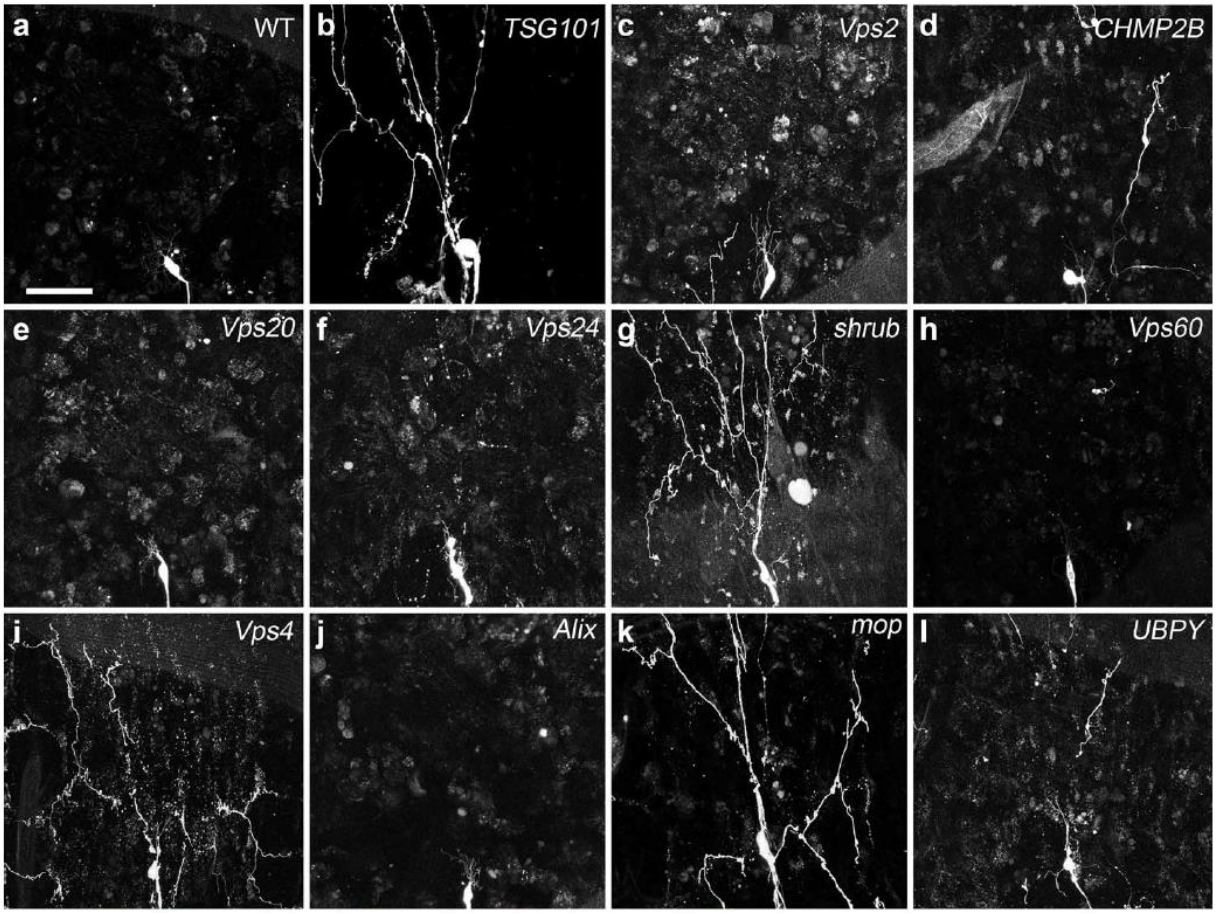

FIGURE 3-15: ESCRT-I,-III AND ACCESSORY PROTEINS ARE REQUIRED FOR DENDRITE PRUNING (LONCLE, AGROMAYOR ET AL. 2015)

(a–l) Results from the siRNAi screen showing representative images of a ddaC neuron at 18 h APF expressing RNAi against ESCRT-I (TSG101), ESCRT-III (Vps2, CHMP2B, Vps20, Vps24, shrub and Vps60), Vps4 and ESCRT-accessory proteins (Alix, mop, and UBPY)(Loncle, Agromayor et al. 2015). Scale bar = 50 μm.

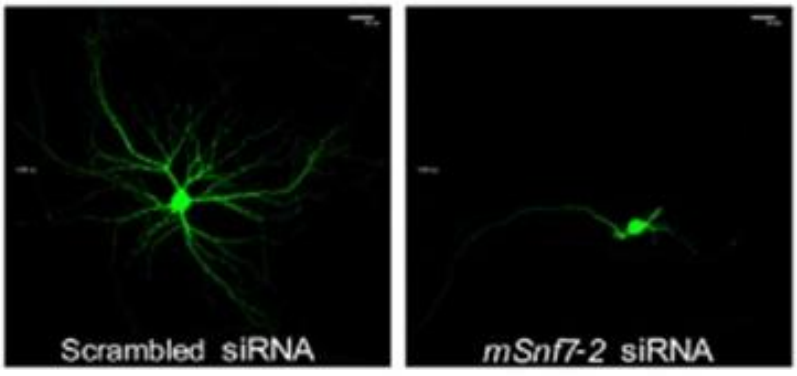

FIGURE 3-16: CHMP4B (MSNF7-2) IS NECESSARY FOR NEURITE DEVELOPMENT (LEE, BEIGNEUX ET AL. 2007)

To determine whether mSnf7-2 (CHMP4B) is required to maintain mature dendritic trees, mSnf7-2 siRNA (533–551) or mSnf7-2 siRNA (482–500) were transfected into 15 DIV mature cortical neurons that exhibit fully elaborated dendritic trees. Results from 18 DIV cortical neuron show that transfection with scrambled siRNA had no effect (right) and that transfection with mSnf7-2 siRNA caused dramatic retraction of the dendritic trees of transfected neurons (left).

Figure 3-17 summarizes the ESCRT-0, -I, -II and –III presence in the different cellular processes discussed above.

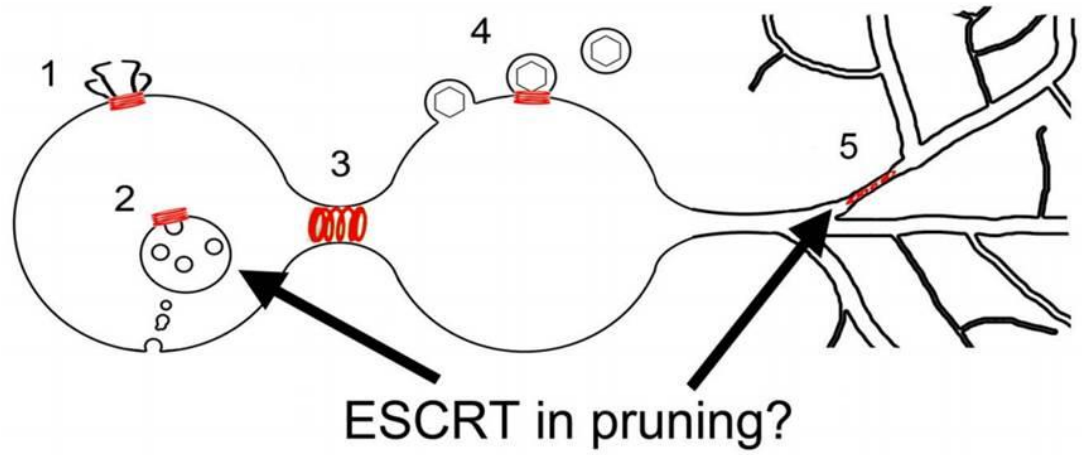

	Cellular process	ESCRT-0	ESCRT-I	ESCRT-II	ESCRT-III	Alix	mop
1	Membrane repair	?	?	?	✓	✓	?
2	MVB formation	✓	✓	✓	✓	✗	✓
3	Cytokinetic abscission	✗	✓	✓	✓	✓	?
4	Viral budding	✗	✓	✗	✓	✓	?
5	Neurite severing	✗	✓	✗	✓	✗	✓

72

FIGURE 3-17: ESCRT COMPLEXES ASSEMBLING AT VARIOUS CELLULAR PROCESSES (LONCLE, AGROMAYOR ET AL. 2015)
Schematic representation of the role of the ESCRT machinery in membrane scission events at different cellular locations at different times in the life of a cell. 1. Membrane repair. 2. MVB formation. 3. Cytokinetic abscission, the requirement of ESCRT-II complex in cytokinesis is proven by (Christ, Wenzel et al. 2016). 4. Viral budding. 5. Neurite branch severing. The table summarizes the deployment of ESCRT components and highlights that specific combinations of ESCRT complexes assemble depending on which membrane-cutting event is required. "?" indicates that at present its role is not known.

3.3 ESCRT-III CRYSTAL STRUCTURE AND CYCLING

The core ESCRT-III components are soluble charged proteins with similarities at the sequence level and in size (221–241 residues) (Obita, Saksena et al. 2007). The ESCRT-III subunits are thereby predicted to share common structural architecture (Muziol, Pineda-Molina et al. 2006; Shim, Kimpler et al. 2007). Up-to-date, the only known crystal structure for the ESCRT-III proteins is that of CHMP3/hVps24 (residues 9–183). It reveals a common domain architecture of four α helices bundled into an N-terminal core domain and followed by the C-terminal region (Muziol, Pineda-Molina et al. 2006). The highly structured positively charged N-terminal region consists of two helices (α1, α2) that form a 7nm hairpin important for membrane binding and homo- or hetero-dimerization (Figure 3-18). This hairpin structure

together with the helices α3 and α4 form an asymmetric anti-parallel four-helix bundle (Muziol, Pineda-Molina et al. 2006; Bajorek, Schubert et al. 2009) (Figure 3-18). This N-terminal core domain is enriched with basic amino acids that bind acidic lipids within lipid bilayers. The C-terminal region, in contrast, is largely unstructured and forms numerous intramolecular contacts along the amino-terminal core domain: it interacts with helix α2 of the core and thereby blocks homo- or heterodimerization of ESCRT-III proteins. Such intramolecular interactions may therefore prevent ESCRT-III protein-protein intermolecular assembly and thus keep the ESCRT-III proteins as inactive monomers in the cytosol in a ''closed'' conformation (Zamborlini, Usami et al. 2006; Shim, Kimpler et al. 2007; Bajorek, Schubert et al. 2009).

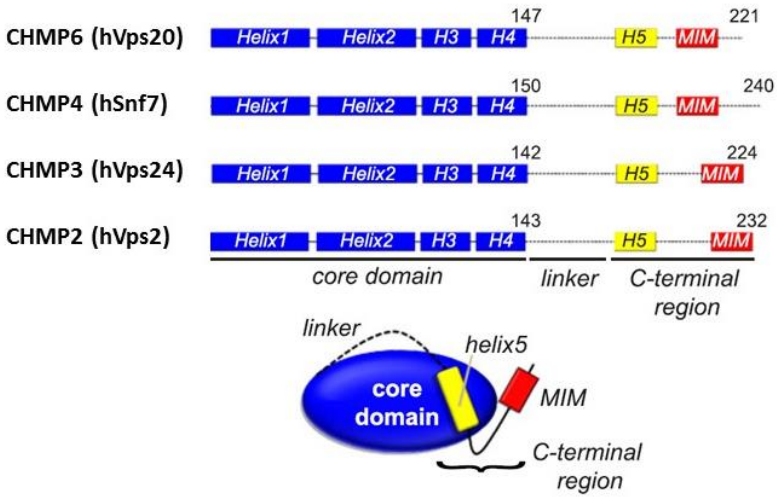

FIGURE 3-18: PREDICTED COMMON STRUCTURE FOR ESCRT-III SUBUNITS (HENNE, BUCHKOVICH ET AL. 2012)
Schema of ESCRT-III subunits architecture. Helices are denoted as boxes. The MIM domain (in red) interacts with the MIT domain of Vps4.

ESCRT-III assembly is both temporally ordered and transient as the subunits cycle between inactive monomers in the cytoplasm and active assembled polymers on membranes (Figure 3-19) (Henne, Buchkovich et al. 2012). The activation of the ESCRT-III subunits requires the release of the folded C-terminal region from the core. Displacement of the C-terminal region rearranges the helical segments and drives both membranes binding and homo- or hetero-oligomerization (Shim, Kimpler et al. 2007; Ghazi-Tabatabai, Saksena et al. 2008; Henne, Buchkovich et al. 2012).

The C-terminal acidic region also carries the so-called MIM domain (MIT Interacting Motif) for interaction with the MIT (Microtubule Interacting and Transport) domain of Vps4 (Scott, Gaspar et al. 2005; Obita, Saksena et al. 2007; Stuchell-Brereton, Skalicky et al. 2007) (Figure 3-19). Each ESCRT-III subunit has either one MIM1 (CHMP2/hVps2, CHMP3/hVps24 and the Vacuolar assembly protein Did2), one MIM2 (CHMP6/hVps20, CHMP4/hSnf7 and CHMP5/hVps60) or both (the ESCRT-III associated factor Ist1).

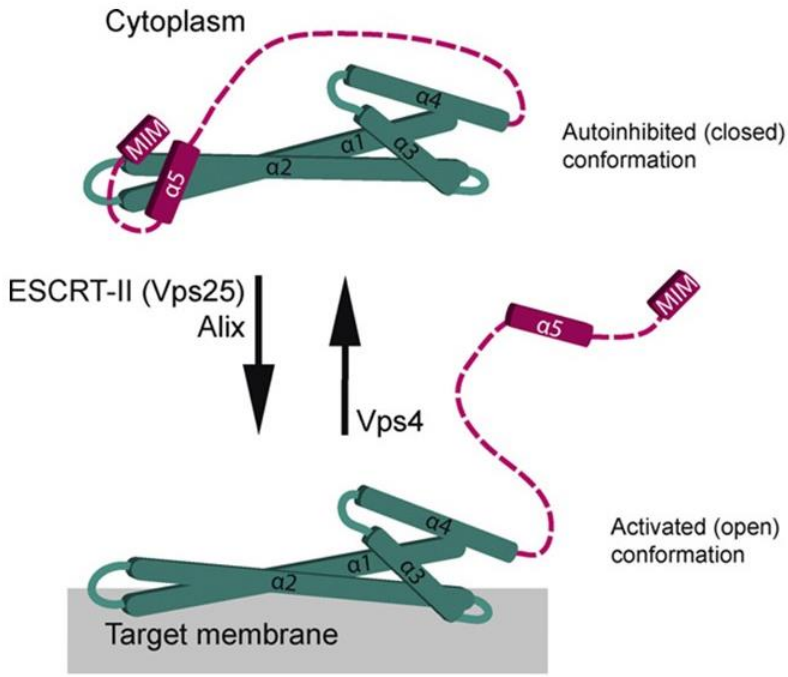

FIGURE 3-19: ESCRT-III CYCLING BY THE AAA-ATPASE VPS4B (ADELL AND TEIS 2011)
Cartoon of an ESCRT-III subunit based on the crystal structure of human CHMP3. Inactive, auto-inhibited ESCRT-III subunits can be activated either by the ESCRT-II subunit Vps25 or by the ESCRT-associated protein Alix. The AAA-ATPase Vps4 resets the active ESCRT-III subunits to the 'inactive' state.

The Vps4 complex consists of the type I AAA-ATPase Vps4 and its co-factor Vta1. In the cytoplasm, Vps4 is an inactive protomer (monomer or dimer). The Vps4 complex is the only ATP consuming factor of the ESCRT machinery. Vps4 subunits have two functional domains, an amino-terminal MIT domain, consisting of three antiparallel helices (α1/α2/α3), and a central AAA-ATPase domain (Scott, Gaspar et al. 2005). The MIT domain is responsible for the interaction of Vps4 with the MIM domains of the ESCRT-III subunits, and the AAA-ATPase domain hydrolyses ATP to disassemble and likely remodel and recycle the ESCRT-III complex in the cytoplasm.

Once recruited to the ESCRT-III complex, Vps4 assembles into a dodecamer, consisting of one or two stacked hexameric rings with a central pore. Binding of Vta1 to Vps4 results in an active Vps4–Vta1 complex with enhanced ATPase activity (Azmi, Davies et al. 2006; Landsberg, Vajjhala et al. 2009; Monroe, Han et al. 2014). Finally, after each round of membrane scission event, Vps4 completes the disassembly of ESCRT-III and then dissociates the ESCRT or the Vps4 complex into inactive protomers (Scott, Chung et al. 2005) (Figure 3-20).

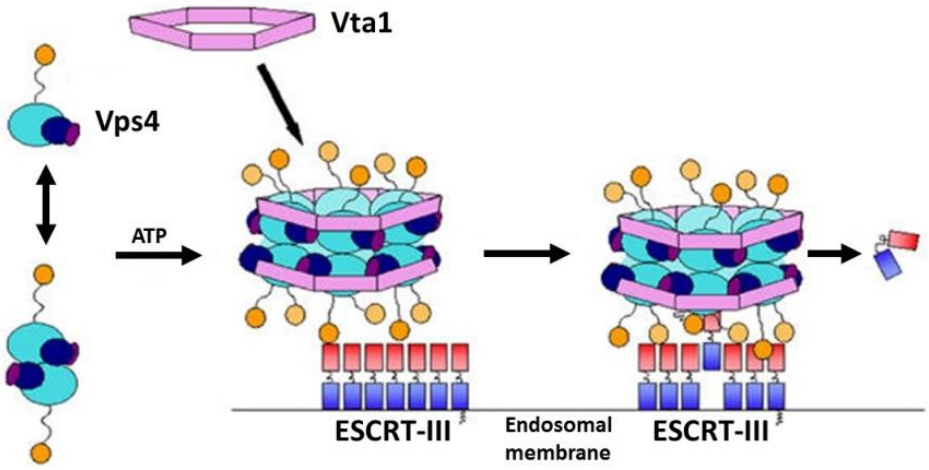

FIGURE 3-20: MODEL FOR THE FUNCTIONAL CYCLE OF VPS4 COMPLEX (SCOTT, CHUNG ET AL. 2005).
Left: At steady state, Vps4 is primarily a monomeric cytoplasmic protein (Fujita, Umezuki et al. 2004), and exhibits a monomer-dimer equilibrium in the absence of bound nucleotide (Babst, Wendland et al. 1998). Vta1 is an oligomer of uncertain stoichiometry. Middle: Vps4 proteins are recruited to sites of vesicle formation at the endosomal membrane by interactions between the N-terminal MIT domain and the C-proximal domains of assembled ESCRT-III lattice (Babst, Katzmann et al. 2002; Lin, Kimpler et al. 2005; Scott, Gaspar et al. 2005). The assembled Vps4 proteins can also bind ATP and Vta1 oligomers via β-domain interactions to form an enzymatically active complex. Right: Bound ESCRT-III subunits are freed from the assembled lattice and released into the cytoplasm as they are pulled up into the narrow central chamber of the Vps4 ring.

One side of the MIT domain (helices α2 / α3) can bind to the helical MIM1 of CHMP2 and Did2 and the MIM1-like element of CHMP3. And, the opposite side of the MIT domain (helices α1/α3) can bind to the unstructured MIM2 on CHMP6 and CHMP4 (Figure 3-21) (Obita, Saksena et al. 2007; Kieffer, Skalicky et al. 2008; Adell, Vogel et al. 2014). The interaction of Vps4 is negligible with CHMP3 and with a low affinity with CHMP4. In contrast, Vps4 interacts strongly with CHMP2 and CHMP6 (Adell, Vogel et al. 2014). Because CHMP6 is thought to only play a nucleator role for the ESCRT-III proteins assembly (discussed in detail in chapter 3.1) (Teis, Saksena et al. 2008; Saksena, Wahlman et al. 2009), its interaction with Vps4 is not considered.

Thus, the interaction of the MIT domain of Vps4 with the MIM1 of CHMP2 is the main responsible for its binding to the ESCRT-III complex and recruitment (Adell, Vogel et al. 2014), CHMP2 is therefore presumed to be the intrinsic timer for ESCRT-III disassembly (Schmidt and Teis 2012). Moreover, the possibility of interaction of Vps4 with several MIMs is believed to stabilize its recruitment and enhance its activity. This way, the recycled ESCRT-III subunits are continuously available and could be involved multiple times in the cell (Adell, Vogel et al. 2014).

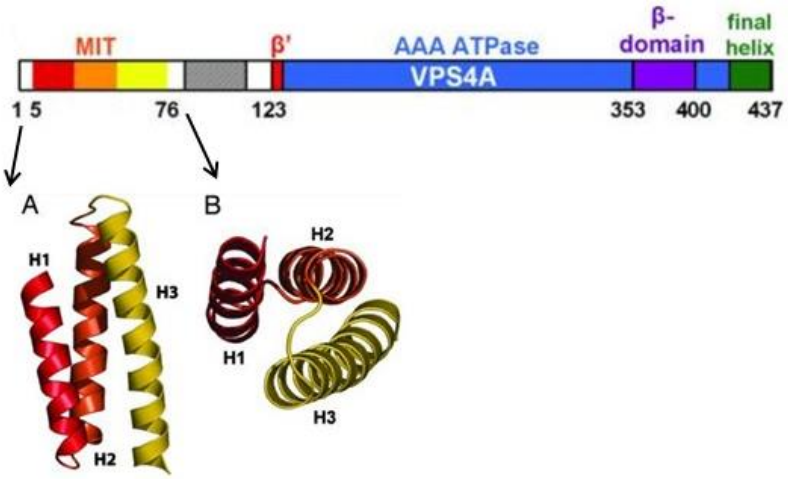

FIGURE 3-21: MIT DOMAIN OF VPS4 (SCOTT, GASPAR ET AL. 2005)
Schematic illustrations of human VPS4A. Shown are the MIT domain (left), the AAA-ATPase domain (middle) and the β-domain (right. (*A*) Ribbon diagram of the VPS4A MIT domain (residues 5–76). (*B*) Top view of the three-helix bundle of the MIT domain, emphasizing the asymmetry in the disposition of the three helices.

3.4 ESCRT-III POLYMER STRUCTURES *IN VIVO* AND *IN VITRO*

In vitro and *in vivo* observations have shown that activated ESCRT-III subunits can assemble into flat spirals, helices and tubes.

3.4.1 ESCRT-III POLYMERS FORM FLAT SPIRALS

CHMP4B forms spirals *in vivo* and *in vitro*. Deep-etch EM (DEEM) of the plasma membranes of cells overexpressing CHMP4 showed that CHMP4 can form flat spirals on membrane (Figure 3-22 / A, C and D) (Hanson, Roth et al. 2008; Cashikar, Shim et al. 2014; McCullough, Clippinger et al. 2015). Indeed, in this case, stoichiometry unbalance due to CHMP4 overexpression favors this type of organization for this protein. This observation was confirmed *in vitro* with Snf7, the yeast *Caenorhabditis elegans* orthologues of CHMP4, showing that the protein alone assembles into flat spirals on solid surfaces (Figure 3-22 / B) (Henne, Buchkovich et al. 2012; Shen, Schuh et al. 2014; Chiaruttini, Redondo-Morata et al. 2015). These studies based on EM and HS-AFM showed that CHMP4 filaments have a preferred radius of curvature ranging between about 21 to 32 nm. In the spirals, their innermost observed ring is slightly overbent (having a radius of curvature of 18 nm), meaning that the coils are bent at a higher curvature than would be predicted by their natural energy minimum. Meanwhile, the outer rings are underbent, meaning that their radii of curvature are greater than the energetically preferred value (Henne, Buchkovich et al. 2012; Shen, Schuh et al. 2014; Chiaruttini, Redondo-Morata et al. 2015).

CHMP2A also forms spirals *in vitro*. C-terminally truncated CHMP2A alone coils up to small rings and can also form spirals (Figure 3-22 / E) (Lata, Roessle et al. 2008; Lata, Schoehn et al. 2008; Effantin, Dordor et al. 2013).

3.4.2 ESCRT-III POLYMERS FORM HELICES AND TUBES

CHMP4 forms tubes *in vivo* when in combination with other ESCRTs. Indeed, depletion of Vps4 leads to formation of tubular exvaginations from cells that are sustained by CHMP4-containing helices (Figure 3-22 / J) (Hanson, Roth et al. 2008; Henne, Buchkovich et al. 2012; Cashikar, Shim et al. 2014). These exvaginations of CHMP4 approximately range between 100 to 120 nm in diameter and extend to varying heights. Moreover, overexpression of CHMP4 and depletion of Vps4 or co-expression of CHMP4 and of a dominant negative mutant of Vps4 results in tightening of CHMP4 flat spirals and thus formation of tubular structures protruding out of the plasma membrane (Hanson, Roth et al. 2008). These tubes are also about 100 nm in diameter.

CHMP2B forms tubes *in vivo*. Overexpressed full-length CHMP2B leads to helical scaffolds deforming the plasma membrane into long rigid tubes protruding out of the cell and reaching up to 400 nm in diameter (Figure 3-22 / H and I) (Bodon, Chassefeyre et al. 2011). But, there is lack of study *in vitro* showing CHMP2B tubular structures.

CHMP2A + CHMP3 co-assemble into tubes *in vivo* and *in vitro*. In the absence of membrane, CHMP2A and CHMP3 co-assemble *in vitro* into heteropolymeric closed tubes with an inner diameter approximately equal to 50 nm (Figure 3-22 / F). The outer surface of these tubes is expected to bind to membranes, whereas the inner surface corresponds to a binding site for the AAA-ATPase VPS4 (Lata, Schoehn et al. 2008; Effantin, Dordor et al. 2013). Furthermore, CHMP2A + CHMP3 tubes were found to be closed at one end forming thus a cone / dome-like structures with a height of 25 nm (Figure 3-22 / G1 and G2). Moreover, helical tubes in the presence of negatively charged liposomes have been observed (Lata, Schoehn et al. 2008), although it is not *a priori* easy to reconcile these different organizations. *In vivo*, helical structures that apparently contain CHMP2A have been imaged by cryo-electron tomography at the midbody of Hela cells (Guizetti, Mantler et al. 2011; Guizetti, Schermelleh et al. 2011). Interestingly, these cytokinesis filaments have a large filament–filament distance of 35 nm (Guizetti, Schermelleh et al. 2011), quite far from the tight packing of pure CHMP2–CHMP3 tubes with a 3.5 nm spacing measured *in vitro*.

IST1–CHMP1B complex forms tubes *in vivo*. The IST1–CHMP1B complex also forms a heteropolymeric tube, with a diameter of 24 nm and a 5.1-nm repeat, and has yielded a high-resolution Cryo-EM reconstruction (Figure 3-22 / K) (McCullough, Clippinger et al. 2015). Interestingly, it was the first ESCRT-III complex described to form an external coat on *positively* curved membranes *in vitro* and *in vivo*.

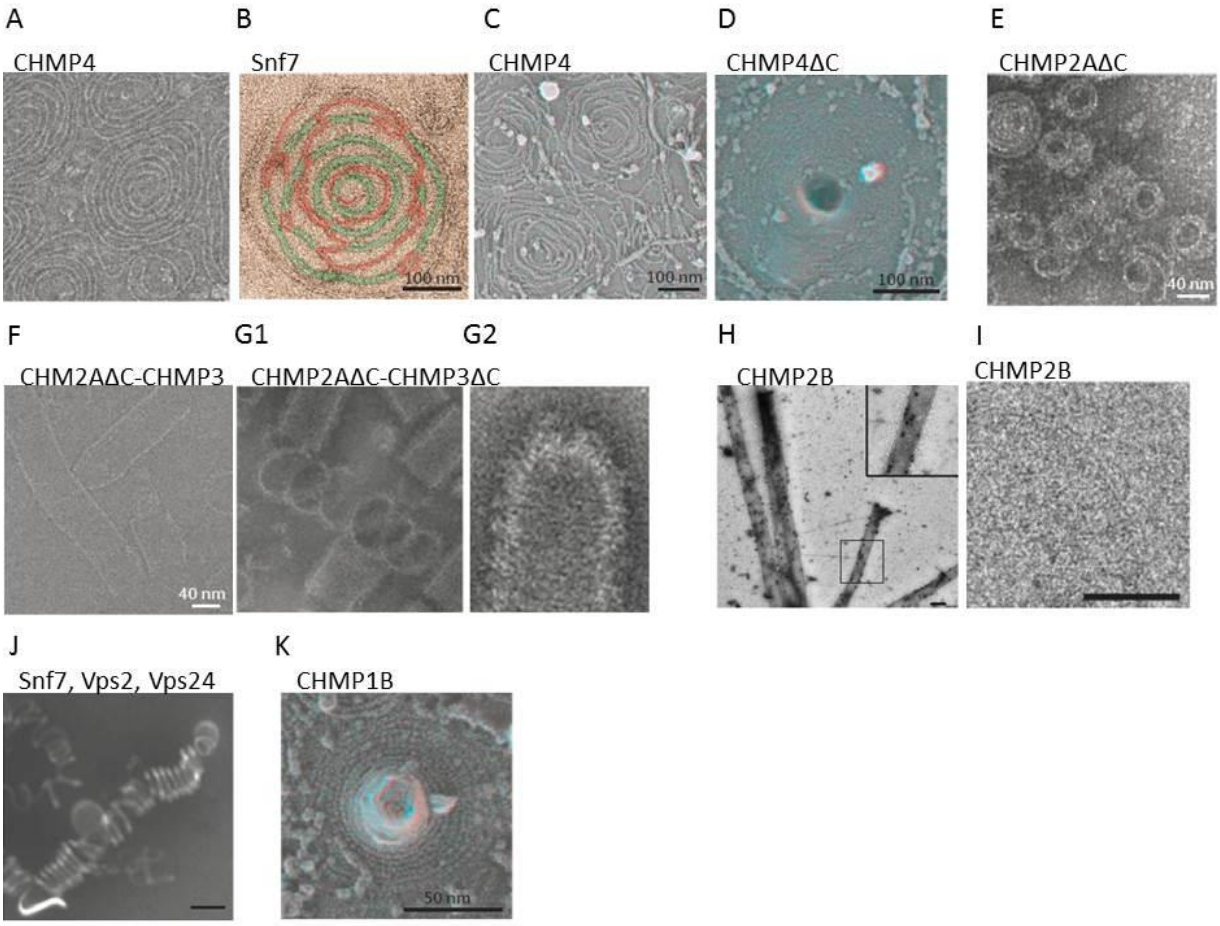

FIGURE 3-22: STRUCTURES OF ESCRT-III POLYMERS

ESCRT subunits can polymerize into a wide range of structures — including spirals, tubes, bells, coils and cones, which have all been visualized by electron microscopy (EM). Spirals of CHMP4 visualized by EM

(A) Spirals of CHMP4 visualized by EM (Shen, Schuh et al. 2014)

(B) Transmission EM of a single spiral of Snf7 (yeast CHMP4) on a membrane (Chiaruttini, Redondo-Morata et al. 2015)

(C) Anaglyph of the plasma membrane from COS-7 cells expressing CHMP4A (Cashikar, Shim et al. 2014)

(D) Filament spirals on COS-7 cell membranes expressing CHMP4A1–164 (McCullough, Clippinger et al. 2015)

(E) Spirals of CHMP2AΔC visualized by negative-stain EM (Effantin, Dordor et al. 2013)

(F) CHMP2AΔC–CHMP3ΔC tubes in the presence of negatively charged liposomes. Tube diameter ~55 nm. (Effantin, Dordor et al. 2013)

(G1) CHMP2AΔC–CHMP3ΔC coils in the presence of negatively charged liposomes, (G2) often cone-shaped (Lata, Schoehn et al. 2008)

(H) Tubes of CHMP2B pelleted from culture media of CHMP2B-expressing cells. P1 pellets of culture medium of CHMP2B-FLAG-expressing cells contain tubes made up of CHMP2B. P1 pellets were fixed, permeabilized, and immunolabeled with anti-CHMP2B antibodies revealed by protein A gold (10 nm) (Bodon, Chassefeyre et al. 2011)

(I) Dome closing one end of a tube. The inner leaflet of the membrane is closely associated with the CHMP2B protein lattice (Bodon, Chassefeyre et al. 2011)

(J) Helices of Snf7 Arg52Glu (R52E), Vps24 (yeast CHMP3) and Vps2 (yeast CHMP2) assembled on membranes (Henne, Buchkovich et al. 2012)

(K) Spirals on COS-7 cells expressing FLAG–CHMP1B (McCullough, Clippinger et al. 2015)

This structural diversity could be related to the complexity of the membrane scission mechanism and to the various roles of the proteins at different points of this process. The full range of these structures forms the basis of the most up-to-date mechanistic hypotheses.

3.5 THEORETICAL MODELS FOR MEMBRANE SCISSION BY THE ESCRT-III POLYMERS

Although ESCRT complexes have been a hot topic in the past decade, the minimal machinery and its mode of action to induce membrane scission remain puzzling. This is mainly because the available data in the field are insufficient to define a unique scission mechanism. ESCRTs are involved in several membrane remodelling processes with highly varying membrane neck diameters. In MVB biogenesis and HIV budding, the ESCRT proteins promote budding and/or scission of membrane necks ranging from 20 to 200 nm, whereas, in cytokinesis, the process is even more complex, and the ESCRT proteins seem to be involved in the narrowing of the cytokinetic neck from ≈ 1 µm all the way to zero, although not demonstrated. Additionally, *in vitro* and *in vivo* observations show that the ESCRT polymers form multiple structures such as spirals or helical structures with large diameters about 50 nm. Hence, based on these apparently heterogeneous observations, it is difficult to disclose the potential mode of assembly of the complex inside a bud neck. Finally, because splitting of membrane necks requires opposing membranes to come as close as approximately 3 nm (Kozlovsky and Kozlov 2003), the large diameters of the structures observed *in vitro* impede the possibility of having spontaneous membrane fission.

Nevertheless, based on the different studies on ESCRTs, several theoretical models have been proposed to explain the mechanism of membrane scission. But none of these speculative models can fully fit and explain all the different ESCRT-III-related membrane narrowing processes. Yet, according to all the *in vitro* and *in vivo* observations, two models seem to be the most appealing. One model suggests that Vps4 induces filament sliding or constriction leading to fission (Henne, Buchkovich et al. 2012), while the second model asserts that ESCRT-III polymers form dome-like structures to conduct neck constriction and membrane fission (Lata, Schoehn et al. 2008; Fabrikant, Lata et al. 2009; Peel, Macheboeuf et al. 2011; Chiaruttini, Redondo-Morata et al. 2015).

3.5.1 SPIRAL SPRING (BUCKLING) MODEL FOR ESCRT-III MEDIATED MEMBRANE SCISSION

A model called "sliding model" (Henne, Buchkovich et al. 2012) was initially proposed for ESCRT-mediated MVB biogenesis consisting in the following steps (Figure 3-23): (1) ESCRT-0, -I, and -II engage ubiquitinated cargoes and concentrate them into a patch on the endosome surface; (2) ESCRT-II initiates the assembly of an Snf7 ring-like polymer by directly binding Vps20; (3) Snf7 flat spiral remodels upon addition of Vps24 and Vps2, ultimately forming a 3D helix or spring-like structure similar to the ESCRT-III-induced membrane tubules *in vivo* (Cashikar, Shim et al. 2014); and (4) the AAA ATPase Vps4 is recruited by ESCRT-III to recycle the ESCRT machinery off the MVB.

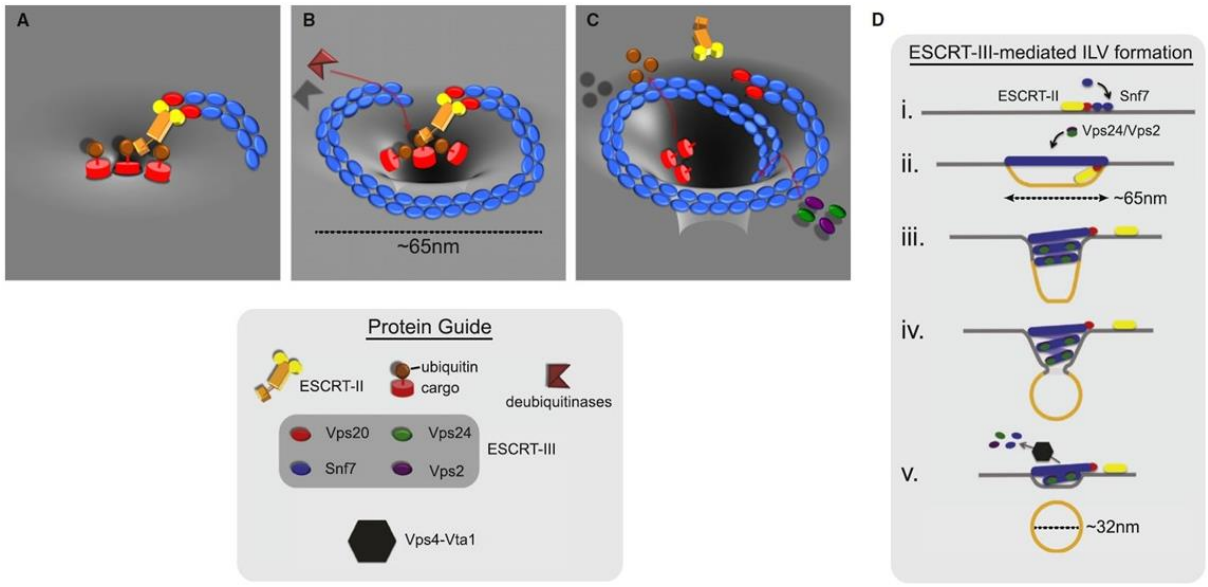

FIGURE 3-23: SLIDING MODEL FOR ESCRT-III-MEDIATED MVB BIOGENESIS (HENNE, BUCHKOVICH ET AL. 2012)
(A–C) Speculative cartoons illustrating three stages in ESCRT-mediated vesicle budding from a ''top'' perspective over the endosome surface. A- ESCRT-II engages cargo and two Vps20 subunits; two Snf7 filaments extend around cargo. B- ESCRT-III forms a ≈65 nm ring defining ILV membrane; Snf7 assembly recruits deubiquitinases. C- Cargo deubiquitylation; Vps24 and Vps2 induce the ESCRT-III helix, driving invagination. (D) A ''side'' view of the proposed mechanism of ESCRT-mediated budding.

HS-AFM of reconstituted Snf7 spirals on supported lipid bilayers provides next a possible mechanism for membrane budding and scissioning. Chiaruttini et al found that Snf7 polymers form spirals on membrane (Chiaruttini, Redondo-Morata et al. 2015) similar to those observed with EM (Hanson, Roth et al. 2008; Shen, Schuh et al. 2014) with an apparent nucleation ring about 25 nm in diameter. This nucleation ring corresponds to a preferred curvature of Snf7 polymers. When Snf7 filaments form spirals outward from the nucleation ring, the filaments underbend and reciprocally overbend when they grow inwards. The "spiral spring" model (Chiaruttini, Redondo-Morata et al. 2015) thus proposes that polymerizing Snf7 spirals become loaded springs as a result of lateral compression induced by neighboring ESCRT-III filaments during growth into the bud neck. Expansion of Snf7 springs back to a flat relaxed configuration would release the mechanical stress and cause at the same time membrane distortion driving membrane instability and scission (Figure 3-24). So far, no model provides details for this instability.

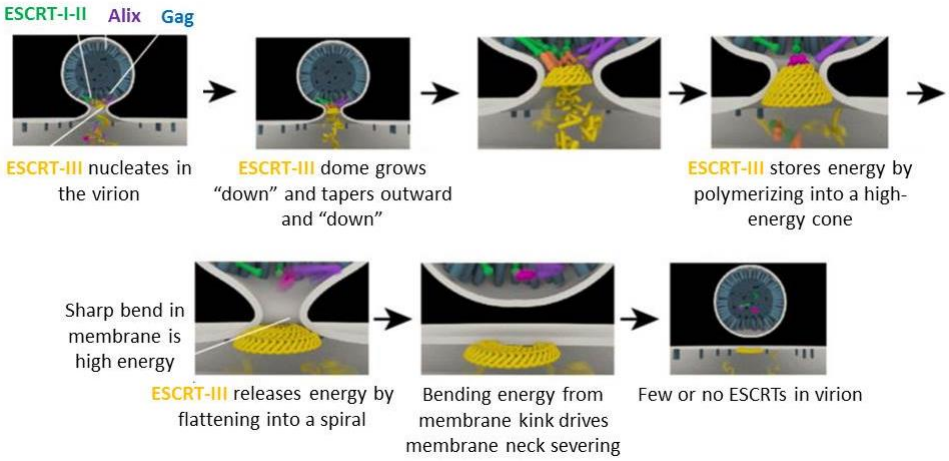

FIGURE 3-24: BUCKLING MODEL FOR ESCRT-MEDIATED SCISSION (ADAPTED FROM (SCHONEBERG, LEE ET AL. 2017)

HIV-1 Gag (blue) accumulates at the membrane (white), causing initial membrane deformation. ESCRT-I/ESCRT-II (green/orange) and ALIX (purple) are recruited by Gag. ESCRT-III (yellow) is recruited by ESCRT-II and ALIX, and polymerizes in the bud neck. ESCRT-III polymerizes outward from the virion towards the cytosol, with consecutive wider rings. The cone is higher in energy than a flat spiral. Conversion of the cone to a spiral releases the tension, but at the cost of creating sharp bends where the virion is attached to the plasma membrane. The high energy of these bends is released when the virion is severed. ESCRTs are released to the cytosol at the end.

3.5.2 THEORETICAL DOME MODEL FOR ESCRT-III MEDIATED MEMBRANE SCISSION

The dome-model presupposes that CHMP4 proteins, either recruited by ESCRT-I and ESCRT-II or Alix, polymerize into spirals and induce a first narrowing of the neck before serving as a platform to recruit either CHMP2A-CHMP3 or CHMP2A or CHMP2B polymers. Based on the *in vitro* observations with pure proteins, this model supposes that the latter proteins assemble into a dome-like structure with the membrane neck wrapped around the dome due to a strong adhesion (Figure 3-25). Then, the successive narrowing of the helical filaments of the dome structure will further bend and mold the membrane, leading thus to a neck constriction down to a diameter of 6 nm which would be energetically favorable for spontaneous scission (Lata, Schoehn et al. 2008; Fabrikant, Lata et al. 2009; Lenz, Crow et al. 2009; Bodon, Chassefeyre et al. 2011) (Figure 3-25).

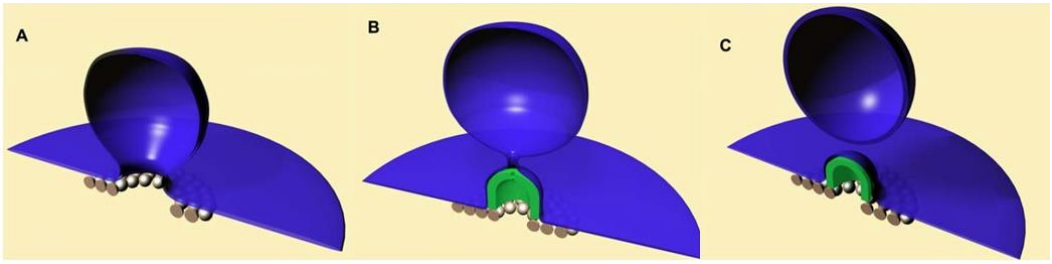

FIGURE 3-25: THE DOME MODEL FOR MEMBRANE BUDDING AND FISSION BY THE ESCRT-III SUB-COMPLEXES (FABRIKANT, LATA ET AL. 2009)

Speculative cartoons Illustrating three stages in ESCRT-mediated vesicle budding from a ''side'' perspective over the endosome surface.

A- Formation of the initial bud by CHMP4 (Snf7).

B- Self-assembly of CHMP2 - CHMP3 nanotube with a dome-like end-cap.

C- Fission of the neck and completion of the vesicle formation.

Albeit none of the models have been proven experimentally, the dome model seems more consistent, because all potential polymers implicated in the final cut (CHMP2A-CHMP3 or CHMP2A or CHMP2B) can form dome-like end-caps *in vitro* or *in cellulo* (Lata, Schoehn et al. 2008; Bodon, Chassefeyre et al. 2011; Effantin, Dordor et al. 2012). And, even though a reconstituted ESCRT-III-catalyzed intraluminal vesicle budding reaction was observed *in vitro* without the AAA-ATPase activity of Vps4 (Wollert, Wunder et al. 2009; Wollert and Hurley 2010), it is likely that Vps4 plays an active role beyond recycling ESCRT-III and is essential for the ESCRT-III machinery regulation (Babst, Davies et al. 2011; Baumgartel, Ivanchenko et al. 2011; Elia, Sougrat et al. 2011; Jouvenet, Zhadina et al. 2011; Elia, Fabrikant et al. 2012; Adell, Migliano et al. 2017).

Dominant negative Vps4 prevents fission of HIV buds (von Schwedler, Stuchell et al. 2003) (Figure 3-26), and Vps4 at viral budding sites disappears before detachment of the virus (Baumgartel, Ivanchenko et al. 2011; Jouvenet, Zhadina et al. 2011) and turnover at the abscission site several minutes before the completion of cytokinesis, simultaneously with the other ESCRT-III subunits (Elia, Sougrat et al. 2011; Guizetti and Gerlich 2012; Adell, Migliano et al. 2017; Mierzwa, Chiaruttini et al. 2017). Hence, apart from disassembling the ESCRT-III complex, Vps4 may as well play a role in providing further energy to induce supplementary stress on the filaments upon disassembly and thereby lead to spontaneous fission (Figure 3-26).

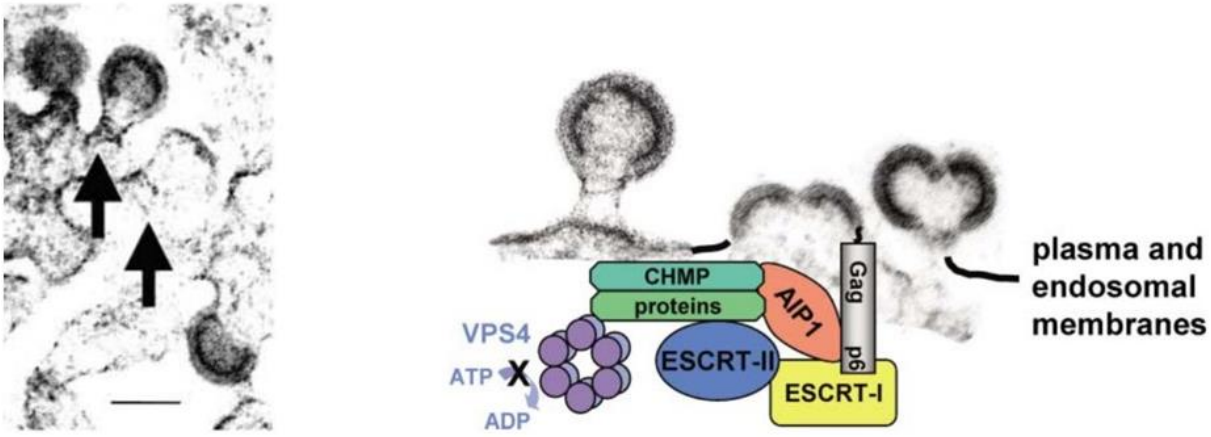

FIGURE 3-26: HIV-1 BUDDING ARREST INDUCED BY DOMINANT-NEGATIVE VPS4B PROTEINS (von Schwedler, Stuchell et al. 2003)
Left: EM images of thin-sectioned 293T cells transfected with HIV DsRed-VPS4B-E235Q. Scale bar is 100 nm. Black arrows indicate striations in the stalks of arrested virions.
Right: Schematic Model for the HIV-1 budding arrest induced by expression of dominant-negative VPS4 Proteins. The illustration emphasizes how nascent viral particles arrest together with class E protein complexes at both endosomal and plasma membranes when VPS4 proteins are unable to hydrolyze ATP (denoted by the black X).

3.6 OBJECTIVE: CHARACTERIZATION OF CHMP2B AND DETERMINATION OF ITS ROLE WITHIN THE ESCRT-III MACHINERY

3.6.1 CHMP2B IS SPECIFIC TO HIGHER ORGANISMS

Among all ESCRT-III subunits, CHMP4, CHMP2A and CHMP3 are conserved throughout Eukaryotes, while CHMP2B is only found in higher organisms. Moreover, CHMP2B appears to be a relatively recent acquisition in the evolution of ESCRT-III complex as a result of a gene duplication event (Leung, Dacks et al. 2008). The fact that in yeast only one Vps2 protein is present might simply reflect the diversification of ESCRT-III function in higher organisms, which mediates membrane scission in many different subcellular contexts. In terms of sequence similarity, both CHMP2A and CHMP2B share a high sequence homology with Vps2 and have therefore been considered as isoforms.

3.6.2 CHMP2B IS IMPLIED IN THE DIVERSIFICATION OF ESCRT FUNCTIONS

Beside the implication of the ESCRT machinery in the MVB pathway, these proteins are involved in many other membrane remodelling processes associated to higher organisms. Interestingly, except for the MVB pathway, CHMP2B seems to be important in all these newly acquired ESCRT-III mediated events (Carlton, Agromayor et al. 2008; Morita, Sandrin et al. 2011; Carlton, Caballe et al. 2012; Jimenez, Maiuri et al. 2014; Olmos, Hodgson et al. 2015; Olmos and Carlton 2016) (Figure 3-27). Nevertheless, its function within the ESCRT machinery is still elusive.

	MVB biogenesis	**HIV release**	**PM repair**	**Cytokinesis**	**NE reformation and repair**
CHMP4	YES	YES	YES	YES	YES
CHMP3	YES	YES	YES	YES	YES
CHMP2A	YES	YES	YES	YES	YES
CHMP2B	**NO**	**YES**	**YES**	**YES**	**YES**

FIGURE 3-27: CHMP2B INVOLVED IN THE NOVEL ESCRT-III DEPENDENT PROCESSES

This table summarizes that while CHMP4B, CHMP3 and CHMP2A are necessary for all the ESCRT-dependent processes, CHMP2B appears to be only involved in the novel ESCRT- mediated membrane remodelling processes.

Studies on cytokinesis and HIV-1 budding and release showed that only a subset of ESCRTs is recruited, notably ESCRT-III and Vps4, which most likely constitute the fission machinery. These studies show that both CHMP2A and CHMP2B localize to the midbody region before the last abscission step in cytokinesis (Figure 3-28).

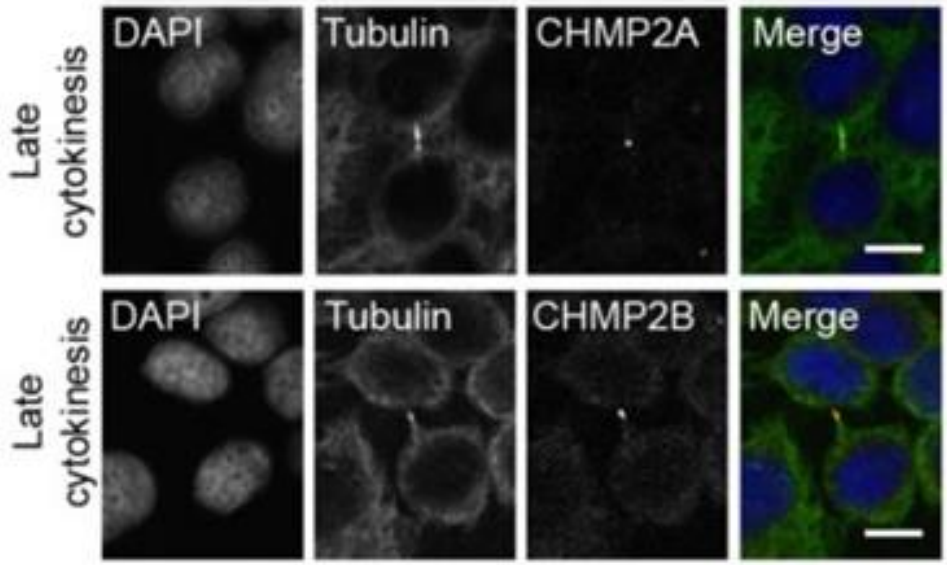

FIGURE 3-28: CHMP2 LOCALISATION TO THE MIDBODY DURING LATE CYTOKINESIS (OLMOS, HODGSON ET AL. 2015)
Immunofluorescence analysis of HeLa cells stained with anti-tubulin, anti-CHMP2A or -CHMP2B and DAPI, showing that endogenous ESCRT-III components CHMP2A and CHMP2B localise to the midbody during late cytokinesis (Olmos, Hodgson et al. 2015).

Furthermore, HIV budding studies indicate that only CHMP4B and CHMP2 (A or B) are essential for virus release and that CHMP3 exerts a significant synergistic effect on the CHMP2A function, but not CHMP2B. These studies also show that in HIV release, co-silencing of CHMP2A and CHMP2B has an additional effect over individual silencing, but functional redundancy between the two proteins has never been shown (Figure 3-29 / left) (Carlton and Martin-Serrano 2007; Morita, Sandrin et al. 2007; Morita, Sandrin et al. 2011; Effantin, Dordor et al. 2013). Additionally, studies by Effantin and al. show that during HIV-1 budding, CHMP3 synergizes much more efficiently with CHMP2A than with CHMP2B (Figure 3-29 / right) (Effantin, Dordor et al. 2013).

Likewise, in neuronal pruning, silencing of CHMP2B or CHMP2A does not have a direct effect on neuronal viability, probably because of mutual compensation. Finally, it was also shown that a mutation in CHMP2B gene could be responsible of a neurodegeneration disease named Fronto-Temporal Dementia (FTD disease) (see chapter 3.6.3).

Thus, to summarize, CHMP2B is involved in the newly acquired human ESCRT-III processes and a mutation in its gene could lead to neurodegenerative disease. But the protein has been so far much less studied than the other main components of the ESCRT-III machinery, thus a more extensive investigation and understanding of CHMP2B role in the ESCRT machinery is now necessary.

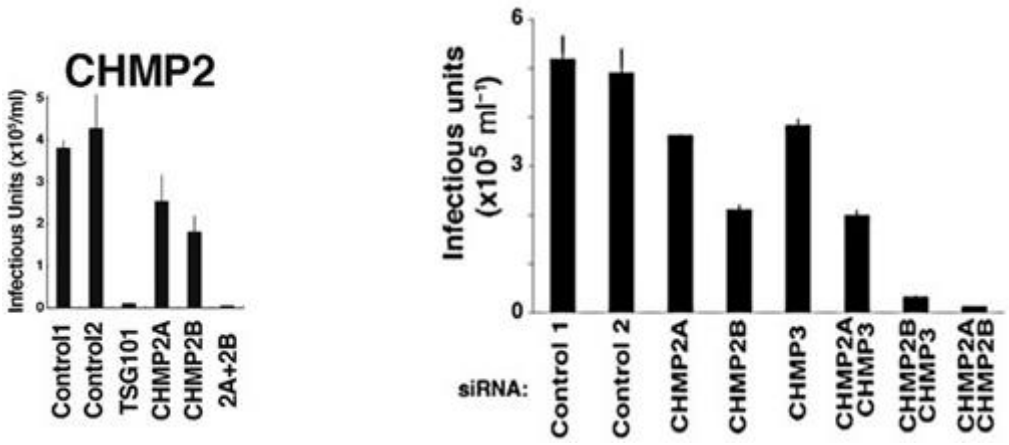

FIGURE 3-29: EFFECT OF THE DEPLETION OF CHMP2 ON HIV BUDDING (MORITA, SANDRIN ET AL. 2011; EFFANTIN, DORDOR ET AL. 2013)

(Left): Viral titers in 293T cells expressing HIV-1 and depleted or co-depleted of the designated CHMP2 family members. SiRNA against the essential budding factor, TSG101, was used as a positive control. And, as expected, TSG101 depletion strongly inhibited viral infectivity. Individual depletion of CHMP2A and CHMP2B caused modest reductions in virus release and infectivity, whereas, co-depletion of CHMP2A and CHMP2B resulted in dramatic reductions in HIV-1 release and infectivity (Morita, Sandrin et al. 2011).

(Right): Viral titers in 293T cells expressing HIV-1 and treated either with control siRNAs (lanes 1 and 2) or with siRNAs that target the indicated ESCRT-III CHMP family members (lanes 3-8). Individual depletion of CHMP2A, CHMP2B and CHMP3 had only modest effects on virion release and infectivity. Depletion of CHMP2A and CHMP3 reduced infectious units by a factor of ～1.4 and CHMP2B knockdown produced a ～2.5-fold reduction. Co-depletion ofCHMP2A and CHMP3 reduced infectivity 2.6-fold, while the double knockdown ofCHMP2B-CHMP3 reduced infectivity 17-fold and the CHMP2A-CHMP2B double knockdown reduced infectivity 46-fold (Effantin, Dordor et al. 2013).

3.6.3 CHMP2B MUTATION LEADS TO A NEUROLOGICAL DISORDER: FRONTO-TEMPORAL DEMENTIA

During normal aging, the number of hippocampal neurons gradually decreases, and the number and length of terminal dendritic branches of remaining neurons increase progressively, probably to compensate for the loss of other neurons. The abnormal growth and degeneration of dendrites are closely associated with many neurodegenerative diseases such as Alzheimer or Fronto-Temporal Dementia (FTD) diseases.

Fronto-Temporal Dementia is considered as the second most common form of senile dementia in individuals above 65 years, accounting for up to 20% of cases (Knopman, Mastri et al. 1990). The most prominent clinical and neuropsychological features of FTD are changes in personality and behavior, such as poor insight, loss of personal awareness and social awareness, lack of empathy, aggressiveness, inappropriate social behaviors, dietary changes, and the development of a new personality. FTD is

genetically heterogeneous, with associated loci identified on chromosomes 3, 9 and 17 (Wilhelmsen, Lynch et al. 1994; Hosler, Siddique et al. 2000; Skibinski, Parkinson et al. 2005).

Northern-blot analysis showed that wild-type CHMP2B is expressed in most cell types and in all major regions of the brain, including the frontal and temporal lobes (Skibinski, Parkinson et al. 2005). CHMP2B seems to be especially vital for proper neuronal function as the neurological disorder FTD-3 Fronto-temporal dementia linked to chromosome 3) could be directly linked to different CHMP2B mutations (Skibinski, Parkinson et al. 2005).The first mutation, leading to the $CHMP2B^{Intron5}$ mutant is unique to Danish kindred with a history of FTD-3. It is a point mutation (G to C substitution) resulting in mRNA splicing and production of mutant CHMP2B proteins lacking the C-terminal 36 aa isoform. This C-terminus truncation causes removal of an important Vps4 binding site as well as the elimination of the normal auto-inhibitory resting state of CHMP2B, thus producing what is believed to be a constitutively active protein. Other mutations have also been reported. $CHMP2B^{\Delta 10}$ is an alternative mRNA transcript generated from the same mutation missing the final 36aa of the normal protein; however, 29aa are added randomly to the C-terminus. $CHMP2B^{Q165X}$ is an unrelated mutation resulting in a 49aa C-terminus truncation; it was found in a Belgian family and appears to result in similar pathology to the $CHMP2B^{Intron5}$ mutant isoform (Figure 3-30 / A). Ectopic expression of the mutant protein $CHMP2B^{Intron5}$ caused misregulation of transmembrane receptors, accumulation of multilamellar structures, abnormal lysosomal morphology, downregulation of a brain-specific microRNA (miRNA-124), abnormal dendritic spine morphology, dendritic retraction (Figure 3-30 / C) prior to neurodegeneration, and cell death (Figure 3-30 / B) (Skibinski, Parkinson et al. 2005; van der Zee, Urwin et al. 2008). $CHMP2B^{Intron5}$ binds CHMP4B, which is essential for neuronal structural integrity and viability, with higher affinity than CHMP2B-WT. $CHMP2B^{Intron5}$ recruits CHMP4B in clusters or aggregates, resulting in sequestration of CHMP4B (Figure 3-30 / D). Thus, $CHMP2B^{Intron5}$inhibits neurite development causing neurodegeneration through its failure to dissociate from ESCRT-III subunit CHMP4B in cortical neurons. Moreover, loss of CHMP4B or $CHMP2B^{Intron5}$ expression caused the accumulation of auto phagosomes in cortical neurons in flies (Lee, Beigneux et al. 2007; Lee and Gao 2008; Lee and Gao 2008). Hence, by sequestering CHMP4B, $CHMP2B^{Intron5}$ forms abnormal complexes containing CHMP4B and could cause rapid neuronal cell loss.

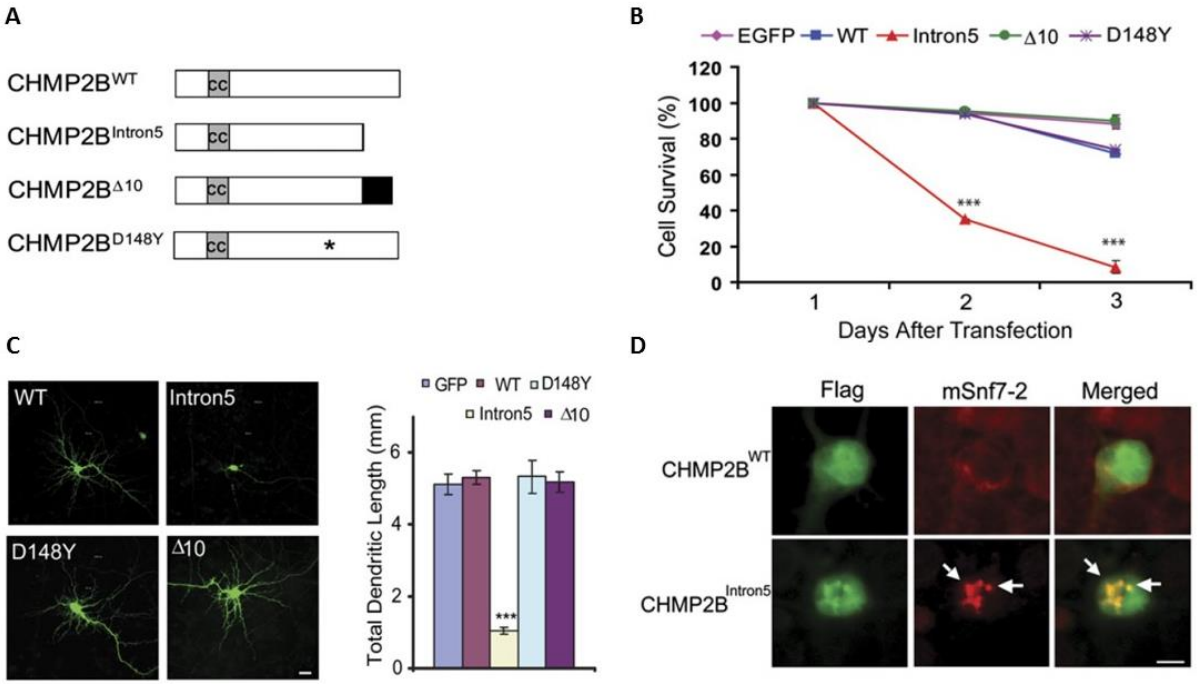

FIGURE 3-30: CHMP2BINTRON5 CAUSES NEURODEGENERATION THROUGH ITS FAILURE TO DISSOCIATE FROM CHMP4B (LEE, BEIGNEUX ET AL. 2007)

(A) Schematics of wild-type (CHMP2BWT) and mutant CHMP2B proteins. ''CC'' stands for coiled-coil domain. The asterisk indicates D148Y. The black box represents an abnormal 29 aa C terminus of CHMP2B$^{\Delta 10}$.

(B) Survival curves of cultured cortical neurons transfected with EGFP alone or with different CHMP2B proteins. Values are the mean 6 SEM of four independent experiments. ***p < 0.001.

(C) Effects of wild-type or mutant CHMP2B proteins on dendritic morphology of 15 DIV mature cortical neurons. Different CHMP2B proteins were co-transfected with GFP, and the dendritic length was measured by MAP2-antibody staining. The scale bar represents 20 mm.

(D) Expression of different CHMP2B mutant proteins in HEK293 cells 18 or 72 hours after transfection. Flag antibody was used for detecting wild-type or mutant CHMP2B proteins. b-tubulin served as the loading control.

3.6.4 THESIS OBJECTIVE: STUDY OF CHMP2B USING MODEL MEMBRANES *IN VITRO*

The current hypothesis for the minimal membrane scission machinery is that CHMP4B recruits either CHMP2A or B, or CHMP3 together with CHMP2A, that act in concert with the ESCRT-III disassembling AAA-type ATPase VPS4 (Adell and Teis 2011; Adell, Migliano et al. 2016) . CHMP2A can bind CHMP4B (Figure 3-31 / A) through basic residues which are also present in the sequence of CHMP2B (Figure 3-31 / B) (Morita, Sandrin et al. 2011).

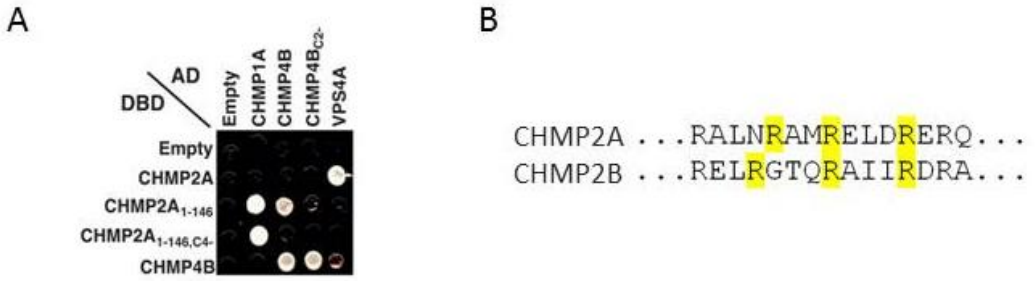

FIGURE 3-31: BINDING OF CHMP2A WITH CHMP4B (MORITA, SANDRIN ET AL. 2011)

(A) Yeast two-hybrid interactions between the designated ESCRT proteins fused to activation (AD) or DNA binding (DBD) domains (or with empty vector controls). The following interactions Were judged to be positive (AD fusions listed first): CHMP1A:CHMP2A1-146, CHMP1A:CHMP2A1-146,C4-, CHMP4B:CHMP2A1-146,CHMP4B:CHMP4B, CHMP4BC2-:CHMP4B, VPS4A:CHMP2A. VPS4A also interacted very weakly with CHMP4B in this assay.

(B) CHMP2A basic residues (in yellow) which are required for the interaction with CHMP4B are present in CHMP2B.

CHMP2A can form tubes with dome-like end cap, but only in the presence of CHMP3. CHMP2B alone can also form tubes both *in vivo* and *in vitro*, but it does not co-polymerize with CHMP3 *in vitro* (Lata, Schoehn et al. 2008; Bodon, Chassefeyre et al. 2011). In HIV release, co-silencing of CHMP2A and CHMP2B has an additional effect over individual silencing, but functional redundancy between the two proteins has never been shown (Morita, Sandrin et al. 2011). And, even though both CHMP2A and CHMP2B are Vps2 human homologs, the MIM domain to bind Vps4 MIT domain is present in Vps2 and conserved in CHMP2A, but absent in CHMP2B (Figure 3-32). Accordingly, CHMP2A / CHMP3 dome-like structures might be well-suited for carrying out the last step of ESCRT-III-mediated scission, whereas, the role of CHMP2B in the membrane scission event as well as its order of recruitment within the ESCRT-III machinery remain unclear.

FIGURE 3-32: MIM-DOMAIN SEQUENCE OF VPS2

Alignment of the C-terminal region of Vps2 from *S. Cerevisiae* and CHMP2A/2B from *H. Sapiens*. Critical residues constituting the MIM domain are colored. The MIM domain, which is required for Vps4 recruitment, is present in Vps2 and conserved in CHMP2A, but absent in CHMP2B.

This is even more striking when considering that mutations in the CHMP2B gene, but not in the CHMP2A or CHMP3 genes, are implicated in the neurodegenerative disease FTD. CHMP2B^{Intron5} forms aggregates in cells and interferes with endosomal / lysosomal fusion, causes autophagosomes accumulation and leads to empowered dendritic spines formation (Lee, Beigneux et al. 2007; Lee and Gao 2008; Lee and

Gao 2008; Urwin, Ghazi-Noori et al. 2009; Belly, Bodon et al. 2010). However, the molecular mechanism responsible for this pathology remains largely obscure, because the function of CHMP2B is still unknown. Along these lines, our aim is to understand the role of CHMP2B in the ESCRT-III machinery.

Our global objective was to use model membrane systems of controlled composition and shape as well as a battery of biophysics and structural technics to study the assembly of CHMP2B on membranes and compare it to CHMP2A and CHMP3. We initially aimed at mimicking the inverted topology of ESCRT-III proteins in cells by using model membranes. The idea was to encapsulate CHMP proteins inside GUVs and using micromanipulation to pull a membrane nanotube out of the GUV. Unfortunately, these experiments appeared not to be feasible in the presence of CHMP2B proteins for numerous reasons that we will describe in the Results chapter. To overcome this impasse, we decided to change the work plan. We studied the interaction of CHMP2B with different lipids and characterized the polymer assembly. Moreover, to understand the role of CHMP2B protein in the fission machinery, we compared all of our obtained results with that of the other CHMP subunits.

CHAPTER 4. MATERIAL AND METHODS

4.1 PROTEIN PURIFICATION

CHMPs proteins used for this work were provided by the team of Prof. Dr. Winfried Weissenhorn, EBEV group at the Institute of Structural Biology in Grenoble. Protein purification and labelling was kindly achieved by Nolwenn Miguet and Christophe Caillat.

Escherichia coli BL21 cells were transformed with plasmids and grown at 37°C in Luria broth medium to an OD_{600} of 0.6. Following expression, CHMP proteins Were concentrated, labelled over night at 4°C with a ratio of Alexa labelling dye per protein of 2 to 1 and immediately frozen in liquid nitrogen with 0.1% of methyl cellulose (Sigma Aldrich) as cryo-protectant. All aliquots were kept at -80°C prior to experiments.

Protein	MW	Vector	TAG	Induction	Purification column	Gel filtration buffer
CHMP2AFL GSCS	25103	pETG30A	GST	3h-37°C- IPTG 1mM	glutathion	20mM HEPES pH7,6 / 150mM NaCl
CHMP2AΔC	62000	Unkown	MBP	1h-37°C- IPTG 1mM	amylose	20mM HEPES pH7,6 / 150mM NaCl
CHMP2BΔC	17755	pETM11	HIS	4h-37°C – IPTG 1mM	Refolding - nickel	50mM Tris pH7,4 / 100mM NaCl
CHMP2BFL	25074	pETM11	HIS	4h-37°C – IPTG 1mM	Refolding - nickel	50mM Tris pH7,4 / 100mM NaCl
CHMP3ΔC GSCS	20621	pBADM30	GST	3h-37°C- Arabinose 0,2%	glutathion	20mM HEPES pH7,6 / 150mM NaCl
CHMP3FL	25100	pproexthtb	HIS	3h-37°C- IPTG 1mM	nickel	20mM HEPES pH7,6 / 150mM NaCl
CHMP4B LINK	68139	pBADM41	MBP	1h-37°C- Arabinose 0,2%	amylose	50mM HEPES pH7,6 / 300mM NaCl /300mM KCl
TEV	28617	pRK793	HIS	3h-37°C- IPTG 1mM	nickel	PBS1X / 10% glycerol / 2mM EDTA / 10mM DTT
VPS4	49302	pproexthtb	HIS	ON-20°C – IPTG 1mM	nickel	25mM Hepes pH 7.5, 150mM NaCl, 0.5mM, DTT

4.2 MODEL MEMBRANE SYSTEMS

To investigate the protein-lipid interaction and the effect of the protein assembly on the membrane surface, we used model membranes for our study.

Membrane model systems with precisely controlled composition are used to investigate fundamental interactions of membrane components under well-defined conditions. The most commonly used model membranes are lipid monolayers (Langmuir monolayers), supported lipid bilayers (SLB) and unilamellar lipid vesicles categorized as a function of their size (small unilamellar vesicles (SUVs), large unilamellar vesicles (LUVs) and giant unilamellar vesicles (GUVs)) (Figure 4-1).

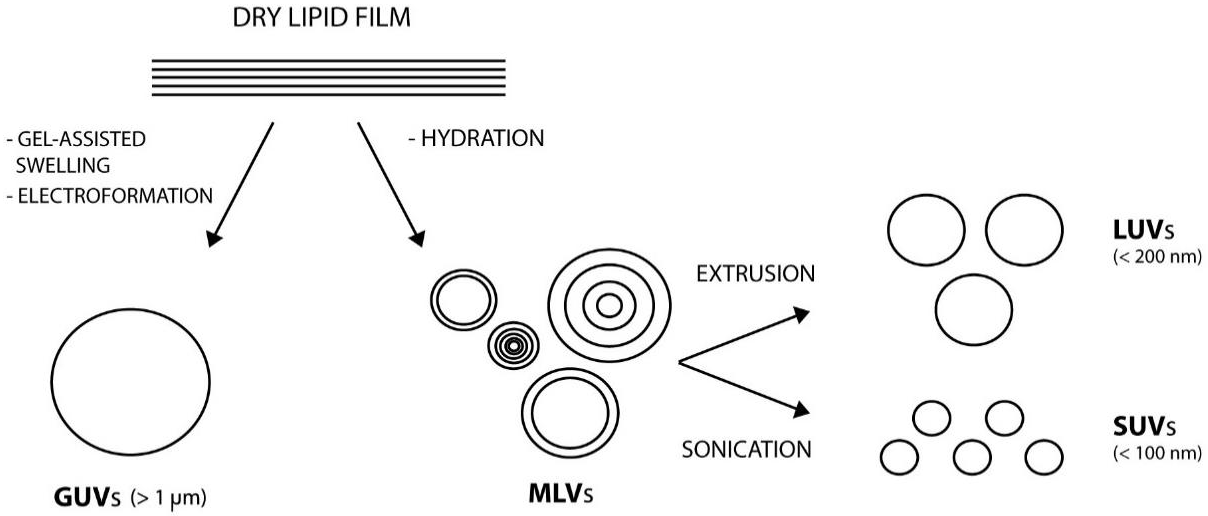

FIGURE 4-1: SUMMARY OF THE DIFFERENT TECHNIQUES USED FOR VESICLE PRODUCTION

4.2.1 REAGENTS

β-casein from bovine milk (>99%), polyvinyl alcohol fully hydrolyzed (PVA) and neutravidin were purchased from Sigma-Aldrich (Sigma-Aldrich, France). Streptavidin conjugated to a Texas Red dye was purchased from ThermoFisher (ThermoFisher Scientific, USA). β-casein and PVA were dissolved in Sucrose 25mM, NaCl 50mM and Tris 25mM (pH 7.5) at 5mg.mL^{-1} and 5% (w/w) respectively. Texas Red dye conjugated Streptavidin and neutravidin were dissolved in ultrapure water at a concentration of 2mg.mL^{-1}. Biotin-PEG-Silane (M.W. 3400) and m-PEG-Silane (M.W 2000) were both purchased from Laysan Bio, Inc (Laysan Bio, U.S.A) and dissolved at 5 mM in DMSO. All the reagents were stored at −20°C in amber vials (Sigma-Aldrich, France).

DOPC (1,2-dioleoyl-sn-glycero-3-phosphatidylcholine), DOPS (1,2-dioleoyl-sn-glycero-3-phospho-L-serine), DOPE (1,2-dioleoyl-sn-glycero-3-phosphatidylethanol- amine), cholesterol (cholest-5-en-3ß-ol), PI(3)P (1,2-dioleoyl-sn-glycero-3-phospho-(1'-myo-inositol-3'-phosphate)), PI(3,5)P_2 (1,2-dioleoyl-sn-glycero-3-phospho-(1'-myo-inositol-3',5'-bisphosphate)), PI(4)P (L-α-phosphatidylinositol-4-

phosphate), PI(4,5)P_2 (L-α-phosphatidylinositol-4,5-bisphosphate), BODIPY TMR-PtdIns(4,5)P_2, C16 (red PI(4,5)P_2), 1-oleoyl-2-6-[4-(dipyrromethene boron difluoride) butanoyl] amino hexanoyl-sn-glycero-3-phosphoinositol-4,5-bisphosphate (TopFluor PI(4,5)P_2),DSPE-PEG2000-Biotin (1,2-distearoyl-sn-glycero-3-phosphoethanolamine-N-[biotynyl(polyethylene glycol)-2000] and Egg Rhod PE (L-α-phosphatidylethanolamine-N-(lissamine rhodamine B sulfonyl) were purchased from Avanti Polar Lipids, Inc (Avanti Polar Lipids, U.S.A.). Stock solutions of lipids were solubilized in chloroform at a concentration of 10 mg.mL^{-1}, except for cholesterol which was solubilized in chloroform at a concentration of 20 mg.mL^{-1}, DSPE-PEG2000-Biotin at a concentration of 0.1 mg.mL^{-1}, Egg Rhod PE which was dissolved at 0.5 mg.mL^{-1} and PIPs, which were solubilized in a mixture of chloroform/methanol (70:30) (v/v) at a concentration of 1 mg.mL^{-1}. All stock solutions were kept with argon and stored at −20°C in amber vials (Sigma-Aldrich, France).

4.2.2 LIPID MIXTURES

The different lipid mixtures used in the present work are summarised below:

TABLE1: LIPID MIXTURES

Lipid mix	% DOPC	% DOPE	% Cholesterol	**% Negatively charged lipids**
1	70	0	0	30 % DOPS
2	60	0	0	40% DOPS
3	80	0	0	10% DOPS, 10% PI(4,5)P_2
4	80	0	0	10% DOPS, 10% PI(3,4,5)P_3
5	**55**	**10**	**15**	**10% DOPS, 10% PI(4,5)P_2**
6	73	10	15	2% DOPS
7	73	10	15	2% PI(4,5)P_2
8	73	10	15	2% PI(4)P
9	73	10	15	2% PI(3,5)P_2
10	73	10	15	2% PI(3)P

Lipid mixtures 1 to 4 were exclusively used for Quartz Crystal Microbalance with Dissipation monitoring (QCM-D) experiments. Lipid mixtures 6 to 10 were exclusively used for Fluorescence-activated cell sorting (FACS) experiments. Lipid mixture 5 was used for all the other experiments performed with confocal fluorescence, EM and AFM setups.

All lipid solutions were stored at −20°C in amber vials (Sigma-Aldrich, France). And, after each use, argon was added to the vials before sealing them with paraffin film (Parafilm, USA) to prevent lipid oxidation.

4.2.3 GUVS PREPARATION

The size of GUVs, ranging from 1 - 100 µm, is well above the diffraction limit and can allow their visualization by optical microscopy such as confocal or fluorescence microscopy, as well as the use of micromanipulation techniques for single vesicles manipulation. These micrometer sized vesicles provide a model of cell-sized membranes with a lipid composition of choice.

Different methods of GUVs preparation have been designed over the years. GUVs can be produced by emulsion-based approaches (Pautot, Frisken et al. 2003; Stachowiak, Richmond et al. 2008) in which water droplets are successively coated with inner and outer lipid monolayers, and by techniques based on lipid film rehydration (Horger, Estes et al. 2009; Meleard, Bagatolli et al. 2009). Emulsion-based methods are advantageous for soluble proteins encapsulation and for the formation of asymmetric GUVs, i.e. with different inner and outer leaflets lipid compositions. However, GUVs formed from emulsions retain traces of solvent altering the mechanical properties of the membrane (Campillo, Sens et al. 2013). Lipid film rehydration methods are based on the formation of a multi-lamellar stack of membranes obtained by drying a lipid film followed by a rehydration in an aqueous buffer step. The solvent pushes the layers apart and at the surface of the stack, individual membranes can detach to form GUVs (Kwok and Evans 1981). Practically, the spontaneous swelling method has a relatively low yield of defect-free GUVs (Rodriguez, Pincet et al. 2005). To improve the yield of defect-free GUVs, electroformation methods have been developed in which an electric AC field is applied during film rehydration (Angelova, Soléau et al. 1992; Mathivet, Cribier et al. 1996). To work at physiological salt conditions, electroformation is performed on platinum wires at high frequency (500 Hz) at a voltage of 350 mV (Meleard, Bagatolli et al. 2009) (Figure 4-2). Alternatively, to rapidly form GUVs in physiological buffers, gel-assisted swelling can be used. This last method consists in depositing the lipid solution onto a polymeric gel substrate, such as polyvinyl alcohol (PVA), drying the film, which eventually leads to GUV formation upon rehydration (Horger, Estes et al. 2009; Weinberger, Tsai et al. 2013).

4.2.3.1 ELECTROFORMATION WITH PLATINUM WIRES

GUVs were prepared by the Electroformation method using platinum wires in high salt conditions (Mathivet, Cribier et al. 1996; Meleard, Bagatolli et al. 2009; Morales-Penningston, Wu et al. 2010) (Figure 4-2). Two platinum wires of 0.5mm diameter (99.9%+ pure, Goodfellow) are inserted into a Teflon chamber holes, crossing the chamber wells (Figure 4-2).

Lipid droplets with the requisite lipid mixture at 3 $mg.mL^{-1}$ are deposited on the platinum wires by using a Hamilton syringe. To remove residual solvent, the lipid film is further dried under vacuum for 20 min at room temperature. Sigillum wax (Vitrex, Denmark) is applied to the chamber sides to prevent leakage

from the platinum wires protruding from the holes. Vacuum grease is applied on the rim of the bottom side of the chamber, which is then closed with a 22 × 40 mm glass coverslip (Menzel-Gläser, Germany). To rehydrate the dried lipid drops, the wells are filled with the growth buffer and the chamber is sealed with a second coverslip. The wires are finally connected to a generator, building up a sine electric field at 350 mV and 500 Hz, for 8 hours at 4°C. GUVs are extracted by pipetting directly from GUV-rich regions from the wires.

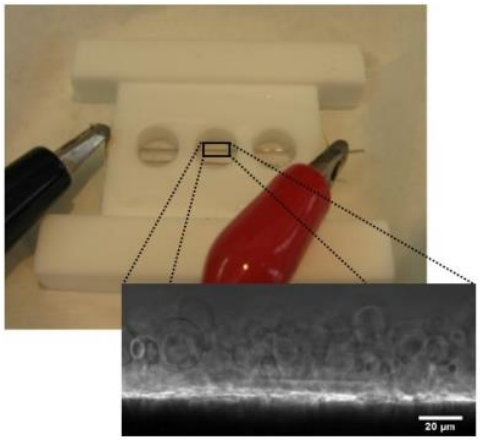

FIGURE 4-2: ELECTROFORMATION ON PLATINUM WIRES (MODIFIED FROM (AIMON, MANZI ET AL. 2011))
A Teflon chamber for GUVs preparation by electroformation on platinum wire (PLW). Insert: phase contrast image of GUVs on a PLW. Scale bar 20 µm.

4.2.3.2 SPONTANEOUS SWELLING WITH PVA

GUVs were also prepared by spontaneous swelling on polyvinyl alcohol (PVA)-based gels (Weinberg et al., 2013). The PVA gel (5% PVA, 50 mM Sucrose, 25 mM NaCl and 25 mM Tris, at pH 7.4) is deposited on plasma cleaned (PDC-32G, Harrick) glass coverslips (18 x 18 mm, VWR International, France). The excess gel was removed. The glass cover slides are then dried for 50 min at 60°C. A volume of 15 µL of lipid solution at 1mg.mL-1 is deposited on the PVA-coated slide by using a Hamilton syringe to get a lipid film as thin as possible. To remove residual solvent, the lipid film is further dried under vacuum for 20 min at room temperature. The lipid film is then rehydrated with the growth buffer at room temperature. Vesicles form within approximately 45 min to 60 min and are extracted by pipetting directly from the slides on top of the PVA gel.

For all the experiments performed using GUVs, the osmolarity of the vesicle growth buffer, of the protein binding buffer and of the observation buffers were measured with an osmometer (Löser Messtechnik-Osmometer, Berlin, Germany) and adjusted to avoid GUV inflation or deflation due to osmotic pressure variation between the inner and outer media. Indeed, it is crucial to work at isotonic conditions to avoid any osmotic shock on the pre-formed GUVs.

4.2.4 MAKING LUVS AND SUVS

Lipid stock solutions are prepared at a concentration 3 $mg.mL^{-1}$ in chloroform. The solvent is then evaporated by rotating the vial to evenly spread the lipids on the bottom and the walls of the glass vial under a gentle stream of nitrogen and at room temperature. To remove excess residual solvent, the lipid film is further dried under vacuum for 20 min at room temperature. Multilamellar vesicles (MLVs) are prepared by rehydrating the lipid film in the appropriate growth buffer solution to obtain a final concentration of 1 $mg.mL^{-1}$. The solution is vortexed for 2 min. The vortexed solution has a turbid-like aspect. MLVs are then either extruded 11 times through a polycarbonate track-etched membrane with pore sizes of 100 nm for LUVs formation (Meleard, Bagatolli et al. 2009) or sonicated for 5 min until obtaining a clear colorless solution for SUVs formation. SUVs produced by sonication have a radius ranging from 20 to 40 nm. The obtained vesicles are stored at −20°C in amber vials (Sigma-Aldrich, France).

4.2.5 MAKING SLBS

Supported lipid bilayers are biomimetic model membranes obtained by adsorption and fusion of SUVs (diameter in the range of 20 - 100 nm) or LUVs (diameter in the range 50-200 nm) onto a solid surface such as mica (for HS- AFM experiments), glass (for AFM nanoindentation experiments), or silicon wafers (for QCM-D experiments) (Figure 4-3). However, the drawback is that the surface-membrane interaction seriously perturbs lipid diffusion. In this model membrane type, the hydrophilic head groups of the first lipid monolayer are facing the support, the hydrophobic hydrocarbon chains of this monolayer are in contact with the chains of the second monolayers, and the hydrophilic head groups of the second monolayer is accessible. SLBs are more stable than GUVs and the overall lipid composition of SLBs can be controlled while it is not the case with vesicles. Because the membrane of supported lipid bilayers is bound to the solid support surface, their characterization could be easily done with different surface-sensitive techniques such as AFM or QCM-D techniques.

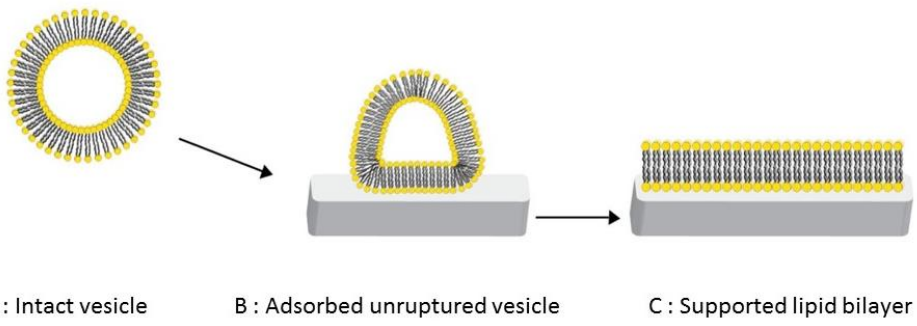

FIGURE 4-3: SUPPORTED LIPID BILAYER FORMATION
Formation of a supported lipid bilayer. Intact vesicles are added in the bulk solution in contact with a wafer solid support (mica, glass or silicon dioxide) (A). The vesicle is first adsorbed as intact - unruptured vesicles (B) and then, when a critical surface coverage is reached, the lipid bilayer is formed spontaneously (C).

4.3 FLUORESCENCE MICROSCOPY

The addition of fluorescently-labelled CHMP proteins to vesicles containing fluorescent lipids enables the observation, quantification and characterization of the protein-membrane binding properties by fluorescence microscopy.

Measurements of fluorescence intensities allow a precise quantification of the protein affinity towards different lipid membranes. Furthermore, using fluorescent microscopy permits the direct observation of the protein supramolecular assembly and dynamics on the surface of the GUV.

4.3.1.1 FLUORESCENCE MICROSCOPY PRINCIPLE

Fluorescence microscopy is a type of microscopy where, instead of magnifying objects based on different absorptions of reflections of visible light, it excites fluorescent molecules and captures their emitted fluorescence. The basic setup is an epifluorescence or a wide field microscope. Here a filter is placed after a high intensity Illumination lamp that selectively let pass only a narrow range of wavelengths. The light is then directed toward a dichroic mirror that reflects beams of certain wavelengths, while letting others pass through. In this case, the mirror reflects the excitation light, which then irradiates the sample. Fluorescence molecules absorb excitation light and through the phenomenon of fluorescence, emit light of lower energy, hence higher wavelength. The emitted light passes through a dichroic mirror, which can filter out any non-absorbed excitation light (same as above), and then goes through the emission filter, which eliminates any other background light, not coming from fluorescent molecules. The caveat of this setup is that the entire visual field of the sample is illuminated creating a lot of noise in imaging. The fluorescence emitted by the specimen outside the focal plane of the objective interferes with the resolution of in focus features. As the sample increases in thickness, the ability to capture fine detail above out-of-focus signal becomes increasingly challenging.

In confocal microscopy, spatial filtering eliminates the light outside the thickness of the focal plane (≈ 100 nm) which effectively increases the resolution and the contrast. The basic configuration comprises a single point of light from a laser and a pinhole placed in front of the detector, in an optically conjugated plane. The use of a pinhole rejects out-of-focus light which improves the lateral and axial resolution: only light from the right focal plane passes through the pinhole. Light from the plane above or below the imaged plane focuses after or before the pinhole and fails to pass through the pinhole. Therefore, only light from one plane is in focus to pass through the pinhole or as the name suggest “confocal”. The depth of the image can be changed by modifying the focus, which allows to obtain a three-dimensional image of the sample.

4.3.1.2 EXPERIMENTAL CONDITIONS

The confocal microscope is composed of an inverted microscope (Eclipse TE2000 from Nikon), two objectives (60x water immersion and 100x oil immersion), a C1 confocal head from Nikon, three lasers (λ=488 nm, λ=561 nm and λ = 633 nm) with the following filters ET 515/30m, ET 585/40m and ET 655LP , respectively, an AOM to set the laser power, a camera to observe the chamber in bright field is placed behind a bandpass filter (750-900 nm, RG9, schott glass) to avoid light pollution. The stage is also equipped with two pipet holders both linked to manometers to control the pressure. The software EZ-C1 was used to make the acquisition of the confocal images and a MatLab routine to view the stage in real time and take movies via the camera.

For the fluorescence microscopy experiments, we used Fluorodish Cell Culture Dishes – 35 mm, 23 mm Well (World Precision Instruments Inc, Germany) and custom-made chambers. Custom-made chambers were prepared using 60 x 20 mm and 40 x 22 mm glass coverslips (Menzel-Gläser, Germany). The bottom coverslip was divided into multiple sample chambers by making walls of plastic paraffin film (Parafilm, USA). The paraffin film was attached by heating it, making it act as glue between the bottom and top coverslips. Prior to each experiment, the chamber was passivated for 15min with a β-casein solution (Sucrose 25 mM, NaCl 50 mM and Tris 25 mM (pH 7.5) at 5 $mg.mL^{-1}$) to prevent the adhesion of the GUVs on the glass surface. Following the passivation step, the chambers were rinsed twice with the experiment buffer before addition of the vesicles co-incubated with CHMP proteins.

4.3.2 SPINNING DISK CONFOCAL MICROSCOPY

4.3.2.1 SPINNING DISK CONFOCAL MICROSCOPY PRINCIPLE

In basic confocal microscopy, the laser beam is scanned point by point in a raster pattern and signal is detected sequentially from each point by a photomultiplier tube until an entire image is created with a trade-off between image resolution and speed. A time skew between the first and last points in the scan is measured as each point will be illuminated at different times. For example, if the array consists of a 512 x 512 pixel array and each point is illuminated for 1 µs, then each scan will take about 262 ms. To compensate for the brief Illumination of each pixel, an intense laser beam is required, and if the specimen is dynamic the time skew can lead to errors in observation.

Spinning disk confocal laser microscopy overcomes this problem by exploiting the multiplex principle. Here, an expanded beam illuminates an array of micro lenses arranged on a disk. Each microlens has an associated pinhole laterally co-aligned on a second (pinhole) disk and axially positioned at the focal plane of the microlenses. The disks are fixed to a common shaft that is driven at high speed by an electric motor. When the disks spin, and the scanner is coupled to a microscope with the pinhole disk located

in its primary image plane, an array of focused laser beams scan across the specimen. The pinholes (and microlenses) are arranged in a pattern, which scans a field of view defined by the array aperture size and the microscope objective magnification. The scanning laser beams excite fluorescent labels in the sample. Fluorescence emission will be most intense where this array is focused. Some fraction of this light will return along the excitation path where it will be preferentially selected by the same confocal pinholes. A dichroic mirror, which reflects emission wavelengths, is located between the two disks. This separates the laser emission from any excitation light reflected or scattered from the microscope optics. And, the geometry of the emission path results in a confocal fluorescence signal with extremely low background noise.

4.3.2.2 EXPERIMENTAL CONDITIONS

To image protein binding to the surface of GUVs and obtain a 3D acquisition of this assembly, we used an Inverted Spinning Disk Confocal Roper/Nikon equipped with Camera: EMCCD 512x512 Andor Technology (pixel size:16 µm), objective (100x CFI Plan Apo VCoil NA 1,4 WD 0,13) and 3 lasers (491, 561, 633, 100mW) with the following filters ET 525/50m Emission Filter 25mm, ET 595/50m Emission Filter 25mm and ET 655LP Emission Filter 25mm, respectively. Spinning disk experiments were performed at The BioImaging Cell and Tissue Core Facility of the Institute Curie (PICT-IBiSA), member of the France-BioImaging national research infrastructure.

All data for quantification based on fluorescence intensity were taken every time on the same microscope with the same camera, using the same settings. The only parameter that was changed between samples was the exposure time. This was necessary to allow imaging of both faint samples and bright samples with the same laser power without saturating the detector. The difference in exposure time was normalized later. Images were taken for each vesicle, independently of its size or amount of bound protein. Only vesicles showing non-spherical shapes, aggregation or being multilamellar were discarded. A time-lapse at the equator of the vesicle was acquired in addition to the above-mentioned imaging procedure for each CHMP-GUV binding assay. Likewise, Z-stacks were acquired on vesicles to determine the morphology/structure of the protein assembly on the surface of the GUVs in three dimensions.

Fluorodish Cell Culture Dishes – 35 mm, 23 mm well (World Precision Instruments Inc, Germany) were used for the protein-GUV binding assay observation. Before use, the dishes were passivated for 15 min with a β-casein solution (Sucrose 25 mM, NaCl 50 mM and Tris 25 mM (pH 7.5) at 5 $mg.mL^{-1}$) to prevent the adhesion of the GUVs and CHMP proteins on the positively charged glass surface. Following the passivation step, the chambers were rinsed twice with the experiment buffer before addition of the vesicles co-incubated with CHMP proteins. The collected GUVs from the electroformation on platinum

wires growth were incubated 15 min with CHMP proteins at variable concentrations ranging from 50 nM to 2 µM in the observation buffer in isotonic conditions.

4.3.3 FLUORESCENCE RECOVERY AFTER PHOTOBLEACHING ASSAY (FRAP)

FRAP experiments were performed in collaboration with Dr. Nicola De Franceschi (Post-Doc in the team).

4.3.3.1 FRAP PRINCIPLE

Fluorescence recovery after photobleaching (FRAP) is a quantitative fluorescence technique that can be used to measure the dynamics or lateral diffusion of a molecularly thin film containing fluorescently labelled probes in 2D by taking advantage of the fact that most fluorophores are irreversibly bleached by incident light of very high intensity.

In practice, FRAP requires that a series of fluorescence intensity images are first collected to give a value for intensity in both the region of interest and the surrounding sample (i.e. background image of the sample before photobleaching). Following this, a defined region of the sample, namely the region of interest (ROI), is illuminated with high intensity light causing the fluorophore within that region to become photobleached. Photobleaching is defined as the permanent destruction of fluorescence by a light-induced conversion of the fluorophore to a chemically non-fluorescent compound. This creates a darker, bleached region, within the sample (Figure 4-4). Photobleached molecules are subsequently replaced by non-bleached molecules over time due to diffusion in GUVs resulting in an increase in fluorescence intensity in the bleached region (Figure 4-4). Recovery of fluorescence into the bleached area occurs because of the diffusional exchange between bleached and unbleached molecules.

The fraction of fluorescent molecules that can participate in this exchange is referred to as the mobile fraction. The fraction of molecules that cannot exchange between bleached and non-bleached regions is called the immobile fraction. And, if the fluorescent molecules are bound to static membrane components, the rate of recovery is thus retarded by a factor related to the association and disassociation coefficients of binding.

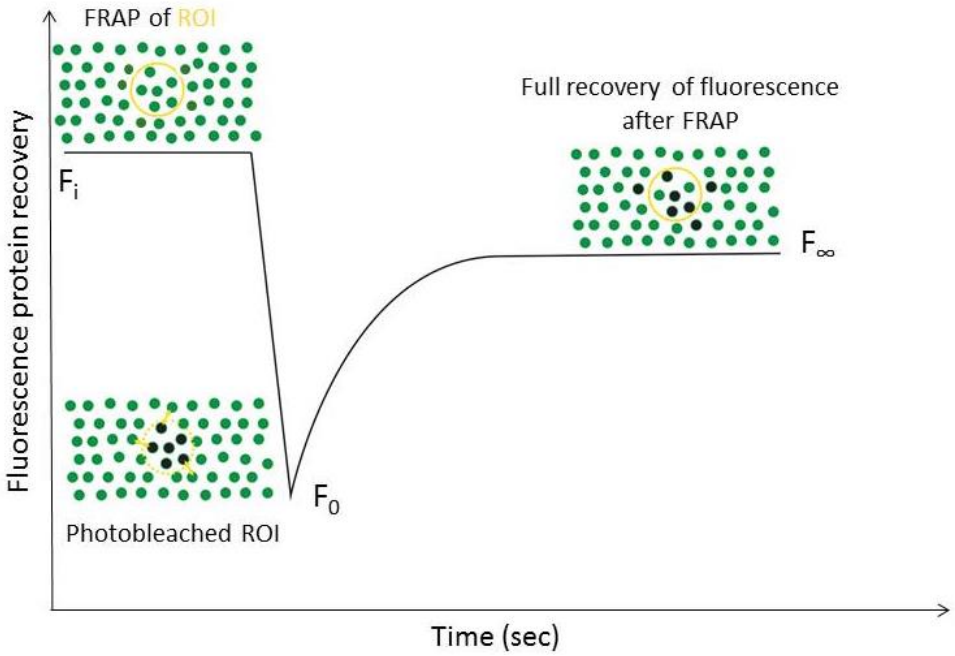

FIGURE 4-4: SCHEMATIC ILLUSTRATION OF FRAP EXPERIMENT ON A SELECTED ROI OF A GUV SECTION

The fraction of proteins that diffuse and contribute to the recovery are called mobile fraction and those who do not are called immobile fraction and corresponds to A and B (with B = 1 - A), respectively (Figure 4-5). The characteristic time of diffusion $\tau_{1/2}$ is measured to characterize and compare the diffusion and thus the mobility of CHMP2A proteins. $\tau_{1/2}$ indicates the time at which half of the fluorescence has recovered and is therefore commonly called the half-time (Salmon, Leslie et al. 1984; Lajoie, Partridge et al. 2007) (Figure 4-5). It is readily extracted from the fit of the normalized FRAP curve *I(t)* with the exponential equation:

$$I = A(1 - e^{-\tau t}) \tag{4-1}$$

Where

$$\tau_{1/2} = \frac{\ln(0.5)}{-\tau} \tag{4-2}$$

The mobile protein fraction can be quantified by measuring the ratio between the fluorescence intensity that eventually moved out of the ROI and the total photobleached sub-population by the following equation (Reits and Neefjes 2001):

$$A = \frac{F_\infty - F_0}{F_I - F_0} \tag{4-3}$$

Where F_∞ is the fluorescence measured after recovery plateau is reached, F_0 is the fluorescence intensity measured just after photobleaching and F_i is the initial measured fluorescent intensity prior to photo-bleaching.

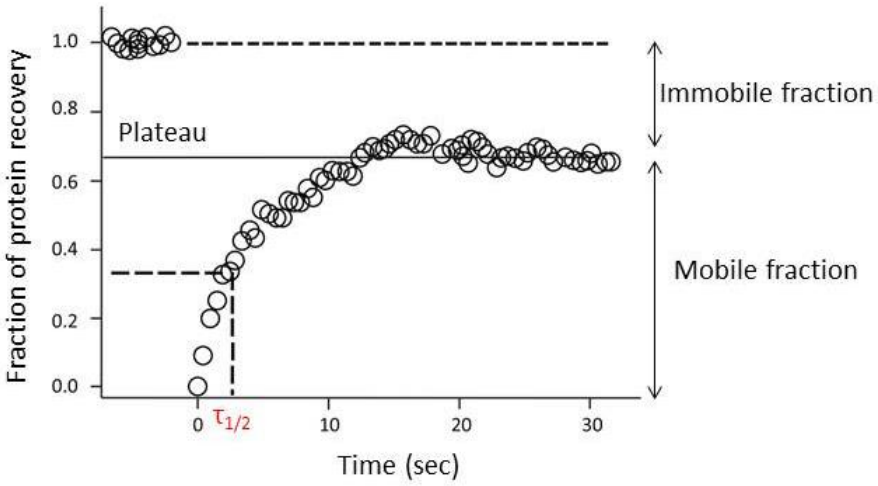

FIGURE 4-5: TYPICAL FRAP RECOVERY CURVE

Moreover, the protein diffusion coefficient D, which provides a quantitative measure of diffusion, can be determined using the Soumpasis equation (Axelrod, Koppel et al. 1976; Soumpasis 1983):

$$D = 0.224\,\frac{r_n}{\tau} \tag{4-4}$$

Where r_n is the radius of the uniformly bleached area and the coefficient 0.224 was numerically determined (Soumpasis 1983).

However, this model assumes that diffusion during photobleaching is negligible which is not the case for confocal FRAP as significant diffusion during the photobleaching may occur in confocal FRAP due to the long scanning time of the confocal scanning microscope. r_n thus may not provide an accurate description of the initial conditions required for this equation to be valid. Thus leading to an underestimation of D especially for fast-diffusing soluble proteins (Braga, Desterro et al. 2004; Weiss 2004; Pucadyil and Chattopadhyay 2006; Kang, Day et al. 2009). This problem can be solved by using the post-bleach fluorescence intensity profile to correct for any diffusion that occurs during the photo-bleaching by incorporating an empirically determined measure, the effective bleach radius r_e from the post-bleach profile (Kang, Day et al. 2009; Kang, Day et al. 2012):

$$D = \frac{({r_n}^2 + {r_e}^2)}{8\tau} \tag{4-5}$$

With r_e the efficient radius of a post-bleached profile, in contrast to the nominal radius r_n, from a used-defined bleaching spot radius.

4.3.3.2 EXPERIMENTAL CONDITIONS

We performed FRAP experiments to check the dynamics of the CHMP proteins supramolecular assembly on the surface of GUVs. We also measured the dynamics of other membrane-associated proteins, i.e. streptavidin, in the presence of CHMP proteins on the GUV surface.

For the FRAP experiments we used an inverted Spinning Disk Confocal Roper/Nikon microscope with a FRAP/Photo Activation module with 60x oil objective (NA=1.4, WD =0.13, pixel size =0.222 µm) and 3 lasers (491, 532, and 561) with the following filters ET 525/50m Emission Filter 25mm, ET 595/50m Emission Filter 25mm and ET 655LP Emission Filter 25mm, respectively. Images were recorded with an EM-CCD Evolve camera. FRAP experiments were performed at The BioImaging Cell and Tissue Core Facility of the Institute Curie (PICT-IBiSA), member of the France-BioImaging national research infrastructure.

For all series of FRAP experiments we bleached the region of interest several times at nominal 100 % laser transmission in the targeted protein laser line. To track protein recovery, multiple images were then captured every 15, 30 or 45 seconds following photobleaching for several minutes.

Fluorodish Cell Culture dishes were used for the protein diffusion assay. Prior to the passivation step, dishes were first coated with 10^{-1} mg.mL^{-1} streptavidin for 30 min to fix our GUVs containing biotinylated lipids to the dish surface. This step helps avoiding vesicle rotation during the photobleaching and image acquisition steps. Then, the dishes were passivated with a β-casein solution (Sucrose 25 mM, NaCl 50 mM and Tris 25 mM (pH 7.5) at 5 mg.mL^{-1}) to prevent further adhesion of the GUVs.

To measure the lateral diffusion of CHMPs proteins alone on the surface of GUVs, the collected vesicles from the PLW electroformation growth were incubated with CHMP proteins at concentrations ranging from 500 nM to 2 µM in the protein binding buffer for 30 min to reach protein-membrane saturation. Next, the solution containing the CHMP-covered GUVs was diluted in the observation buffer and added to the observation chamber. The dilution step is essential to avoid signal recovery on the GUV surface from free soluble CHMP proteins in the bulk.

To measure the diffusion of streptavidin on vesicles fully covered with CHMP proteins, GUVs were first incubated for 30 min with 500 nM CHMP2B-ΔC or with 500 nM CHMP2A-ΔC + 1 µM CHMP3FL, for 30 min. Then, the CHMP-covered GUVs were transferred to a solution containing 500nM streptavidin conjugated to TR-Ceramide for 30 min. We also measured the diffusion of streptavidin on vesicles covered with a non-complete assembly of CHMP2B-ΔC proteins, vesicles were incubated with 500 nM CHMP2B-ΔC for 15 min then with 500 nM streptavidin conjugated to TR-Ceramide for 30 min. The

control experiment here consisted on measuring the diffusion membrane-bound streptavidin in the absence of CHMPs proteins.

To follow the protein recovery on the bleached region of GUV surface, confocal images were taken before bleaching, after bleaching and during recovery. To determine the protein fraction of recovery on the bleached area of the GUV we measured using Image J software, the IntDen value (product of vesicle area and the protein mean fluorescence intensity) in the defined ROI for all the acquired confocal images. The background was subtracted. And, due to vesicle photobleaching during image acquisition, we normalized the bleached region of interest by the mean fluorescence intensity measured within a non-bleached region of the vesicle taken from the last image frame. Eventually, the fraction of recovery over time is plotted.

4.3.4 FLUORESCENCE-ACTIVATED CELL SORTING (FACS)

FACS experiments were performed in collaboration with Dr. Nicola De Franceschi (Post-Doc in the team).

4.3.4.1 FACS PRINCIPLE

The principle of flow cytometry is based on the passage of single cells or particles placed in a microfluidic chamber in front of a laser where both fluorescence and light scattering are measured so they can be detected, counted and sorted. It is generally used to study cells and kinetics of absorption of proteins or functionalized nanoparticles. But it can also be used for GUVs (Lamblet, Delord et al. 2008; Jalmar, García-Sáez et al. 2010).

A laser beam is directed at a hydrodynamically-focused stream of fluid that carries here the GUVs. Several detectors are carefully placed around the stream, at the point where the fluid passes through the light beam. One of these detectors is aligned with the beam to measure Forward Scattered light signals (FSC) and another detector is placed perpendicular to the stream and is used to the side measure Side Scattered light signals (SSC). Since fluorescent labels are used to detect the different objects, fluorescence detectors are also in place. The suspended objects, which in theory range from 0.2 µm to 150 µm diameter, pass through the beam and scatter the light. As the fluorescently labelled cell passes through the interrogation point and interacts with the laser beam, it creates a pulse of photon emission over time (a peak). These are detected by the photo-multiplying tubes (PMT) and converted by the electronics system to a voltage pulse, typically called an "event". The total pulse height and area is measured by the flow cytometer instrument, and the voltage pulse area will correlate directly to the fluorescence intensity for that individual event. These events are assigned channel numbers based on

its measured intensity (pulse area). The higher the fluorescence intensity, the higher the channel number the event is assigned. This signal can be amplified by increasing the voltage running through the PMT. In a flow cytometry experiment, every cell or particle (here GUV) that passes through the interrogation point and is detected will be counted as a distinct event. If many events are detected at the same intensity, they will be represented as a peak on the histogram. And the plot will represent the number of events in function of the relative fluorescence intensity (Figure 4-6).

FACS technique is based on the count of events, here our vesicles ± CHMP2B proteins, by fluorescence light refraction or emission. Fluorescent light is emitted simultaneously by fluorescent CHM2B and lipids dyes after excitation by the appropriate wavelength laser. In flow cytometry every detected particle in the solution (i.e. vesicles ± CHMP2B proteins) is classified as a distinct event. Every event is plotted independently in function of the fluorescence channel in which it was detected. Thus the fluorescence intensity of the membrane and the fluorescence intensity of the proteins are respectively proportional to the amount of fluorophores in the vesicle (thus, to its size) and proteins bound to it or present in the detection zone and unbound. The protein fluorescence appears in the left upper quadrant of the plot or protein positive region and the lipid (vesicle) fluorescence signal in the right lower quadrant or lipid positive region.

To quantify the amount of protein bound to the vesicles, one must look at the colocalization of both the protein and the lipids fluorescence signals called the double-positive region (protein positive region + lipid positive region) (Figure 4-6). A gate is placed around this region and a histogram of the protein fluorescence over the number of events of this region is plotted (Figure 4-6). The mean value of the fluorescence plot for each studied condition is subtracted from the histogram plot.

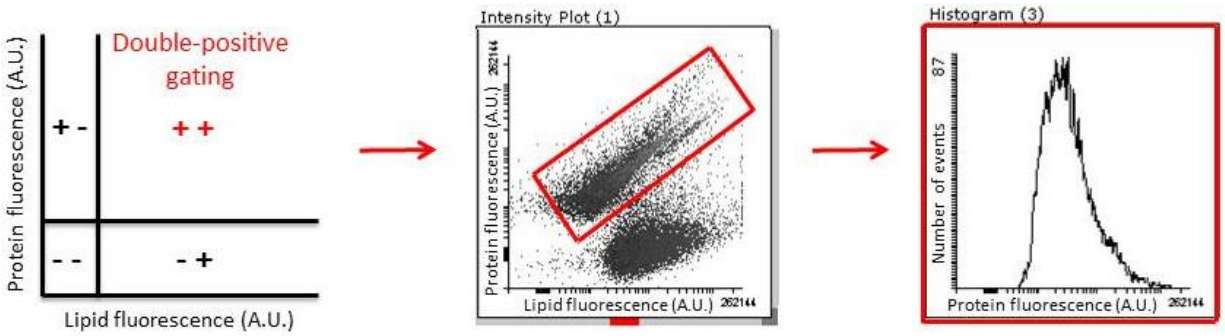

FIGURE 4-6: DESCRIPTION OF THE FACS EXPERIMENT
The double-positive where protein and lipid fluorescence colocalized is gated. Then a histogram of the protein fluorescence for the number of events counted in the gated region is plotted. And, the mean fluorescence value is deduced from the histogram plot.

4.3.4.2 EXPERIMENTAL CONDITIONS

We used flow cytometry to precisely measure the binding of CHMP proteins on the surface of GUVs with different lipid composition. With the FACs technique, a very large number of GUVs can be analyzed in a very short time, as compared to image analysis with confocal or spinning-disk microscopes. Indeed, we measured the protein-lipid interaction for 10 000 events (GUVs) per condition or lipid mixture in a very short period of time.

GUVs obtained with the PVA-swelling method were incubated 30 min with CHMP proteins at different concentrations, ranging from 0 nM to 4 µM, in the protein binding buffer. Then GUVs with bound CHMP proteins were diluted in the observation buffer to remove free soluble proteins from the bulk. Gating and sorting of protein and lipid fluorescence intensity were measured using a BD LSRFORTESSA flow cytometry instrument (lasers 488, 532, 633) available on the Curie platform. Data analysis was done using FlowJo software to gate the protein-bound vesicles region. To compare the protein affinity towards the different PIP species, the mean fluorescence intensity value of the protein for each condition is deduced from the histogram plot of the gated region.

4.4 CRYO-ELECTRON MICROSCOPY

The planning for the Cryo-EM experiments was cooperatively performed with Dr. Aurélie Bertin, in our lab.

4.4.1 CRYO-EM PRINCIPLE

Cryo-electron microscopy (Cryo-EM) is a method of transmission electron microscopy (TEM) where the sample is studied at cryogenic temperatures (generally liquid-nitrogen temperatures).

2D imaging was performed at about 10 electrons per $Å^2$. To carry out cryo-tomography experiments, gold beads (10 nm size) were added to the sample solution before being plunge-frozen. Tilted series were collected in low dose mode from -60 to +60 degrees, every two degrees, using a Tecnai G2 (FEI, Eindhoven, Netherlands) microscope operated at 200 kV and equipped with a 4kX4k CMOS camera (F416, TVIPS). The dose per image was 0.8 electrons per $Å^2$.

The imaging was performed at a magnification of 50,000 and each image was binned twice for a final pixel size of 4.26 Å. The consecutive images were aligned using the IMOD software. Back projection and thus 3-D reconstruction was performed using IMOD and SIRT reconstruction was carried out using Tomo3d. Segmentation was performed manually using IMOD.

4.4.2 EXPERIMENTAL CONDITIONS

For Cryo-EM experiments, 500 nM CHMPs were added to pre-formed LUVs (see chapter 0) in BP buffer (50 mM NaCl, 25 mM Tris at pH=7.5). Then, 5 µL of the sample was applied on the carbon side of a lacey grid (Ted Pella), previously glow discharged for 30 seconds. The sample was then blotted on the reverse side and plunge-frozen in liquid ethane using an EMGP automated apparatus (Leica). Grids were stored at liquid nitrogen temperature until they were loaded in a 200 kV G2 Tecnai (FEI, Eindhoven) microscope equipped with a LaB6 filament and operated at 200 kV. Images were acquired with the software suite EMTools under low dose conditions at a magnification of 50k using a 4K X 4K CMOS camera (F416, TVIPS) at a pixel size of 2.13 A/pixel.

4.5 MICROPIPETTE ASPIRATION ASSAY

Micropipette aspiration technique was used to study the membrane mechanical properties in the absence and in the presence of CHMPs assemblies bound to the surface of the GUV.

4.5.1 MICROPIPETTE ASPIRATION PRINCIPLE

This technique was first introduced in 1979 by Waugh and Evans to study the elastic properties of red blood cells (Waugh and Evans 1979; Kwok and Evans 1981; Mohandas and Evans 1994; Hochmuth 2000) before being applied on Giant Unilamellar Vesicles (GUVs). It consists in measuring the evolution of the membrane excess area of the GUV as a function of a controlled aspiration, by measuring the length of the aspirated tongue in a micropipette. Using principles on membrane elasticity, in particular the relation between excess area and membrane tension, the membrane elastic moduli can be extracted (Evans and Rawicz 1990). The setup is the following: a micropipette is connected to a water circuit, ending in a reservoir with adjustable height. The pipette is attached to a three-axis mechanical micromanipulator, to allow its displacement in all three directions within the experimental chamber (Figure 4-7). By moving down the reservoir connected to the micropipette, the hydrostatic pressure inside the pipette decreases leading to the increase of the aspiration and consequently the applied tension on the GUV can be controlled. The membrane tension is proportional to the difference of pressure ΔP between the interior of the micropipette and that of the chamber and can be derived by applying the Young-Laplace equation at both interfaces between the inside and the outside of the GUV:

$$\sigma = \frac{\Delta P \times Rp}{2\left(1 - \left(\frac{Rp}{Rv}\right)\right)} \quad (4\text{-}6)$$

Where Rp and Rv are the radius of the pipette and vesicle respectively (Figure 4-8), and the aspiration pressure ΔP is given by:

$$\Delta P = \rho g h \tag{4-7}$$

Where ρ is the density of water at room temperature, g is the standard gravitational acceleration, and h is the height of the reservoir relative to that of the experiment chamber (Kwok and Evans 1981).

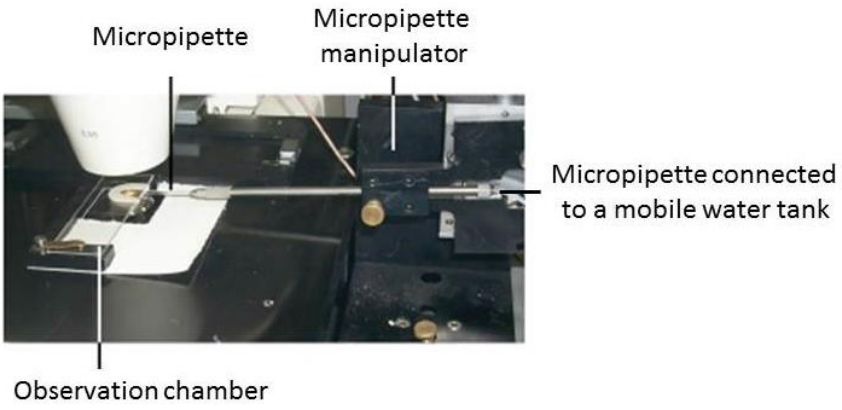

FIGURE 4-7: MICROPIPETTE ASPIRATION SETUP (ADAPTED FROM P. GIRARD PHD THESIS)

At very low aspiration, the vesicle is just held by the micropipette and when the tension increases, a portion of the GUV, called « membrane tongue », is aspirated inside the micropipette (Figure 4-8). The measurement of the longue length aspirated into the pipette allows the direct measurement of the membrane excess area of the membrane (Figure 4-9).

The excess area is given by:

$$\alpha = \frac{A - Ap}{A} \tag{4-8}$$

The excess area represents the difference between the microscopic area of the membrane *A* and the observed apparent area *Ap*. In general, the difference between an aspiration corresponding to α and a reference state α_0, where a very low aspiration is applied, is considered:

$$\Delta\alpha = \alpha_0 - \alpha \tag{4-9}$$

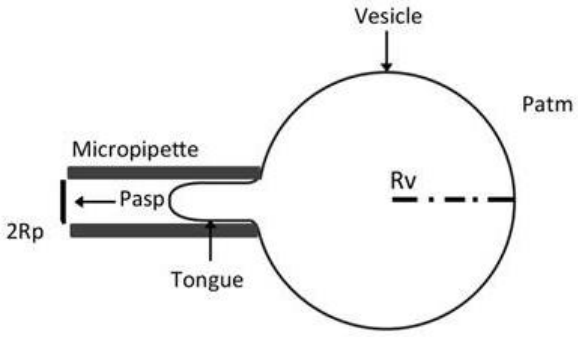

FIGURE 4-8: SCHEMA OF A VESICLE ASPIRATED INTO A MICROPIPETTE

For membrane mechanics analysis, the following criteria are strictly required:

- Constant volume of the vesicle
- Constant number of lipid molecules in the vesicle
- Free membrane sliding in the pipette, i.e. no membrane adhesion into the pipette
- The cylindrical part of the membrane aspirated in the pipette is ended by a spherical part with a radius *Rp* (which means that the length of the tongue $\Delta L \geq Rp$)
- Small imposed deformation ($\Delta A/A$ < 10%) (Drury and Dembo 1999).

From geometrical arguments, the difference of surface of the vesicle between the aspiration state and the reference state Δα can be related to the variation of the tongue length $\Delta L = L - L_0$ (Kwok and Evans 1981):

$$\Delta\alpha = \left(\frac{((Rp - Rv)^2) - ((Rpip - Rv)^3)}{2Rp}\right) \times \Delta L \qquad (4\text{-}10)$$

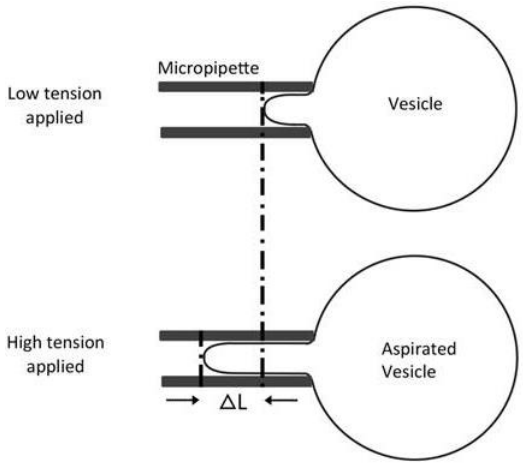

FIGURE 4-9: PRINCIPLE OF MICROPIPETTE ASPIRATION OF A GUV

Membrane mechanical properties are obtained by converting measurements of aspirated tongue length versus pipette aspiration pressure to apparent area excess area Δα versus tension. Micropipette pressurization of giant vesicles is used to measure both the bending rigidity modulus κ (detailed in chapter 2.2.1.3) and the area stretching modulus χ (detailed in chapter 2.2.1.1) of fluid-phase membranes (Kwok and Evans 1981; Evans and Needham 1987; Evans and Rawicz 1990; Rawicz, Olbrich et al. 2000) (Figure 4-10). The bending rigidity modulus κ is derived from measurements of Δα at low tension (0.001– 0.5 mN.m^{-1}), which is dominated by smoothing of thermal undulations (entropic regime, as described in chapter 2.3). The stretching modulus χ is obtained from measurements of vesicle surface expansion at high tension (0.5 mN.m^{-1} and above), which involves an increase in area per molecule and a small, yet important contribution from smoothing of residual thermal undulations (enthalpic regime, as described in chapter 2.3). Both the bending modulus κ and the stretching modulus χ can be derived from the Canham-Helfrich Hamiltonian as following:

$$\Delta\alpha = \left(\frac{k_B T}{8\pi\kappa}\right) \ln\left(1 + c\sigma\frac{A}{\kappa}\right) + \sigma\chi \quad (4\text{-}11)$$

Where $\Delta\alpha$ the variation of the apparent area, A the vesicle area, c a constant related to face undulations (~0.1), k_BT the thermal energy (~4x10^{-21} J) and σ the micropipette applied tension on the membrane.

In the entropic regime (in the low tension regime), the apparent excess area $\Delta\alpha$ is dominated by smoothing of thermal undulations, and the bending rigidity modulus κ is revealed by the logarithmic dependence of the apparent area on tension (Figure 4-10 / A):

$$\ln\left(\frac{\sigma}{\sigma_0}\right) \sim \left(\frac{8\pi\kappa}{k_B T}\right)\Delta\alpha \quad (4\text{-}12)$$

κ is obtained from the plot of the logarithmic value of the tension as a function of the apparent area. It is given by the slope of the curve multiplied by $(k_BT/8\pi)$. Monounsaturated lipid chains have typically a bending modulus equal to $\kappa \approx 21$ k_BT for diC18:1 (Δ9-Cis) (DOPC) (Rawicz, Olbrich et al. 2000). This value increases with the chain length: $\kappa \approx 30$ k_BT for diC22:1 and diminishes for long chains with 2 or more cis-double bonds along the chain(s): $\kappa \approx 11$ k_BT for diC20:4 (Rawicz, Olbrich et al. 2000).

On the other hand, in the enthalpic regime (at high tension), an increase in the apparent area $\Delta\alpha$ is governed by the elastic area stretching modulus χ, which increases linearly with the tension following the equation (Figure 4-10 / B):

$$\sigma \sim \chi\,\Delta\alpha \quad (4\text{-}13)$$

Where typical value of $\chi \approx 265$ mN.m^{-1} for diC18:1 and about 250 mN.m^{-1} for diC20:4 (Rawicz, Olbrich et al. 2000).

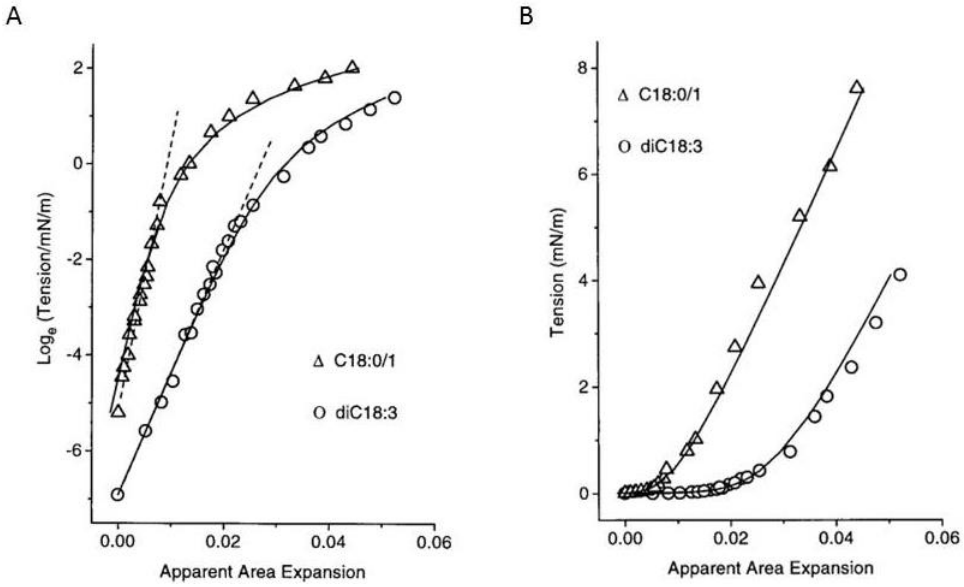

FIGURE 4-10: VARIATION OF THE APPARENT AREA EXPANSION WITH TENSION, AS MEASURED WITH MICROPIPETTE ASPIRATION (RAWICZ, OLBRICH ET AL. 2000).
Examples of the variation of the apparent area expansion versus tension from 10^{-6} to 8 mN/m for two vesicles made from C18:0/1 and diC18:3 PC, showing the two stretching regimes
(A) Apparent area expansion measured in the entropic regime for low tensions. Semilog plot of tension versus apparent area expansion. Slopes of the linear fits (dashed lines) applied to the range of very low tensions yield elastic bending moduli κ (x 8π/kBT) for each bilayer ($\kappa \approx 0.9 \times 10^{-19}$ J for C18:0/1 and $\kappa \approx 0.4 \times 10^{-19}$ J for diC18:3).
(B) Apparent area expansion measured in the enthalpic regime for high tensions. Linear plot of tension versus apparent area expansion. The initial soft-exponential rise of tension with area expansion reveals smoothing of thermal shape fluctuations, which is followed by the onset of the linear increase in tension as the bilayer begins to stretch.
The solid curves in A and B are the fit of the elastic compressibility relation over the entire four-order-of-magnitude range of tension, using the values of bending elasticity and a common value of the direct expansion modulus ($\chi \approx 230$ mN/m) for both lipid vesicles.

In the entalpic regime, residual thermal undulations introduce a small (but important) area dilation which can contribute to the membrane area expansion. Thus, when the value of the bending modulus is known, a correction should be used at high tension (Rawicz, Olbrich et al. 2000):

$$\Delta\alpha' = \Delta\alpha + \alpha' \tag{4-14}$$

Where the area dilation due to residual thermal undulations $\alpha' = -\frac{kT}{8\pi\kappa}\ln\frac{\sigma}{\sigma_0}$.

The stretching modulus is thus deduced from the slope of the corrected apparent area Δα' versus the tension.

4.5.2 EXPERIMENTAL CONDITIONS

Experimental chambers are made using 9 x 35 mm glass coverslips (VWR International, France) to form the upper side and a 10 x 30 mm glass coverslips (VWR International, France) to form the bottom side. The chamber is passivated with a β-casein solution (Sucrose 25 mM, NaCl 50 mM and Tris 25 mM (pH

7.5) at 5 mg.mL^{-1}) for 15 min to prevent GUVs and CHMP proteins from adhering to the glass surface. Then a micropipette, also passivated with β-casein solution, is introduced into the chamber. This way, the experimental chamber and the inner and outer surfaces of the micropipette are passivated prior to GUVs addition.

Micropipettes are made of borosilicate capillaries of 1 mm outer diameter and 0.58 mm inner diameter (Harvard Apparatus, UK). They are produced using a micropipette puller (P-2000, Sutter Instrument, USA), which pulls on both ends of the capillary while heating it in the middle with a laser beam. This creates a thin elongated tip that is closed at its end by the merged glass walls. Subsequently, the pipette is forged (MF-830 microforge, Narishige, Japan) by generating a smooth opening and its size can be precisely defined. We worked with micropipettes with diameters ranging from 4 µm to 10 µm.

Following the passivation step with the β-casein solution, the chamber is rinsed several times with the observation buffer. Then, GUVs pre-incubated with CHMP proteins are added to the chamber. The chamber is sealed with mineral oil, 20 min after vesicles addition so that the osmolarity of the external buffer increases due to evaporation and vesicles become floppy. Once the chamber is sealed, the zero pressure is measured and the aspiration assay can begin by decreasing the water height gradually, thus increasing the applied tension on the vesicle.

One confocal plane image was taken for each set tension. The explored tensions for the aspiration experiments with the different CHMP proteins range from 0.5 to 1 mN.m^{-1} (corresponding to the membrane enthalpic regime). And, few measurements were performed below 0.5 mN.m^{-1}.

The micropipette aspiration assay normally prescribes to pre-stretch the GUVs at very high tension before the measurements to get rid of any hidden excess area in the GUV residual from the GUV preparation. Note that such a pre-stretching was not performed in our experiments. Since we could not inject the proteins on our GUVs, which were pre-incubated with the CHMPs prior the micropipette experiments instead, no pre-stretching could be performed in those experiments. Accordingly it was neither done on bare membranes as we had to perform the micropipette aspiration experiments in the exact same conditions to precisely compare the effect of the presence of the proteins on membrane elasticity.

I performed these experiments in Chalmers University (Gothenburg, Sweden) in collaboration with Dr. Marta Bally, in the laboratory of Prof. Dr. Frederik Hook.

4.6.1 QCM-D PRINCIPLE

QCM-D is based on an oscillating quartz crystal resonator which is excited with an electric field applied over the electrodes. The surface of the disk-shaped sensor performs a shear oscillation, i.e. with periodic motion back and forth parallel to the sensor surface. Two parameters, frequency of oscillation of the sensor and dissipation (or damping of the oscillator) are monitored simultaneously (Höök, Rodahl et al. 1998). The frequency of oscillation of the sensor is reduced when mass is attached to the surface. The relation between the frequency shift Δf and the mass of material adsorbed on the sensor, Δm, is given by the Sauerbrey equation (Sauerbrey 1959):

$$\Delta m = -C\frac{\Delta f}{n} \tag{4-15}$$

Where C is the mass sensitive constant, equal to 17,7 ng/cm^2/Hz^1 at f = 5 MHz (fundamental frequency) and $n=1,3,5,7$ is the sensor overtone. the This relationship is only valid for acoustically rigid films with low dissipation (Cho, Frank et al. 2010).

The energy dissipation of the oscillator, ΔD, is defined as the fraction of the total energy stored in the oscillator that is dissipated during one oscillation cycle. It indicates a change in the viscoelastic and structural properties of the mass coupled to the oscillator. The energy dissipation of the oscillator, ΔD, is defined by the equation:

$$\Delta D = \frac{1}{Q} = \frac{1}{2\pi} \times \frac{E_{\text{dissipated}}}{E_{\text{stored}}} \tag{4-16}$$

Where Q is the quality factor, E_{stored} and $E_{dissipated}$ are respectively the energy stored and lost during one period of oscillation. High ΔD value correspond to a soft film whereas low ΔD value to a stiff film.

4.6.2 TYPICAL EXPERIMENT

Quartz crystal microbalance with dissipation monitoring (QCM-D) was used to study the binding of CHMP proteins to different lipid bilayer compositions. This instrument is a real-time, in-situ, label-free technique for measuring surface phenomena such as adsorption, desorption and structural properties of a material deposit on the substrate.

QCM-D measurements were performed using a Q-Sense E4 system (Q sense; Gothenburg, Sweden) with four temperature controlled flow modules. The mass sensor is a silicon dioxide-coated quartz crystal

microbalance SiO_2 (QSX-303 Lot Quantum Design France) with a fundamental frequency of 4.95 MHz. The liquid flow was controlled using a high precision multichannel dispenser (IPC; ISMATEC – Germany). Prior to all experiments, the sensors were cleaned with a solution of SDS 2% and stored in the same solution. They were subsequently rinsed with Milli-Q water, dried under nitrogen flow and placed in an UV Ozone Cleaner for 45 minutes (ProCleaner™ Plus; BIOFORCE Nanosciences USA). Immediately after UV Ozone cleaning, the sensors were inserted in the QCM-D system. After mounting, the sensors were further cleaned with a solution of 2 % SDS for 10 min at a flow rate of 25 $\mu L.min^{-1}$ and then with Milli-Q water for 10 min at 50 $\mu L.min^{-1}$.All experiments were performed at constant temperature equal to 295 K with a flow rate of 50 $\mu L.min^{-1}$.

A typical QCM-D experiment is presented in Figure 4-11. After baseline stabilization with 150 mM NaCl, 10 mM Tris buffer at pH 7.5, the LUVs are injected, in their preparation buffer, leading to a rapid and irreversible adsorption on the substrate. They are first adsorbed as intact - unruptured vesicles (Figure 4-11 / B1) and then, when a critical surface coverage is reached, the lipid bilayer is formed spontaneously leading to a frequency shift $\Delta\vartheta 1$ (Figure 4-11 / B2).

To form a supported lipid bilayer (SLB) with LUVs the electrostatic repulsion between lipid vesicles and the substrate must be minimized either by screening or reducing the negative charges with salt addition and divalent ions to favor fusion of negatively charged membranes (Leckband, Helm et al. 1993; Hed and Safran 2004). The formation of SLB made from lipid mixtures 1 and 2 (respectively 70% DOPC, 30% DOPS and 60% DOPC, 40% DOPS) was performed in a buffer containing Ca^{2+} (150 mM NaCl, 10 mM Tris (at pH 7.5) + 2 mM Ca^{2+}), which is also known to promote interaction between negatively charged lipids and the substrate (Rossetti, Bally et al. 2005). After SLB formation, the bilayer is rinsed with the same buffer but containing EDTA ((150 mM NaCl, 10 mM Tris (at pH 7.5) + 10 mM EDTA) to remove Ca^{2+} excess. In the case of SLBs containing phosphoinositide lipids, it has been shown that Ca^{2+} induced the formation of PIP clusters in membranes either in giant unilamellar vesicles (Carvalho, Ramos et al.) or in SLB (Wang, Collins et al. 2012). For these reasons, the formation of SLB for lipid mixtures 3 and 4 (respectively 80% DOPC, 10% DOPS, 10% $PI(4,5)P_2$ and 80% DOPC, 10% DOPS, 10% $PI(4,5)P_3$) was achieved in 150 mM KCl, 20 mM citrate at a low pH (pH=4.8), which decreases the net negative charge of the lipids and thus allows for a reproducible rupture and spreading of the LUVs on the substrate (Braunger, Kramer et al. 2013).

After the formation of the lipid bilayer, the sensors are washed again with 150 mM NaCl, 10 mM Tris buffer at pH 7.5 to remove all free vesicles. The sensors are then re-equilibrated with 50 mM NaCl, 10 mM Tris at pH 7.5 (protein binding buffer (BP). Next, CHMP proteins are t injected under a continuous

flow in BP at a concentration of 200 nM. The interaction between the proteins and the lipid bilayer is directly measured from the frequency shift. Continuous perfusion of the proteins is achieved until this frequency shift reaches a constant value, indicating that the SLB is saturated with proteins (Figure 4-11). When protein saturation on the bilayer is reached, the sensors are washed with the BP buffer during 15 – 30 min to remove the additional unbound proteins. The frequency $\Delta\vartheta_2$ and dissipation ΔD_{sat} shifts due to the interaction between the different CHMP proteins and the SLB are subsequently quantified.

After quantifying the protein affinity to the different SLBs, we studied their detachment by injecting a high ionic strength buffer (500 mM NaCl, 10 mM Tris at pH 7.5) for at least 30 min to significantly reduce the proteins-lipids electrostatic interactions. The sensors are then washed again with BP to reach stable values for the frequency and the dissipation. The frequency shift is eventually measured to quantify the degree of detachment for each type of protein.

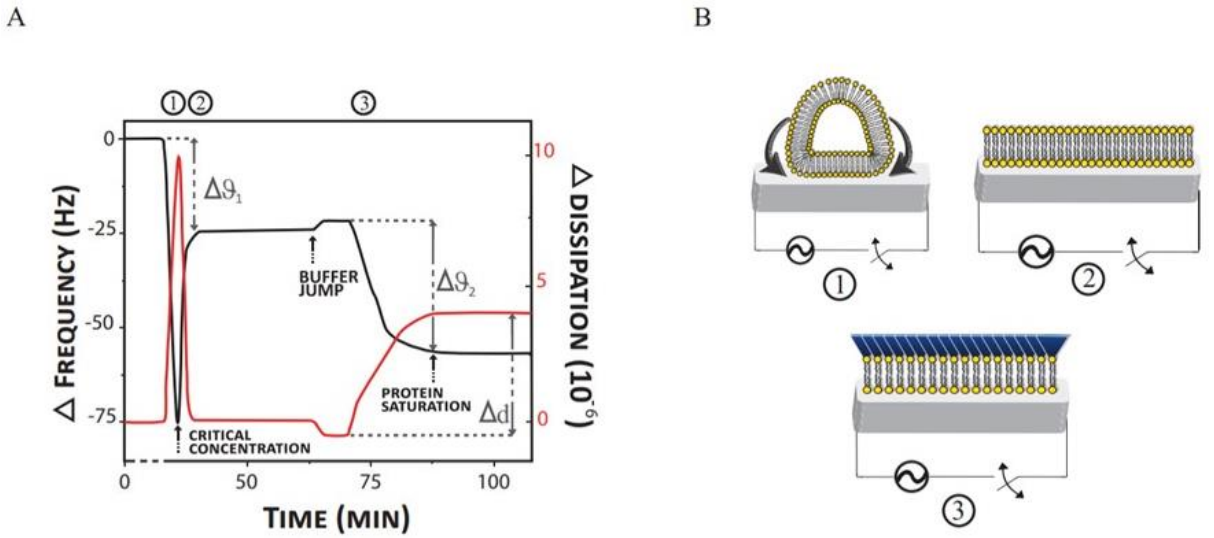

FIGURE 4-11: A TYPICAL QCM-D EXPERIMENT

(A) Typical QCM-D experiment measuring simultaneously the frequency (black) and the dissipation (red) shifts as a function of time.

(B) Mechanism of bilayer formation: SUVs are first adsorbed as intact - unruptured vesicles (1) and then, when a critical surface coverage is reached, the lipid bilayer is formed spontaneously (2), leading to a frequency shift $\Delta\vartheta_1$. The SLB is extensively washed with proteins buffer leading to a small frequency and dissipation shift (buffer jump). After stabilization of the baseline, CHMP proteins are added until saturation on the SLB (3). The corresponding frequency and dissipation shifts $\Delta\vartheta_2$ and shift ΔD are measured.

4.7 ATOMIC FORCE MICROSCOPY (AFM)

Imaging structures at the single molecular level is crucial in biological sciences. But often, images with high spatial resolution only are not sufficient for understanding a biological event; dynamical informations and sufficient spatio-temporal resolution might be required additionnally to decipher a mechanism.

Atomic force microscopy (AFM) provides high-resolution images including surface height information leading to three-dimensional information on sample morphology. AFM can be operated both in air and in buffer solutions, which allow imaging at physiological conditions and enhance the biological relevance of the obtained results. Moreover, it has the capacity to determine mechanical material properties via the force spectroscopy mode. Using AFM, proteins and membranes can be imaged at nanometer resolution (Ando 2014). Besides nanometer spatial resolution, high temporal resolution can be achieved with high-speed AFM (HS-AFM) with imaging rates higher than 10 frames per second. HS-AFM is essential to investigate in real-time dynamic processes (Ando 2017).

For the indentation and HS-AFM experiments, we collaborated with Prof. Dr. Wouter Roos (Groningen, the Netherlands). The experiments were performed by Dr. Sourav Maity in Prof. Dr. W. Roos's group.

4.7.1 PRINCIPLE OF AFM

AFM image acquisition is based on the interacting (attractive/repulsive) force between the tip and the surface, which deflects the cantilever. In combination with a feedback control, the topography of the sample surface can be reconstructed (de Pablo 2011).

For the measurement of the bending of the cantilever, a laser beam is focused on the rear side of the cantilever. The reflected light is directed to a quadrant photodiode (dual photodiode for HS-AFM), which detects positional alterations in the reflected light. Whenever the interaction force between the tip and the sample surface changes, the cantilever bends, and thus the position of the laser spot on the photodiode moves (Figure 4-12). The measured signals are transmitted to the feedback electronics, processed and converted into a voltage, which is used to retract or extend the piezoelectric actuator supporting the sample. The actuator is used to change the position of the sample, thus the deflection of the cantilever to keep the interaction force at a set value.

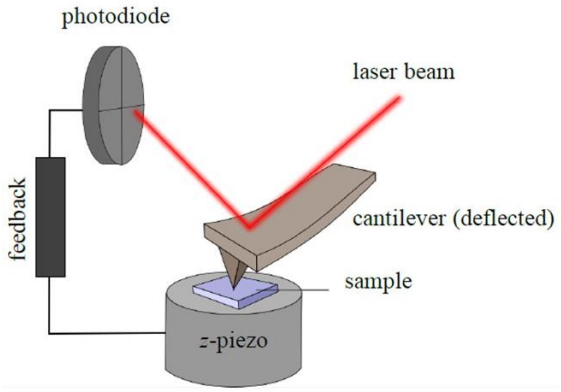

FIGURE 4-12: SCHEMA OF AFM SETUP COMPONENTS

The cantilevers used for the experiments were 7 µm length and 2 µm in width. The cantilever spring constant is of 0.15 $N.m^{-1}$. The resonance frequency which defines the limit for the scanning speed is equal to 1.2MHz in air and it is around 600 kHz in liquid.

In general, AFM works in different modes, depending on the user-defined interaction force between the cantilever and the surface. In the present work we have used HS-AFM, which in fact, works in the "tapping mode"; therefore, we will only describe this imaging mode. In tapping mode, when the cantilever is far away from the sample surface it is commanded (by the user) to oscillate at its resonance frequency with defined amplitude (free amplitude). When approaching the surface, the tip experiences a dampening of the free amplitude (Close-contact mode in Figure 4-13). Approach of the cantilever continues until predefined damped amplitude (set point) has been achieved. In this way the cantilever tip continuously taps on the surface without being in contact continuously. In tapping mode, the set point amplitude and the set frequency (near resonance) will be conserved during the imaging process. As can be seen, the difference between the free amplitude of the cantilever and the set point amplitude is directly related to the applied tapping force on the sample surface. We can also use this force (of imaging) to investigate the mechanical properties of our samples.

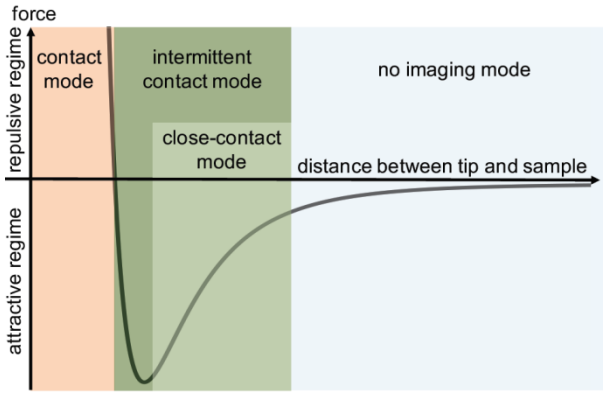

FIGURE 4-13: FORCE DESCRIPTION FOR A TYPICAL AFM EXPERIMENT

4.7.2 EXPERIMENTAL CONDITIONS

For all the experiments PI(4,5)P_2-SUVs (lipid mixture 5) were added in BP to a chamber with a mica substrate. Following, 1 µM of CHMP2B, or CHMP4B, or CHMP4B then subsequently CHMP2B were added.

For the HS-AFM all images were acquired at 5 s per frame rate with a minimal force of approximately 100 pN. Image acquisition of CHMP4 polymerization on supported lipid membrane is done a few minutes after protein addition as it takes about 5 to 10 min for the spirals to form. For the measurement of membrane mechanics in the presence of CHMP2B, we measured the relative deformation of the

membrane through imaging as a function of the tapping force. Image acquisition was first performed at minimal force required to image a vesicle (around 100 pN), then step by step tapping force was increased by 10 % increment. After reaching the maximal force, around 80% or 180 pN, the tapping force was diminished returning back again to its lowest value (100 pN). For the study of the effect of CHMP2B on CHMP4 spiral, we first checked the spiral formation on flat lipid bilayer as a control. Then we added CHMP2B and directly imaged the vesicles thus covered with both polymers.

CHAPTER 5. RESULTS

5.1 OPTIMIZATION AND CHARACTERIZATION OF CHMP2B PROTEIN INTERACTION WITH MODEL MEMBRANES

The aim of this part is to characterize *in vitro* the interaction of CHMP2B proteins with lipids using biomimetic model membranes. Our purpose is to find the appropriate lipid mixture with highest affinity for the interaction with CHMP2B proteins. Moreover, to work at physiological conditions we have optimized the chemical properties of the experimental buffers.

5.1.1 STUDY OF CHMP2B PROTEIN STABILITY

Before studying the interaction of CHMP2B proteins with lipids, we first checked the stability of the protein over time and the effect of the buffer. We used Dynamic Light Scattering (DLS) technique to check the protein stability over time at room temperature. DLS measures the autocorrelation of the fluctuations of the refractive-index in the solution. The scattering is related to the hydrodynamic radius by the Stokes–Einstein equation:

$$R = \frac{k_B T}{6\pi\eta D} \quad (5\text{-}1)$$

Where R is the hydrodynamic radius, D the translational diffusion coefficient, k_B the Boltzmann's constant, T the thermodynamic temperature and η the dynamic viscosity.

Particles of different sizes and aggregation status are recognized by their different hydrodynamic radius values.

Figure 5-1 presents the variation of the hydrodynamic radius of CHMP2B-ΔC proteins (CHMP2B protein with C-terminus truncation) in the storage buffer (NaCl 100 mM, Tris 50 mM at pH 7.4) over time (30 min, 60 min and 120 min). CHMP2B proteins size distribution does not vary (particle hydrodynamic radius ≈ 1 nm) for one hour at room temperature in their storage buffer, meaning that they do not tend to polymerize/aggregate and remain stable in their storage buffer at room temperature. At 1 hour, protein aggregation was observed meaning that the proteins started to deteriorate. At 2 hours, the protein aggregation was not observed anymore, perhaps due to sedimentation of the largest aggregates. Thus for all our experiments, CHMP2B proteins were used immediately after protein defreezing.

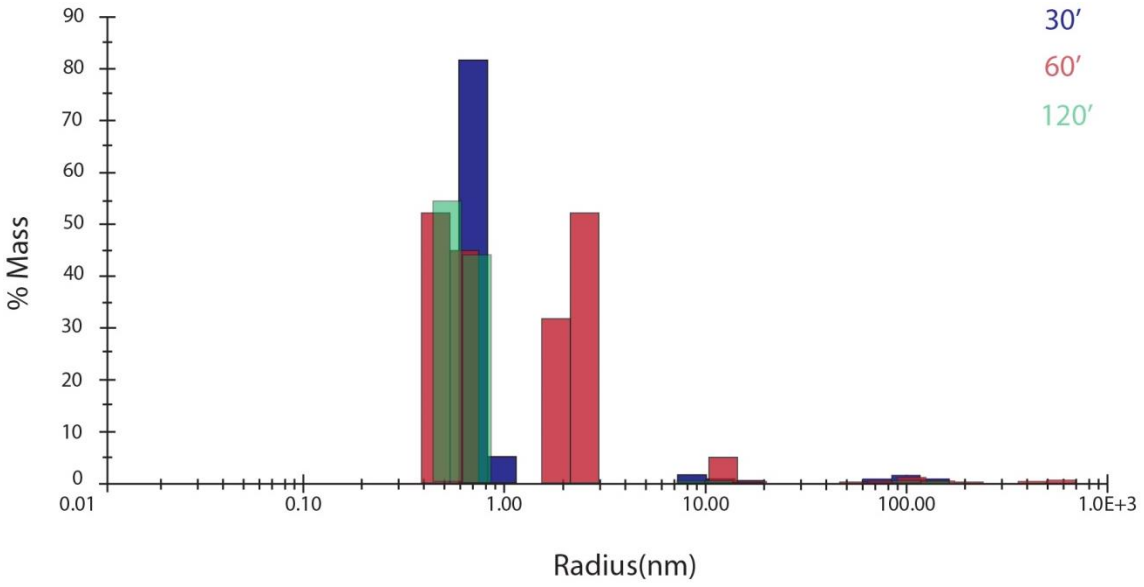

FIGURE 5-1: VARIATION OF THE HYDRODYNAMIC RADIUS OF CHMP2B OVER TIME STUDIED BY DLS
Size distribution at different times.

Although stable at room temperature in their storage buffer up to 30 min with a high salt content, CHMP2B proteins have to be transferred to a low ionic strength buffer to bind efficiently the lipid membrane. Indeed, CHMP2B proteins are positively charged and require negative lipids to bind membranes. Since binding is governed by electrostatic interactions, we wanted to test protein binding and stability in buffers of different ionic strengths. We incubated CHMP2B proteins during 30 min at 500 nM with GUVs made of lipid mixture 5 (DOPS/PI(4,5)P_2 (10:10)) in buffers with different salt concentrations ranging from 0 mM NaCl to 100 mM NaCl (+ 25 mM Tris at pH 7.5) and we recorded the green protein fluorescence signal on the membrane with confocal microscopy (Figure 5-2).

In the absence of NaCl, we did not detect CHMP2B protein binding on the lipid membranes. We could thus suspect that without salt in solution, the proteins are unstable and have aggregated (Figure 5-2). For buffers with NaCl concentrations of 75 mM and 100 mM, protein-lipid binding is diminished as compared to 50 nM, because electrostatic interactions between CHMP2B proteins and the underlying lipid membrane are screened. Moreover, proteins seem to be aggregated on the membrane.

To sum up, interaction between CHMP2B proteins and membranes is enhanced when the buffer contains 50 mM NaCl, 25 mM Tris at pH 7.5 (named the protein binding buffer (BP)).

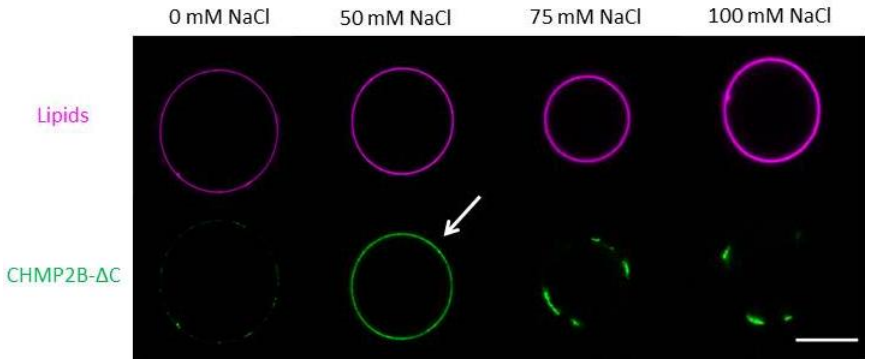

FIGURE 5-2: TEST OF PROTEIN BINDING AT DIFFERENT IONIC STRENGTH BUFFERS
Pre-formed vesicles were incubated with CHMP2B-ΔC in buffers with different salt concentrations ranging from 0 mM to 100 Mm NaCl (+Tris 25mM at pH 7.5). After 30 min incubation, vesicles were transferred to the same salt buffer free of proteins. Fluorescent images were taken for each condition with a confocal microscope. Lipid signal is shown in magenta and protein signal in green. Scale bar = 5 µm.

To further characterize CHMP2B stability on membrane over time at 4°C, we did a sucrose flotation assay (Figure 5-3). We incubated 500 nM CHMP2B with GUVs made of the same lipid mixture 5 (DOPS/PI(4,5)P_2 (10:10)) in BP (50 mM NaCl, 25 mM Tris at pH 7.5 buffer) and in the protein storage buffer (NaCl 100 mM, Tris 50 mM at pH 7.4). With this method, CHMP2B proteins are mixed with the GUVs at the bottom of a sucrose gradient and are then ultra-centrifuged (Figure 5-3). If the proteins and lipids interact, the complex floats in the upper fractions of the centrifugation tube (Figure 5-3). The presence of the proteins on the different fractions is checked with SDS page gel.

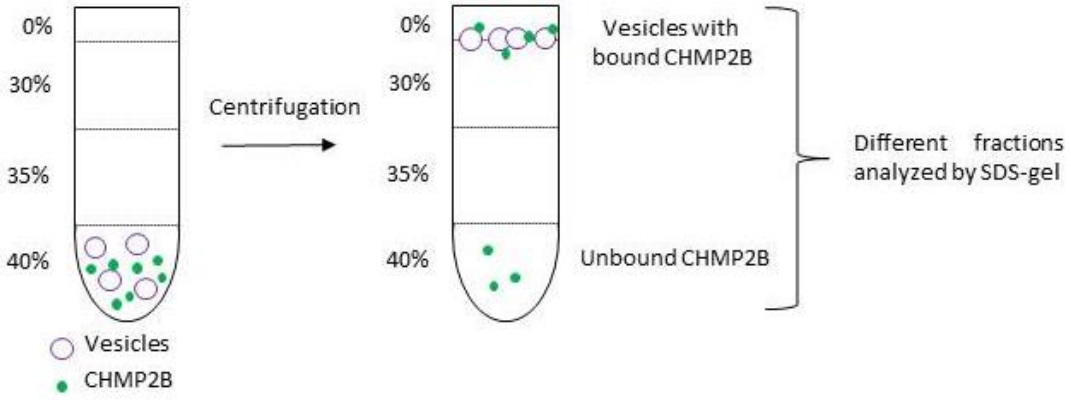

FIGURE 5-3: PRINCIPLE OF THE SUCROSE FLOTATION ASSAY

Figure 5-4 displays a SDS-page of the different fractions collected from the sucrose gradient (in the protein storage buffer (A) and in BP (B)). CHMP2B proteins interaction with the vesicle was observed in the upper fraction of the tube. However, CHMP2B protein signal was detected in the lower fractions of the tube, in the 20 % sucrose fraction with the high salt storage buffer and even in the 30% sucrose fraction with the low salt buffer (with 50 mM NaCl). These results are the signature of protein polymerization or aggregation in both buffers, more particularly at 50 mM.

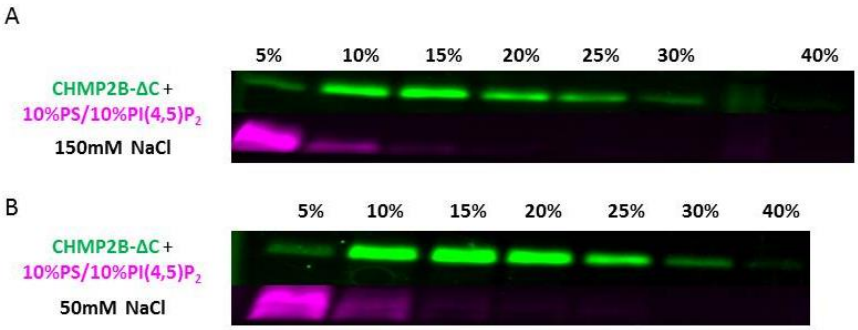

FIGURE 5-4: SDS-PAGE GEL SHOWING CHMP2B STABILITY IN DIFFERENT BUFFERS
(A) Different pooled fractions from the sucrose gradient of CHMP2B + lipids (lipid mixture 5) in the protein storage buffer.
(B) Different pooled fractions from the sucrose gradient of CHMP2B + lipids (lipid mixture 5) in the protein binding buffer.

Based on these protein stability tests, we have used the BP buffer to bind CHMP2B proteins to membranes in all the following experiments. Moreover, to collect data before protein suffers from deterioration, experiments have been performed within a short period of time inferior to 1 hour after transfer to BP buffer.

5.1.2 CHMP2B PROTEINS BIND PREFERENTIALLY TO PI(4,5)P2-CONTAINING MEMBRANES

Phosphoinositides constitute a minority of the phospholipids family with a concentration lower than 1% in cell membranes. Nevertheless, PIP lipids play an essential signaling role in cells. The main phosphatidylinositide present in the endosomal compartment in the MVB pathway, where the ESCRTs were first identified, is PI(3)P, and it has been used in purified systems to reconstitute MVB formation using yeast proteins (Wollert and Hurley 2010). However, more recently discovered ESCRT-III-mediated scission events occur on membranes enriched in $PI(4,5)P_2$, ,notably at the plasma membrane, including for instance HIV virus egress, plasma membrane repair and cytokinesis events, or at the nuclear envelope (Di Paolo and De Camilli 2006; Garnier-Lhomme, Byrne et al. 2009). We therefore wondered whether CHMP2B, which appears to be important in all these processes on $PI(4,5)P_2$-containing membranes, would preferentially bind $PI(4,5)P_2$ lipids. We used two different approaches for our study both involving the use of model membranes. We have tested (i) the binding of CHMP2B on supported lipid bilayers (SLBs) and (ii) the interaction on the surface of giant unilamellar vesicles (GUVs). The advantage of using both approaches is that we have been able to study the assembly of CHMP2B proteins on different surfaces, respectively on stiff non-deformable surfaces (SLB) and on flat deformable surfaces (GUV).

For the first approach using SLBs, the protein interaction with different lipid compositions was measured with the Quartz Crystal Microbalance with Dissipation monitoring technique (QCM-D) (previously described in chapter 4.6.1). Recording the variation in frequency of oscillation of a quartz crystal enables

us to directly quantify the amount of adsorbed proteins and assess their affinity to different lipid bilayers according to Sauerbrey's equation (equation 4-15 in chapter 4.6):

$$\Delta m = -C\frac{\Delta f}{n}$$

An advantage of the QCM-D technique is that it does not require the use of labelled proteins.

For the second approach, fluorescently labelled CHMP2B proteins, at various concentrations were added to pre-formed GUVs. FACS method and Spinning Disk confocal microscopy (SD) were used to respectively measure the affinity of CHMP2B proteins for different PIPs species (PI(3)P, PI(3,5)P_2, PI(4)P and PI(4,5)P_2).

For all the GUV sets of experiments, CHMP2B proteins were labelled with Alexa Fluor™ 488 and the different lipid mixtures contained PE lipids fluorescently tagged with Rhodamine.

5.1.2.1 STUDY OF THE BINDING OF CHMP2B PROTEINS ON SUPPORTED LIPID BILAYERS

To study the protein-lipid interaction, precisely electrostatic dependent interactions, we compared the binding of CHMP2B proteins to membranes incorporating different negatively charged lipids. We first tested the binding of CHMP2B proteins to 30% DOPS and 40% DOPS-containing membranes (lipid mixtures 1 and 2, with respectively (DOPC/DOPS (70:30); DOPC/DOPS (60:40)). Then, we compared the effect of the presence of PI(4,5)P_2 and PI(3,4,5)P_3 in the membrane (lipid mixtures 3 and 4, with respectively DOPC/DOPS/PI(4,5)P_2 (80:10:10) and DOPC/DOPS/PI(3,4,5)P_3 (80:10:10)). After formation of the SLB, CHMP2B proteins at a concentration of 200 nm in BP buffer (NaCl 50 mM, Tris 25mM at pH 7.5) were injected with a continuous flow system. The interaction between CHMP proteins and the lipid membrane leads to a decrease of the measured frequency (Figure 5-5 / A). CHMP2B protein injection was stopped when a plateau was observed on the graph indicating that protein saturation on the membrane is reached. Next, the SLB was washed with BP buffer to remove free-unbound proteins in solution and we measured the frequency shift $\Delta\vartheta_2$ for the different SLBs (Figure 5-5 / A). The variation of the frequency $\Delta\vartheta_2$ is directly related to the amount of proteins bound to the membrane, according to the equation mentioned above. Figure 5-5 / B shows the variation of the frequency $\Delta\vartheta_2$ as a function of time for CHMP2B-ΔC on SLB made of 10% PI(4,5)P_2.

The interaction of CHMP2B-ΔC proteins was found to be highly dependent on the lipid composition (Figure 5-5 / C). The amount of proteins adsorbed to the bilayer increased by 50 % when the amount of DOPS was increased from 30 % (grey bar) to 40 % (dark grey bar) (Figure 5-5 / C). Indeed, increasing the number of negatively charged lipids in the membrane increases the amount of proteins adsorbed on it. This implies that electrostatic interactions play a key role in mediating the interaction between the proteins and the membrane in agreement with the exposure of basic surfaces in ESCRT-III polymers (McCullough, Clippinger et al. 2015; Tang, Henne et al. 2015). The frequency shift $\Delta\vartheta_2$ measured for SLB

containing PI(4,5)P_2 averages to 50 Hz whereas the frequency shift measured for SLB containing 30 % DOPS is approximately equal 20 Hz (Figure 5-5 / C). Thus, when PI(4,5)P_2 is present in the membrane (10 % DOPS, 10 % PI(4,5)P_2 and 80 % EPC) (blue bar), the amount of proteins interacting with the membrane lipids is significantly increased by 66 % and 150 %, respectively, compared with membrane containing 30 % and 40 % DOPS (Figure 5-5 / C). This indicates that the amount of proteins is nearly doubled for SLB containing PI(4,5)P_2 in comparison with SLB containing 30 % DOPS (Figure 5-5 / C). Interestingly, if one considers that DOPS has a net charge of -1 at pH 7.5 and PI(4,5)P_2 has a net charge of -4 at pH 7.5 (McLaughlin, Wang et al. 2002), the total net charge of SLB containing 60 % EPC; 40 % DOPS is similar to that made with 80 % EPC; 10 % DOPS; 10 % PI(4,5)P_2. When PI(4,5)P_2 lipids in the SLB are replaced by the same fraction of PI(3,4,5)P_3 (magenta bar), the amount of proteins on the SLB decreases significantly and is almost equal to the amount of proteins bound to SLB containing 30 % DOPS. Surprisingly, while PI(3,4,5)P_3 lipids have a higher negative net charge (-6) as compared to PI(4,5)P_2 lipids (-4) (it was assumed that one of the oxygen atoms in the phosphate of the inositol ring in PIP_2 and PIP_3 is protonated) (McLaughlin, Wang et al. 2002), we found that the interactions between CHMP2B-ΔC proteins and the SLB are higher with PI(4,5)P_2 lipids, further supporting the hypothesis that there is a preferential interaction with PI(4,5)P_2 lipids. We conclude that the interaction between SLBs and CHMP2B-ΔC is partially governed by electrostatic interactions. In addition, CHMP2B-ΔC specific interactions with PI(4,5)P_2 lipids increase protein affinity for membranes containing this type of lipid, e.g. the plasma membrane. Interestingly, CHMP2B-ΔC interaction with PI(3,4,5)P_3 lipids is much weaker. In addition, we could measure the kinetics of adsorption of CHMP2B-ΔC on the different negatively charged membranes (Figure 5-5 / D). The frequency shift $\Delta\vartheta_2$ curves were fitted with exponential time decay. And, the corresponding characteristic time τ is deduced from the equation:

$$\Delta\vartheta = \vartheta_0 e^{-(t-t_0)/\tau} \qquad (5\text{-}2)$$

Depending on the lipids, the kinetics of adsorption is different. τ values range from 11 ± 0.5 to 50 ± 1.0 sec depending on the lipids (Figure 5-5 / D). The kinetics of adsorption is slower (≈ 50 ± 1.0 sec) for SLBs containing PI(4,5)P_2 lipids, although when PI(4,5)P_2 is present in the membrane, the total quantity of proteins bound to the membrane is highly increased (Figure 5-5 / D). On the contrary, the kinetics is faster (≈ 15 ± 0.5 sec) for SLBs containing PI(3,4,5)P_3 lipids, which bind less proteins (Figure 5-5 / D). Thus, a higher amount of bound protein is correlated with a slower kinetic rate. This difference might be due to protein rearrangements on the surface. When the protein density on the surface is low because of the protein weak affinity to the membrane, equilibrium is reached fast. If the protein density is high due to strong membrane affinity, protein reorganization is necessary in order to adsorb furthermore proteins.

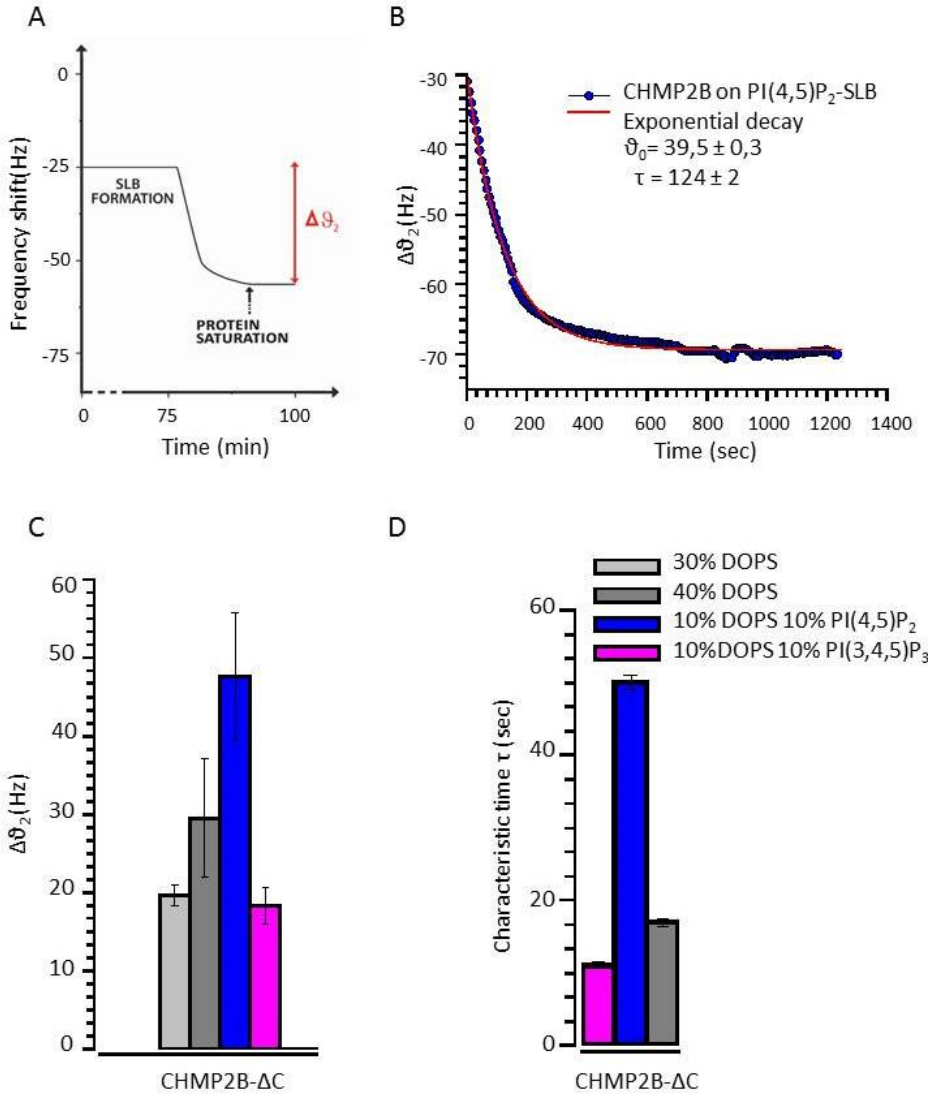

FIGURE 5-5: INTERACTION OF CHMP2B WITH DIFFERENT TYPES OF SUPPORTED LIPID BILAYERS
(A) Schematic representation of the measurement of the frequency versus time.
(B) Variation of the frequency shift $\Delta\vartheta_2$ for CHMP2B-ΔC for the PI(4,5)P_2 lipid composition. The exponential decay fit is shown.
(C) Variation of the frequency shift $\Delta\vartheta_2$ for CHMP2B-ΔC as a function of the lipid compositions (Light grey: 30% DOPS; Grey: 40% DOPS; Light Blue: 10% PI(4,5)P_2; Magenta: 10% PI(3,4,5)P_3). n=5.
(D) Characteristic adsorption time measured for CHMP2B-ΔC proteins for various lipid compositions (Grey: 40% PS; Light blue: PI(4,5)P_2; Magenta: PI(3,4,5)P_3). n=5.

5.1.2.2 STUDY OF CHMP2B BINDING ON GIANT UNILAMELLAR VESICLES

To study the binding of CHMP2B proteins on giant unilamellar vesicles, we first produced GUVs with lipid mixtures 6 to 10, with respectively 2% DOPS, 2% PI(4,5)P_2, 2% PI(4)P, 2% PI(3,5)P_2 and 2% PI(3)P. The preformed GUVs were then incubated for 30 min in BP buffer (NaCl 50 mM, Tris 25 mM at pH 7.5) with CHMP2B-FL (full length) and CHMP2B-ΔC (CHMP2B protein with C-terminus truncation) proteins at variable concentrations to check the effect of the C-terminus truncation on the protein interaction with membranes. We used flow cytometry (FACS) to analyze the protein and vesicle fluorescence signals.

FACS technique is based on the count of events, here our vesicles ± CHMP2B proteins, by light scattering and fluorescence emission simultaneously. Fluorescence is emitted by fluorescent CHMP2B and lipids dyes after excitation by the appropriate laser. In flow cytometry every particle detected in the solution (i.e. vesicles ± CHMP2B proteins) is classified as a distinct event. Every event is plotted independently as a function of the fluorescence channel in which it was detected.
Thus the fluorescence intensity of the membrane and the fluorescence intensity of the proteins are respectively proportional to the amount of fluorophores in the vesicle (thus, to its size) and proteins bound to it or present in the detection zone and unbound. The protein fluorescence appears in the left upper quadrant of the plot or protein positive region and the lipid (vesicle) fluorescence signal in the right lower quadrant or lipid positive region.

To quantify the amount of protein bound to the vesicles, one must look at the colocalization of both the protein and the lipids fluorescence signals, corresponding to the right upper quadrant or double-positive region (protein positive region + lipid positive region) (Figure 5-6 / A).

Figure 5-6 / B shows a typical FACS experiment. It represents the intensity plot of CHMP2B proteins on DOPS lipid mixture (control sample). In this condition, we observed no significative presence of double-positives in the right upper quadrant, meaning that the interaction of the proteins with the DOPS lipid vesicles is low. The histogram plot on the right represents the number of counted events for the protein fluorescence. It shows two peaks, the first corresponding to the proteins signal only and the second to the detected protein signal on vesicles.

Figure 5-6 / C shows the scatters plot for the protein and PI(4,5)P_2 lipid fluorescence signal (sample 1). It clearly shows the detection of protein bound to vesicles in the right upper quadrant (highlighted by the red rectangle in the figure) and vesicles without proteins in the right lower quadrant. We also see in the double -positive quadrant a linear variation of the protein signal with the lipid signal, suggesting that the total signal of the proteins bound increases with the size of the vesicles. Practically, the analysis did not include a renormalization of the protein intensity by the lipid intensity. Instead, the histogram of the "gated" region (Figure 5-6 / C - right) is plotted. It shows one peak showing that CHMP2B is bound to the vesicles. The median intensity of this peak is then considered as the average density of proteins bound to the vesicles in arbitrary unit. This intensity value can be compared for the different lipid compositions.

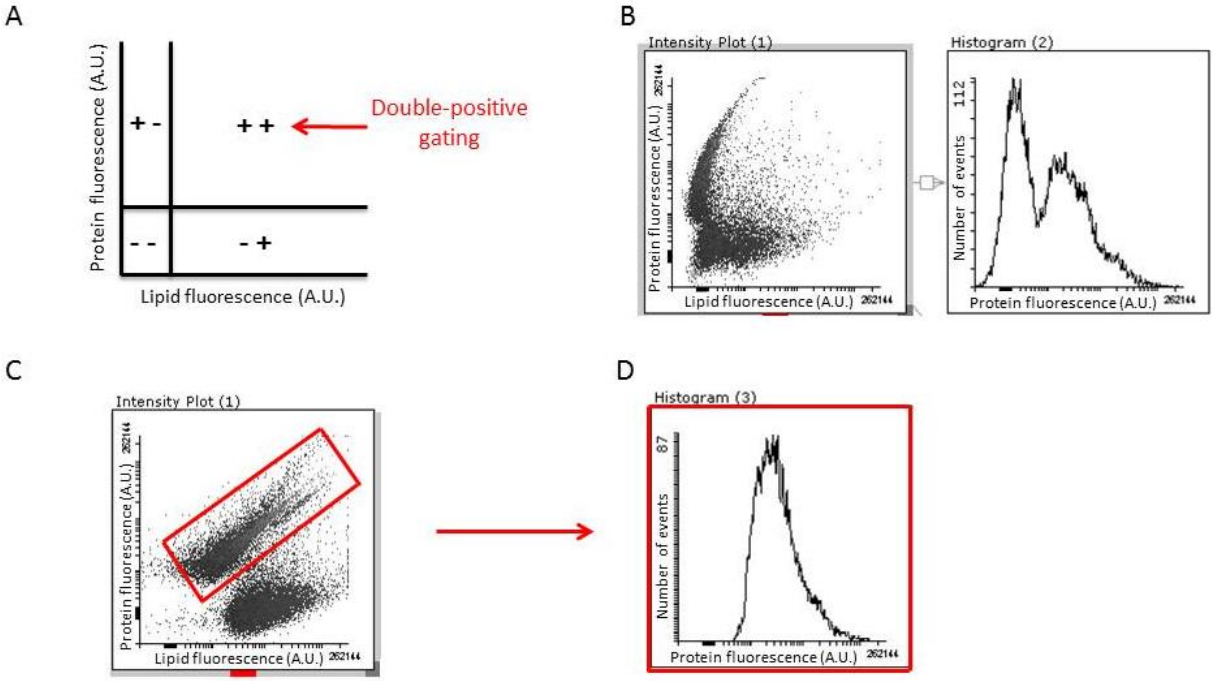

FIGURE 5-6: MEASUREMENT OF THE FLUORESCENCE INTENSITY OF CHMP PROTEIN BOUND TO GUVS BY FACS
(A) Bivariate histogram showing the possible combinations of positive and negative staining for two different dyes. Red arrow highlights the double-positive gated fluorescence, i.e. when proteins are bound to vesicles.
(B) Example with CHMP2B protein binding to DOPS (control sample). The intensity plot and the distribution of the protein fluorescence are shown.
(C) Example with CHMP2B binding to PI(4,5)P_2 containing vesicles. The intensity plot shows the signal for CHMP2B protein as a function of the lipid signal in the PI(4,5)P_2-vesicles. Red box defines the gated double-positive population.
(D) Histogram of the gated population (displayed in panel C) showing the distribution of the fluorescence signal of CHMP2B bound to PI(4,5)P_2 vesicles.

We measured the average fluorescence signal (green) of the protein bound to vesicles of different lipid membranes in the double positive region. To compare the binding efficiency of CHMP2B-ΔC for the different lipids, we plotted the protein fluorescence density in arbitrary unit normalized by the density of DOPS (Figure 5-7 / A – in green). We found that in agreement with the QCM-D observations, CHMP2B-ΔC exhibits preferential binding to GUVs containing PI(4,5)P_2 lipids as compared to the other PIP species. This increase of binding in the presence of PI(4,5)P_2 lipids is almost doubled when compared to the other PIPs lipid mixtures, including PI(3,5)P_2. Note that PI(4,5)P_2 and PI(3,5)P_2 have the same number of negative charges, yet CHMP2B binds more PI(4,5)P_2, further demonstrating that the interaction is not just a matter of electrostatic interaction. We also confirm that the interaction of CHMP2B-ΔC proteins is almost equal for PI(3,5)P_2-GUVs, PI(4)P-GUVs and PI(3)P-GUVs. These values are however 2 times higher than the value of the density of CHMP2B-ΔC with DOPS lipids. Consequently, we conclude that CHMP2B, in addition to electrostatic interactions with charged membranes, has a specific preference for PI(4,5)P_2 lipids, in agreement with its contribution to ESCRT-mediated processes only at the plasma membrane and the nuclear envelop.

We next tested the effect of the C-terminal deletion of CHMP2B proteins. Therefore, we repeated the same experiment and incubated the full length protein CHMP2-FL at 500 nM with GUVs made of the same different PIP species. We observed that the preferential binding to $PI(4,5)P_2$ is also conserved for CHMP2B-FL (Figure 5-7 / A – in black). Nevertheless, CHMP2B-FL has a lower binding affinity than CHMP2B-ΔC for all lipid compositions, including the $PI(4,5)P_2$ lipid mixture.

In addition Figure 5-7/ B shows the average protein density (in arbitrary unit) on $PI(4,5)P_2$-GUVs as a function of CHMPB-ΔC and CHMP2B-FL bulk concentration. CHMP2B-FL binds 4 times less than CHMP2B-ΔC on $PI(4,5)P_2$-GUVs at 4 µM protein concentration in bulk. We also tried to estimate the value of the binding constant Kd by varying the CHMP2B protein bulk concentration. However, since no saturation could be observed in the accessible concentration range, this measurement was not possible. Indeed, above 4 µM in BP buffer, we observed that both CHMP2B-ΔC and CHMP2B-FL proteins aggregate and form clusters with the lipids, which completely compromises the measurement. These results indicate that the Kd value for CHMP2B-ΔC and CHMP2B-FL proteins is relatively high (probably above 1-2 µM). Moreover, the C-terminal truncation is expected to result in a constitutively active protein with a higher membrane binding capacity. Thus, our results show that CHMP2B-FL protein can nevertheless bind membranes but more weakly that CHMP2B-ΔC, in particular on $PI(4,5)P_2$ membranes for which the constitutively active form has 4-times stronger affinity.

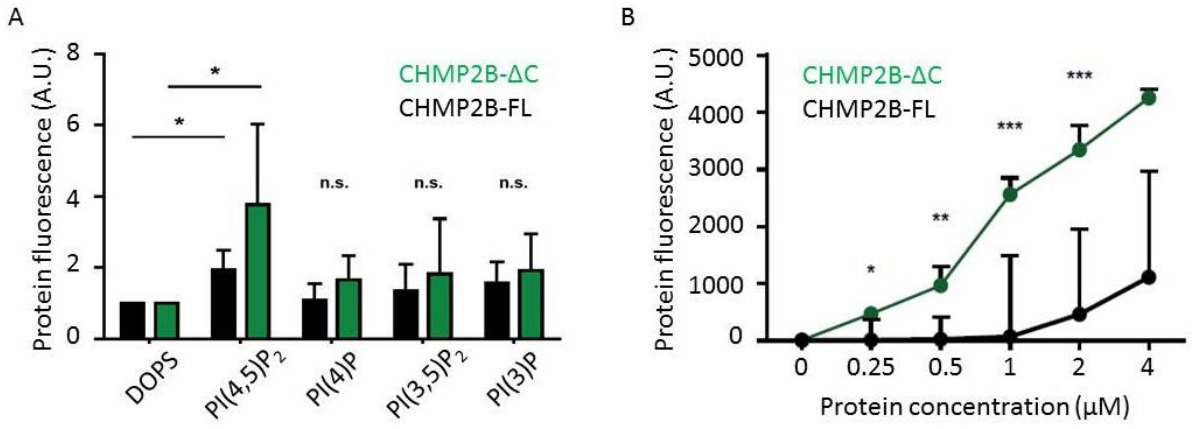

FIGURE 5-7: AFFINITY OF CHMP2B-ΔC VS. CHMP2B-FL TOWARDS NEGATIVELY CHARGED MEMBRANES MEASURED BY FACS

(A) Quantification of CHMP2B-FL and CHMP2B-ΔC binding to GUVs containing DOPS and different PIPs by flow cytometry. Equimolar amount of DOPS and different PIPs (2% mol/mol of total lipids) have been used. Results were normalized to the fluorescence intensity of DOPS-containing vesicles. *=p-value<0.05 (Student's t-test); n=6 (number of FACS experiment with 10^4 counted event per experiment, per condition).

(B) Titration curve of CHMP2B-FL and CHMP2B-ΔC binding to GUVs containing PI(4,5)P2.

*=p-value<0.05; **=p-value<0.01; ***=p-value<0.001 (Student's t-test); n=6 (number of FACS experiment with 10^4 counted event per experiment, per condition).

In addition, we have observed that for the same conditions (i.e. $PI(4,5)P_2$ lipid mixture, BP buffer and bulk protein concentration) CHMP2B binding could vary significantly among $PI(4,5)P_2$ binding assays. More precisely, we realized that CHMP2B proteins have to be incubated within an hour or less, following GUVs production to significantly bind GUV membranes. These binding variations are related to $PI(4,5)P_2$ stability and preservation over time (*Beber. A et. al* 2017, in revision in Langmuir journal). Therefore, in all our following experiments, proteins were added for binding and imaging less than an hour after vesicles preparation ahead of $PI(4,5)P_2$ solubilization out of the membrane or oxidation..

5.1.3 ENCAPSULATION OF CHMP2B PROTEINS INSIDE GUVS TO MIMIC ESCRTS INVERTED TOPOLOGY

After the characterization of the CHMP2B–lipid interaction, we aimed to encapsulate CHMP2B proteins inside GUVs to study the correct physiological topology. *In vivo*, ESCRT proteins interact with the cytosolic side of the membrane to induce membrane scission of buds toward the exterior of the cell or the interior of the endosomes, i.e. with a negatively curved membrane. Our initial aim was to use the tube pulling assay with encapsulated CHMP proteins (this system was previously developed and used in the team) (Prévost, Zhao et al. 2015) to mimic the neck of the biological buds where the protein is functioning. We reasoned that binding the internal side of a nanotube would replicate for the ESCRT (in particular CHMP2B) the topology of a bud neck (Figure 5-8).

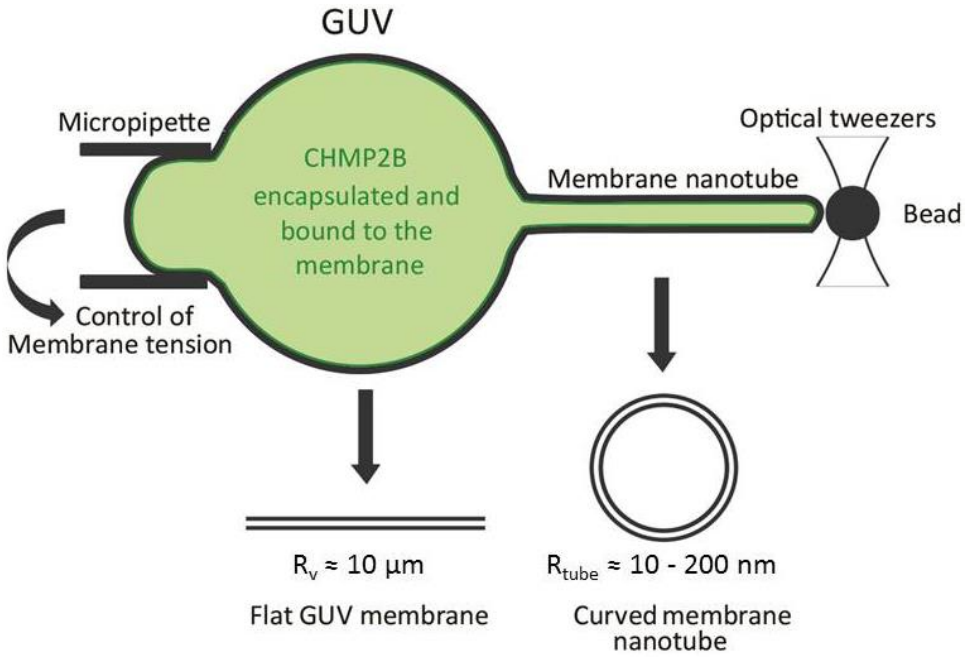

FIGURE 5-8: SCHEMATIC REPRESENTATION OF THE MEMBRANE NANOTUBE PULLING ESSAY
First, the GUV is moved up at about 20 µm from the bottom of the chamber with a micropipette. Second, a streptavidin-coated bead is trapped in the focus plane with the optical tweezers and moved into contact with the GUV in the equatorial plane of the vesicle. Third, a membrane nanotube is pulled out of the vesicle by moving the GUV away from the trapped bead. Schematic illustration not to scale.

5.1.3.1 ENCAPSULATION OF CHMP2B PROTEINS INSIDE GUVS BY INVERTED EMULSION AND PVA SWELLING

To mimic the negative membrane curvature *a priori* required for ESCRT action, the first step consists in the encapsulation of CHMP2B inside GUVs. We tried several techniques that were already published. One is the "inverted emulsion" method. It was initially designed by S. Pautot (Pautot, Frisken et al. 2003) and some improvements were proposed over the past years (Pontani, van der Gucht et al. 2009; Abkarian, Loiseau et al. 2011). This technique consists first in preparing an inverted emulsion of aqueous droplets containing the protein of interest into mineral oil containing lipids (lipid mixture 5 (10% DOPS, 10% $PI(4,5)P_2$)), and thus forming a monolayer at the droplet surface. Practically, the oil mixture and the aqueous solution containing CHMP2B proteins in BP buffer are mixed to make an inverted emulsion (Pautot, Frisken et al. 2003). Because of their amphipathic nature, the lipids form a monolayer around the droplets of protein solution (Figure 5-9 / A). Next, the emulsion is placed in contact with an aqueous solution that will eventually form the external medium of the GUVs, forming an interface covered with an additional lipid monolayer. The coated lipid droplets are then pushed by centrifugation through this monolayer at this oil/water interface (Figure 5-9 / B and C), thus creating a lipid bilayer around the protein solution and producing GUVs with proteins inside and the lipid bilayer around (Figure 5-9 / C). The osmolarity of the aqueous solution must match that of the protein solution in the droplets, to obtain stable GUVs. The group of M. Abkarian in Montpellier had improved the method, using microfluidic to produce droplets of homogeneous size continuously injected into an oil (plus lipids) solution placed over a rotating disk. This method is called cDICE ("continuous Droplet Interface Crossing Encapsulation") (Abkarian, Loiseau et al. 2011). The water droplet size can be adjusted to be of the order of the ten microns' range. To produce GUVs with CHMP2B proteins surrounded by a bilayer containing 10% DOPS + 10% $PI(4,5)P_2$ lipids, we used cDICE, but also the "manual" method with a syringe to produce the emulsion (Pontani, van der Gucht et al. 2009). Unfortunately, because of the presence of negatively charged lipids, a significant amount of oil is trapped in between the bilayer leaflets (C.Prevost PhD thesis), more than in the absence of charged lipids (Campillo, Sens et al. 2013). Indeed, we observed that in tube pulling experiments, the force on the tube was not stable, even in the absence of proteins, which precluded us from doing any quantitative measurement with this system. We tried to remove residual oil within the bilayer by using cyclodextrin, a molecule that has a strong affinity for hydrophobic molecules, for instance cholesterol (Roux, Cuvelier et al. 2005); we expected that cyclodextrin could extract the oil residues from the bilayer. Unfortunately, we observed that cyclodextrin also solubilized most of the $PI(4,5)P_2$ present in the membrane, which induces a significant reduction of the protein affinity for the membrane. For this reason, the inverted oil emulsion technique was abounded. We tried then the gel-assisted swelling technique on polyvinyl alcohol (PVA) gel.

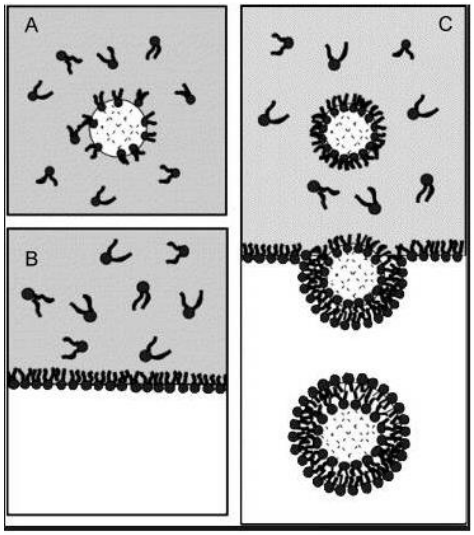

FIGURE 5-9: SCHEMATIC REPRESENTATION OF THE PRINCIPLE OF THE INVERTED EMULSION TECHNIQUE TO PRODUCE GUVS (Pautot, Frisken et al. 2003)
(A): The lipids solubilized in the oil phase adsorb on water droplets, with their hydrophilic heads facing the water phase.
(B): The lipids adsorb at the interface between the oil phase and the aqueous phase forming the external buffer.
(C): The water droplets, covered with a first monolayer of lipids, are forced through this interface by centrifugation, leading to the addition of a second monolayer around the droplet.

The PVA spontaneous swelling technique (see chapter 4.2.3.2) consists in first drying the lipid film made of the lipid mixture 5 on the PVA gel, and then rehydrating it with a solution made of CHMP2B protein diluted in BP buffer. We expected to obtain GUVs with CHMP2B proteins in the inner medium (inside) and bound to the membrane (Figure 5-10 / ideal case).

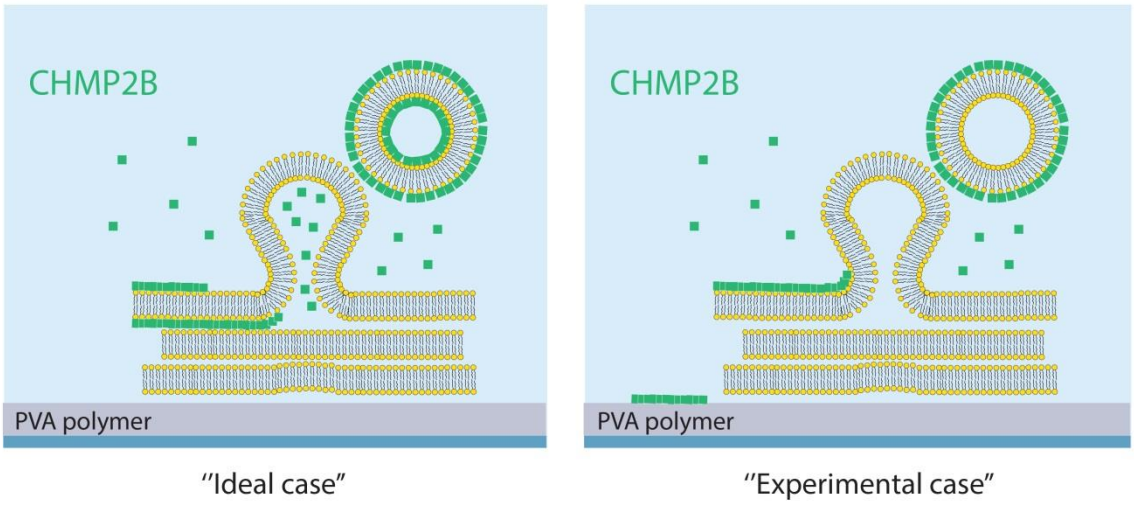

FIGURE 5-10: POSSIBLE ORIGIN OF THE NON-ENCAPSULATION OF CHMP2B INTO GUVS FORMED BY PVA-ASSISTED SWELLING TECHNIQUE
Left: In the "ideal case", swelling of the lipids bilayers with the protein solution leads to the spontaneous formation of GUVs with proteins bound on both sides of the bilayer.
Right: in our case, with CHMP2B, we suspect that either CHMP2B strongly binds to the PVA gel or to the surface of the lipid film and that the proteins do not penetrate into the PVA gel.

Practically, this was not the case: we observed that it was not possible to incorporate any CHMP2B protein in the produced GUV, even by adding up to 10 µM protein in the growth buffer (Figure 5-11 / A). We first thought that due to its size, the protein did not penetrate into the gel. But surprisingly, we managed to encapsulate other CHMP proteins (i.e. CHMP2A, CHMP3 separately and CHMP2A + CHMP3) that have the same size range (Figure 5-11 / B). Thus we supposed that either the CHMP2B proteins strongly adhere to the gel during vesicle growth and for this reason could not be encapsulated, or because of its high affinity to PI(4,5)P_2 lipids it directly interacts with the most accessible PI(4,5)P_2 lipids present on the surface of the lipid film (Figure 5-10 / experimental case). We thus switched to another method.

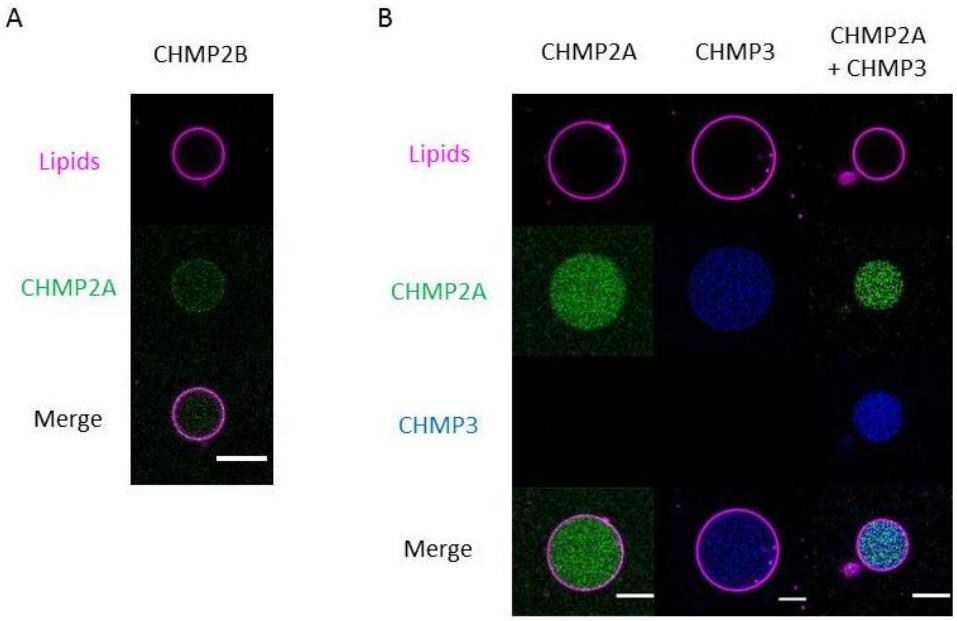

FIGURE 5-11: ENCAPSULATION OF CHMP PROTEINS USING PVA SPONTANEOUS SWELLING TECHNIQUE
Confocal images showing the result of the encapsulation of CHMP proteins by PVA-assisted spontaneous swelling technique. CHMP2B fluorescence signal (in green) is very weak inside the GUV implying a low rate of encapsulation; no signal is observed at the GUV surface. In contrast, fluorescence signal for CHMP2A (in green), CHMP3 (in dark blue) and CHMP2A + CHMP3 complex (merge: in light blue) indicate that those are significantly present inside GUVs. Scale bar = 10 µm.

5.1.3.2 ENCAPSULATION OF CHMP2B PROTEINS INSIDE GUVS BY PLW ELECTROFORMATION

Another alternative to encapsulate CHMP2B was to use the electroformation technique on platinum wires (PLW). This technique has been used in our team to successfully encapsulate I-BAR proteins (Prévost, Zhao et al. 2015).

To work at physiological salt conditions (i.e. high salt concentrations), GUVs cannot be produced by electroformation on ITO plates. Instead, vesicles were produced using the PLW electroformation technique (see chapter 4.2.3.1). However, CHMP2B protein encapsulation with PLW revealed to be very challenging. Practically, the growth chamber is made of a Teflon block with three holes. Two platinum

wires are inserted into the Teflon and the lipids are deposited on them (see chapter 4.2.3.1) (Figure 5-12 / left). Lipid droplets in chloroform are deposited on the platinum wires, dried and rehydrated under an electric field (500 Hz, 35mV). GUVs were grown in the presence of 500 nM CHMP2B proteins diluted in the growth buffer. When vesicle growth was done in BP buffer, we were able to produce GUVs, yet all the proteins were strongly bound to the membrane. We could never observe any protein in the lumen of the GUVs, as it was also the case with the PVA-spontaneous swelling technique. Thus, we supposed that because of the high affinity to the $PI(4,5)P_2$ membrane, all proteins added in the vesicle growth buffer were bound to the membrane, leaving no free protein in bulk. To check this hypothesis, we prepared GUVs in the presence of 500 nM CHMP2B proteins diluted in a growth buffer at a higher salt concentration: NaCl 150 mM, Sucrose 50 mM and Tris 25 mM at pH 7.5. In these conditions, we did not observe protein interaction with the membrane due to the screening of the electrostatic interaction between CHMP2B and the lipids. Yet we did not see CHMP2B green fluorescence signal in the vesicle inner medium, meaning that the encapsulation of the protein was not successful although CHMP2B protein was "in principle" in excess in the bulk. At this point, we examined more closely our GUV production method. We realized that CHMP2B proteins were mostly aggregated and adhered strongly to the glass cover slips used to seal the growth Teflon chamber (one in the bottom and one on the top of the chamber).

To solve this problem, we produced customized chambers made of Teflon only (Figure 5-12 / right). These "all-Teflon" chambers were tricky to use. First, it was impossible to observe the vesicle growth. Second, the hydrophobic surface of the chamber often favoring leaking of the growth buffer, which in turn, caused a dewetting of the wires. To sum up, making GUVs in "all-Teflon" chambers was not reproducible.

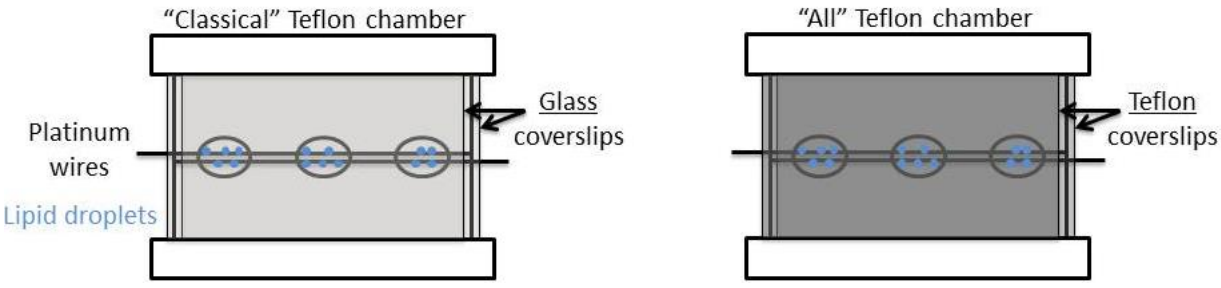

FIGURE 5-12: SCHEMATIC ILLUSTRATION OF THE TEFLON CHAMBERS USED FOR PLW ELECTROFORMATION
In the "classical" Teflon chamber, two glass coverslips are used to seal the chamber (Left), whereas in the "All" Teflon chamber they were replaced by Teflon coverslips (Right).

Consequently, we had to return to the "classical" electroformation chambers and treat the glass slide surfaces to avoid interaction between the protein and the glass surface. Glass passivation with β-casein (at a concentration of 5 $mg.mL^{-1}$ in NaCl 100 mM, Tris 25mM at pH 7.5) was not sufficient and the only efficient way was by cleaning the glass coverslips with a Piranha solution.

"Piranha" solution is a mixture of 70 % sulfuric acid (H_2SO_4) and 30 % hydrogen peroxide (H_2O_2), used to remove most organic matter. It can also hydroxylate glassy surfaces and make them highly hydrophilic for a more efficient binding of the β-casein solution. Only after "Piranha" treatment followed by β-casein passivation, CHMP2B proteins adhesion to the glass surface was limited and proteins encapsulation was possible (Figure 5-13).

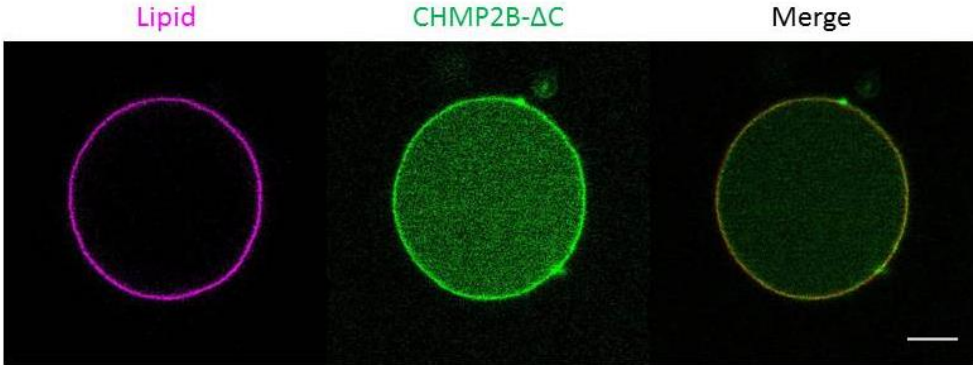

FIGURE 5-13: ENCAPSULATION OF CHMP2B PROTEIN INSIDE GUV BY PLW ELECTROFORMATION AFTER "PIRANHA" TREATMENT PLUS B-CASEIN PASSIVATION OF THE GLASS COVERSLIPS
The membrane is in magenta, the protein in green and the merge in yellow. Because CHMP2B protein is present in the growth buffer, it is present inside the GUV and bound to the membrane inner and outer leaflets. Scale bar = 10 µm. n=50.

Thus, with this method we obtained GUVs with CHMP2B proteins present in the inner and outer medium, bound to the membrane inner and outer leaflets. So to reach our goal of tube pulling with CHMP2B proteins only present inside the vesicle, with the topologically correct membrane negative curvature, it is crucial to remove the proteins bound to the external leaflet of the GUVs. Indeed, the protein presence on both sides of the membrane could interfere with our measurements.
In the following, we will explain the different strategies we employed to detach CHMP2B proteins from the membrane outer leaflet.

5.1.4 CHMP2B PROTEINS INTERACTION WITH PI(4,5)P_2 LIPIDS IS IRREVERSIBLE

Here again we used QCM-D technique to monitor the detachment of CHMP2B proteins from lipid membranes. We formed the different lipid bilayers and injected continuously 200 nM CHMP2B proteins in BP until protein saturation on the membrane was reached. Then we rinsed the bilayer with BP buffer to remove unbound proteins. Next, to detach the bound proteins from the SLB membrane, we increased the salt concentration by flowing continuously a solution made of NaCl 500 mM and Tris 25 mM at pH 7.5. An increase in salt concentration is meant to screen the electrostatic interactions between the proteins and the membrane and thus should promote CHMP2B proteins desorption from the lipid bilayer.

In Figure 5-14 / A, we present two extreme scenarios for the variation of the frequency during a QCM-D experiment: either a 100 % detachment of CHMP2B proteins where the frequency value would return to $\Delta\vartheta_1$ (frequency shift value measured upon lipid bilayer formation and before addition of the protein) or a 0 % detachment of the proteins in which the frequency value would remain equal to $\Delta\vartheta_2$ (frequency shift value measured after protein saturation on the SLB).

After complete saturation of CHMP2B-ΔC proteins on the SLB made of the different lipid mixtures (i.e. t > 110 min) (Figure 5-14 / A), we injected the high ionic strength buffer solution (500 mM NaCl, 10 mM Tris at pH 7.5) during a period ranging from 30 min to overnight and then rinsed with the protein binding buffer BP (NaCl 50 mM, Tris 25mM at pH 7.5).

To quantify the percentage of CHMP2B protein detachment, we measured the frequency change between the protein saturation and the last washing step. In Figure 5-14 / B, we present the percentage of detachment of CHMP2B as a function of lipid mixtures.
For all lipid mixtures, only a limited fraction of CHMP2B-ΔC proteins were detached from the membrane. We measured 30 % detachment for the DOPS lipid mixture (dark grey) and a only 5 % for the $PI(4,5)P_2$ lipid mixture (blue) and 10 % for the different $PI(3,4,5)P_3$ lipid mixture (magenta).

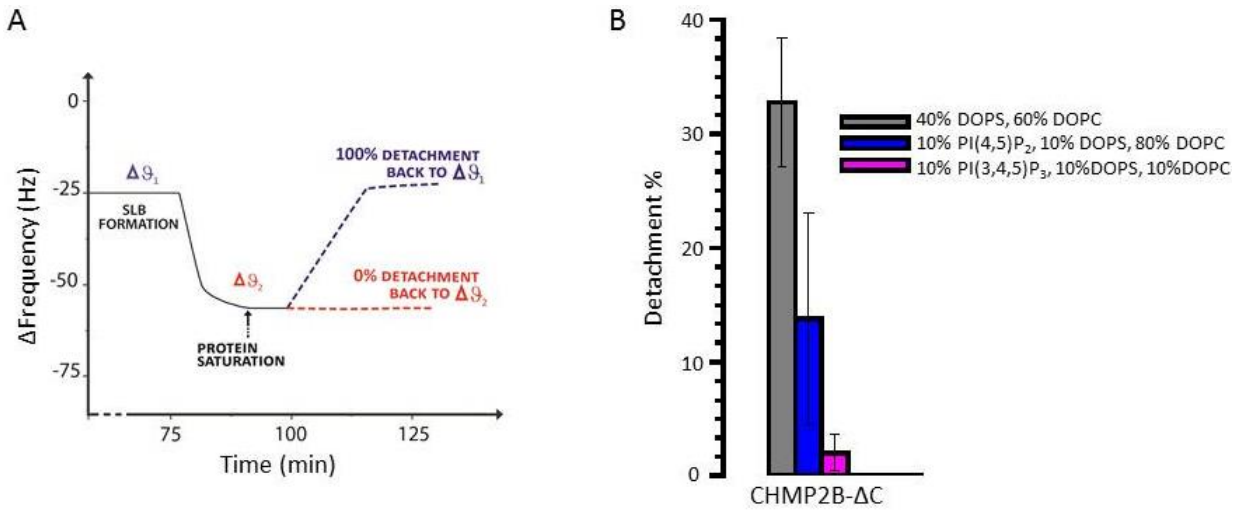

FIGURE 5-14: DETACHMENT OF CHMP2B PROTEINS BOUND TO DIFFERENT LIPID BILAYERS
(A) Typical detachment curve in a QCM-D experiment. Scheme showing two extreme scenarios for the detachment of CHMP proteins from a SLB after washing with a 500 mM NaCl, 10mM Tris pH 7.5 buffer: variation of the frequency shift as a function of time when proteins are completely detached or remain fully bound to the SLB.
(B) Detachment of CHMP2B proteins bound to different lipid bilayers. Percentage of CHMP2B-ΔC proteins detached from the SLB after washing with a 500 mM NaCl, 10mM Tris pH 7.5 buffer for at least 30 min as a function of the lipid composition (Grey: 40% DOPS; Light Blue: $PI(4,5)P_2$ and Magenta: $PI(3,4,5)P_3$). n=5.

We then aimed at confirming these results with GUVs, knowing that the charged lipids incorporation in GUVs is much lower than in SLBs. GUVs were grown overnight in the absence of proteins using the PLW technique in 300 mM sucrose, 100 mM NaCl and 25 mM Tris at pH 7.5. Subsequently, they were transferred and kept for at least 30 min at room temperature in a CHMP2B-ΔC 500 nM in 400 mM glucose, 50 mM NaCl and 25 mM Tris at pH7.5. In this case, the CHMP proteins are thus bound onto the external leaflet only. Part of this sample was diluted 20 times in the same buffer for protein binding control imaging. Another part was diluted 20 times in 250 mM NaCl and 25 mM Tris at pH=7.5, to detach the bound proteins from the outer leaflet. Osmolarity of the different buffers was matched to avoid vesicle deflation or inflation due to an osmotic difference. For each sample, at least 20 vesicles were imaged in the green channel (protein channel) by confocal fluorescence microscopy. Figure 5-15 presents the interaction between GUVs and CHMP2B before and after being subjected to the high ionic strength buffer (NaCl 500 mM). No detachment of CHMP2B protein was observed, confirming here again that the interaction of CHMP2B protein with $PI(4,5)P_2$-containing membranes is not just due to electrostatic interactions but more likely to specific interactions, possibly a protein insertion into the membrane.

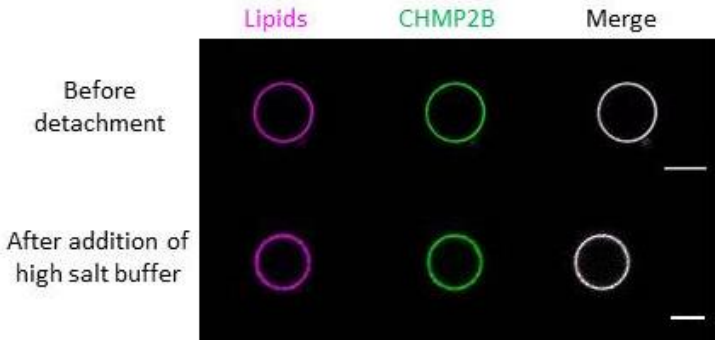

FIGURE 5-15: HIGH IONIC STRENGTH BUFFER DETACHMENT ASSAY ON VESICLES COVERED WITH CHMP2B PROTEINS
Detachment assay of CHMP2B proteins (in green) – covered GUVs (in magenta). One confocal plane images are taken before and after 1h incubation in high ionic strength buffer. Scale bar = 5 µm.

Because CHMP2B proteins bind irreversibly the $PI(4,5)P_2$ membrane and could not be detached by increasing the salt concentration, we tried to remove the proteins bound to the membrane outer leaflet by enzyme digestion. The experiments were performed with two proteases: Pronase (a combination of proteases) and Proteinase K (Figure 5-16). In the presence of both proteases, we observed a decrease with time of the protein signal on the vesicle rim, indicating that both enzymes digested the outside-bound proteins (Figure 5-16). But, we also noticed that the number of vesicles was remarkably reduced after enzyme addition implying that the enzymes not only digested the proteins but could also induce GUVs leakage and eventually destabilize them.

To test whether the enzyme induced vesicles leakage, protein-bound vesicles were transferred to a buffer containing the enzyme and Cascade Blue, a soluble fluorescent dye. This fluorescent dye does not interact with the vesicles and in normal condition cannot cross the lipid bilayer. It is very convenient for testing GUV leakage (Garten, Mosgaard et al. 2017): if the vesicles leak, the Cascade Blue dye present outside enters in the vesicle which can be detected with the fluorescence signal. As a control, we checked whether the enzymes induce membrane leakage in the absence of CHMP2B. No leakage was detected on CHMP2B-free vesicles before and after incubation with the enzymes. In contrast, in the presence of CHMP2B, the dye was observed inside the GUVs, confirming the vesicle leakage (Figure 5-16). This could be due to CHMP2B insertion into the membrane and/or to the formation of defects in the bilayer after protein cleavage by the protease.

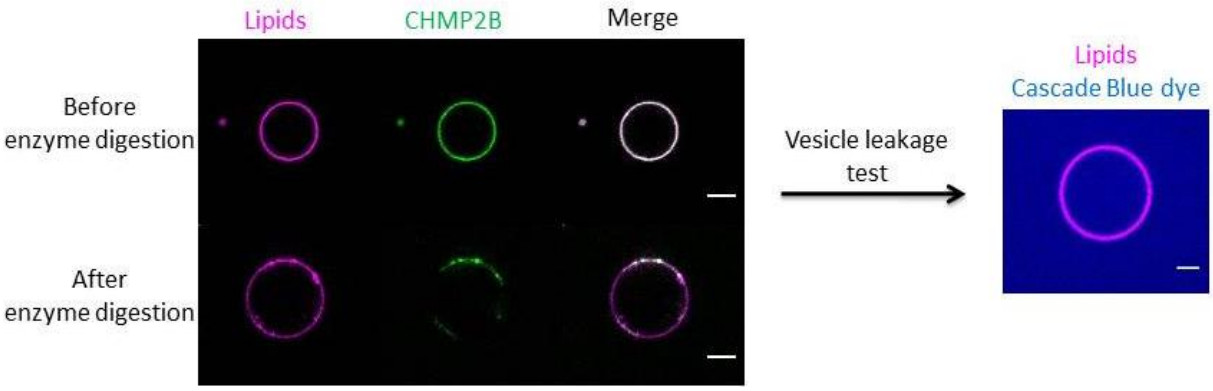

FIGURE 5-16: DETACHMENT ASSAY BY ENZYME DIGESTION ON VESICLES COVERED WITH CHMP2B PROTEINS
One confocal plane images are taken before and after 1h incubation with Protease K enzyme (left). One confocal plane image is taken after incubation with cascade blue dye to test vesicle leakage (right). Scale bar = 5 µm. n = 30.

Although we could not find a good method for having CHMP2B only on the internal leaflet of the GUVs, we nevertheless tried to pull membrane nanotubes from CHMP2B-bound GUVs to study how the proteins redistribute between the quasi-flat GUV and the highly curved nanotube.

Tube pulling experiments are achieved as following: GUVs are added to the passivated experimental chamber together with 2 µl of streptavidin coated polystyrene beads (3.05 µm in diameter, diluted 400 times, part no. SVP-30-5, Spherotech). The beads and vesicles are then left to sediment at the bottom of the chamber for about 20 to 60 min. During this time, the experiment buffer gradually evaporates causing the osmolarity to slowly increase in the medium, and thus leading to a flow of water outside of the GUVs. Consequently, membrane tension decreases, which facilitates tube pulling. When the vesicles are floppy enough and optically fluctuate, the chamber is sealed with mineral oil (Sigma-Aldrich, USA) to prevent further evaporation. The streptavidin-coated bead is then trapped with the optical tweezers and a membrane tube is pulled by bringing the micropipette-aspirated vesicle containing biotinylated lipids into contact with the bead and then moving it away from the bead. The bead position, and thus the force, is then tracked at different membrane tensions by changing the micropipette aspiration. The

bead is tracked for at least 1 min at each tension to give the system time to reach steady state. Fluorescent confocal images are acquired at each step to measure the membrane and protein fluorescence signal intensities at the vesicle rim and on the tube.

We realized during these experiments that in contrast with bare vesicles without proteins, the vesicles encapsulating CHMP2B were rarely floppy which made aspiration and tube pulling hard tasks. However, we succeeded to pull membrane nanotubes when a very low amount of proteins were bound to the membrane (Figure 5-17) (around 1 to 2 pulled tubes out of 20 trials per experiment). Protein clusters / aggregation were often observed on the tube and never on the surface of the vesicle (Figure 5-17). Interestingly, these clusters move along the tube when tension is varied. Figure 5-17 shows the cluster displacement from the tube neck towards the bead when tension is increased.

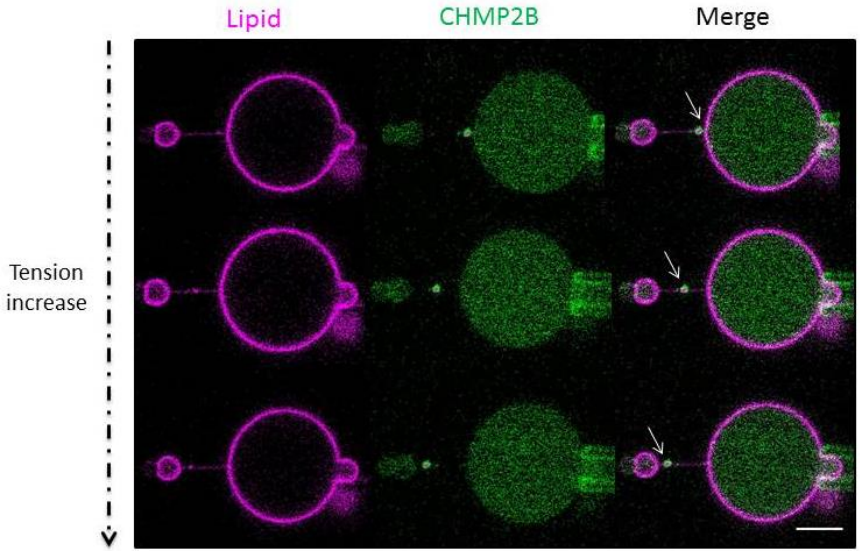

FIGURE 5-17: EXAMPLE OF TUBE PULLING EXPERIMENT WITH ENCAPSULATED CHMP2B PROTEIN
A membrane nanotube pulled from a GUV encapsulating CHMP2B proteins. In this case, no protein binding was detected on the GUV membrane. A protein polymerization/aggregation is observed on the membrane nanotube only (pointed by the white arrow). A displacement of this protein cluster is observed when membrane tension is increased. Scale bar = 10 µm.

In addition, in rare cases, more protein clusters formed on the tube when the applied tension on the membrane was increased. We supposed that the protein polymerization/aggregation on the tube could be membrane curvature dependent and that the additional clusters could be formed when a threshold tube radius is reached, like in the case of dynamin (Roux, Koster et al. 2010). Since in our experiments, CHMP2B proteins were bound to both inner and outer membrane leaflets i.e. on negative and positive curvatures (Figure 5-18 / A), we had to test CHMP2B binding on positively curved only (Figure 5-18 / B). A priori, we expected not to observe any binding in this case, considering the *in vivo* geometry of the bud necks, with a negative curvature.

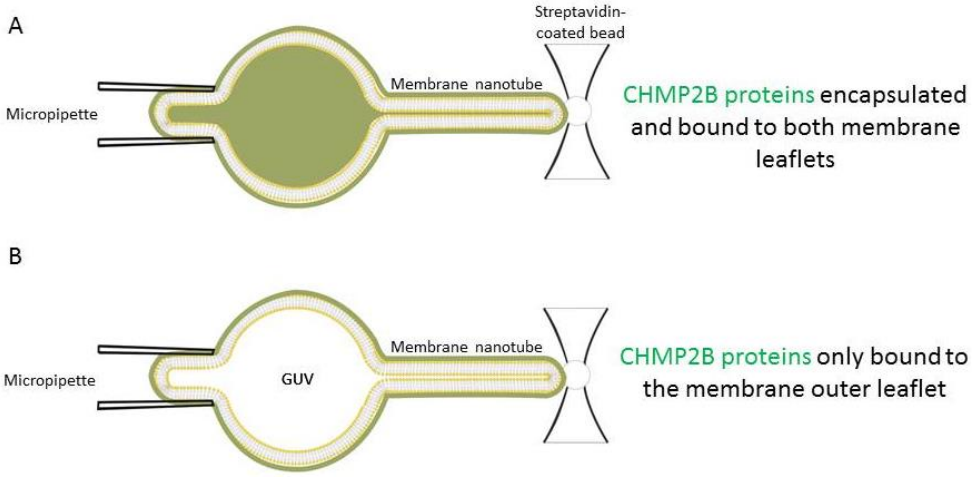

FIGURE 5-18: SCHEMATIC ILLUSTRATION OF THE DIFFERENT CURVATURES EXPERIENCED BY PROTEINS IN OUR TUBE PULLING EXPERIMENTS.
(A) With our encapsulation protocol, proteins are bound to both the inner and the outer leaflet of the membrane tube. Thus the effects of positive and negative curvature are detected at the same time.
(B) Proteins are bound to the external leaflet only and the effect of positive curvature can be probed.
Both schematic illustrations are not in scale.

To do so, CHMP2B proteins must be bound to the outer membrane leaflet of the tube only. We performed tube pulling experiments with CHMP2B proteins added outside instead of being encapsulated inside vesicles (Figure 5-18 / B). To do so, CHMP2B proteins were injected with a second micropipette placed close the previously pulled membrane nanotube (Figure 5-19). We measured the intensity signal of the protein on the tube as well as the force to get information on the curvature sensing properties of the protein.

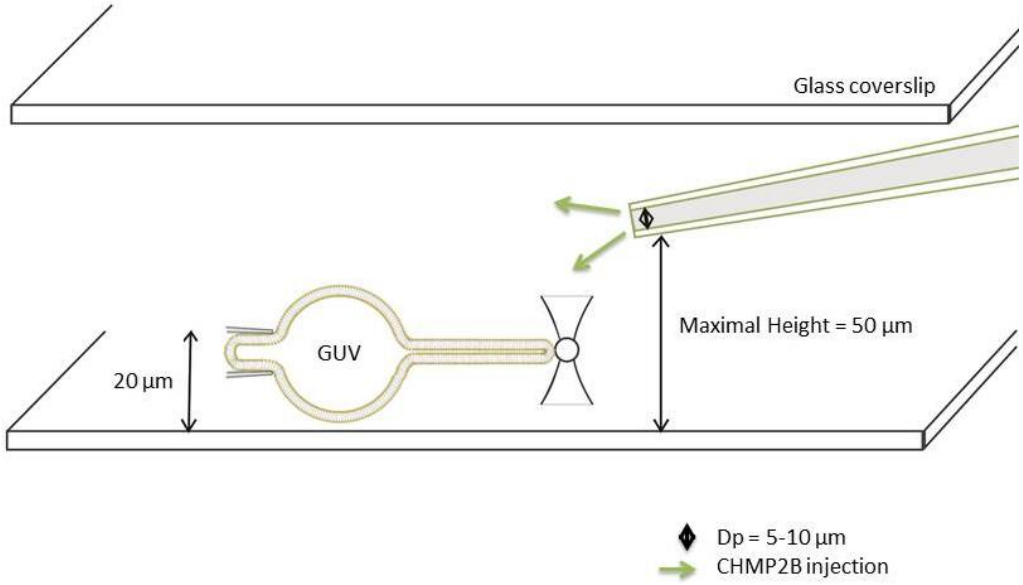

FIGURE 5-19: SCHEMATIC ILLUSTRATION OF THE PROTEIN INJECTION SYSTEM
After pulling a membrane nanotube out of the micropipette-aspirated vesicle we proceed to protein injection by a second micropipette (diameter Dp), which is brought close to the tube. Proteins are blown out of the pipette by varying the hydrostatic pressure inside the micropipette. Schematic illustration not to scale.

When proteins were injected at concentrations below 1 µM, we observed the same type of spots on the tube as observed with encapsulated proteins (Figure 5-20 / A). Moreover, the spots did not grow with time, as observed for instance for dynamin polymers nucleating and growing on tubes (Roux, Koster et al. 2010). We did not measure any effect on the tube diameter or on the force, even when the tension was changed. Thus, we supposed that these clusters are an experimental artifact seen in the tube pulling experiments with encapsulated CHMP2B protein. Aiming to see an induced effect of the protein on the tube such as for instance tube buckling or tube diameter constriction, we repeated the experiment and injected greater protein concentration (up to 10 µM). By increasing the concentration of the injected protein, we wanted to first completely cover the tube with the proteins in order to see their consequent effect on the tube. Against all expectations, we did not observe any further protein assembly on the tube or protein full assembly on the tube even after prolonged injection time on the same pulled nanotube (60 min). In reality, only bigger aggregates were observed on the tube and in the experimental chamber (Figure 5-20 / B). By seeing these aggregates we wondered if the observed clusters corresponded to experimental artifact instead protein polymerization on the tube. Because we already faced problems with CHMP2B protein adhesion and aggregation on the glass coverslips (see part 5.1.3.2), we filled the micropipette used for the injection with CHMP2B proteins (as we usually did for the injection experiment) and the inspected the pipette glass surface under the microscope. By doing so, we realized that the protein aggregation observed during CHMP2B injection experiment (Figure 5-20 / B) was originally nucleated on the micropipette glass surface. And it was later further injected into the chamber by decrease of the hydrostatic pressure inside the pipette. We thus looked for an alternative to glass pipette for our injection system.

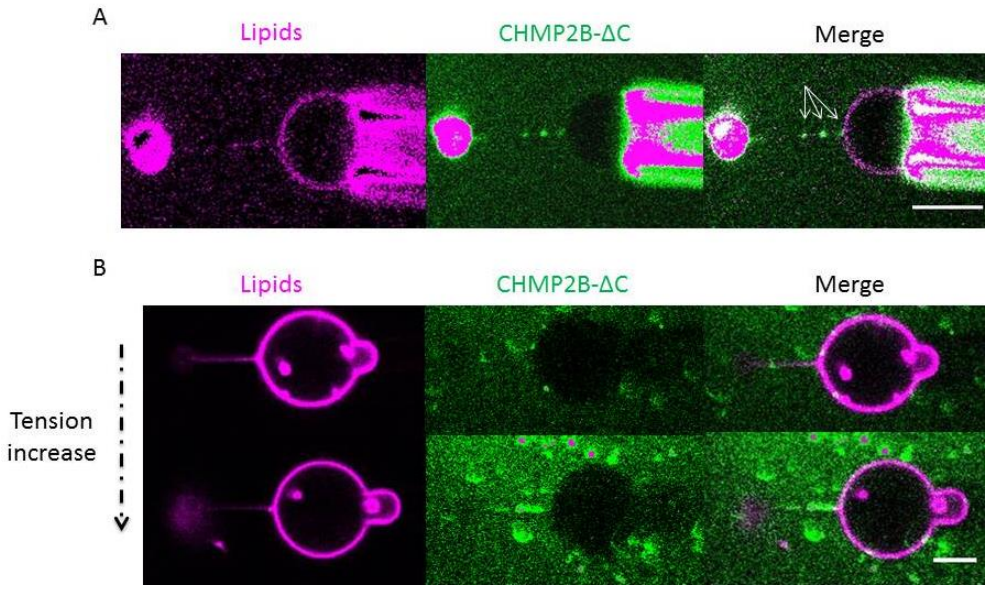

FIGURE 5-20: EXAMPLES OF CHMP2B PROTEIN INJECTION ASSAY ON MEMBRANE NANOTUBE
(A) Formation of three CHMP2B protein clusters on positively curved membrane nanotube. Scale bar = 5 µm.
(B) CHMP2B protein aggregation upon long-time injection. Many protein aggregates are visible in the bulk, on the GUV and on the tube. Scale bar = 10 µm.

We tried to replace glass micropipettes by PEEK tubes that have Teflon's similar non-adhesive properties (in collaboration with S. Descroix from the microfluidics group of the UMR168). CHMP2B protein aggregation was largely reduced by using PEEK tubes. However, since protein diffusion is slow, injection must be performed close to the nanotube. This implies that the PEEK tube diameter must be smaller than 50 µm. We thus pulled on PEEK tubes to reduce their diameter. Yet, protein injection was not possible because CHMP2B proteins tend to rapidly aggregate inside the tube and obstruct it. Eventually, due to all these issues, we have decided to give up experiments on the interaction of CHMP2B with curved membrane nanotubes.

As a conclusion for this part, we have been able to characterize the interaction between lipids and CHMPS2B proteins. We found that CHMP2B proteins require negative lipids to bind the membrane, specially PI(4,5)P_2. We showed that CHMP2B-FL interacts less than CHMP2B-ΔC with the membrane confirming thus that the C-terminal truncation of CHMP2B results in a constitutively active protein.
We then aimed at studying the curvature sensitivity of CHMP2B with tube pulling experiments. We adapted the growth chamber previously developed in the team by C. Prevost (Prévost, Zhao et al. 2015) using glass coverslips cleaned with "Piranha" solution and passivated with β-casein solution to limit protein adherence to the glass and aggregation. We succeeded to encapsulate CHMP2B proteins, but we could not get rid of the proteins bound on the external leaflet. Unfortunately, we succeeded to pull membrane nanotubes out of GUVs only when a very low density of proteins was bound to the membrane. In addition, protein binding on nanotube was impossible to investigate since it requires using glass micropipette, which systematically induces protein aggregation.

For all these reason, **we have decided to focus our work and effort on the study of protein assembly on the surface of GUVs and of their mechanical properties by micropipette aspiration and HS-AFM.** We first studied CHMP2B and compared it with the other ESCRT-III subunits.

5.1.5 CHMP2B PROTEINS FORM A RETICULAR-LIKE STRUCTURE ON GUVS

To further characterize the protein-membrane interaction and study the effect of protein binding on the elastic properties of the membrane, CHMP2B-ΔC proteins were added to pre-formed GUVs containing 10% DOPS, 10% PI(4,5)P_2 (lipid mixture 5) at different bulk concentrations in BP buffer (50 mM NaCl, 25 mM Tris at pH 7.5).
To define how CHMP2B proteins assemble on GUVs and to look for possible protein-induced membrane deformations, we acquired confocal and spinning disk images on the GUV surface, along the vesicle z-axis. A 3D reconstruction of the z-stacks gives information about the proteins distribution on the entire vesicle surface. At high protein concentrations, above 1 µM in bulk, CHMP2B-ΔC proteins fully cover the

GUV surface and no distinctive structure is observed besides some protein-lipid clusters on the surface of the GUVs (Figure 5-21 / upper panel). At optical resolution, CHMP2B-ΔC appears homogeneously distributed on the surface of the vesicles, with the additional presence of some larger structures. At lower bulk concentrations, 500 nM and below, after 15 min incubation in the protein binding buffer BP (50 mM NaCl, 25 mM Tris at pH 7.5), CHMP2B-ΔC proteins polymerize on the GUV surface forming a very unique network or reticular-like structure wrapping around the whole vesicle (Figure 5-21 / lower panel). When compared to the experiments at higher protein concentration where full protein coverage was observed, we propose that this network become denser when bulk concentration is increased leading to an apparent continuous coverage at high concentration or longer incubation time, at least at optical resolution.

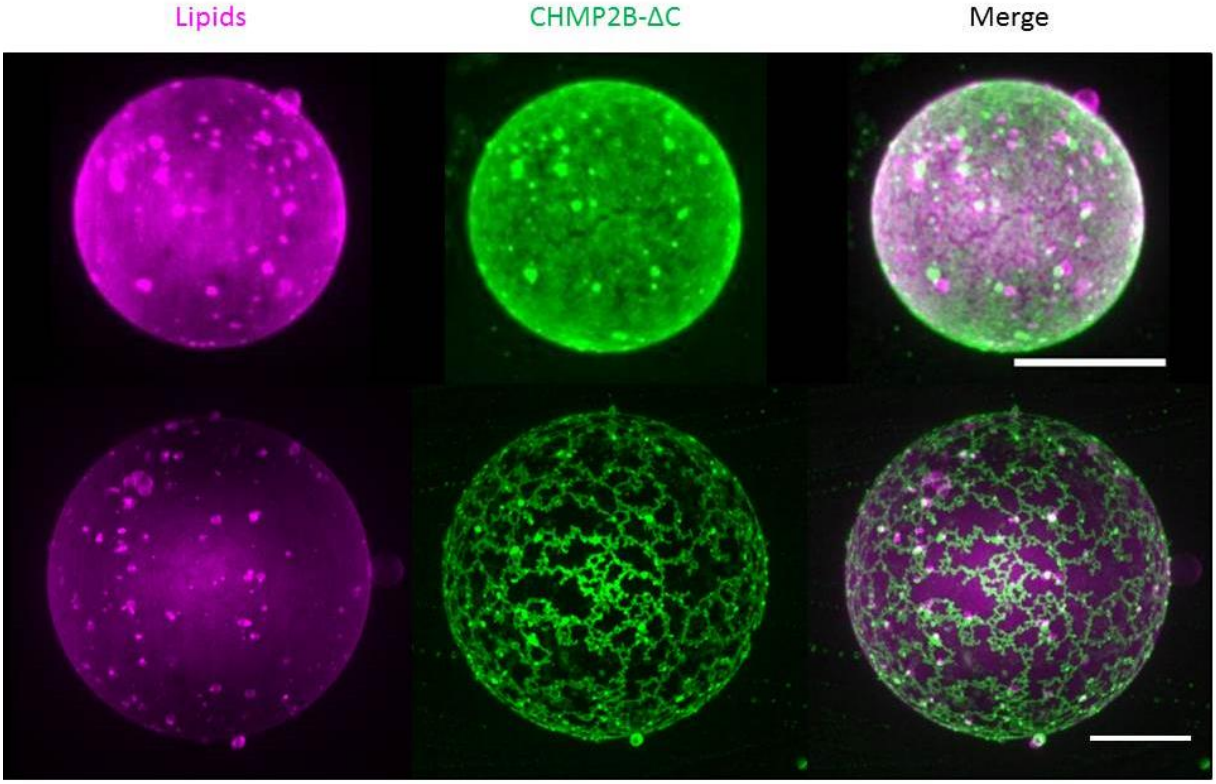

FIGURE 5-21: CHMP2B-ΔC ASSEMBLY ON GUV
Supramolecular assembly of CHMP2B-ΔC in BP buffer on PI(4,5)P2-containing GUVs. At high protein concentration around 1 µM, CHMP2B-ΔC fully covers the vesicle surface (upper panel), whereas at lower protein concentration, at 500 nM, CHMP2B-ΔC assembles into a reticular-like structure on the GUV (lower panel). A z-projection of the whole GUV is shown. Scale bar = 10 µm.

We next compared with CHMP2B-FL and we repeated the experiment. At high CHMP2B-FL protein concentration (1 µm) full coverage could not be reached with the full length protein, probably due to its lower affinity for $PI(4,5)P_2$ (Figure 5-22 / A). Yet, we observed the same reticular-structure formation on the vesicle surface (Figure 5-22 / A). This result confirms that the C-terminal truncation does not change dramatically the way CHMP2B assembles on the GUVs' surface.

To further characterize and compare the interaction of CHMP2B-ΔC and CHMP2B-FL on GUVs, we measured their respective area fraction on the vesicle surface from the analysis of fluorescence intensity. To do so, using the Cellprofiler software, we applied the "Otsu Global" greyscale threshold method and set the pixels below the threshold to zero. From there, we can calculate on each vesicle, the number of pixels and the intensity corresponding either to lipids or to proteins. We measured the vesicle area, reticulum area and total intensity of the protein on the vesicle.

Figure 5-22 / B shows the area fraction covered by CHMP2B-ΔC and CHMP2B-FL on GUVs. This calculation has been deduced from the equation:

$$\%\, Coverage = \frac{Reticulum\ area}{GUV\ area} * 100 \qquad (5\text{-}3)$$

Where the reticulum area corresponds to the total number of pixels measured for the protein signal and GUV area the total number of pixels measured for the lipids signal.

The box plot gives the median value (X = 0.5), the lower quartile (X = 0.25), the upper quartile (X = 0.75), the lower whisker (X = 0.05), the upper whisker (X = 0.95) as well as the minimal and maximal values (see cross). While the coverage fraction of CHMP2B-ΔC at a bulk concentration of 1 µM on PI(4,5)P_2-GUVs is close to 100 % (average value ≈ 86.4 ± 21.6 and median value ≈ 99.7) after 15 min incubation, it is less than 50 % in the presence of CHMP2B-FL (average value ≈ 43.4 ± 25.9 and median value ≈ 33.3).

Figure 5-22 / C shows the mean CHMP2B protein fluorescence intensity on the GUVs. This quantification has been deduced from the following the equation:

$$D = \frac{I\ (protein)}{\text{GUV area}} \qquad (5\text{-}4)$$

Where I (protein) correspond to the sum of all pixel intensities for the protein. The box plot gives the median value (X = 0.5), the lower quartile (X = 0.25), the upper quartile (X = 0.75), the lower whisker (X = 0.05), the upper whisker (X = 0.95) as well as the minimal and maximal values (see cross). The measured fluorescence intensity is at least 1.5 times higher with the protein truncated version (average value ≈ 6.6 ± 2.3 x 10^{-3} A.U. and median value ≈ 7.5 x 10^{-3} A.U. for CHMP2B-ΔC against average value ≈ 4.3 ± 4.1 x 10^{-3} A.U. and median value ≈ 2.2 x 10^{-3} A.U. for CHMP2B-FL).

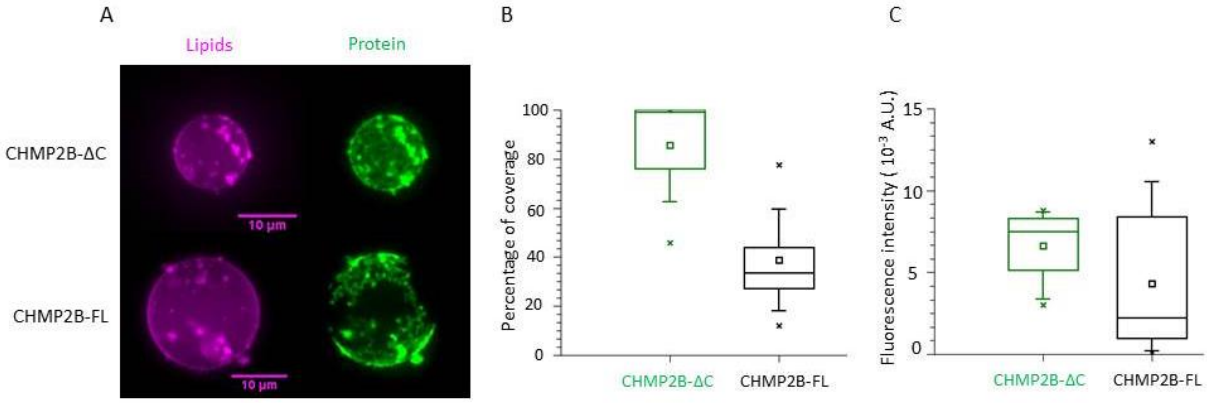

FIGURE 5-22: COMPARISON OF CHMP2B-ΔC AND CHMP2B-FL ASSEMBLY ON THE GUV SURFACE
(A) Comparison of CHMP2B-ΔC and CHMP2B-FL polymers assemblies on GUVs (lipid mixture 5 with 10 % PI(4,5)P_2). CHMP2 proteins were added to pre-formed GUVs at a concentration of 1 µM. A z-projection of the GUV is shown. Scale bar = 10 µm.
(B) Quantification of the percentage of coverage of CHMP2B-FL and CHMP2B-ΔC polymers bound to GUVs. n=40.
(C) Quantification of the fluorescence intensity of CHMP2B-FL and CHMP2B-ΔC polymers bound to GUVs. n=40.

These observations by spinning disk microscopy confirm again that the C-terminal truncation of the protein increases the affinity of the protein for PI(4,5)P_2 membranes.

To get further insights into the formation of the observed network structure, experiments were performed with fluorescently labelled PI(4,5)P_2 lipids (lipid mixture 5 with 8% PI(4,5)P_2 instead of 10% PI(4,5)P_2 and 0.5% Fluo-PI(4,5)P_2 instead of 0.8% PE-Rhodamine). Co-localization between the CHMP2B-ΔC reticulum and Fluo-PI(4,5)P_2 was detected, indicating that CHMP2B-ΔC proteins recruit the negatively charged PI(4,5)P_2 lipids underneath the network structure (Figure 5-23).

The clustering of Fluo-PI(4,5)P_2lipids within CHMP2B-ΔC reticulum, further stresses the importance of the interaction between CHMP2B-ΔC proteins and PI(4,5)P_2 lipids.

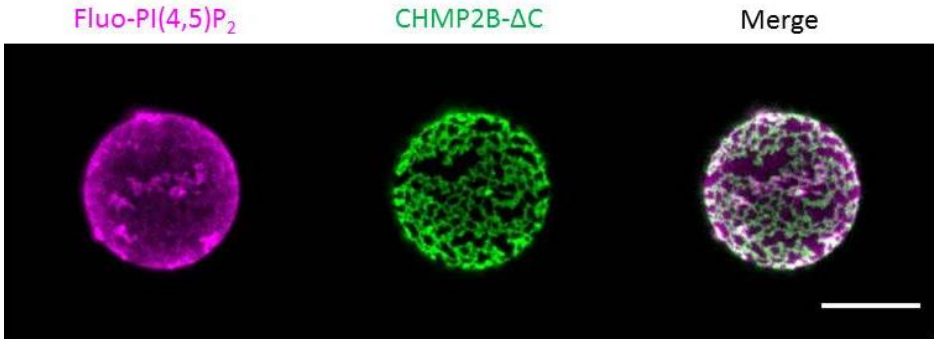

FIGURE 5-23: PI(4,5)P2 IS CLUSTERED BY CHMP2B-ΔC POLYMERS
Co-localization between Fluo-PI(4,5)P_2 and CHMP2B-ΔC on GUVs. A z-projection spanning the upper part of the GUV is shown. Scale bar = 10 µm.

5.1.6 CHMP2B ASSEMBLES INTO RING-LIKE STRUCTURES AT THE NANOSCALE

Optical imaging of GUV reveals the global organization of the protein at the micron scale. We thus aimed at studying the organization and mode of polymerization of CHMP2B proteins at molecular scale and high resolution. Therefore, Cryo-EM and HS-AFM experiments were performed by Dr. A. Bertin and Dr. S. Maity from the groups of Dr. D. Levy and Prof. W. Roos, respectively, on LUVs and SLBs covered with CHMP2B proteins.

CHMP2B proteins at a concentration of 500 nM were added to pre-formed LUVs (see chapter 4.2.4) made of the lipid mixture 5 (10% DOPS, 10% PI(4,5)P_2 in the protein binding buffer BP (50 mM NaCl, 25 mM Tris at pH 7.5) and kept at room temperature during 30 min. Samples were then vitrified and observed by Cryo-EM. CHMP2B visualization by EM was a real challenge as we could rarely see the protein and often only indirectly observed the effect of its binding onto membranes (in contrast with the other CHMP subunits that could be easily detected by EM). Nevertheless, we managed to image the protein assembly of CHMP2B proteins on a membrane for the first time. CHMP2B proteins have a peculiar nanoscopic organization: they form rings and at high density and assemble into a dense "honeycomb-like" pattern (Figure 5-24 / A). The mean diameter of the CHMP2B rings within the honeycomb lattice measured by Cryo-EM is equal to 13.6 ± 1.8 nm (Figure 5-24 / B).

By HS-AFM on PI(4,5)P_2-SLBs (see chapter 4.2.5) coated with CHMP2B proteins at a concentration of 1 µM, same results were obtained. CHMP2B proteins assemble in rings on SLB. Figure 5-24 / C represents these ring structures. The ring structures that protrude from the surface (highlighted by a white asterisk) correspond to stacks of two CHMP2B rings on top of each other (Figure 5-24 / C). In Figure 5-24 / D, the height profile is measured by HS-AFM over a single ring on the surface (orange line on the image). CHMP2B rings have a height of about 1.5 nm. In addition, the mean ring diameter is equal to 16.4 ± 0.4 nm, not too different from the value obtained by Cryo-EM (Figure 5-24 / E). This ring diameter value is consistent with the measured diameter of CHMP2B tubular structures at the narrowest points *in-vivo (Bodon, Chassefeyre et al. 2011).* In fact, previous Cryo-EM study by Bodon et al. shows that overexpressed CHMP2B, polymerizes into a tightly packed helical polymer intimately associated with the inner leaflet of the bilayer. These CHMP2B tubular structures vary in diameter from 100 to 400 nm and in some cases, are constricted from a diameter of ~80 to ~16 nm.

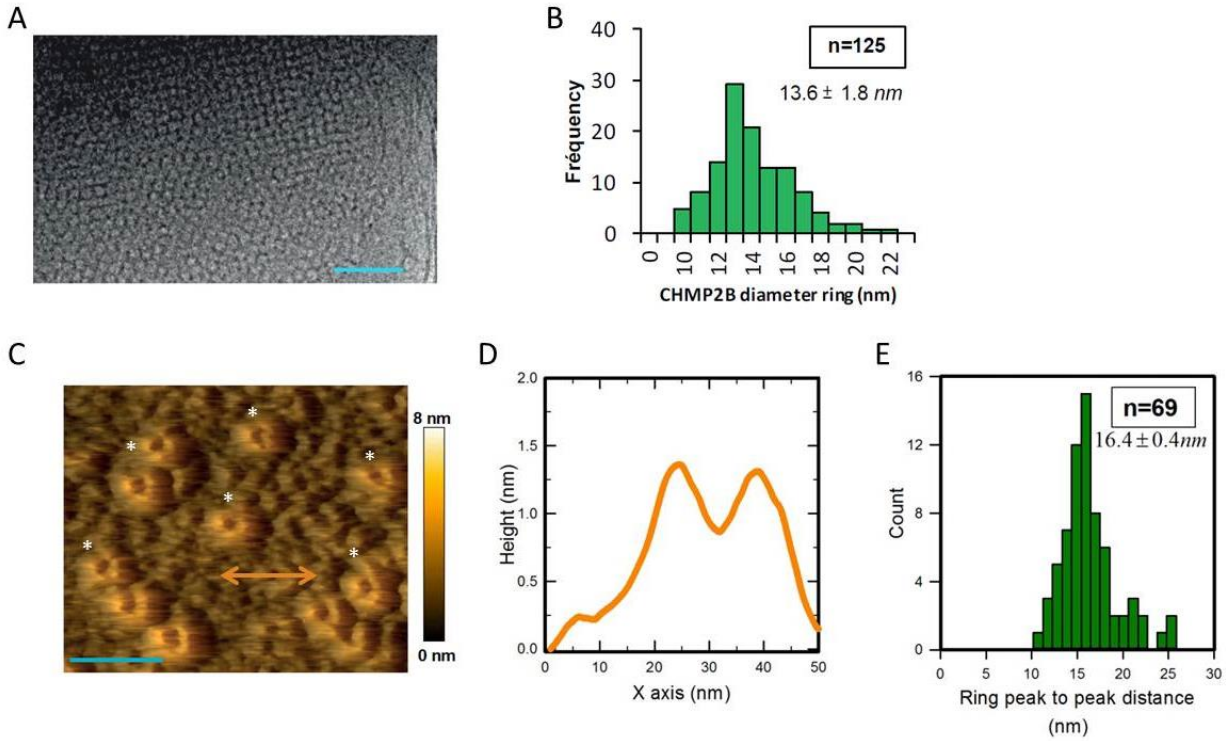

FIGURE 5-24: OBSERVATION OF CHMP2B ASSEMBLY AT HIGH RESOLUTION
(A) Representative Cryo-EM image showing the assembly of CHMP2B on LUVs. Scale bar: 100 nm.
(B) Distribution of CHMP2B ring sizes (from the Cryo-EM acquired images)
(C) Representative image taken with HS-AFM showing the assembly of CHMP2B on a SLB. Scale bar: 50 nm.
(D) Height profile of CHMP2B rings (from the HS-AFM acquired images)
(E) Distribution of CHMP2B rings sizes (from the HS-AFM acquired images)

5.2 CHMP2B POLYMERS MODULATE MEMBRANE ELASTIC PROPERTIES

We have next investigated the influence of the presence of CHMP2B proteins on the elastic properties of model lipid membranes. We observed during tube pulling experiments that it was not possible to form a tube from GUVs as soon as a detectable amount of proteins was present on the GUV. This pointed to a stiffening of the membrane induced by CHMP2B binding and assembling on the GUV surface. The elastic properties of the membrane in the absence and in the presence of CHMP2B proteins were studied using three different techniques: (i) applying osmotic shocks on GUVs, (ii) micropipette aspiration of GUVs and (iii) AFM deformation experiments of SUVs.

5.2.1 INVESTIGATION OF CHMP2B MECHANICAL PROPERTIES BY APPLYING OSMOTIC SHOCKS

It is well known that bare lipid membranes cannot sustain stretching larger than about 5% (Rawicz, Smith et al. 2008), and rupture if the strain is too high (Motta, Gohlke et al. 2015). This is the case when GUVs are immersed in a hypo-osmotic buffer. Conversely, in a hyperosmotic medium, GUVs loose volume, change shape and even tend to become unstable when the shock is too strong (Bernard, Guedeau-Boudeville et al. 2002). Indeed, the increase of the external osmotic pressure induces an efflux

of water through the lipid and the water pores, causing a decrease of the volume of the GUV. We thus studied how much CHMP2B-coated GUVs resist to hyper-osmotic shocks. As before, we used GUVs made of the lipid mixture 5 (10% DOPS, 10% PI(4,5)P_2). They were either transferred to the BP buffer free of proteins or incubated containing 500 nM of CHMP2B for 15 min in BP (osmolarity equal to 125 mOsm.L^{-1}). We then applied a hyperosmotic shock by increasing the sodium chloride concentrations in the GUV outer medium.

The effect of the osmotic shock was evaluated using confocal microscopy and measuring the eccentricity of the vesicles. The eccentricity is the ratio of the between-foci distance and the major axis length of an object. If the semi-major axis is *a* and the semi-minor axis is *b*, then the eccentricity is given by:

$$e = \sqrt{(1 - \frac{b^2}{a^2})} \tag{5-5}$$

Eccentricity ranges between 0 (for a circle) and 1 (for a line segment). Thus, a high eccentricity value corresponds to a strongly deformed GUV (Figure 5-25).

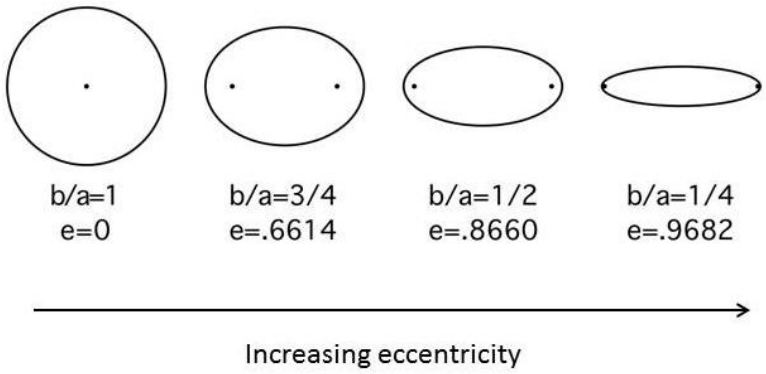

FIGURE 5-25: CIRCULARITY DEVIATION WITH ECCENTRICITY INCREASE
Shown are different circularity deviation in function of increasing eccentricity with a and b corresponding to the semi-major axis and the semi-minor axis, respectively.

In the control experiments without CHMP2B proteins, the osmotic difference between both sides of the membrane caused a strong deformation on the surface of the GUVs. For osmotic shock higher than 20% (osmolarity of the external medium= 150 mOsm L^{-1} versus osmolarity of the inner medium= 120 mOsm L^{-1}) we observed a deflation or shrinkage effect on the GUV shape. And for osmotic shock above 50 % (osmolarity of the external medium ≥ 190 mOsm.L^{-1}), we observed a net decrease in the number of vesicles in the experimental chamber due to their strong instability.

Figure 5-26 / A (see control) displays the change in shape of the vesicle after their transfer in a solution with an osmolarity of 315 mOsm L^{-1} corresponding to a relative osmotic pressure difference equal to 150%. Figure 5-26 / B data in magenta display the eccentricity average for bare vesicles. The lowest and highest measured eccentricities are shown and are equal to 0.56 and 0.82, respectively. And, the eccentricity average is equal to 0.72 ± 0.11, indicating an important deviation in the vesicle circularity.

In high contrast, vesicles covered with CHMP2B polymer remained spherical for higher osmotic values. Figure 5-26 / A shows a vesicle with a preserved spherical shape after a 150% applied osmotic shock. Figure 5-26 /B presents the eccentricity value for CHMP2B-coated vesicles in green. It shows that the eccentricity average is equal to 0.35 ± 0.03 with the highest eccentricity value about 0.39 and the lowest equal about 0.31. Moreover, vesicles covered with CHMP2B proteins could even stand a 300 % osmotic shock with a solution osmolarity equal to 500 mOsm L^{-1}, showing again that CHMP2B polymer assembly on the GUV surface prevents the vesicle from deformation. As a conclusion, these observations suggest that the CHMP2B protein assembly on the GUV surface probably induces a membrane stiffening which preserves it from external stresses.

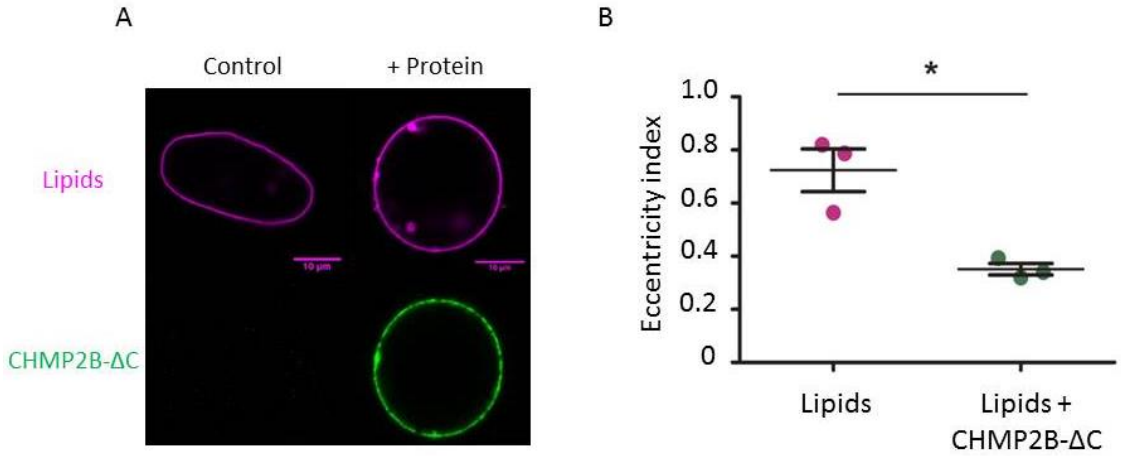

FIGURE 5-26: HYPEROSMOTIC SHOCKS APPLIED TO VESICLES COVERED WITH CHMP2B PROTEINS
(A) Hyperosmotic shock (150%) applied to GUVs with or without pre-incubation with CHMP2B-ΔC. Scale bar = 10 µm.
(B) Eccentricity is measured after 150% osmotic shock for GUVs alone or covered with CHMP2B polymer.
Note that the reference value for a non-deformed, circular-shaped vesicle is 0.
*=p-value<0.05 (Student's t-test). n=40.

5.2.2 STUDY OF CHMP2B MECHANICAL PROPERTIES BY MICROPIPETTE ASPIRATION

We next used the micropipette aspiration technique to further investigate the mechanical properties of CHMP2B assembly on the surface of GUVs. Here, the elasticity of lipid membranes is measured on GUVs both in the absence and in the presence of CHMP2B proteins, as first described by (Kwok and Evans 1981). The micropipette aspiration method (see chapter 4.5.1) consists in applying a tension on the membrane and measuring its elastic response to the induced stress. The tension can be calculated using the Young-Laplace equation (equation 4-6 in chapter 4.1):

$$\sigma = \frac{\Delta P \times Rp}{2\left(1 - \left(\frac{Rp}{Rv}\right)\right)}$$

Where Rp and Rv are the radius of the pipette and vesicle respectively and ΔP the hydrostatic pressure. When the tension increases, the vesicle is aspirated with formation of a characteristic "tongue" (or cylindrical part) inside the pipette (Figure 5-27).

The excess area due to membrane fluctuations α is the difference between the macroscopic area of the membrane (A) and the membrane apparent area (A_p). When the GUV is not aspirated, the tension on the membrane is minimal ($\sigma = \sigma_0$) and the excess area due to fluctuations is maximal ($\alpha=\alpha_0$). On the other hand, when the vesicle is aspirated, its membrane tension increases ($\sigma > \sigma_0$) and the excess area decreases ($\alpha < \alpha_0$). The observed increase of area upon pipette aspiration $\Delta A/A_0$ is thus linked to the variation of excess area (equation 4-10 in chapter 4.1):

$$\Delta\alpha = \frac{(Aasp - A0)}{A0} = \left(\frac{((Rp - Rv)^2) - ((Rpip - Rv)^3)}{2Rp}\right) \times \Delta L$$

By plotting the variation of the apparent area Δα versus the membrane tension, in the enthalpic regime (for tensions above 0.5 $mN.m^{-1}$), the stretching modulus can then be extracted from the slope value of the curve following (equation 4-13 in chapter 4.1):

$$\sigma \approx \chi\, \Delta\alpha$$

Where χ is the stretching modulus and Δα the variation of excess area from the reference state.

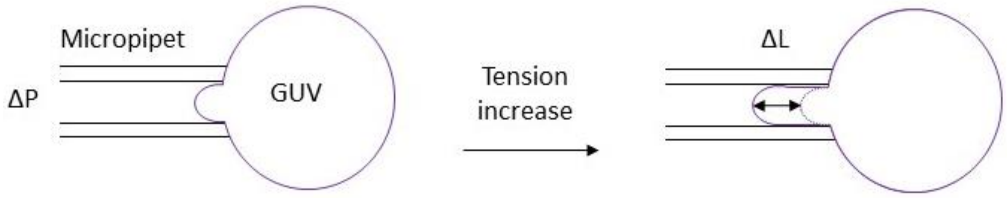

FIGURE 5-27: SCHEMA OF MICROPIPETTE ASPIRATION FOR THE MEASUREMENT OF MEMBRANE MECHANICAL PROPERTIES
A GUV is held in a micropipette by aspiration. When the aspiration pressure is increased, (from left to right) membrane tension increases, which results in an increase in membrane apparent area.

For our experiments, preformed $PI(4,5)P_2$-GUVs (lipid mixture 5 with 10% DOPS, 10% $PI(4,5)P_2$) were incubated with 500 nM CHMP2B-ΔC in BP until full coverage of CHMP2B proteins on the GUV surface is reached (approximatively 30 min). Then CHMP2B-covered GUVs were aspirated. Vesicle pre-stretching was not possible due to the presence of the protein.

Figure 5-28 displays the effect of the tension increase and shows that in the absence of CHMP2B, vesicles can be aspirated easily with formation of the characteristic tongue inside the pipette. In contrast, CHMP2B-covered GUVs could not be aspirated even at high tensions above 10^{-3} $N.m^{-1}$. However, during aspiration at high tension, we could sometimes observe an occasional rupture of the

CHMP2B-ΔC coat, which allowed the formation of a short tongue inside the micropipette devoid of proteins (Figure 5-28), indicating that CHMP2B polymer itself could not be aspirated or deformed.

Because we did not see any tongue formation in the presence of CHMP2B bound to the GUVs, the tension calculation was biased. Indeed, to calculate the membrane tension with the Young-Laplace law, it is assumed that the tongue radius (cylinder radius) is equal to the pipette radius, whereas in our case the tongue length is less than the pipette radius even at high tensions of the order of 10^{-3} N.m^{-1}. Moreover, for the same reason we could not as well measure the variation in the apparent area Δα. Thus, the micropipette aspiration technique was not adapted to measure the stretching modulus according to Evan's theory. However, even though the technique was not adapted for quantifying the membrane bending modulus in the presence of CHMP2B, these results still show that the polymerization of CHMP2B-ΔC on the surface of GUVs leads to membrane stiffening and eventually explain why tube pulling experiments on GUVs with bound CHMP2B were not feasible.

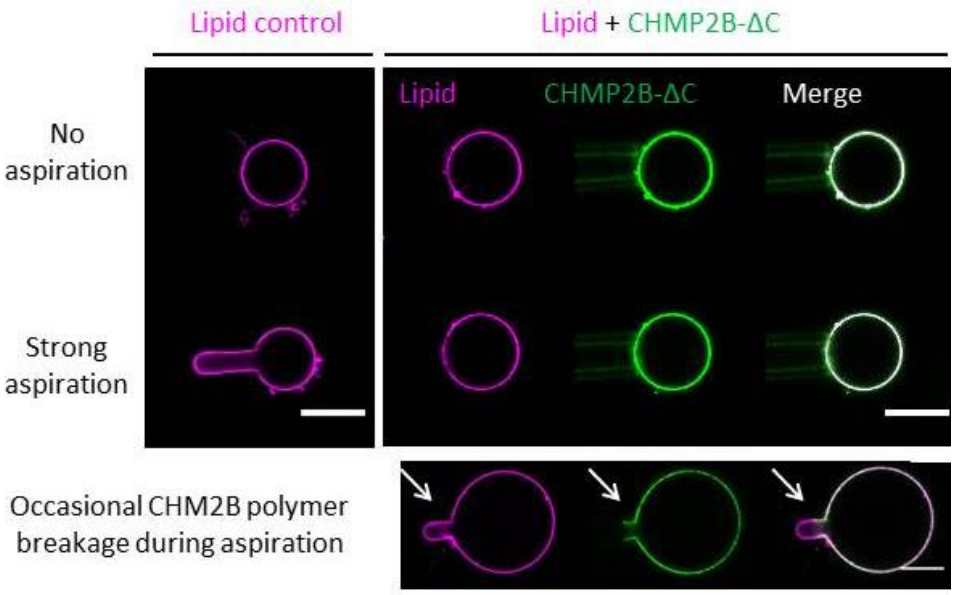

FIGURE 5-28: MEASUREMENT OF CHMP2B RIGIDITY BY MICROPIPETTE ASPIRATION TECHNIQUE
Representative confocal single-plane images of micropipette aspiration of a bare GUV containing PI(4,5)P_2-(left) and of a GUV coated with CHMP2B-ΔC (right). Strong aspiration was performed at σ averaging 10^{-3} N.m^{-1}. Bottom: Occasional rupture of CHMP2B polymer at high tension (σ ≈ 2.10^{-3} N.m^{-1}) is shown. The white arrow highlights the polymer breakage and tongue formation inside the pipette. Scale bar = 10 µm. n=30.

To conclude, our experiments suggest that CHMP2B can drastically modify the membrane elastic properties. CHMP2B polymer is strongly bound to the underlying membrane and forms a shell-like structure covering the vesicle that confers to the membrane a high stiffness and shape stability and resistance to osmotic shocks and external mechanical stresses.

5.2.3 STUDY OF CHMP2B MECHANICAL PROPERTIES BY AFM

To assess if the mechanical rigidity of CHMP2B polymer observed at the micrometer scale is a property conserved at nanometer scale, we measured the effect of CHMP2B polymer on the membrane elastic properties of SUVs by High-Speed Atomic Force Microscopy (HS-AFM) (see chapter 4.7.1).

This technique is usually used for direct visualization of dynamic structural changes and dynamic processes of functioning biological molecules in physiological solutions, at high spatio-temporal resolution. Dynamic molecular events unselectively appear in detail in an AFM movie, facilitating the understanding of how biological molecules operate. Here, the study of membrane mechanics was performed for the first time using HS-AFM technique by Dr. Sourav Maity in Prof. Dr. W. Roos's group.

Vesicle imaging by HS-AFM involves a very fast point by point tapping locally on the membrane surface. The advantage of the tapping mode is that the elastic modulus is independent of the vesicle size in contrast with the AFM classical indentation. Indeed, by HS-AFM very fast scanning, each pixel corresponds to a local membrane indentation and thus a high throughput measurement. To measure the membrane mechanics, the imaging set point is decreased leading to an increase of the damped amplitude and tapping force on the vesicle. As a result to this indentation, the vesicle surface deforms and its relative height decreases with the applied force (Figure 5-29/ A). By measuring the difference in vesicle height as a response to the local indentation, we thus measured the relative variation of the vesicle topology. The mechanical resistance to the local tapping on CHMP2B-free SUVs and CHMP2B-bound SUVs was characterized (Figure 5-30).

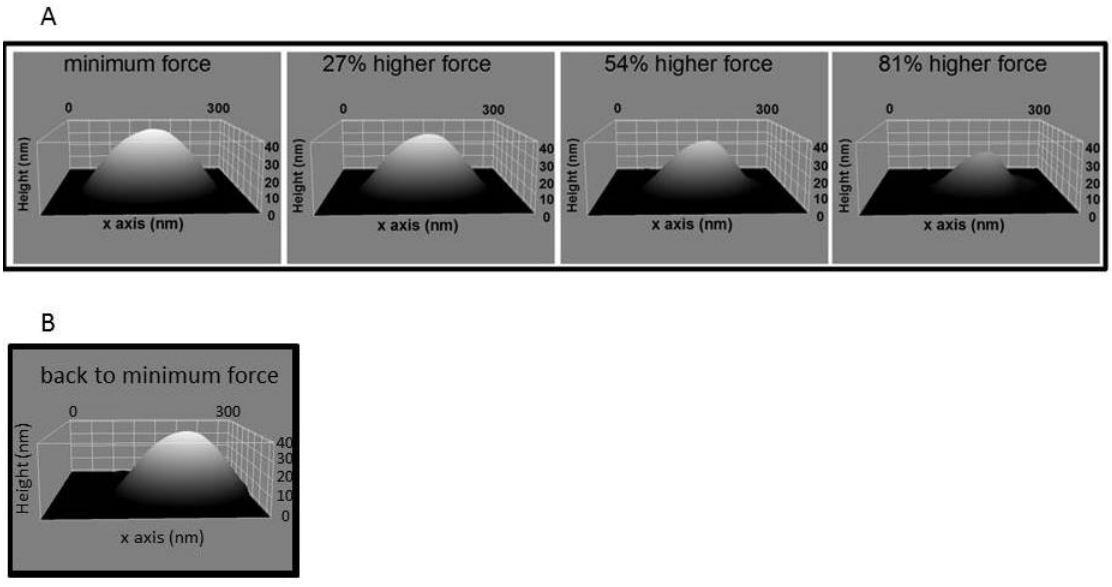

FIGURE 5-29: SUV DEFORMATION BY HS-AFM

Schematic illustration of the indentation experiment on a vesicle covered with CHMP2B protein by AFM.

(A) Surface features of indented vesicles. The different frames show vesicle deformability upon increased applied force. Vesicles height and width (in nm) are shown. The increased percentage of force represents the increased relative force during vesicle scanning. Imaging started at the minimum force required to acquire an image (around 100 pN) and was increased by maximum 81 % force (≈ 180 pN).

(B) Surface features of an indented vesicle after the applied force returns to the lowest force required for imaging (≈ 100 pN).

The size distribution of the vesicles in the chamber ranged from 20 nm to 100 nm. It was difficult to perform this experiment (image while increasing force) on larger vesicles due to their higher degree of thermal fluctuations, leading to a "parachute effect" or to loss of contact with the cantilever tip during the scan and thus limiting the maximum scan speed. We did not observe any significative effect of the presence of the protein on the vesicles' size. The only observed outcome was a slight remodelling of the surface with a heterogeneous-like aspect of the membrane surface when CHMP2B are bound (Figure 5-30 / B), in contrast to the smooth-like membrane aspect in the absence of proteins (Figure 5-30 / A). Imaging was initially acquired at the minimum required force to image considered as the lowest force (or the zero force increment) around 150 pN (Ruan, Miyagi et al. 2017). The force applied to the sample was minimized by adjusting the free amplitude to approximatively 10 Å and the imaging amplitude set point to almost 90 % (i.e., ≈ 9 Å) of the free amplitude. Then a higher force in roughly 1 Å increment of set point amplitude, per data point (≈10 % force increase per data point) was applied. The force increment was increased up to approximatively 81 % of the initial value (≈ 250 pN) and then decreased back to initial value (back to 0 % force increment). In both cases vesicles were deformed at first and then returned back to their original form with a height recovery superior to 80 %, indicating that the system behaves as an elastic system and that the measurement (vesicle pressing) was done within the elastic limit of the vesicles (Figure 5-29 / B). Therefore, we can apply General Hooke spring law as:

$$k_{\text{vesicle*}} = \frac{force\ increment}{relative\ height\ deformation} \tag{5-6}$$

Where, $k_{vesicle*}$ is the relative vesicle stiffness.

In line with the results obtained with micropipette aspiration experiments, we observed that vesicle deformability upon increased applied force is still reduced in the presence of CHMP2B polymer (Figure 5-30 / C). Figure 5-30 / D shows the variation of the mean relative deformation versus relative force increment for the control vesicles (without proteins, in red) and for the protein-covered vesicles (in blue), calculated from panel Figure 5-30 /C. The mean deformation is higher in the absence of proteins. We also calculated the slope of each curve (equal to $1/k_{\text{vesicle*}}$) in Figure 5-30 /C (both red and blue lines) and comparative histograms are plotted in Figure 5-30 / E. A Gaussian fitting to the histogram brings the relative stiffness of the vesicles without CHMP2B ($k_{vesicle*}$ ≈ 0.3 ± 0.04 A.U.) and covered with CHMP2B proteins($k_{vesicle + CHMP2B*}$ ≈ 0.89 ± 0.07 A.U.). Since, in amplitude modulation (AM) tapping mode AFM, the absolute calculation of applied force is difficult, we have investigated the relative stiffness rather than absolute values. Now, if $k_{vesicle*}$ ≈ 0.3 ± 0.04 A.U. and $k_{vesicle + CHMP2B*}$ ≈ 0.89 ± 0.07 a.u. then, $k_{vesicle + CHMP2B*}/ k_{vesicle*}$ = 0.89 ± 0.07 A.U. / 0.3 ± 0.04 A.U. implies, $k_{vesicle + CHMP2B*}$ ≈ 3 $k_{vesicle*}$. Therefore, we can conclude that the vesicles covered with CHMP2B proteins are approximately 3 times stiffer than

the vesicles without. And, this indicates that the mechanical rigidity of CHMP2B polymer observed at the mesoscale is a property conserved at the nanoscale.

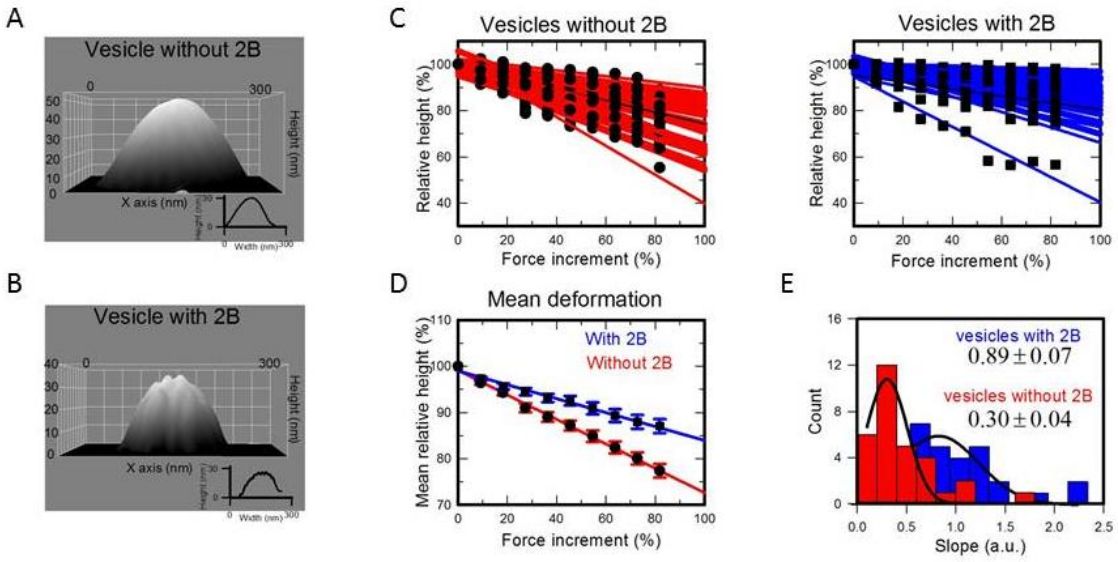

FIGURE 5-30: AFM DEFORMATION EXPERIMENT ON SUVS COVERED WITH CHMP2B PROTEINS
(A) AFM image of a vesicle without proteins, prior to deformation. Vesicles height and width (in nm) are shown.
(B) AFM image of a vesicle coated with CHMP2B proteins, prior to deformation. Vesicles height and width (in nm) are shown.
(C) Variation of the relative height of the bare vesicles (left, in red) and vesicles coated with CHMP2B (right, in blue) as a function of the force increment. 100% height corresponds to the initial height value without deformation, corresponding to 0 % force increment. n=31 for each condition.
(D) Variation of the mean relative height of the vesicles as a function of the force increment for vesicles in the absence and in the presence of CHMP2B proteins.
(E) Distribution of the slopes of the curves plotted in (C). The mean average values are given for both conditions
.

5.2.4 MOBILITY OF CHMP2B SUPRAMOLECULAR ASSEMBLY ON GUVS

We have shown that CHMP2B proteins assemble into networks on membranes that induce membrane stiffening. We next aimed at studying the dynamics of these CHMP2B networks and thus the mobility of the CHMP2B molecules. We thus performed FRAP experiments on vesicles covered with CHMP2B proteins. Figure 5-31 illustrates the experiment. A laser beam focused on a defined region of the vesicle (region of interest ROI) irreversibly destroys the fluorescence emission of the fluorescent molecules in this area (dark section in square in Figure 5-31 and in Figure 5-32 / A). If molecules diffuse in the membrane, or exchange with fluorescent molecules from the bulk, a subsequent recovery of fluorescence into the region should occur (Figure 5-31). Recording the changes in CHMP2B fluorescence intensity over time within the region yields measurements of the protein mobility (see chapter 4.3.3.1). The mobile protein fraction can be quantified by measuring the ratio between the fluorescence intensity variation at steady state after recovery in the ROI and the total photobleached sub-population by the following (equation 4-3 in chapter 4.3.3) (Reits and Neefjes 2001):

$$A = \frac{F_\infty - F_0}{F_I - F_0}$$

Where F_∞ is the fluorescence measured after recovery plateau is reached, F_0 is the fluorescence intensity measured just after photobleaching and F_i is the initial measured fluorescent intensity prior to photo-bleaching.

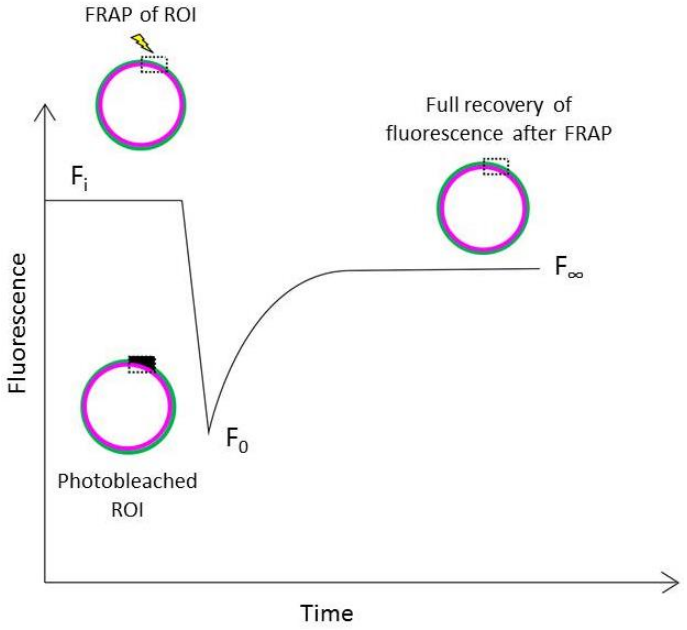

FIGURE 5-31: SCHEMA OF FRAP EXPERIMENT ON CHMP2B COVERED GUVS
A region of CHMP2B-covered GUV is defined (ROI). The fluorescence intensities of the ROI, before photo-bleaching F_i, after photo-bleaching F_0 and after recovery F_∞ are measured.

GUVs made of the lipid mixture 5 (10% DOPS 10% PI(4,5)P_2) were incubated with 500 nM CHMP2B-ΔC proteins for 15 to 30 min to obtain a full coverage of CHMP2B on the surface of the giant vesicles. Then, vesicles covered with CHMP2B proteins were transferred in the observation chamber with a 10 times dilution factor of CHMP2B protein concentration in bulk. Thus, no free CHMP2B protein monomers were present in the solution and fluorescence recovery could only be achieved by diffusion of the proteins already assembled on the GUV surface.

To follow the protein recovery on the bleached region of GUV surface, confocal images were taken before bleaching, after bleaching and during recovery (Figure 5-32 / A). To determine the fraction of recovery on the bleached area of the GUV over time we measured using Image J software, the mean fluorescence intensity in the defined ROI for each recovery images. The background I_B was subtracted. And, due to vesicle photobleaching during image acquisition, we normalized the FRAPed region of interest by the mean fluorescence intensity measured within a non-FRAPed region of the vesicle taken from the last image frame. The measured fraction of recovery over time is plotted in Figure 5-32 / B.

Approximately 4 minutes after photobleaching, we observed a very low protein signal recovery on the photobleached area (average fraction of recovery equal to 0.085 ± 0.05 at 250 sec after bleaching), indicating that once assembled, no exchange of monomers occurs on the membrane surface. It suggests that CHMP2B-ΔC assembles into a polymer network or scaffold that is not dynamic at this time (5 min.) and space (a few microns) scale. Furthermore, we obtained identical results in the presence of CHMP2B-FL proteins (average fraction of recovery below 0.1), confirming that CHMP2B-ΔC and CHMP2B-FL both form static scaffolds independently of the C-terminal truncation (Figure 5-32 / B).

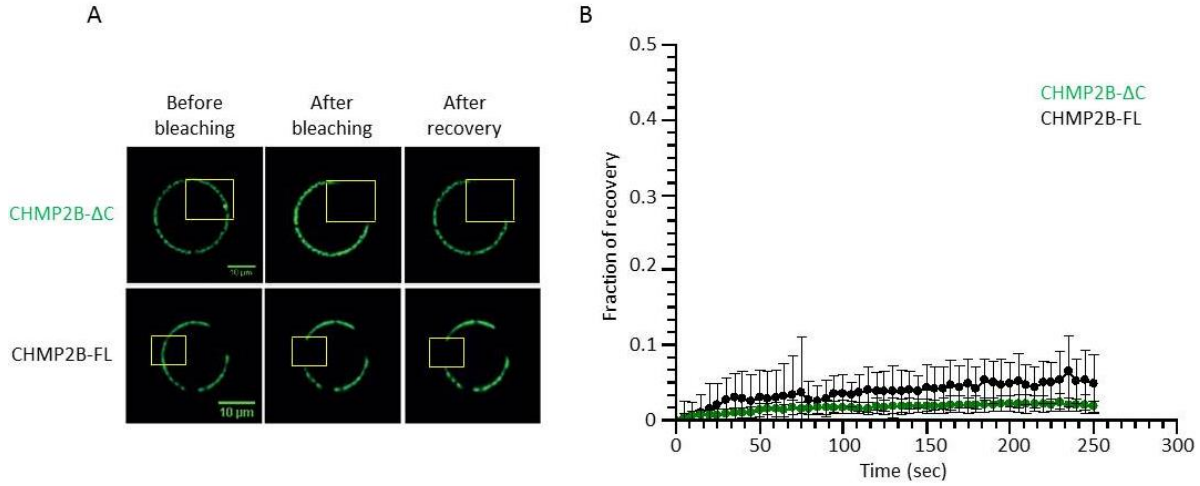

FIGURE 5-32: FRAP EXPERIMENT TO MEASURE THE DIFFUSION OF CHMP2B-ΔC AND CHMP2B-FL BOUND TO A GUV SURFACE

(A) CHMP2B proteins were photobleached and protein recovery was imaged over time. Yellow square represents the photobleached ROI. Scale bar = 10 µm.

(B) Mean recovery curves for CHMP2B proteins (truncated and full length) over time. The Error bars correspond to the standard deviation of the mean recovery. n=60.

5.2.5 DIFFUSION OF MEMBRANE-ASSOCIATED PROTEIN ON GUVS COVERED BY CHMP2B ASSEMBLIES

We then wondered if the rigid polymeric structure formed by CHMP2B proteins could also affect the lateral diffusion of transmembrane proteins or membrane-associated proteins, a property which might be of biological relevance. Indeed, we reasoned that if CHMP2B forms polymeric structures tightly bound to $PI(4,5)P_2$ lipids, it might form a barrier for membrane-bound proteins that protrude from the membrane surface. As a model system, we used the streptavidin coupled to biotinylated lipids system. Streptavidin is a 52.8 kDa non-glycosylated protein that is isolated from bacteria and has a near-neutral isoelectric point. It has a very large affinity for biotin (vitamin B_7) The streptavidin molecule is about 2-3 nm high (Yamamoto, Nagura et al. 2009) and has an approximate volume of approximately 105 nm^3 (Lee, Cho et al. 2009). The small size of streptavidin similar to that of membrane associated proteins makes it a good candidate to study the effect of the presence of CHMP2B on the dynamics of transmembrane or membrane associated proteins. Practically, GUVs containing biotinylated lipids and

fully covered with 500 nM CHMP2B proteins were incubated with 500 nM red-labelled fluorescent streptavidin for 30 min and streptavidin (coupled to biotinylated lipids) dynamics was measured by FRAP (Figure 5-33).

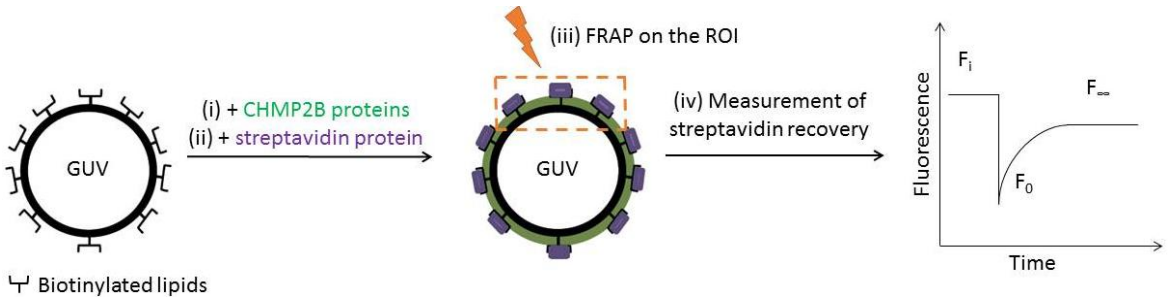

FIGURE 5-33: STREPTAVIDIN DIFFUSION EXPERIMENTS BY FRAP
Schematic representation of the measurement of streptavidin diffusion on GUVs covered with CHMP2B-ΔC proteins.

The lipid mixture used for this set of experiments is the lipid mixture 5 including 10% $PI(4,5)P_2$ complemented with 0.1% DSPE-PEG-2000-Biotin. No PE-Rhodamine fluorescent lipid dye was present in the lipid mixture to measure the recovery of streptavidin only. Vesicles were grown in a buffer containing 50 mM Sucrose, 25 mM NaCl and 25 mM Tris at pH 7.5. Next, the vesicles were transferred to BP buffer with 500 nM CHMP2B (Alexa Fluor 488) for 30 min incubation. Half of the CHMP2B-vesicles were then transferred to BP buffer containing 500 nM red-labelled streptavidin (Alexa Fluor 561) and the other half to BP buffer without any diluted protein (control sample) for 30 min to reach full protein coverage.

We performed FRAP on Alexa 561-labelled streptavidin bound to biotinylated lipids on the surface of GUVs. In the absence of CHMP2B, we observed a fast diffusion and recovery of the streptavidin molecules leading to full recovery of the streptavidin fluorescence signal on the membrane of the bleached ROI (Figure 5-34 / A upper panel). Indeed, in Figure 5-34 / B – magenta curve, more than 60 % of the streptavidin (coupled to biotinylated lipids) fluorescence signal was recovered in less than 20 sec (fraction of recovery ≈ 0.64 ± 0.18 at 20 sec) and we measured full recovery in less than a min after bleaching (fraction of recovery about 0.87 ± 0.25 only 50 sec). The diffusion coefficient could not be calculated due to ROI geometry. Indeed, we did not bleach an almost flat area of the GUV (top or bottom), but an area around the equatorial plan; the area of the ROI was thus not well defined.

In strong contrast, in the presence of CHMP2B-ΔC polymer, we did not observe any recovery of the streptavidin fluorescence signal in the bleached ROI (Figure 5-34 / A lower panel). The fraction of streptavidin (coupled to biotinylated lipids) recovery after photobleaching as a function of time remained constant and very weak (fraction of recovery about 0.07 ± 0.06 at 270 sec) (Figure 5-34 / B – green curve), indicating that the diffusion of streptavidin is almost completely blocked when GUVs are covered with CHMP2B proteins.

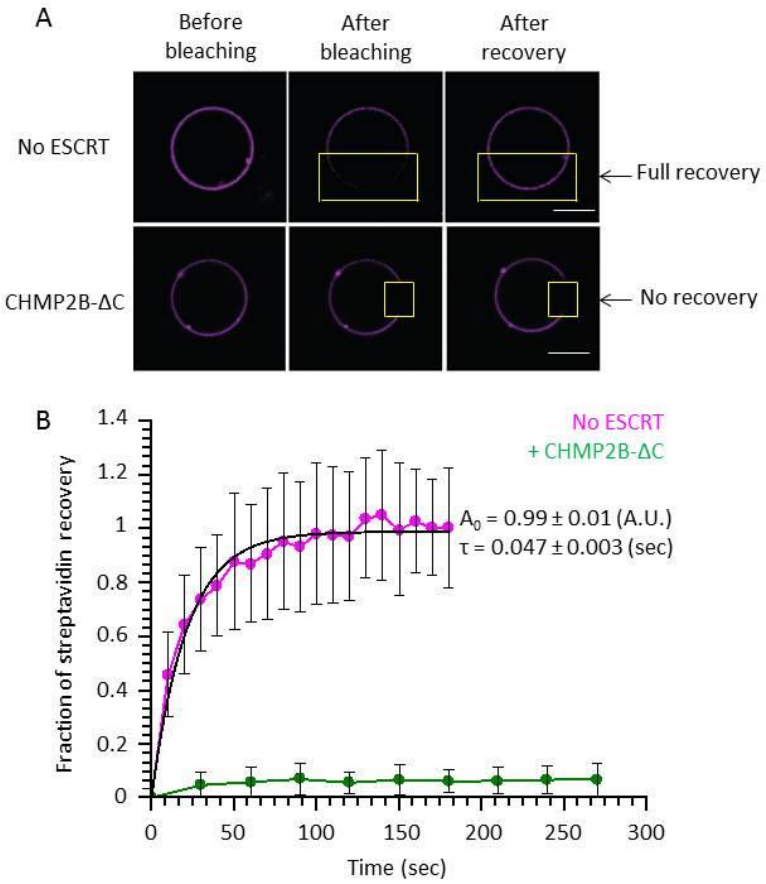

FIGURE 5-34: MOBILITY OF STREPTAVIDIN BOUND TO GUVS COVERED WITH CHMP2B

(A) Pre-formed vesicles with biotinylated lipids were incubated with CHMP2B-ΔC and streptavidin proteins. The ROI is highlighted by the yellow square. Scale bar = 10 µm.

(B) Fraction of streptavidin recovery after photobleaching as a function of time for vesicles with bound CHMP2B proteins (green curve). A control experiment is performed in the absence of CHMP2B-ΔC (magenta curve). Error bars correspond to the standard deviation of the recovery. n = 20.

In these experiments, vesicles were incubated with CHMP2B proteins long enough to reach full coverage of the protein on the GUV surface. Next, we wondered if the observed diffusion barrier could be due to this full coverage of CHMP2B and if the recovery of streptavidin fluorescence would be modified and / or fostered with partial coverage of the protein on the vesicle surface.

To answer this question, streptavidin recovery had to be measured on vesicles partially covered with CHMP2B proteins, i.e. with vesicles wrapped-up with CHMP2B reticulum as described in Figure 5-21. Therefore, we repeated the same experiment but decreased the protein-lipid incubation time to 15 min. Again, upon photo bleaching, we did not observe any recovery of the fluorescence signal of the red-labelled streptavidin showing that the protein diffusion was blocked. However, remarkably, maintained/prolonged bleaching during image acquisition generated a decrease in fluorescence intensity beyond the bleached area, but in a localized zone with non-regular contours (Figure 5-35).

Normally, in the case of diffusing molecules, a prolonged bleaching on the ROI would first induce the loss of the fluorescence of the area nearby, in a homogeneous and regular manner. Then, if bleaching

continues, all the diffusing particles on the surface will be bleached and a general loss of fluorescence should be observed. In our case, upon continuous bleaching of a small ROI (see yellow square in Figure 5-35 / A) we also observed a loss of streptavidin fluorescence in a region larger than the ROI, very irregular and more or less limited by the polymer "reticulum" (see green irregular shape in Figure 5-35 / B). As a consequence, we propose that the streptavidin molecules bound to the biotinylated lipids are only able to diffuse within the region delimited by CHMP2B protein network, which is able to confine the molecules. Thus, the restriction of streptavidin diffusion can also occur when the CHMP2B does not cover membrane in a dense manner. Our experiments suggest that CHMP2B networks probably partition the membrane in discrete patches and strongly limit streptavidin diffusion between patches. In conclusion, CHMP2B strongly restricts the diffusion of membrane-associated proteins, thus acting as a diffusion barrier. Thus, lack of streptavidin diffusion is not due to a high density of CHMP2B protein at the membrane. Indeed, CHMP2B reticulum probably prevents streptavidin diffusion and partition the membrane in discrete patches. In conclusion, CHMP2B blocks the diffusion of membrane-associated proteins, thus acting as a diffusion barrier.

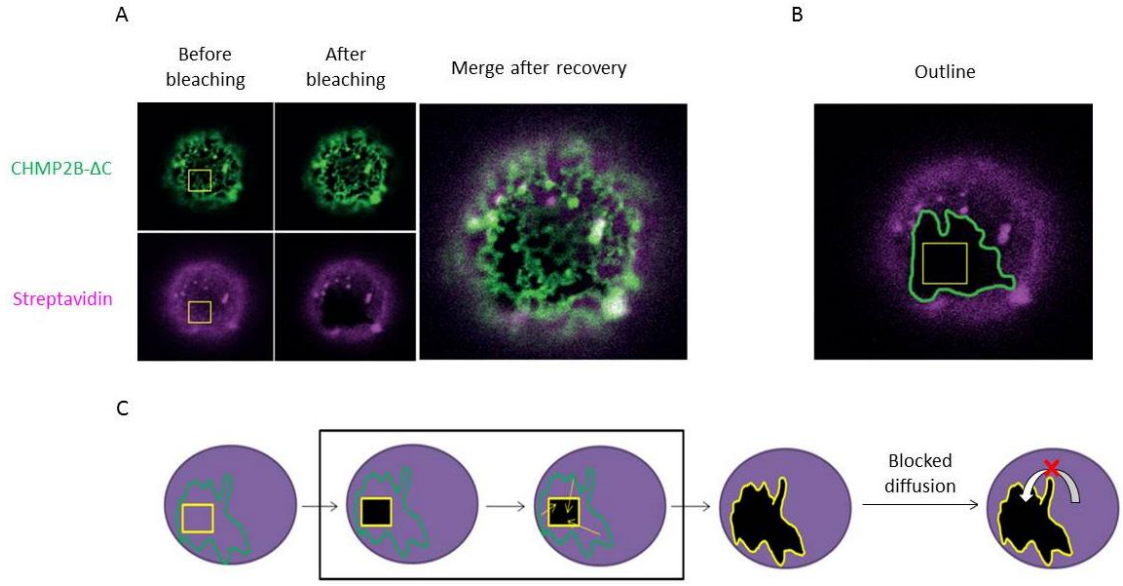

FIGURE 5-35: FLUORESCENCE LOSS OF STREPTAVIDIN UPON CONTINUOUS BLEACHING
(A) Streptavidin recovery after prolonged photobleaching on biotinylated-GUVs with CHMP2B-ΔC reticulum.
(B) Outline of the streptavidin fluorescence loss after continuous photobleaching. The yellow square indicates the photobleached region and green outline indicates the streptavidin diffusion limited by CHMP2B-ΔC reticulum barrier.
(C) Schematic illustration of streptavidin diffusion and fluorescence loss during prolonged bleaching. The streptavidin diffusion is delimited by CHMP2B protein network.

All these sets of experiments allowed us determining the characteristics of CHMP2B interaction with lipids. CHMP2B binds irreversibly and specifically to PI(4,5)P_2 lipids, clusters them and forms a network all over the vesicle surface. CHMP2B polymer is not dynamic and behaves as a diffusion barrier for membrane components. Finally, CHMP2B polymer can induce a degree of rigidity to the underneath membrane preserving it from external stress and preventing membrane deformation.

These results are very striking, since CHMP2B is part of the ESCRT-III complex that remodels membranes up to fission. We next compare these characteristics with those of CHMP2A proteins. CHMP2A protein is the closest homologous to CHMP2B protein in terms of sequence similarity. Therefore, we repeated the same sets of experiments to compare CHMP2A and CHMP2B proteins on model membranes.

5.3 CHMP2A AND CHMP2B DISPLAY OPPOSITE PROPERTIES ON MODEL MEMBRANES

As detailed in Chapter 3, the hypothesis for the minimal membrane scission machinery is that CHMP4B recruits either CHMP2A or B, or CHMP3 together with CHMP2A (Adell and Teis 2011; Adell, Migliano et al. 2016). CHMP2A and CHMP2B are both considered as Vps2 human homologs. Both CHMP2A and CHMP2B can bind CHMP4B through basic residues (Morita, Sandrin et al. 2011). Yet, even though presenting sequence similarity, CHMP2B lacks a MIM domain that is required to bind Vps4 MIT domain. To investigate the functional homology of CHMP2A and CHMP2B in the ESCRT machinery, we first studied their effect on the elastic properties of model membranes.

5.3.1 STUDY OF CHMP2A PROTEIN INTERACTION ON MODEL MEMBRANE

To compare the assembly of CHMP2A proteins with that of CHMP2B proteins on model membranes, we first tested the binding of CHMP2A on supported lipid bilayers (SLBs) and next the interaction on the surface of giant unilamellar vesicles (GUVs). For the first approach using SLBs, CHMP2A protein interaction with different lipid compositions was measured with the QCM-D technique (previously described in chapter 4.6.1). For the second approach, FACS was used to measure the affinity of CHMP2A proteins towards GUVs containing the different PIPs species (PI(3)P, PI(3,5)P_2, PI(4)P and PI(4,5)P_2). Eventually, SD microscopy was used to study the assembly of CHMP2A proteins on the surface of GUVs. The aim of these two different approaches is to (i) confirm by QCM-D that CHMP2A also has higher affinity to the membrane when additional negatively charged lipids are added, (ii) check by FACS microscopy on GUVs that equivalently to CHMP2B proteins, CHMP2A displays specific binding to PI(4,5)P_2 and (iii) find out by SD microscopy if CHMP2A assembles similarly to CHMP2B on the surface of GUVs by forming a reticulum-like structure.

For all the GUV sets of experiments, CHMP2A proteins were labelled with Alexa Fluor™ 488 and the different lipid mixtures contained PE lipids fluorescently tagged with Rhodamine.

5.3.1.1 STUDY OF CHMP2A PROTEIN INTERACTION ON SLB

We used Quartz Crystal Microbalance experiments with Dissipation monitoring (QCM-D) to study and compare the interaction of CHMP2A and CHMP2B proteins on supported lipid bilayers (SLBs) made of different lipid compositions. After formation of the SLB, CHMP2A-FL proteins were injected in a

continuous flow at a concentration of 200 nM in BP buffer until observation of a characteristic plateau indicating that protein saturation on the different lipid bilayers (lipid mixtures 1 to 4) is reached. Similarly to CHMP2B, CHMP2A proteins show a higher affinity towards the membrane when the percentage of negatively charged DOPS lipids is increased from 30 % (light grey bar) to 40 % (dark grey bar) (Figure 5-36 / A). Also, for equal amount of negative charges in the membrane, CHMP2A proteins show a preferential binding towards supported lipid bilayers containing PI(4,5)P_2 lipids (blue bar) with almost 2-fold increase in the adsorbed amount of proteins, as compared to the binding to a 40% DOPS-containing SLB. Both CHMP2A and CHMP2B reach saturation on PI(4,5)P_2- containing bilayers with an equal final amount of adsorbed proteins ($\Delta\vartheta_2 \approx 50$ Hz for both CHMP2A and CHMP2B proteins on PI(4,5)P2 SLB meaning that the adsorbed mass is equivalent) (Figure 5-36 / A). We then quantified the characteristic time (see chapter 4.6.2) of interaction of CHMP2A and CHMP2B proteins with the different lipid mixtures (Figure 5-36 / B). For all tested lipid compositions, we found that CHMP2A has a slower interaction rate as compared to CHMP2B proteins. For instance, the characteristic time of CHMP2B proteins with a PI(4,5)P_2-SLB (blue bar) averages to 50 sec, whereas it is larger than 120 sec for CHMP2A proteins (Figure 5-36 / B).

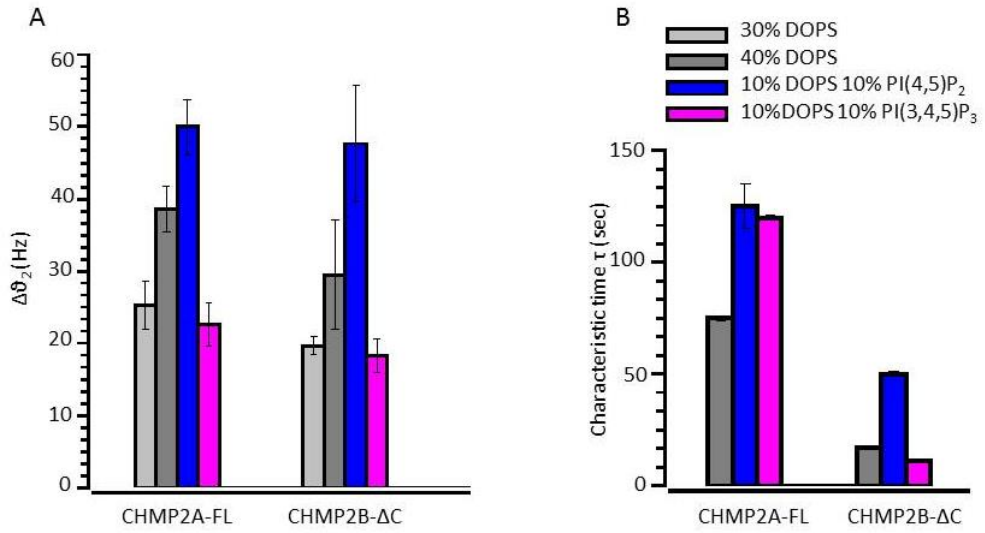

FIGURE 5-36: COMPARISON OF THE AFFINITY OF CHMP2A AND CHMP2B PROTEINS FOR DIFFERENT SLBS WITH QCM-D

(A) Variation of the frequency shift $\Delta\vartheta_2$ for CHMP2A-FL and CHMP2B-ΔC as a function of the lipid compositions (Light grey: 30% DOPS; Grey: 40% DOPS; Blue: 10% PI(4,5)P_2; Magenta: 10% PI(3,4,5)P_3). n = 5.

(B) Characteristic time of interaction measured for CHMP2A-FL and CHMP2B-ΔC for various lipid compositions (Grey: 40% PS; Blue: PI(4,5)P_2; Magenta: PI(3,4,5)P_3). n = 5.

Apart from measuring the frequency shift $\Delta\vartheta_2$, the QCM-D technique also enables us to measure the dissipation shift ΔD, defined as the fraction of the total energy stored in the oscillator that is dissipated during one oscillation cycle. It provides information about the viscoelastic and structural properties of the mass coupled to the oscillator by the equation 4-16 in chapter 4.1 :

$$\Delta D = \frac{1}{Q} = \frac{1}{2\pi}\frac{Edissipated}{Estored}$$

Where *Q* is the quality factor, *Estored* and *Edissipated* are respectively the energy stored and lost during one period of oscillation.

We measured the dissipation shifts ΔD as a function of time after addition of CHMP2A and CHMP2B proteins respectively. A decrease in the value of the dissipation shift ΔD corresponds to a stiffer film in the presence of the protein whereas an increase in ΔD value indicates a soft film. Table 2 sums up ΔD values for CHMP2A and CHMP2B proteins as a function of the different SLB lipid compositions. For all lipid mixtures, dissipation shift values are always higher by almost a factor 2 in the presence of CHMP2A proteins as compared to CHMP2B, which implies that the overall structure is looser in this case. For PI(4,5)P_2– SLBs, at protein saturation, CHMP2A proteins have a dissipation value of 3,2 ± 0.3 (10^{-6} A.U.) against 1,5 ± 0.1 (10^{-6} A.U.) for CHMP2B proteins (Table 2; Figure 5-37 / A).

However, to precisely characterize the different adsorption behaviors, one must plot the dissipation as a function of the frequency shift. The slope of the dissipation shift versus the frequency shift graph characterizes the viscoelastic property of the surface (Höök, Rodahl et al. 1998), a higher slope being the signature of a loose structure with more viscous properties whereas a lower slope characterizes a more rigid structure. For CHMP2B proteins, the dissipation shift versus the frequency shift curve is linear with a slope equal to 0.038 ± 0.005 $.10^6$ Hz^{-1}. This very low value is the signature of a rigid structure on the QCM-D sensor, possibly due to a strong adsorption of the proteins lying flat on the lipid bilayer (Figure 5-37 / B). This is very different for CHMP2, where at least 2 regimes are visible: linear for the low frequencies and a plateau at high frequencies, indicating at least two different kinetic processes during adsorption. For the low frequency shift, the slope of the curve of CHMP2A bound to PI(4,5)P_2-SLB is equal to 2.8 10^{-7} Hz^{-1} which is close to the reported value of 2×10^{-7} Hz^{-1} for BSA (Bovine Serum Albumine) bound to citrate-coated surface (Brewer, Glomm et al. 2005) and where the adsorbed layer is supposed to have viscoelastic properties (Figure 5-37 / B). Consequently, during the first stage of the kinetic process in the presence of CHMP2A proteins, the membrane overall structure is not stiff in contrast with what is observed with CHMP2B proteins.

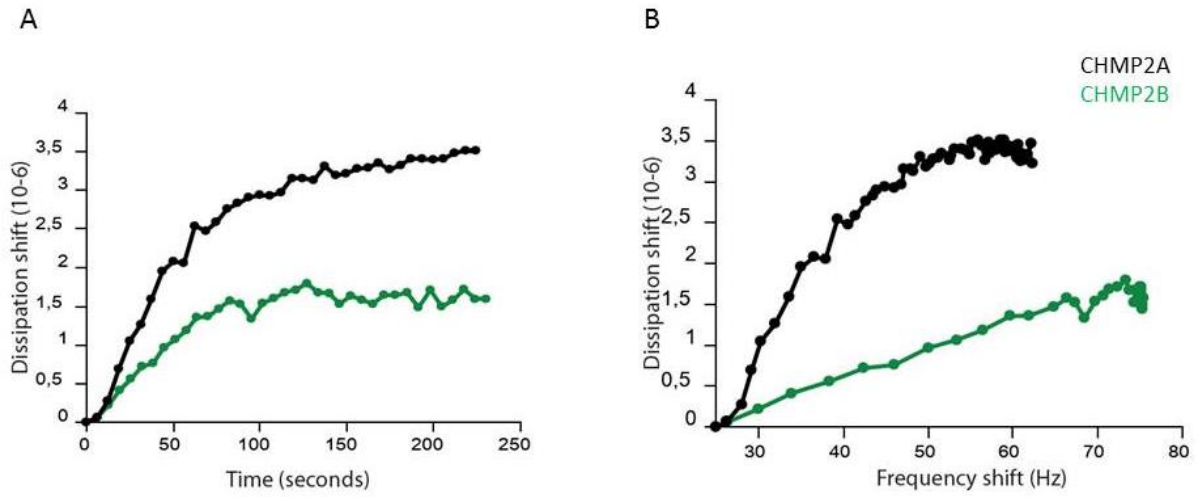

FIGURE 5-37: VISCO-ELASTICITY OF CHMP2 PROTEINS (2A AND 2B) ON A PI(4,5)P2-CONTAINING SLB BY QCM-D
(A) Variation of the dissipation shift ΔD as a function of time for CHMP2A (black curve) and CHMP2B (green curve) proteins. n=5.
(B) Variation of the dissipation shift ΔD as a function of the frequency shift for CHMP2A proteins (black curve) and CHMP2B proteins (green curve). n=5.

TABLE 2: DISSIPATION VALUES FOR CHMP2 PROTEINS IN PRESENCE OF DIFFERENT NEGATIVELY CHARGED SLBS

Dissipation shift (10^{-6})	30% DOPS, 70% DOPC	40% DOPS, 60% DOPC	10% DOPS, 10%PI(4,5)P2, 80% DOPC	10% DOPS, 10%PI(3,4,5)P3, 80% DOPC
CHMP2A-FL	1,8 ± 0.1	2,7 ± 0.3	3,2 ± 0.3	1,8 ± 0.1
CHMP2B-ΔC	1,9 ± 0.1	1,21 ± 0.06	1,5 ± 0.1	0,90 ± 0.04

As a conclusion, we found that CHMP2A and CHMP2B proteins bind similarly the different tested SLBs. However, CHMP2A has a slower rate of interaction with the membrane and a softer overall structure in contrast with the stiff SLB structure observed in the presence of CHMP2B proteins.

5.3.1.2 CHMP2A AND CHMP2B PROTEINS HAVE A DIFFERENT BINDING AFFINITY FOR PI(4,5)P_2-GUVS

In order to compare the two proteins affinity for the different PIP species, we investigated the interaction of CHMP2A with GUVs containing different PIPs.

We have incubated GUVs made of the lipid mixture 5 with 500 nM MBP-CHMP2A-ΔC or CHMP2A-FL proteins in BP for 60 min. Surprisingly, we found that with the truncated version of CHMP2A (supposedly the active form), almost no binding on GUVs is observed (Figure 5-38 / A upper panel and C). Also, no binding at all was observed with CHMP2A-FL. The difference of affinity with our above results on supported lipid bilayers with QCM-D with theoretically the same membrane composition could be due to variations in the membrane preparation. In the SLB experiments, due to the preparation method

(SUVs fused on the substrate), charged lipids are 100 % incorporated in the bilayer, while this is not the case for electroformed GUVs. Indeed, we observed with CHMP2B- ΔC that saturation on the membrane is reached at 200 nM protein concentration in a short period of time on SLBs, whereas with GUVs, saturation was never reached even at high protein concentration (4 µM) and longer incubation time (Figure 5-7). Consequently, protein binding is limited in GUVs by the reduced fraction of charged lipids in the bilayer. We therefore decided to consider separately these two different techniques for our study although the overall obtained results remain complementary. Moreover, the decrease of affinity of CHMP2A-ΔC to the GUV membrane in comparison with CHMP2B-ΔC, could also be enhanced by the fact that the protein sequence is supplemented with an MBP Tag at the N-terminus. Cleavage of the MBP-Tag is not possible as it is prevents aggregation of CHMP2A-ΔC protein and stabilizes it. So, perhaps because of the presence of the Tag, the N-terminus is no longer accessible and by that protein polymerization and interaction with the membrane by insertion of its N-terminal is not possible (see chapter 3.3) (Buchkovich, Henne et al. 2013). However, it has been shown that the combination of CHMP2A-ΔC and CHMP3-FL co-polymerize to form tubes with dome-like structure in the absence of membrane (Lata, Schoehn et al. 2008), but no polymerization occurs for both proteins independently. This suggests that these proteins have a strong mutual affinity. Thus, we decided to add CHMP3-FL to MBP-CHMP2A-ΔC and study the affinity for the membrane of the complex CHMP2A-CHMP3.

We prepared GUVs using the lipid mixture 5 (10% DOPS, 10% PI(4,5)P_2) and then transferred them to a solution made of BP buffer and 500 nM CHMP2A-ΔC + 2 µM CHMP3-FL for 60 min before image acquisition. We found that CHMP2A proteins strongly bind GUVs in the presence of CHMP3 proteins (Figure 5-38 / A lower panel). The quantification of the fluorescence intensity of CHMP2A proteins on GUVs by confocal microscopy shows that the affinity of CHMP2A to the membrane is increased by a factor of at least 2.5 in the presence of CHMP3. FACS measurements confirm this observation (Figure 5-38). Moreover, with this technic that involves a flow, no binding of CHMP2A-ΔC is detected on the GUVs when alone in solution. When CHMP3-FL is incubated in the absence of CHMP2A-ΔC, a very weak signal is detected with FACS, but as previously observed for CHMP2A-ΔC, binding boosting by a factor of about 7 fold occurs when the other component (CHMP2A-ΔC) is present (Figure 5-38 / B and C). Therefore, it seems that CHMP2A and CHMP3 mutually enhance each other's binding to the membrane in a sort of "positive feedback loop", which is consistent with functional data *in vivo* showing their functional cooperative effect (Morita, Sandrin et al. 2011).

In addition, to check if CHMP2A + CHMP3 have a preferential binding to one of the PI derivatives, we repeated the FACS experiments with the different PIPs. GUVs made of the lipid compositions 6 to 8 were co-incubated with 500 nM CHMP2A-ΔC + 2 µM CHMP3-FL for 60 min before FACS acquisition. We observed no preferential affinity to a particular specie of PIP derivates, such as for CHMP2B towards PI(4,5)P_2 lipids (Figure 5-38 / D grey data). Eventually, by SD confocal microscopy we observed the

assembly of CHMP2A + CHMP3 copolymers on GUVs' surface. No reticulum-like structure was observed, in contrast to CHMP2B proteins. However structures protruding from the GUV surface are present (Figure 5-38 / E, and zoom-in). These structures contain CHMP2A-ΔC, indicating that they might correspond to the tubular polymers previously reported (Lata, Schoehn et al. 2008). Lipids fluorescence signal is also detected in some of the protruding structures, showing that these protrusions contain both proteins and lipids, yet the lipids intensity signal is considerably lower to that of CHMP2A-ΔC proteins (Figure 5-38 / E). It might indicate that CHMP2A + CHMP3 are able to induce very thin membrane tubules at the surface of the GUVs (thus, the low lipid signal) when assemble into polymers. Nevertheless, these tubules are much shorter that those observed at high density in the presence of BAR-domain proteins (Sorre, Callan-Jones et al. 2012; Shi and Baumgart 2015).

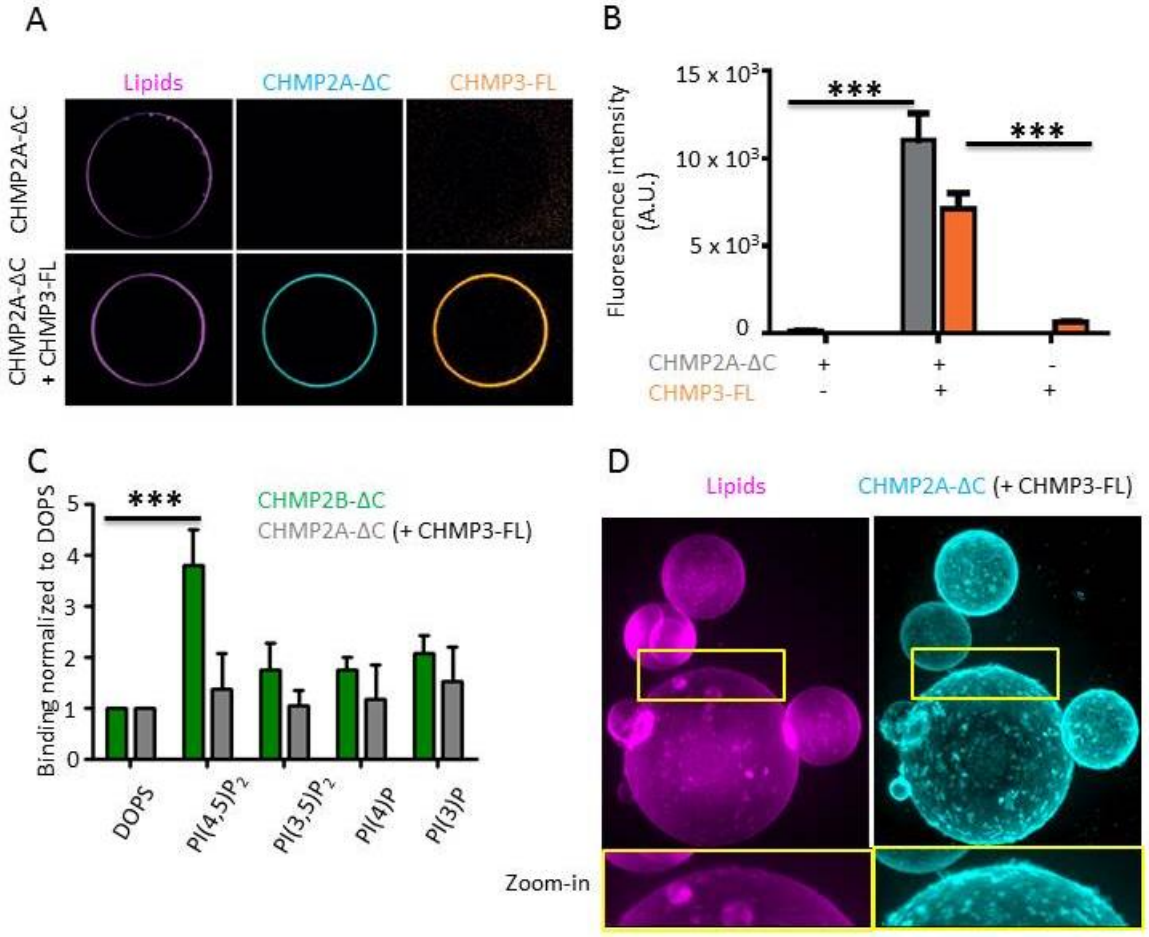

FIGURE 5-38: CHMP2A + CHMP3 SUPRAMOLECULAR ASSEMBLY ON THE SURFACE OF GUVS

(A) Binding of MBP-CHMP2A-ΔC + CHMP3 to GUVs containing PI(4,5)P_2. A single confocal plane is shown.

(B) MBP-CHMP2A-ΔC and CHMP3 binding to GUVs containing PI(4,5)P_2 by flow cytometry. ***=p-value<0.001 (Student's t-test); n=4 (number of FACS experiment with 10^4 counted event per experiment, per condition).

(C) Comparison of the binding of MBP-CHMP2A-ΔC + CHMP3-FL co-polymer to the different PIP species with that of CHMP2B-ΔC measured by flow cytometry. The values are normalized to binding to DOPS. n=4 (number of FACS experiment with 10^4 counted event per experiment, per condition).

(D) Supramolecular assembly of MBP-CHMP2A-ΔC + CHMP3-FL co-polymer (here, only CHMP2A-ΔC is fluorescent) on GUVs containing PI(4,5)P_2 lipids. A z-projection is shown including a zoom-in in the right panel, showing short protrusions at the surface of the GUV.

To further compare the mode of polymerization of CHMP2A (+CHMP3) proteins with that of CHMP2B proteins, we worked at a high spatial resolution, using Cryo-EM. CHMP2A-ΔC and CHMP3-FL proteins were added respectively at a concentration of 500 nM and 2 µM to pre-formed LUVs (see chapter 4.2.4) made of the lipid mixture 5 in the protein binding buffer BP (50 mM NaCl, 25 mM Tris at pH 7.5) and kept at room temperature during 60 min. With our LUV preparation and after resuspension of the dried lipids (see chapter 4.2.4), we usually obtain a combination of vesicles with some irregular tubular membranes (with an average diameter of 30 nm).

In the absence of proteins, both vesicles and tubes display a smooth contour with a clearly visible bilayer (Figure 5-39 / A, see red arrow). In the presence of CHMP2A + CHMP3 proteins regular protein spirals can be seen around membrane tubules (Figure 5-39 / A, see blue arrow). In addition, we also observe a hairy-like structure at the edge of the vesicles (Figure 5-39 / B see blue square). Moreover, the bilayer of vesicles and tubes becomes blurry (see Figure 5-39 / C). These different features confirm that CHMP2A + CHMP3 proteins are bound to membranes. The "hairy membrane" aspect can indicate that CHMP2A + CHMP3 proteins assemble into short continuous filaments (with a diameter of approximately 10 nm) on the pre-formed vesicles. However, we did not observe any vesicle deformation or change in the tube morphology due to CHMP2A + CHMP3 assembly (Figure 5-39).

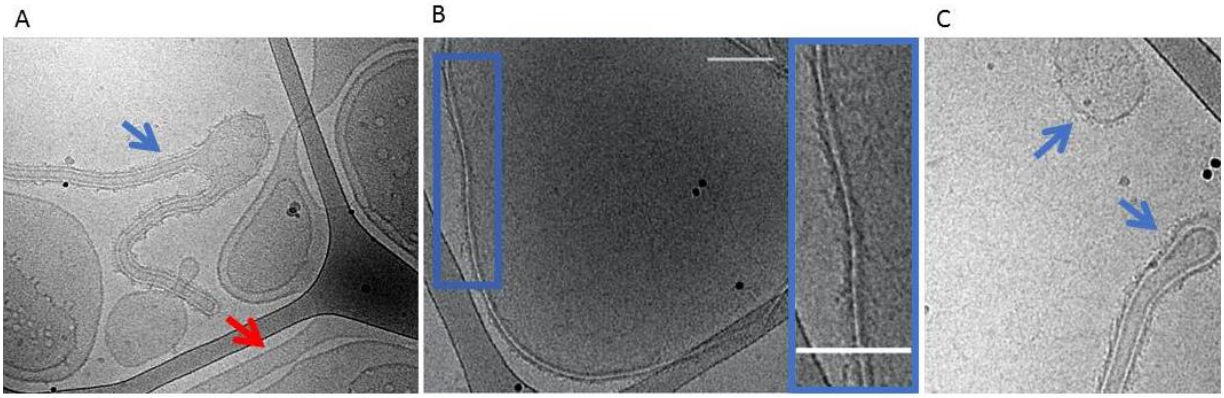

FIGURE 5-39: ASSEMBLY OF CHMP2A + CHMP3 ON MEMBRANES IMAGED BY CRYO-EM
(A) Assembly of CHMP2A-ΔC + CHMP3-FL on tubular membranes. A spiral is visible around the tube (blue arrow). A bilayer without proteins is highlighted by the red arrow.
(B) Image of a hairy structure at the edge of a flattened vesicle. Blue rectangle: zoom-in of CHMP2A-ΔC + CHMP3-FL polymer assembling perpendicularly to the membrane axis. Scale bar = 100 nm.
(C) Image of a small vesicle and a tube with blurry bilayers (blue arrows) indicating the assembly of CHMP2A-ΔC + CHMP3-FL co-polymer.

To summarize, CHMP2A and CHMP2B display differences in terms of protein-protein interaction and interaction with PIPs. First, CHMP2A requires the presence of CHMP3 proteins to strongly bind the membrane in contrast with CHMP2B that has a strong binding alone. Secondly, CHMP2A + CHMP3 do not have any exclusive preferential interaction to a PI derivatives such as CHMP2B towards PI(4,5)P_2 lipids. Next, the supramolecular assemblies of CHMP2A + CHMP3 and CHMP2B on PI(4,5)P_2-GUVs are very different since a reticulum-like structure is observed with CHMP2B only. Finally, at the nanoscopic

scale, CHMP2B and CHMP2A+CHMP3 also organize differently. While CHMP2B forms rings that assemble in a honeycomb-like pattern on membranes, CHMP2A + CHMP3 form short filaments. These filaments could correspond to those observed in previous in vitro studies in the absence of membranes (Lata, Schoehn et al. 2008; Effantin, Dordor et al. 2013). No purely *in vitro* data exist for CHMP2B to be compared with, besides the formation of very rigid tubes in cells when it is overexpressed (Bodon, Chassefeyre et al. 2011). Analysis with Cryo-EM of tubes pelleted from these cells revealed a very characteristic striation pattern with circular structures related to CHMP2B regularly aligned perpendicular to the tube axis at 3.2 nm and tube diameters ranging between 16 to 80 nm. The authors proposed that CHMP2B organized into a helical structure with a regular pitch but a variable diameter. Considering the dimensions of CHMP2B rings obtained with AFM and Cryo-EM (1.5 nm thick and about 16 nm wide), we could also propose that the striations correspond to stacks of CHMP2B rings in the narrowest regions, but with variations that could be due to the interaction with other CHMP proteins, such as CHMP4. In addition, we could not detect CHMP2B on tubes, but we observed the formation of spiral structures with CHMP2A + CHMP3 around straight tubular membranes, different from the spiraled tubes previously described in (Effantin, Dordor et al. 2013). In conclusion, CHMP2B and CHMP2A+CHMP3 exhibit contrasting properties in terms of protein-lipid affinity and protein-protein interaction, as well as supramolecular organization at the mesoscale and at the nanoscale.

5.3.2 CHMP2A AND CHMP2B PROTEINS DISPLAY OPPOSITE MECHANICAL PROPERTIES ON MEMBRANE

Because CHMP2A+CHMP3 and CHMP2B appear to assemble differently on membranes, we next compared the consequence of their binding on the mechanical properties of membranes. We thus repeated the micropipette aspiration assay on GUVs in the presence of CHMP2A + CHMP3 proteins.
We prepared PI(4,5)P2-vesicles made of lipid mixture 5 and co-incubated them with CHMP2A-ΔC + CHMP3-FL proteins in BP at a concentration of respectively 500 nM and 2 µM for 60 min. Interestingly vesicles were easily deformed during aspiration, in contrast to CHMP2B. In Figure 5-40 / A, we can observe an increase of the tongue length inside the micropipette as a response to the tension increase. And after release of aspiration, the vesicle returned back to a spherical shape (Figure 5-40 / A). This variation of the tongue length in the presence of CHMP2A + CHMP3 proteins translates into a change of the vesicle surface before and after aspiration and indicates that the protein-lipid structure is elastic, in contrast with CHMP2B protein-lipid very stiff structure.

In Figure 5-40 / B, the variation of the area Δα in function of the applied tension on the membrane is plotted. Unlike CHMP2B, the membrane elastic properties are very moderately perturbed when CHMP2A + CHMP3 proteins are bound to the GUV surface. The values of the variation of the apparent

area Δα in function of the applied tension on the membrane are close for vesicles free of proteins and vesicles covered with CHMP2A-ΔC + CHMP3-FL proteins (Figure 5-40 / B). The slope of the protein-free vesicles curve (magenta) plotting the tension versus Δα provides a measurement of the stretching modulus χ = 120 ± 0.04 mN/m (coefficient of determination R^2 = 0.99). This stretching modulus value is lower than the typical phospholipids stretching modulus value of 250 mN/m commonly found in the literature (Evans and Needham 1987; Rawicz, Olbrich et al. 2000). We suppose that this difference is due to the fact that we do not pre-stretch the vesicles prior to aspiration, keeping thus membrane reservoirs. This is visible in the very large range of excess area that can be obtained (more than 10% when Δα is normally limited to 5% maximum). This effect is well-known and mentioned in different papers from E. Evans. Actually, as our purpose was to compare the membrane elasticity with and without proteins, the experimental conditions had to be identical. And because vesicle pre-stretching is not possible when CHMP proteins are bound to the membrane, thus we similarly did not pre-stretch bare GUVs. For the (CHMP2A + CHMP3)-covered GUVs we measured a slightly lower stiffness (blue) with χ = 95 ± 0.06 mN/m (coefficient of determination R^2 = 0.97). This indicates that the combination of CHMP2A-ΔC + CHMP3-FL proteins might loosen the membrane, perhaps due to the excess area from the protein-membrane protrusions induced by the co-polymer on the GUV surface (Figure 5-38). While the protein-membrane overall structure in presence of CHMP2B proteins is rigid, it is not in the presence of CHMP2A proteins where the membrane elasticity is almost unaltered. Thereby, CHMP2B and CHMP2A modulate differently the membrane elasticity.

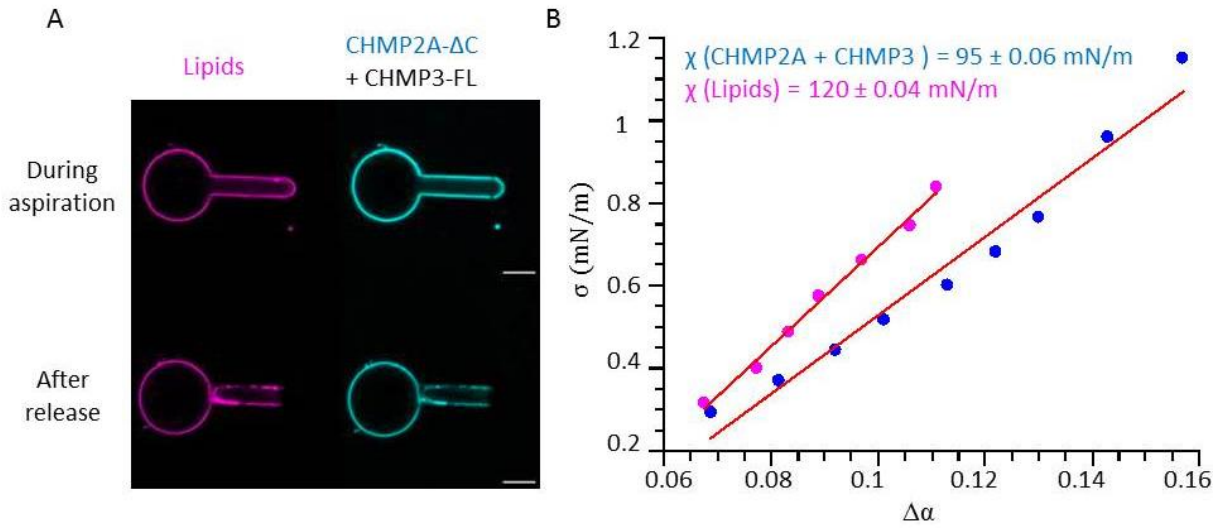

FIGURE 5-40: ASPIRATION EXPERIMENTS PERFORMED ON CHMP2A + CHMP3 CO-POLYMER BINDING TO GUVS
(A) Mechanical manipulation applied to CHMP2A-ΔC + CHMP3-FL -covered GUV by micropipette aspiration. One confocal plane is shown at zero-tension and high-tension.
(B) Quantification on the variation of the excess area as a function of the applied tension. The fits of the data are shown (red line). n=20.

5.3.3 CHMP2A + CHMP3 SUPRAMOLECULAR ASSEMBLY ON MEMBRANE IS DYNAMIC IN CONTRAST WITH CHMP2B

We have shown that CHMP2A + CHMP3 and CHMP2B organize differently on membrane and have different effects on its elasticity. We next investigated the dynamics of the CHMP2 + CHMP3 supramolecular assembly on GUVs by FRAP (see chapter 4.3.3.1).

We incubated PI(4,5)P_2-GUVs (lipid mixture 5) with 500 nM CHMP2A-ΔC proteins and 2 µM CHMP3-FL proteins in BP for 60 min to obtain a homogeneous coverage of the proteins on the surface of the vesicles. Then, vesicles covered with CHMP2A-ΔC + CHMP3-FL proteins were transferred into the observation chamber with a 10 times dilution factor of the protein concentration in bulk to remove free protein monomers from the solution. This way, only the diffusion of previously assembled proteins on the bleached section of the GUV was measured by FRAP. The experiments were performed with only one of the two proteins being fluorescent at a time. And due to the heterogeneity in the size of the GUVs in the sample, the defined ROI varied from a vesicle to another (see yellow square in Figure 5-41 / A).

Figure 5-41 / A shows the fluorescence intensities of CHMP2A-ΔC (in blue) and CHMP3-FL (in yellow) in the context of CHMP2A + CHMP3 co-assembly and of CHMP2B-ΔC (in green) before FRAP, after FRAP and after recovery (350 sec after FRAP). Upon photobleaching, we observed an almost complete recovery of the fluorescence signal for both CHMP2A-ΔC and CHMP3-FL proteins, in less than 2 minutes, implying that both proteins diffuse on the membrane in the presence of the other. This result is completely opposite to the CHMP2B dynamics that does not recover at all on vesicles.

Figure 5-41 / B presents the fraction of fluorescence recovery over time for CHMP2A + CHMP3 (in blue) and CHMP2B (in green). Note that the error bars in the plot correspond to the standard deviation of the measured recovery over time for 42 photobleached GUVs. The errors bars are relatively large due to the spreading of the ROI sizes. Indeed, the fluorescence recovery in a small region is faster than in a bigger one. The ROI size could not be fixed due to experimental conditions, in particular vesicle size heterogeneities and movement in the experimental chamber. For instance, a large ROI is defined on moving vesicles to ensure a recovery acquisition over time in case the vesicle rotates.

Figure 5-41 / B shows that CHMP2A + CHMP3 co-polymer did not fully recover (fraction of recovery below 1) with a plateau of recovery at about 0.8. As explained in chapter 4.3.3.1, this indicates that some of the FRAP-bleached proteins in the ROI are immobile and did not contribute to the recovery since they are not replaced by unbleached molecules. The fraction of proteins that diffused and contributed to the recovery are called mobile fraction and those who did not are called immobile fraction and corresponds to A and 1 - A, respectively. Another possibility for the incomplete recovery is that the bleached molecules represent a non-negligible fraction of the total number of molecules of the

GUV (i.e. the ROI being large as compared to the GUV size); in this case, the total GUV fluorescence is reduced and full recovery should correspond to this reduced intensity, not to the initial one. In our experiments, we did not correct for the variation of the fluorescence of the GUVs.

The characteristic diffusion $\tau_{1/2}$ time is measured to characterize and compare the diffusion and thus the mobility of proteins knowing the area of the ROI. $\tau_{1/2}$ indicates the time at which half of the fluorescence has recovered and is therefore commonly called the half-time. It is calculated from the fit of the normalized FRAP curve I(t) with the exponential equation (4-1 in chapter 4.3.3):

$$I = A(1 - e^{-\tau t})$$

Where

$$\tau_{1/2} = \frac{\ln(0.5)}{-\tau}$$

The measured mobile fraction from the fit A = 0.85 ± 0.04 A.U. (85% of the proteins are mobile) and $\tau_{1/2}$ ≈ 18 sec. In conclusion, the dynamics of CHMP2A and CHMP2B on GUVs are extremely different. CHMP2A and CHMP3 proteins are mobile on the surface of GUVs while CHMP2B proteins are immobile.

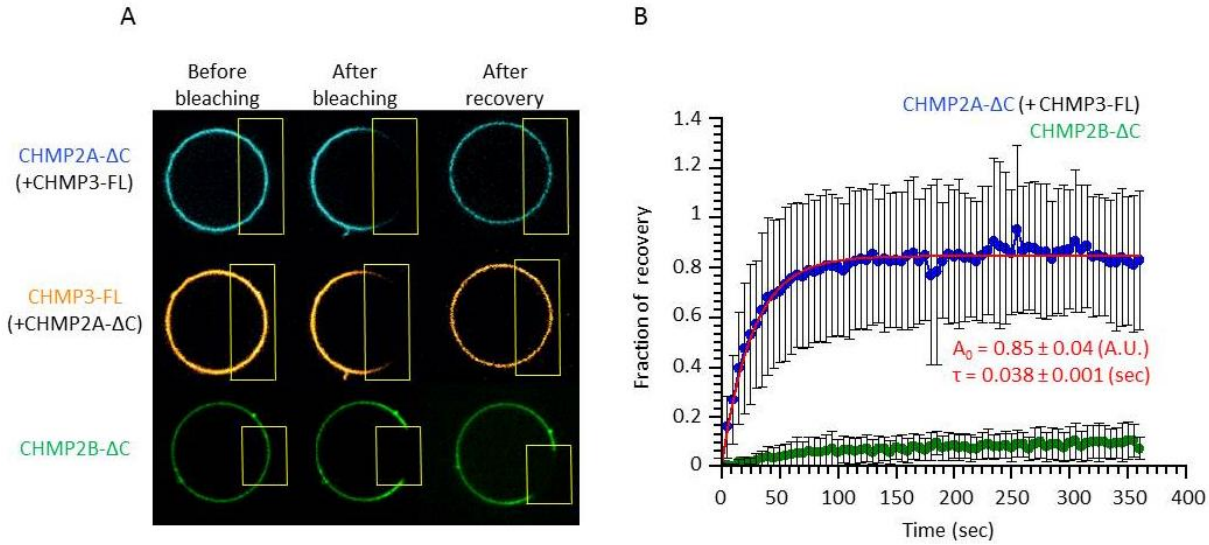

FIGURE 5-41: COMPARISON OF THE DIFFUSION OF CHMP2B-ΔC AND OF CHMP2A-ΔC + CHMP3-FL PROTEINS BOUND TO GUVS BY FRAP

(A) CHMP2A-ΔC + CHMP3-FL and CHMP2B-ΔC are photobleached and fluorescence recovery is imaged over time (350 sec after FRAP). Yellow square indicates the photobleached ROI.

(B) Recovery fraction over time of the mean fluorescence of CHMP2A-ΔC + CHMP3-FL and CHMP2B-ΔC polymers after photobleaching. Errors bars correspond to the standard deviation. n=42.

We observed a very characteristic reticulum-like structure for CHMP2B at low surface fraction (see Figure 5-21), showing a tendency for this protein to assemble over large distances. At higher density, these structures probably overlap and cannot be distinguished any more, considering the optical resolution of our experiments. Nevertheless, our FRAP results suggest that CHMP2B proteins cannot diffuse anymore when these structures are formed, like in a static 2D network.

In contrast, CHMP2A and CHMP3 in spite of their tendency to form polymers, obviously do not form any entangled network, since recovery occurs. With our photobleaching geometry, we cannot easily extract a diffusion coefficient from the recovery time; thus, we cannot conclude whether the proteins move in a polymeric form on the GUV surface, or as individual entities. Nonetheless, this demonstrates once again that CHM2A and CHMP2B proteins display very different properties on membranes.
To further compare CHMP2A and CHMP2B assemblies on GUVs and their effect on membrane-associated proteins such as streptavidin, we repeated the FRAP experiment to membrane-bound streptavidin (see section 5.2.5) in the presence of CHMP2A-ΔC + CHMP3-FL.

GUVs were incubated with 500 nM CHMP2A-ΔC + 2 µM CHMP3-FL in BP for 60 min. Following, half of the (CHMP2A + CHMP3) - covered vesicles were transferred to BP buffer containing 500 nM red-labelled streptavidin (Alexa Fluor 561) and the other half to BP buffer without any diluted protein (control sample). (CHMP2A + CHMP3) - vesicles were incubated with streptavidin during 30 min.

We performed FRAP on Alexa 561-labelled streptavidin bound to biotinylated lipids on the surface of GUVs. In the presence of CHMP2A + CHMP3 proteins on the membrane, we observed full recovery of the streptavidin fluorescence signal in the ROI (Figure 5-42 / A). This indicates that the diffusion of streptavidin is not blocked when CHMP2A + CHMP3 proteins are bound to the GUV surface. Figure 5-42 / B shows the fraction of streptavidin fluorescence recovery after photobleaching over time for vesicles without proteins (magenta curve), vesicles with (CHMP2A + CHMP3) proteins (blue curve) and vesicles with CHMP2B proteins (green curve). In the absence of protein, the fraction of mobile streptavidin is about 0.99 and the half-time equals $\tau_{1/2} \approx 15$ sec (Figure 5-42 / B).

Similar results were obtained on vesicles covered with CHMP2A + CHMP3 proteins with 0.90 mobile proteins and a half-time of 23 sec. The slower recovery of streptavidin is probably due to CHMP2A + CHMP3 protein crowding on the membrane. Moreover, the 90 % protein recovery implies that CHMP2A-ΔC + CHMP3-FL co-polymers do not significantly affect mobility of streptavidin, meaning that the co-polymer does not form a structure that confines streptavidin proteins and pointing to an absence of long-distance 2D organization of these proteins. This is completely opposite to the diffusion in the presence of CHMP2B, probably forming a dense entangled network on the membrane. To sum up, these FRAP experiments performed on streptavidin show again opposite results between CHMP2B and CHMP2A (+ CHMP3) proteins and further stress the difference between these two proteins.

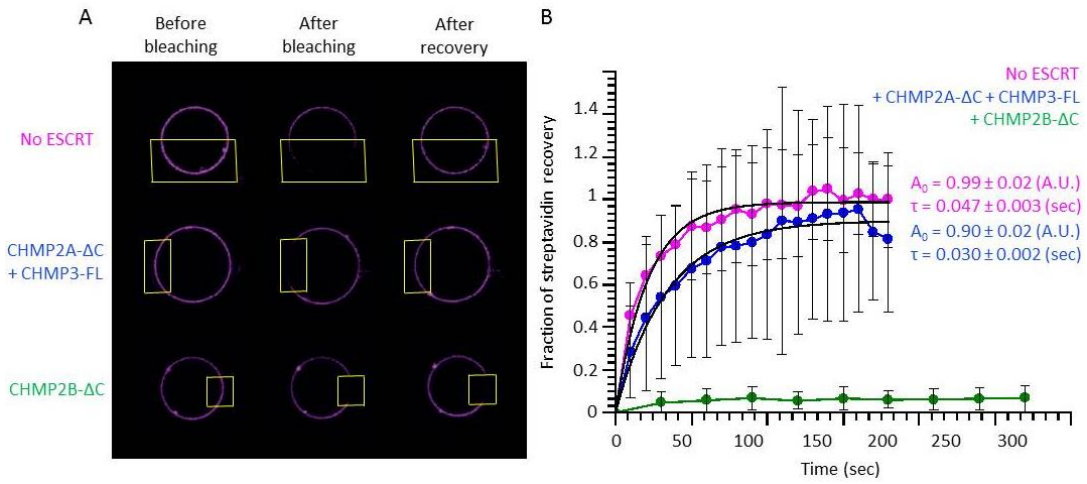

FIGURE 5-42: FRAP MEASUREMENTS OF STREPTAVIDIN-BOUND TO GUVS CONTAINING ESCRT PROTEINS
Streptavidin recovery after photobleaching on biotinylated-GUVs.
(A) Photobleaching of streptavidin bound to GUVs previously covered with CHMP2A-ΔC + CHMP3-FL and CHMP2B-ΔC. The recovery of the fluorescence of streptavidin over time (300 sec after FRAP) is imaged by confocal microscopy. The yellow square indicates the photobleached ROI.
(B) Recovery fraction over time of streptavidin for different conditions. Error bars correspond to the standard deviation of the fraction of recovery of the photo-bleached ROI. n = 50.

5.4 CHMP3 PERTURBS CHMP2B POLYMERIZATION AND ASSEMBLY ON MEMBRANES

As described previously, we found that CHMP2A has very weak interactions with membrane unless CHMP3 is present. We next addressed the question of the effect of CHMP3 on CHMP2B. We also wondered if the differences observed between CHMP2A and CHMP2B proteins could be due to the presence of CHMP3 proteins in the experiments with CHMP2A. We have thus studied the effect of the co-incubation of CHMP3 proteins with CHMP2B proteins on GUVs. In this chapter we have used SD and FRAP confocal microscopy techniques to study the assembly and mechanical properties of CHMP2B-ΔC + CHMP3-FL co-polymer on GUVs. We will (i) characterize the supramolecular assembly of (CHMP2B + CHMP3) co-polymer on the surface of GUVs, (ii) study the co-polymer dynamics and (iii) check the effect of the addition of CHMP3 on the membrane mechanical properties by CHMP2B-ΔC.

5.4.1 CHMP3 BLOCKS CHMP2B POLYMERIZATION ON MEMBRANES

We first studied the effect of CHMP3 on the polymerization of CHMP2B proteins on GUVs. We incubated PI(4,5)P_2-GUVs made of the lipid mixture 5 with 500 nM CHMP2B-ΔC proteins and 2 µM CHMP3-FL in BP buffer for 60 min. By SD confocal microscopy, we observed that unlike results obtained with CHMP2A, the addition of CHMP3 together with CHMP2B results in reduced CHMP2B binding to the surface of the vesicles (Figure 5-43 / A). Figure 5-43 / B shows the quantification of the fluorescence signal of CHMP2B proteins on GUVs in the absence and in the presence of CHMP3. It indicates a decrease of CHMP2B fluorescence intensity by a factor of 2 when CHMP3 is co-incubated with CHMP2B.

In addition, FACS measurements allowed to compare the interactions with PI(4,5)P_2-vesicles with CHMP2B-ΔC, CHMP3-FL, CHMP2B alone or in combination. They show in particular that the interaction of CHMP2B is stronger in the absence of CHMP3, but conversely, that CHMP3 affinity is enhanced in the presence of CHMP2B (Figure 5-43 / C). Figure 5-43 / D shows one single confocal plane image of the binding of CHMP3 on GUVs. In the absence of CHMP2B (in green) we could not detect any signal for CHMP3 binding. In contrast, when both proteins are co-incubated, CHMP3 is bound to the membrane and in perfect co-localization with CHMP2B (in yellow). These results confirm that CHMP3 proteins require the presence of CHMP2A or CHMP2B to bind the membrane. However, when associated to CHMP2A, CHMP3 binding is stronger than in association with CHMP2B. We propose that CHMP3 plays a double role: while CHMP3 increases the affinity of CHMP2A to the membrane consistent with their synergistic role in HIV budding, it interferes with CHMP2B polymer formation in agreement with their lack of synergy in the virus egress. In summary, while CHMP3 amplifies CHMP2A binding to the membrane, it might also refrain CHMP2B polymerization.

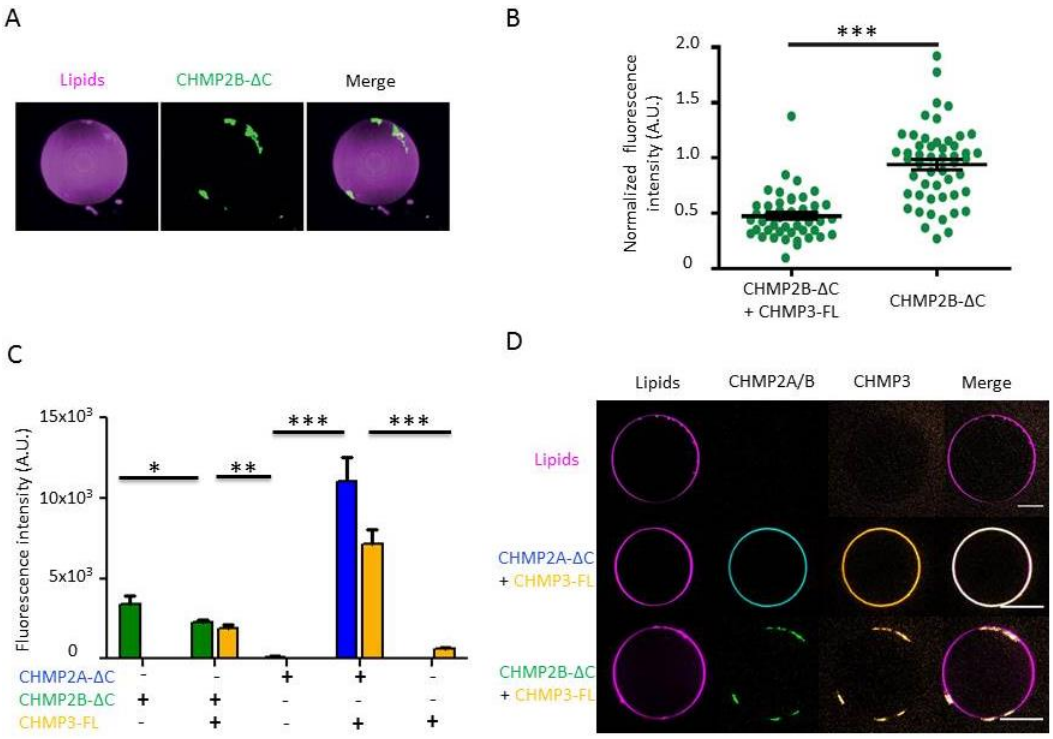

FIGURE 5-43: SUPRAMOLECULAR ASSEMBLY OF CHMP2B + CHMP3 PROTEINS ON GUVS

(A) Supramolecular assembly of CHMP2B-ΔC in the presence of CHMP3-FL on the surface of a GUV containing PI(4,5)P_2 lipids. A z-projection is shown.

(B) Effect of CHMP3 on CHMP2B-ΔC binding to GUVs containing PI(4,5)P_2 lipids obtained from the quantification using cell profiler software of CHMP2B fluorescence from images taken by SD confocal microscopy. Fluorescence intensity of CHMP2B-ΔC + CHMP3-FL-covered vesicles was normalized to the fluorescence intensity of CHMP2B-ΔC-covered vesicles. ***=p-value<0.001 (Student's t-test). n= 48.

(C) Quantification by FACS of the fluorescence intensities of CHMP2A-ΔC ± CHMP3, CHMP2B-ΔC ± CHMP3 and CHMP3 ± CHMP2A/B-ΔC co-polymers bound to PI(4,5)P_2-containing GUVs. *=p-value<0.05; ** = p-value < 0.01; ***=p-value<0.001 (Student's t-test). n=4 (number of FACS experiment with 10^4 counted event per experiment, per condition).

(D) Effect of CHMP2A and CHMP2B-ΔC co-incubation with CHMP3-FL on the binding of each protein to GUVs containing PI(4,5)P_2. A single confocal plane is shown. Scale bar = 10 µm.

5.4.2 CHMP2B + CHMP3 SUPRAMOLECULAR ASSEMBLY IS NOT DYNAMIC

We showed in chapter 5.2.4 that CHMP2B alone forms a very stable and static network over GUVs. To study whether the presence of CHMP3 changes the assembly dynamics, we incubated GUVs made of the lipid mixture 5 with 500 nM CHMP2B-ΔC proteins and 2 µM CHMP3-FL proteins in BP for 60 min. Then, vesicles covered with CHMP2B-ΔC + CHMP3-FL co-polymer were transferred in the observation chamber to perform FRAP experiment.

Measurement of CHMP2B-ΔC and CHMP3-FL recovery after photo-bleaching shows that CHMP3 does not affect CHMP2B-ΔC dynamics on the membrane. We observed no recovery of the fluorescence signal of both CHMP2B and CHMP3 in the photobleached region when present together (Figure 5-44 / A, see yellow square). The quantification of the fraction of recovery of CHMP2B with and without CHMP3 in Figure 5-44 / B (about 3% in 5 minutes), very similar to CHMP2B alone, confirms that the addition of CHMP3 has no effect on the CHMP2B assembly stability. Interestingly, while CHMP3 freely diffuses and fully recovers after photobleaching when associated to CHMP2A-ΔC, it does not recover when associated to CHMP2B-ΔC.

In conclusion of this part, CHMP3 protein binding depends on CHMP2B and its dynamics follows that of the CHMP2B assembly, suggesting that either CHMP3 copolymerize with CHMP2B or binds onto the CHMP2B network assembly.

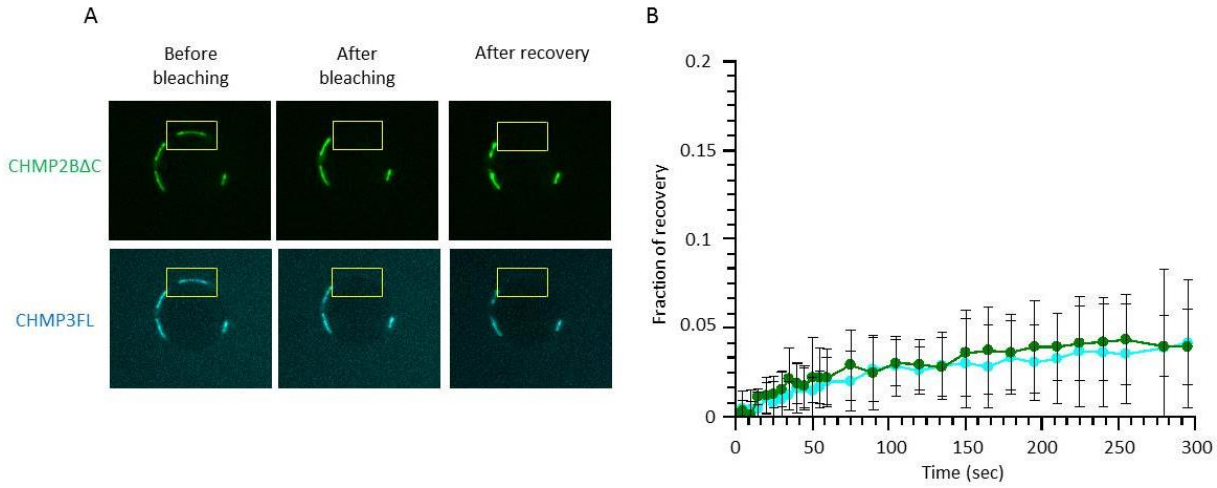

FIGURE 5-44: PHOTOBLEACHING EXPERIMENTS PERFORMED ON CHMP2B + CHMP3 ASSEMBLIES BOUND TO A GUV SURFACE
(A) FRAP experiment on CHMP2B-ΔC + CHMP3-FL co-polymer. Both proteins were photo-bleached at the same time. Yellow squares indicate the photobleached.
(B) Time variation of the recovery fraction of CHMP2B in the presence and in the absence of CHMP3. Error bars correspond to the standard deviation. n=18.

5.4.3 CHMP3 MODULATES THE MECHANICAL PROPERTIES OF CHMP2B POLYMERS

Next we tested if, in addition to limiting CHMP2B polymerization, CHMP3 co-assembly affects CHMP2B mechanical properties on the membrane. We therefore prepared GUVs made of lipid mixture 5 (10% DOPS, 10% PI(4.5)P_2) and incubated them in BP for 30 min with 500 nM CHMP2B-ΔC proteins. Then, GUVs were transferred to a solution of BP buffer + 2 µM CHMP3-FL. We chose to add CHMP3 proteins after complete assembly of CHMP2B proteins on the vesicle to observe the direct effect of CHMP3 on CHMP2B polymer and consequently on the membrane mechanical properties.

As seen previously in chapter 5.2.2, CHMP2B alone is able to stiffen the underlying membrane and to prevent its deformation by micropipette aspiration. Surprisingly, incubation of a pre-formed CHMP2B-ΔC polymer with CHMP3-FL results in the loosening of the CHMP2B-ΔC "shell", which can now be deformed by micropipette aspiration (Figure 5-45 / A). CHMP3 proteins can thus weaken the CHMP2B proteins rigid structure, which can be systematically broken by micropipette aspiration (Figure 5-45 / A and B). This softening/weakening of the CHMP2B shell allows CHMP2B polymer breakage and thus the aspiration of a lipid tongue but deprived of protein (Figure 5-45 / A – top panel). Occasionally, CHMP2B + CHMP3 polymer deformation occurs and a tongue covered with both proteins can be detected (Figure 5-45 / A – lower panel).

Figure 5-45 / B shows the percentage of aspirated vesicles in the presence of CHMP2B only or in the presence of CHMP2B + CHMP3. It clearly indicates that while less than 20 % of the CHMP2B-coated GUVs could be aspirated in the absence of CHMP3, probably after occasional shell rupture (see chapter 5.2.2), almost 100 % of the CHMP2B-coated GUVs could be aspirated when CHMP3 proteins are added (CHMP2B polymer weakening). Unfortunately because of the strong adhesion of CHMP2B to the micropipette glass surface (see for instance, in Figure 5-45 / A, the green CHMP2B fluorescence detected on the pipette), the membrane strongly adhered to the pipette during all the aspiration process and measurements of the variation of the apparent area $\Delta\alpha$ as a function of the increasing applied tension on the membrane were biased. Globally, this suggests that the CHMP2B-CHMP3 assembly on the membrane is much more deformable than CHMP2B alone.

Hence, CHMP3 proteins need to co-assemble with CHMP2A or CHMP2B proteins to bind membranes. However, CHMP3 proteins induce opposite effects upon interaction with CHM2A or CHMP2B proteins. On the one hand, they strikingly increase CHMP2A affinity towards the membrane, and on the other hand, they perturb CHMP2B polymerization and weaken the polymer stiffness.

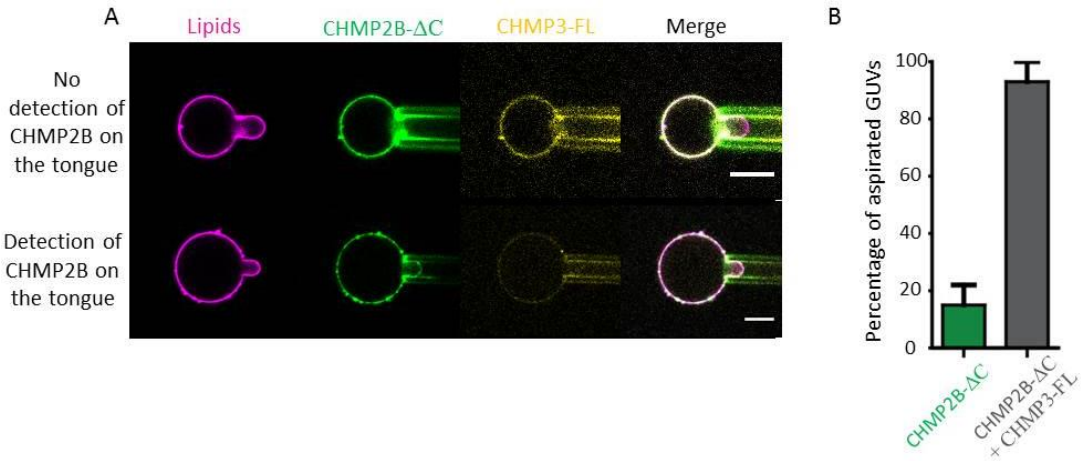

FIGURE 5-45: INVESTIGATION OF THE MECHANICAL PROPERTIES OF THE CHMP2B + CHMP3 ASSEMBLY ON VESICLES

(A) Micropipette aspiration of 2 GUVs covered with a pre-formed CHMP2B-ΔC polymer subsequently incubated with CHMP3-FL. Top: no CHMP2B, nor CHMP3, are visible on the tongue (Note that on this image, proteins were covering the surface of the micropipette. Bottom: Both CHMP2B and CHMP3 are present on the aspirated tongue. Yellow arrow shows that CHMP2B is present on the tongue inside the micropipette.

(B) Percentage of aspirated GUVs. Comparison between CHMP2B and pre-assembled CHMP2B incubated with CHMP3. n=14.

In conclusion of the sections 4.1, 4.1 and 5.4, even though CHMP2B and CHMP2A have been so far expected to be functionally and structurally homologous, both their organization and their resulting biophysical properties are different as summed-up in the following table:

Protein properties	CHMP2B	CHMP2A
Preferential affinity to PI(4,5)P_2	✓	✗
CHMP3 requirement	✗	✓
Assembly at the mesoscale	Network	No network
Assembly at the nanoscale	Rings	Short filaments & spirals
Rigidity	✓	✗
Mobility	✗	✓
Diffusion barrier	✓	✗

(i) From a phylogenetic point of view, CHMP2A and CHMP2B are different. CHMP2A sequence comprises a MIM domain, crucial for the AAA-ATPase VPS4 binding, but CHMP2B not.

(ii) CHMP2A does not display any preferential affinity to PI(4,5)P2 lipids in strong contrast with CHMP2B proteins.

(iii) CHMP2A requires the presence of CHMP3 to bind to lipid membranes and vice versa, whereas CHMP2B binds alone, with a strong affinity for PiP_2-containing membranes, and its binding is diminished in the presence of CHMP3.

(iv) At the micron scale, their assemblies are much contrasted. CHMP2B proteins form a reticulum-like stable network on membranes while CHMP2A (combined with CHMP3) binds in a homogeneous fashion. The CHMP2B network on membranes is very stable and can confine membrane-associated proteins, whereas the CHMP2A+CHMP3 assembly is very dynamic and does not significantly perturb diffusion.

(v) At the nanoscale, significant differences are observed as well, using Cryo-EM. CHMP2B forms rings that assemble into a dense honeycomb-like pattern on "flat" membranes while CHMP2A + CHMP3 bind the membrane as short filaments and form helical structures around tubules.

(vi) Finally, CHMP2B alters dramatically the mechanical properties of membranes. It strongly rigidifies membranes at the mesoscale and also at the nanoscale as observed by micropipette assays and by AFM, respectively. In contrast, the CHMP2A+CHMP3 assembly is softer than CHMP2B alone, as observed with the micropipette aspiration experiments.

Therefore, CHMP2A and CHMP2B cannot be considered as functional homologues and occupy the same role in the human ESCRT-III machinery, which is perhaps the reason why they require a distinctively opposite mode of regulation by CHMP3.

5.5 CHMP2A AND CHMP2B MODULATE CHMP4B ASSEMBLY ON MEMBRANES

CHMP4 is the most abundant ESCRT-III subunits. According to several studies in yeast, CHMP4 is responsible for the recruitment of CHMP2A or CHMP2B, or CHMP3 together with CHMP2A complex (Babst, Katzmann et al. 2002; Teis, Saksena et al. 2008; Adell and Teis 2011; Adell, Migliano et al. 2016).

This motivated us to first characterize the interaction and mechanics of CHMP4 on $PI(4,5)P_2$ membranes by SD microscopy and micropipette aspiration, respectively. Then, we observed by EM and AFM the effect of the addition of CHMP2A (+CHMP3) or CHMP2B proteins on CHMP4 assembly on membranes.

5.5.1 CHMP4B ASSEMBLY ON MEMBRANES

Recombinant human CHMP4B was purified with an N-terminal MBP Tag that can be removed by incubation with TEV protease (at a ratio of CHMP4B : TEV of 3 to 1). For the yeast homologue Snf7, It is known that the interaction with membranes is achieved by insertion of its N-terminal (Buchkovich, Henne et al. 2013). The presence of the MBP Tag on the N-terminus of CHMP4 blocks its interaction with the membrane.

Figure 5-46 / A shows in the upper panel that the fluorescence signal of the protein (blue) is very weak when the MBP tagged CHMP4 is not cleaved. However, when the MBP tag is removed, CHMP4B binds to membranes (Figure 5-46 / A, lower panel). Thus, in the following, the MBP tag is systematically cleaved for the experiments. As we did for the other CHMP proteins, we have investigated the affinity of CHMP4 to the different PIP species with FACS.

Interestingly, CHMP4B does not show any preferences toward any particular phosphoinositide. CHMP4 binds equally all the negatively charged lipids including DOPS as shown on Figure 5-46 / B that provides a comparison with the other CHMPs. From this figure, we conclude that only CHMP2B exhibits preferential affinity to $PI(4,5)P_2$.

This is on line with CHMP2B playing a role in membrane scission and reparation processes essentially at the plasma membrane where these lipids are enriched.

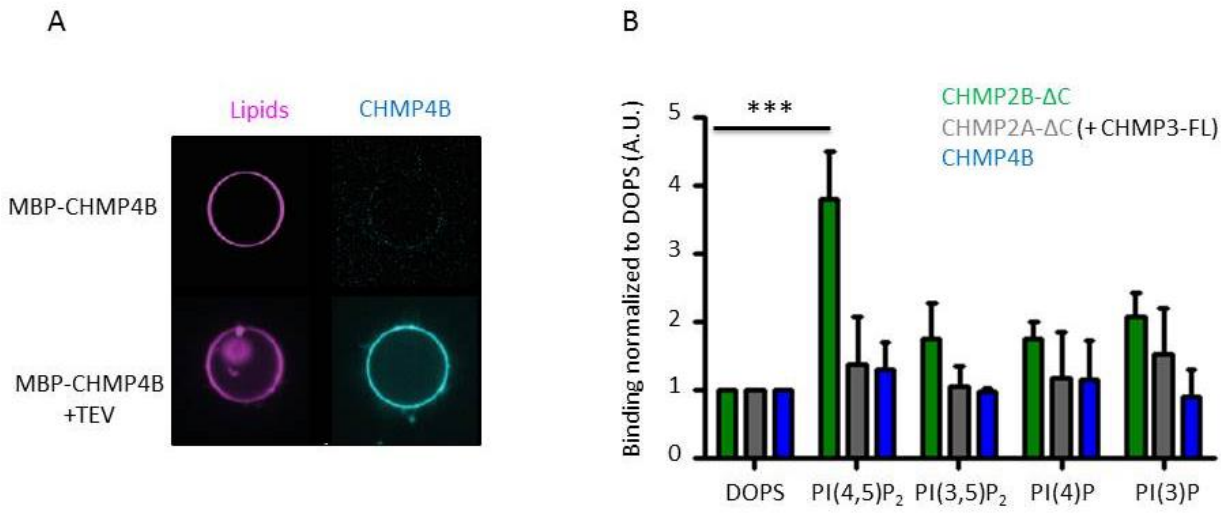

FIGURE 5-46: CHMP4B BINDING TO MEMBRANE
(A) Comparison between MBP-CHMP4B and CHMP4B binding to $PI(4,5)P_2$-GUVs , showing that it is essential to cleave the MBP tag.
(B) Comparison between CHMP2B, CHMP2A + CHMP3 and CHMP4B proteins for their affinity to different PIP species, measured by FACS.

5.5.1.1 CHMP4B ALONE FORMS SPIRALS ON FLAT MEMBRANES

Using LUVs, we aimed at testing whether CHMP4 deforms biomimetic membranes in 3D (i.e. tubulates) as suggested in the published theoretical models (Henne, Buchkovich et al. 2012; Chiaruttini, Redondo-Morata et al. 2015). We thus studied the effect of CHMP4 polymerization on solid membrane surfaces (SLBs) and on quasi-flat and easily deformable membranes (GUVs).

We prepared LUVs (made of the lipid mixture 5) as mentioned in chapter 4.2.4 and incubated them in BP with 500 mM CHMP4B (with TEV protease to cleave the MBP tag) for 15 min. Then, we imaged CHMP4B assembly on membrane using both AFM and Cryo-EM microscopy (experimental conditions for Cryo-EM and AFM experiments are respectively described in chapter 4.4.2 and in chapter 4.7.2).

By AFM, on supported lipid bilayers, we observed that CHMP4B proteins self-assemble into spirals without deforming the membrane in 3D (Figure 5-47 / A). Similarly, by Cryo-EM on vesicles we visualized flat spirals (200 - 300 nm of external diameter) (Figure 5-47 / B). And likewise, CHMP4B proteins did not deform the membrane; they did not induce any membrane tubulation (Figure 5-47 / B) and rather flatten the surface of the LUV as shown in Figure 5-47 / C with a Cryo-tomograph. With AFM, we measured the mean value of the spiral center diameter and found approximately 29 nm (Figure 5-47 / A – see bottom section “2”, magenta line and respective quantification). This measured value is consistent with earlier published studies by HS-AFM on Snf7, the yeast homologue of CHMP4 (Chiaruttini, Redondo-Morata et al. 2015). The authors show that Snf7 is as well forms spirals with a preferred radius of curvature of 25 - 30 nm. They also show that this radius decreases to about 14 nm when the spiraling increases from 2 to 3 concentric circles with an average innermost circle radii equal to 18 ± 3 nm. We also measured the peak to peak distance by AFM (mean value = 11.3 ± 0.2 nm) (Figure 5-47 / A - see top section “1”, cyan line and respective quantification) and the mean distance between filaments within a spiral by Cryo-EM (mean value = 7.2 ± 1.4 nm) (Figure 5-47 / B).

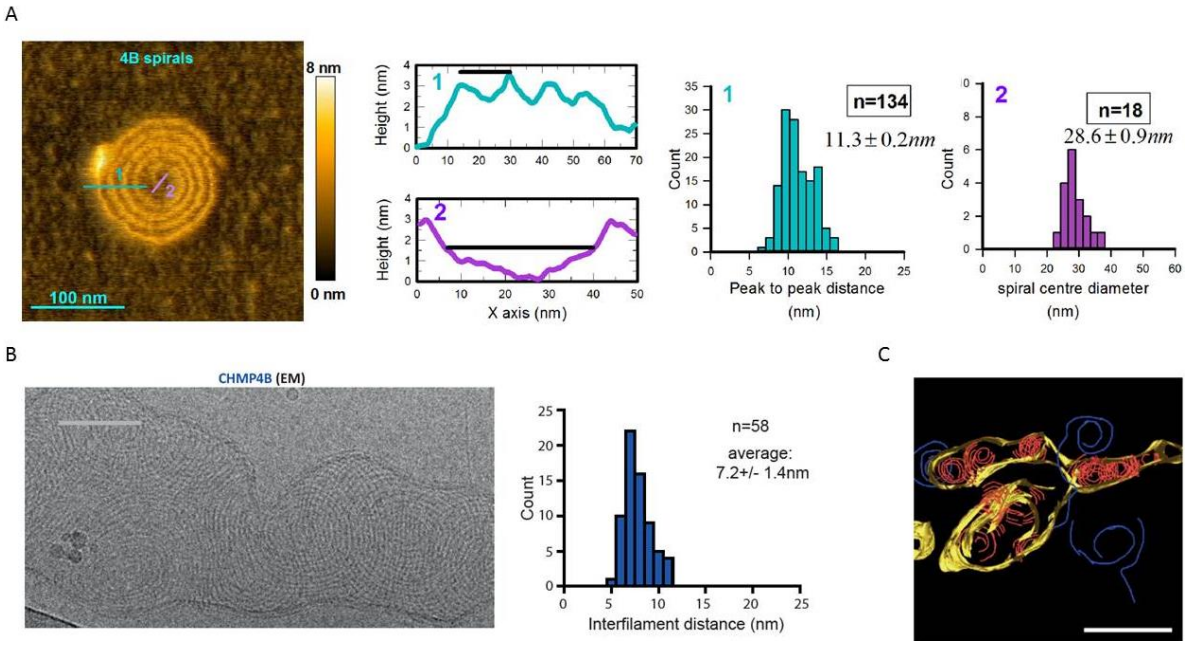

FIGURE 5-47: CHMP4B FORMS SPIRAL STRUCTURES ON MEMBRANES

(A) Representative image of CHMP4B assembly on Supported Lipid Bilayer (SLB) imaged by High-Speed Atomic Force Microscopy (HS-AFM). 2 z-profiles corresponding to the magenta and cyan sections in the left image Scale bar: 100nm. Distribution of the spiral peak to peak distance as measured from the cyan line in the top section. Distribution of the diameter of the spiral center as measured from the magenta line in the bottom section.

(B) Representative Cryo-Electron Microscopy (EM) image showing the assembly of CHMP4B on vesicles. Scale bar = 100 nm. Distribution of interfilament filament distances as measured by Cryo-EM is shown.

(C) Cryo-EM tomogram depicting CHMP4B assembly on vesicles. Colour code: yellow: lipids; red: CHMP4B assembly on lipids; blue: CHMP4B assembly on EM grid. Scale bar = 100 nm.

In the initial vesicle preparation for EM experiments, it is possible to have some tubular structures with a percentage of 15.6 ± 3.4 % in the absence of proteins (from a quantification of 15 EM images with a total of 265 counted structures: 225 vesicles versus 40 tubular structures). By Cryo-EM, we observed tubular irregular structures with diameters of about 35 nm covered by CHMP4 polymers (Figure 5-48 / A). The percentage of tubular structures increases weakly in the presence of CHMP4B and is about 20.4 ± 14.2 % (from a quantification of 15 EM images with a total of 265 counted structures: 214 vesicles versus 51 tubular structures). These tubes are generally not straight but present some helicity when they are thin enough (below 50 nm), although not regular. Onto those tubes, we found CHMP4 polymers either oriented parallel to the main axis of the tube or randomly oriented on tubes with a diameter above 40 - 50 nm (Figure 5-48 / A). We also have used preformed rigid nanotubes of 25 nm diameter made of galactosylceramide lipids (Galcer tubes) (Mears and Hinshaw 2008). Interestingly, we see that when a tube cannot be deformed, CHMP4 are almost straight on the rigid Galcer tubes, i.e. twisted with a very large pitch. These polymers are either single or can form bundles (Figure 5-48 / B). Globally, these experiments show that when a tube is preformed, CHMP4 can assemble on its surface, thus on a membrane with a positive curvature. It forms filaments that are

either (i) parallel to the main tube axis and induce some helicity of the tubular structure on flexible tubes, or (ii) weakly twisted around the tubes on rigid tubes.

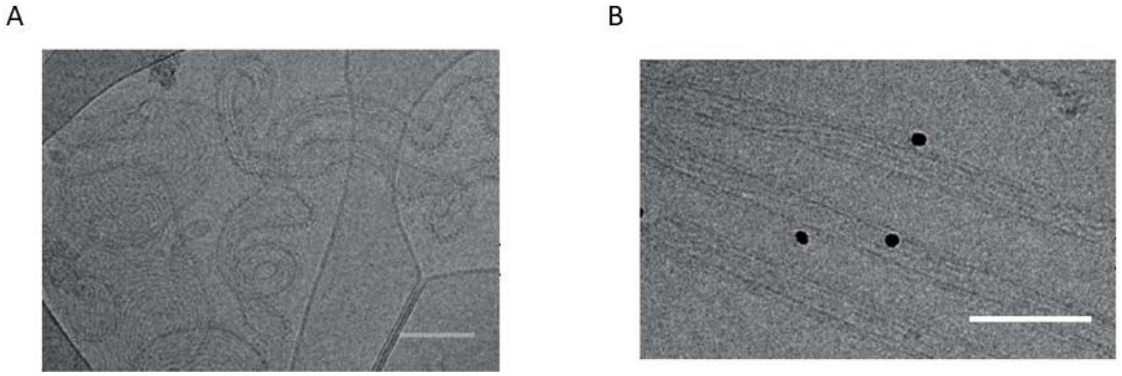

FIGURE 5-48: ASSEMBLY OF CHMP4B POLYMERS ALONG TUBES
(A) Cryo-EM image showing the assembly of CHMP4B on soft (unconstrained) preformed tubular membrane. Scale bar = 100 nm.
(B) Cryo-EM image showing the assembly of CHMP4B on rigid tubular membrane with a 25 nm diameter. Black dots correspond to gold beads used for Cryo-tomography. Scale bar = 100 nm.

5.5.1.2 MECHANICAL PROPERTIES OF GUVS COATED WITH CHMP4B

To investigate the mechanical proprieties of CHMP2B-ΔC and CHMP4B co-assemblies, we first analyzed the mode of assembly of CHMP4B on PI(4,5)P_2-GUVs made of the lipid mixture 5. CHMP4B at a concentration of 500 nM binds homogeneously the GUV membrane in BP buffer, in agreement with published data showing as well a homogeneous fluorescence of the yeast homologue protein Snf7 on GUVs (Chiaruttini, Redondo-Morata et al. 2015).

Very importantly, although some protein clusters are visible; no spontaneous membrane tubulation was visible at the surface of the GUV (Figure 5-49).

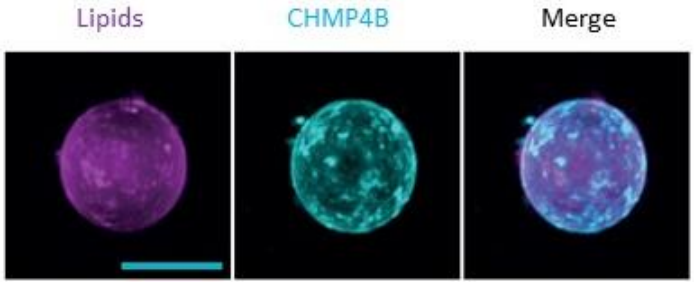

FIGURE 5-49: CHMP4B BINDING ON THE SURFACE OF GUVS.
Assembly of CHMP4B polymers on GUVs containing PI(4,5)P_2 lipids. A z-projection is shown. Scale bar = 10 µm.

Next, to investigate the effect of CHMP4B on membrane elasticity, we performed micropipette aspiration experiments of GUVs covered with CHMP4B and compared them with CHMP2B micropipette aspiration experiments. As described in chapter 5.2.2, CHMP2B-ΔC polymerization on the surface of GUVs impedes aspiration of the membrane even at high tension (σ = 0.6 mN.m^{-1}) (Figure 5-50 / A), clearly indicating that CHMP2B makes the membrane very stiff. In contrast, GUVs coated with CHMP4B

can be aspirated easily with an apparition of the “characteristic tongue” inside the pipette (Figure 5-50 / B). Interestingly, the CHMP4B-coated GUVs keep a deformed shape after being released for the micropipette (Figure 5-50 / C), suggesting that the membrane acquires a plastic behaviour when CHMP4 polymerizes at its surface. This result is again in agreement with Chiaruttini et al. results showing a Snf7-coated GUV plastic behaviour after micropipette aspiration release (Chiaruttini, Redondo-Morata et al. 2015).

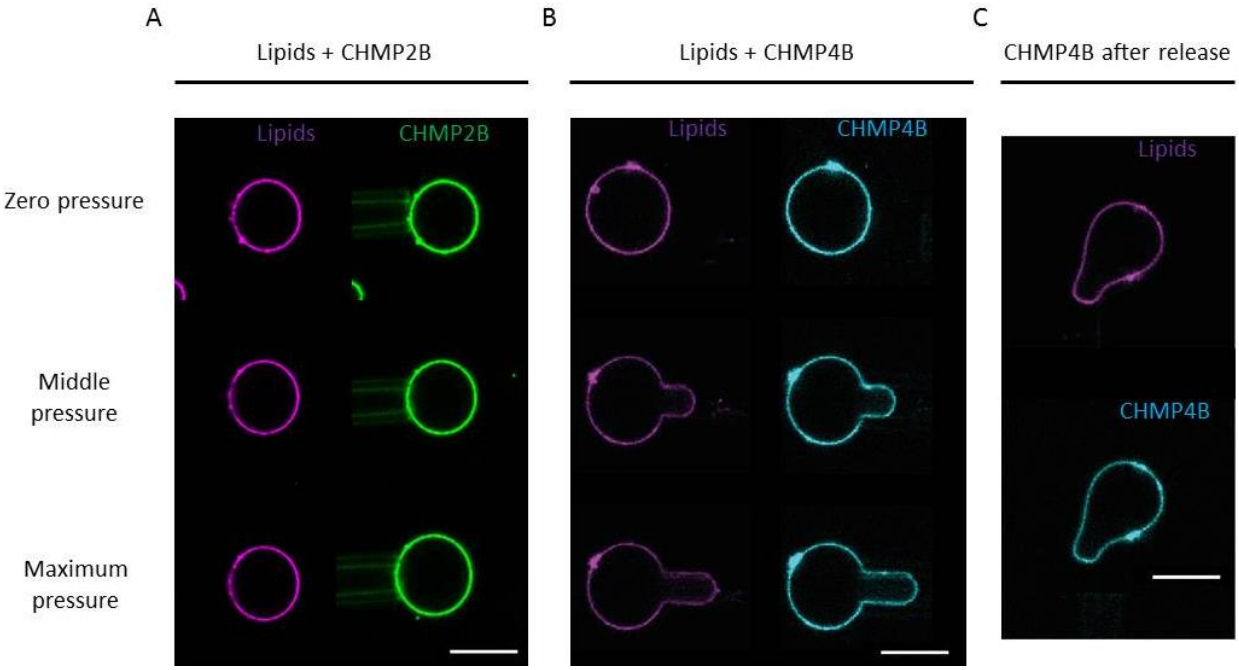

FIGURE 5-50: IMAGES OF ASPIRATION EXPERIMENTS ON CHMP2B AND CHMP4B BOUND TO GUVS
(A) Micropipette aspiration of a GUV incubated with CHMP2B-ΔC (green) at different aspiration pressures: zero (top), medium (middle, σ = 0.4 mN/m) and maximum (bottom, σ = 0.6 mN/m). The corresponding image of the lipids (magenta) is shown. Scale bar = 10 µm.
(B) Micropipette aspiration of a GUV incubated with CHMP4B polymer (cyan). Same pressures as above. Scale bar = 10 µm.
(C) Single confocal plane images of a GUV incubated with CHMP4B polymer (cyan) after aspiration release. Scale bar = 10 µm.

Moreover, micropipette aspiration assays on vesicles covered with CHMP4B polymer proved that CHMP4B binding does not significantly change the membrane elastic properties compared to bare membranes. The quantification of the slope of the plot of tension versus excess area $\Delta\alpha$ in Figure 5-51 / A shows that the stretching modulus of vesicles without proteins (magenta) and CHMP4-GUVs (blue curve) are close (χ_{lipids} = 120 ± 0.04 mN/m, coefficient of determination R^2=0.99 and χ_{CHMP4B} = 113 ± 0.07 mN/m, coefficient of determination R^2=0.98). Importantly, when we checked the effect of addition of CHMP2B to CHMP4B (green), we observed a stiffening of the overall structure (Figure 5-51 / B). The measured stretching modulus of CHMP4B-covered GUVs is equal to χ_{CHMP4B} = 113 ± 0.07 mN/m, coefficient of determination R^2=0.99 versus $\chi_{CHMP4B+CHMP2B}$ = 326 ± 0.15 mN/m for CHMP4B+CHMP2B-covered vesicles, coefficient of determination R^2=0.99 (Figure 5-51 / B). This 3-fold increase in the membrane stretching modulus signifies that the pre-existing CHMP4 polymer can also be rigidified by CHMP2B polymer, but conversely, it implies that in the presence of CHMP4, the membrane covered with CHMP2B is softened.

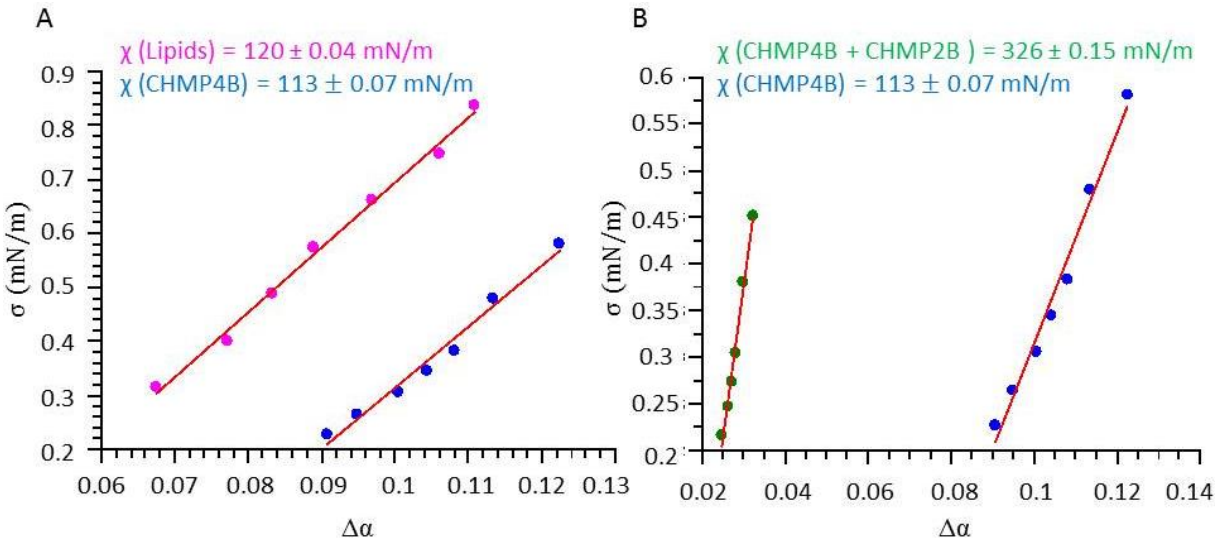

FIGURE 5-51: COMPARISON OF MICROPIPETTE ASPIRATION EXPERIMENTS WITH CHMP4B AND CHMP2B
Micropipette aspiration on a GUV sequentially incubated with CHMP4B and CHMP2B-ΔC.
(A) Variation of the excess area as a function of the applied tension for GUVs coated with CHMP4B proteins and bare GUVs as a comparison. Fits are in red. n=25.
(B) Comparison of the stretching experiments for GUVs coated with CHMP4B alone and CHMP4B + CHMP2B.Fits are in red. n=18.

As we did before for the other components, we next compared the mobility of CHMP2B and CHMP4B on the surface of GUVs. We prepared GUVs with the lipid mixture 5 and then incubated them in BP (NaCl 50 mM, Tris 25 mM at pH 7.5) for 30 min with CHMP4B or CHMP2B to reach full coverage of the polymer on the membrane. Once full coverage was reached, we diluted the vesicles with bound CHMP2B or CHMP4B proteins in BP, then, transferred them to the observation chamber and proceeded to the FRAP experiments.

As seen previously in chapter 5.2.4, upon photobleaching, CHMP2B-ΔC does not diffuse on the membrane surface, indicating that, once assembled, CHMP2B-ΔC polymer is no more dynamic. In contrast, the fluorescence signal of CHMP4B proteins recovers after photobleaching (Figure 5-52 / A) with CHMP4B mobile fraction about 25 % with $\tau_{1/2}$ around 23 sec).

This result proves that the CHMP4B proteins diffuse on the surface of the GUV. If we consider based on our AFM and EM images that CHMP4B forms spirals on membranes, our FRAP measurements suggest that these structures can move independently relative to each other but slowly considering their size and the crowding of the surface.

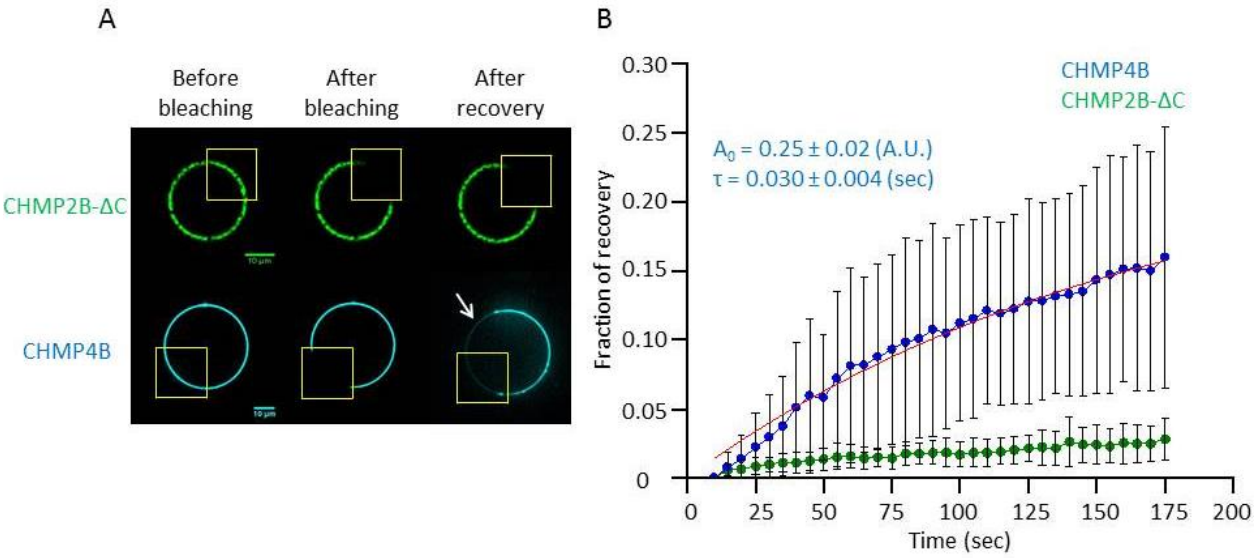

FIGURE 5-52: FRAP EXPERIMENTS ON CHMP4B VERSUS CHMP2B PROTEINS BOUND TO GUVS
FRAP experiments on vesicles covered either with CHMP2B-ΔC or CHMP4B.
(A) Confocal images showing fluorescence recovery for CHMP2B-ΔC and CHMP4B protein polymers after photobleaching. Yellow squares indicate the photobleached ROIs. White arrow shows the loss of fluorescence in an unbleached area of the GUV. Scale bar = 10 µm.
(B) Recovery versus time after photo-bleaching of CHMP2B-ΔC and CHMP4B polymers. n=45

5.5.2 CHMP2B DISORGANIZES CHMP4B SPIRALS ON FLAT SURFACES

We incubated CHMP4B-covered LUVs with CHMP2B and imaged the effect of the addition of CHMP2B by Cryo-EM. We observed a noticeable change in the arrangement of CHMP4B filaments (Figure 5-53 / A). On flat deformable LUVs, CHMP4B/CHMP2B spirals appear enlarged, with increased spacing between filaments. On average, the spacing between filaments within the spirals is larger than for CHMP4B alone: a mean value of 8.1 ± 1.8 nm versus 7.2 ± 1.4 nm, respectively (Figure 5-53 / A).

By HS-AFM, we also observed perturbations of the CHMP4B spirals on the membrane-coated mica support. We first formed CHMP4 spirals on the SLB then added CHMP2B proteins. With HS-AFM, we could follow the changes live. A reorganization of the spiral is observed when CHMP2B is added on SLB membrane bound CHMP4B (Figure 5-53 / B). CHMP4B spirals are locally disrupted, with some filaments pushed away and other compressed; the spirals thus become very irregular (Figure 5-53). We characterized the changes in the filament organization by measuring the spiral interfilament distance in the regions away from the “holes” appearing when CHMP2B is added, i.e. (see red section "4" in Figure 5-53 / B and C). Quantification of the filament distances indicates a mean value of 8.8 ± 0.2 nm. Sections were also performed at the position of the hole/disturbance of the spiral (see green section "3" in Figure 5-53 / B and C) showing a larger local distance between filaments 13.7±1.7 nm. We also observe that addition of CHMP2B leads to the enlargement of the diameter of the spiral center to 40.6 ± 1.3 nm (see blue section "5" in Figure 5-53 / B and C).

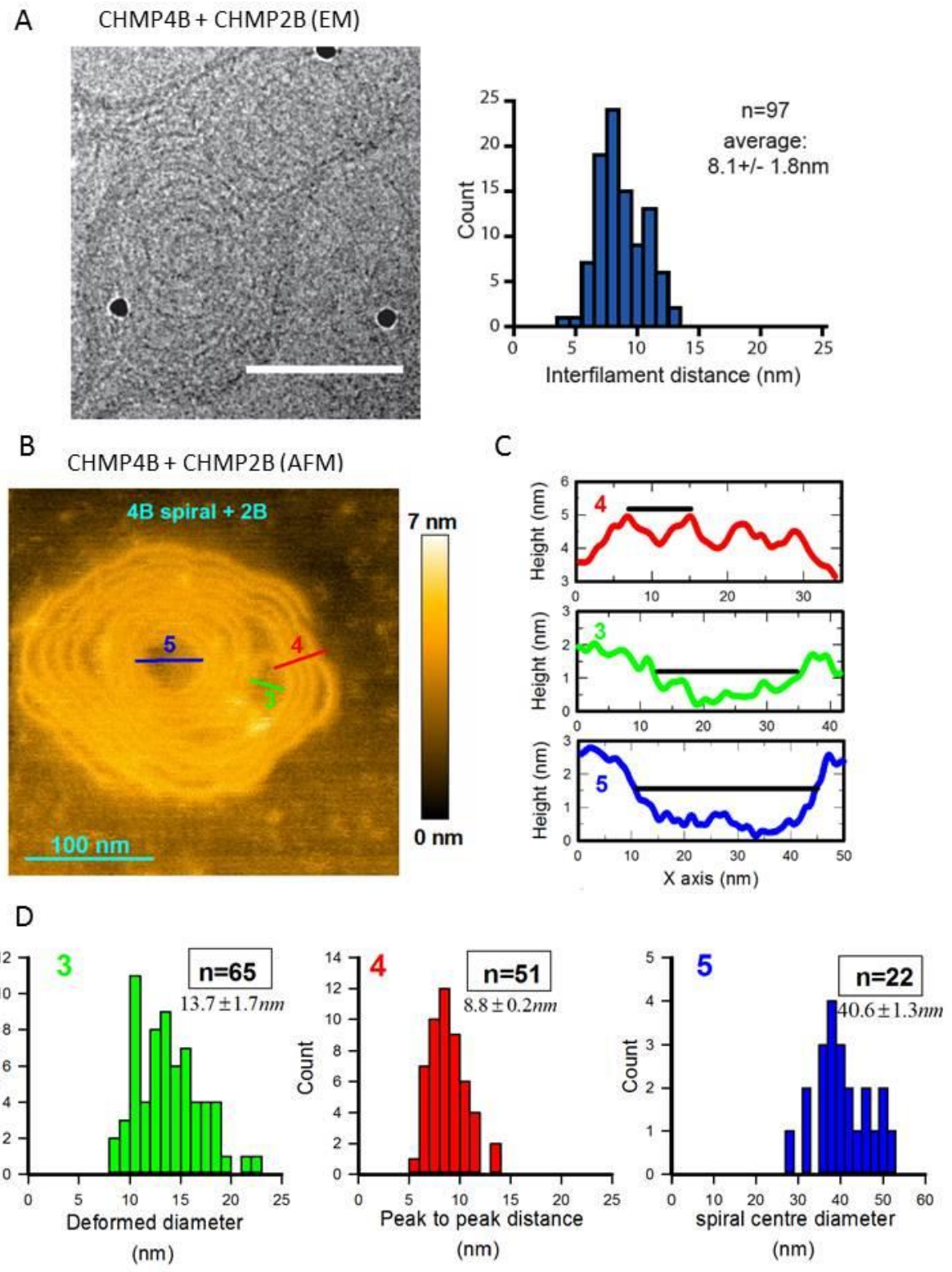

FIGURE 5-53: EFFECT OF CHMP2B ON CHMP4B POLYMERIZATION ON MEMBRANE

(A) Cryo-EM image showing the modulation of CHMP4B spirals on LUV membrane by addition of CHMP2B. Scale bar = 100 nm. Quantification of interfilament distance is shown on the right.

(B) AFM image showing the modulation of CHMP4B spirals on SLB membrane by addition of CHMP2B. Scale bar = 100 nm.

(C) Profiles of sections of the spiral shown in (B) between deformed filaments (green), between filaments far from the "holes" (red) and across the spiral center(blue).

(D) Histograms showing different distances between distorted/deformed filaments (i.e. diameter of the holes) (green), the peak to peak between filaments far from perturbance (red) and the spiral center diameter (blue).

It was possible to image live by HS-AFM the effect of CHMP2B on LUVs with a diameter about 20 to 100 nm, covered with CHMP4B. Surprisingly, whereas the vesicles remained more or less spherical with CHMP4B alone, we observed the gradual emergence of single or multiple protrusions OUT of the vesicle a few seconds (around 9 sec) after addition of CHMP2B. Figure 5-54 shows this vesicle distortion.

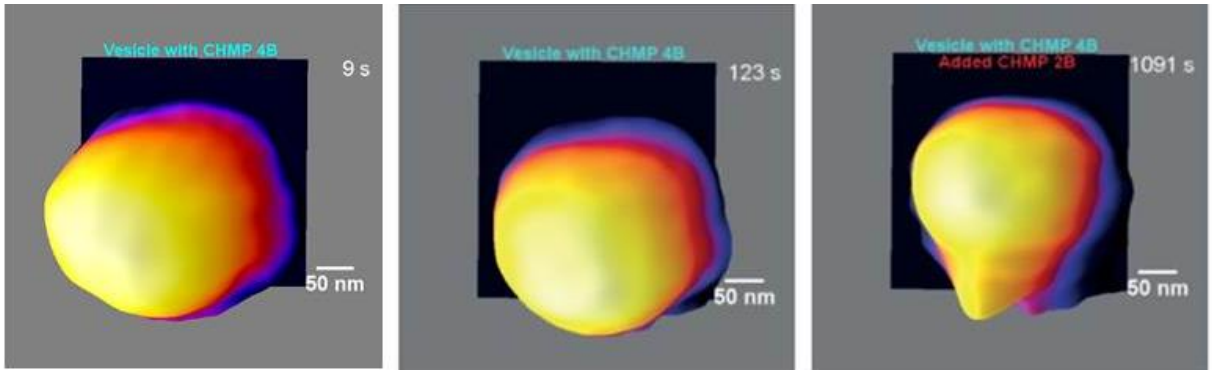

FIGURE 5-54: DISTORSION OF CHMP4B-COVERED GUV BY ADDITION OF CHMP2B
Individual frames of AFM movie capturing the deformation over time of a vesicle pre-incubated with CHMP4B by the addition of CHMP2B (t=0 corresponds to CHMP2B addition). Scale bar: 50 nm.

Moreover, to confirm that this effect is only due to the addition of CHMP2B proteins and not a result of a change in the buffer salinity or time, we imaged CHMP4B spirals in a different buffer (NaCl 150 mM, Tris 25mM at pH=7.5) and in BP over time without CHMP2B. These control experiments showed a preservation of the original spiral organization, thus confirming the strong deforming effect of CHMP2B. Note that the topology of the deformation is surprising since an invagination would be expected with the opposite curvature following the current models on ESCRTs. Moreover, it shows that with CHMP2B, the co-polymer structure is now stiff enough to deform a vesicle.

5.5.3 CHMP2A AND CHMP2B INDUCE DEFORMATIONS ON CHMP4 ASSEMBLY ON MEMBRANE TUBES

We next studied the effect of CHP2B and CHMP2A+3 on tubules covered with CHMP4B. As explained previously, our sample preparation usually contains vesicles and a small amount of tubes (percentage of tubes = 15.4 ± 3.4 % in the absence of proteins). Surprisingly, the presence of CHMP2B or CHMP2A+CHMP3 significantly increased the number of these tubes as shown in the low magnification Cryo-EM image (Figure 5-55). Due to the striking number, quantification wasn't possible to do.

Thus it shows that both CHMP2B proteins and also CHMP2A, induce CHMP4B-bound membrane budding and tubulation, in agreement with AFM observations.

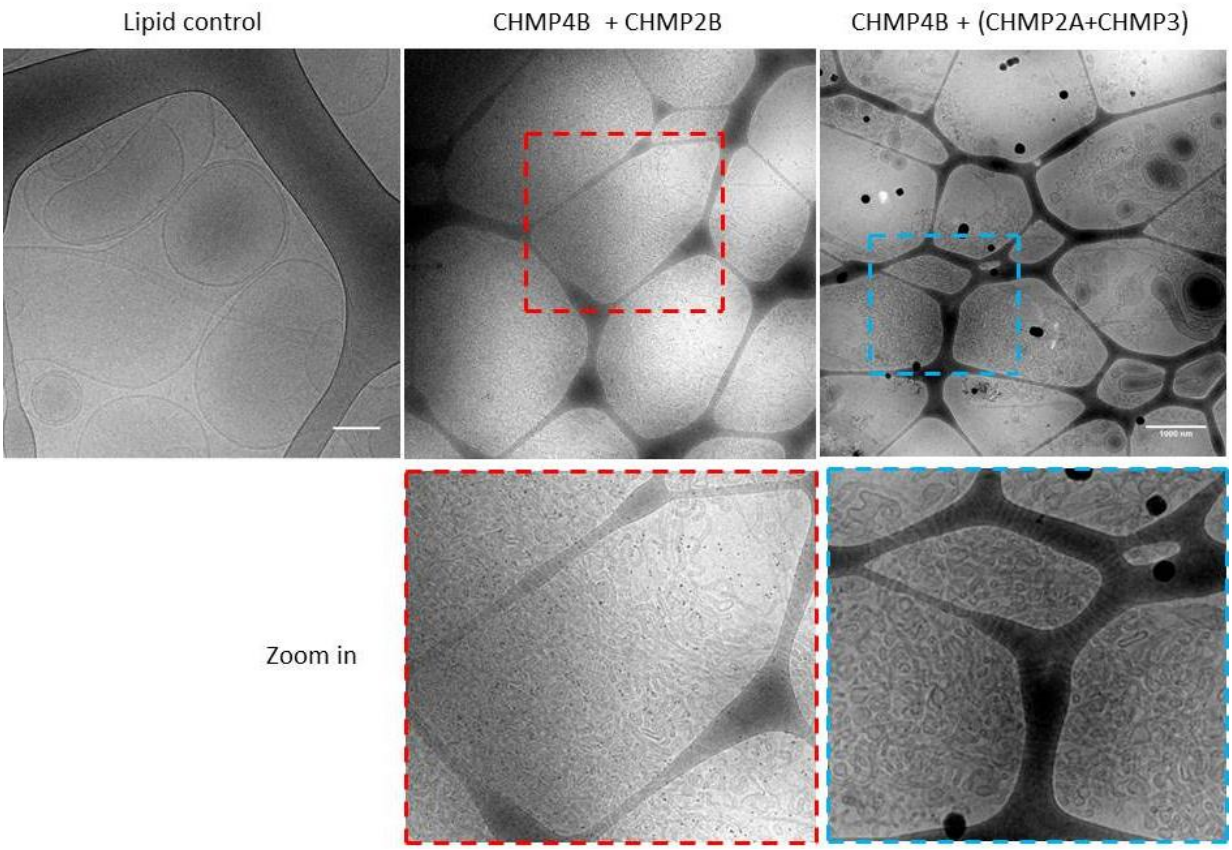

FIGURE 5-55: LOW-MAGNIFICATION CRYO-EM IMAGE SHOWING TUBULATION AFTER ADDITION OF CHMP2B OR CHMP2A+CHMP3 TO CHMP4B-BOUND LUVS
Scale bar = 1000 nm.

By Cryo-EM, we observed that the addition of CHMP2B causes an overall striking deformation of the tube, but keeping the CHMP4B filaments parallel to the main axis of the tube. Indeed, tubes tend to have a regular helical shape ("corkscrew-like") (Figure 5-56 / A). The diameter of these tubes is very regular and about 29.8 ± 9 nm (Figure 5-57 / E). The periodicity of the helical tubes is about 83.7 ± 22 nm, with a width (diameter) of spiral equal 97.7 ± 23 nm. CHMP4 polymers are aligned along the axis of the tubes, and are quite regularly distributed around the tube perimeter, as can been seen at each turn of the spiral, where a section of the tube with the perpendicular polymers is visible (Figure 5-56 / A). However, at this resolution, CHMP2B is not visible on the tubes (Figure 5-56 / A – zoom-in), thus we cannot conclude on its organization with regard to CHMP4B.

This rearrangement of CHMP4B polymer on the underlying deformable membrane supports the idea that CHMP2B acts mechanically on CHMP4B filaments, inducing a conformational change that promotes the transition of CHMP4B filaments to a 3D helical arrangement. Eventually, this transition is transmitted to the underlying membrane, provided that the membrane is not mechanically constrained.

Addition of CHMP2A + CHMP3 to pre-formed CHMP4B flat spirals formed on vesicles induces a similar effect as with CHMP2B. Enlarged spirals are observed in Cryo-EM with a distance between CHMP4 filaments equal to 11.9 ± 3.1 (Figure 5-57 / B). When CHMP2A + CHMP3 are added on tubular membrane with CHMP4 polymers bound, helical tubular structures are also observed by Cryo-EM, although less regular than when CHMP2B is added (Figure 5-56 / C). The tube diameters are on average lower (about 18.8 ± 7 nm) (Figure 5-57 / E). The spiral diameter and pitch of the helical tubes are similar those observed with CHMP4B + CHMP2B.

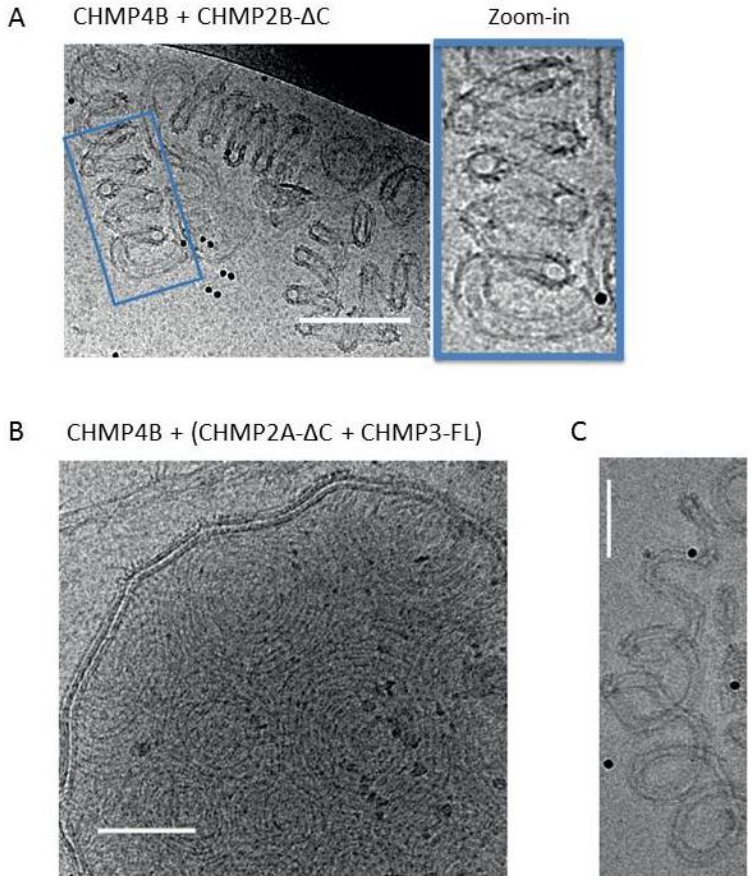

FIGURE 5-56: MODULATION OF CHMP4B ASSEMBLY BY CHMP2A AND CHMP2B PROTEINS IMAGED BY CRYO-EM
(A) Sequential addition of CHMP2B on tubular membrane pre-incubated with CHMP4B. Corkscrew tube magnification is shown on the right panel. Scale bar = 100 nm.
(B) Sequential addition of CHMP2A (+CHMP3) on pre-formed CHMP4B spirals on vesicles. Scale bar = 100 nm.
(C) Sequential addition of CHMP2A (+CHMP3) on tubular membrane pre-incubated with CHMP4B. Scale bar = 100 nm.

To conclude, CHMP2B and CHMP2A (+ CHMP3) induce a mechanical deformation of CHMP4B filaments, resulting in a transition to a more regular 3D spiral. This transition can be quantified by measuring helix length (Figure 5-57 / A). The features of the CHMP2B and CHMP2A spirals are rather similar in terms of length and width (Figure 5-57 / B and C). Helix periodicity and tube diameter appear to be smaller in case of CHMP2A + CHMP3 (Figure 5-57/ D and E). It seems that CHMP2B and CHMP2A plus CHMP3 induce similar three-dimensional deformations and membrane remodeling even though, individually, they organize quite differently.

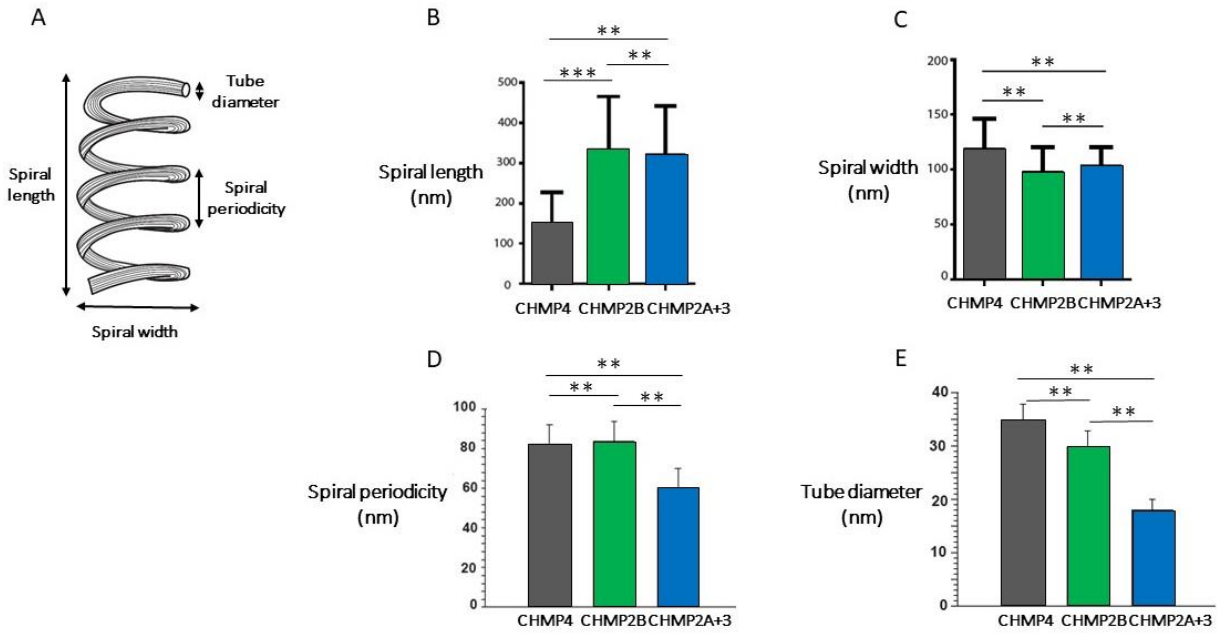

FIGURE 5-57: COMPARISON OF CHMP4B SPIRAL MEASUREMENTS IN PRESENCE OF CHMP2A/B PROTEINS
(A) Schema illustrating the 3D helix parameters quantified from Cryo-EM data
(B) Quantification of spiral length from Cryo-EM data. *=p-value<0.05; ***=p-value<0.001 (Tukey's multiple comparison test).
(C) Quantification of spiral width from Cryo-EM data. (Tukey's multiple comparison test).
(D) Quantification of helix periodicity from Cryo-EM data. (Tukey's multiple comparison test).
(E) Quantification of the interfilament spacing from Cryo-EM data. (Tukey's multiple comparison test).

CHAPTER 6. CONCLUSIONS AND PERSPECTIVES

In this study, we have first investigated *in vitro* how the ESCRT-III protein CHMP2B assembles on lipid membranes and the consequences on membrane mechanical and dynamical properties. We have next compared CHMP2B to CHMP2A since, so far, both proteins were supposed to be homologous. We have next added CHMP3 that was known to co-polymerize with CHMP2A and again compared its interaction with CHMP2B. Eventually, towards a reconstitution of the minimal ESCRT scission machinery, we have added CHMP4 and compared the assemblies of CHMP4 with CHMP2B on the one hand and with CHMP2A + CHMP3 on the other hand. Our main results are summarized below.

- CHMP2B. We have shown that CHMP2B has a strong preference for PI(4,5)P_2 lipids, in contrast with the other ESCRTs that we have studied that bind indifferently negatively charged membranes. This higher affinity for PI(4,5)P_2 lipids fits well with the role *in vivo* of CHMP2B's on membranes containing PI(4,5)P_2 lipids only: at the plasma membrane for HIV virus egress, membrane repair and cytokinesis and at the nuclear envelop for damage repair (Di Paolo and De Camilli 2006; Garnier-Lhomme, Byrne et al. 2009). With Cryo-EM and HS-AFM, we have obtained for the first time the structure of CHMP2B assemblies on membranes: it forms very small rings that organize into honeycomb-like network at large densities. At larger scale, protein binding results into a reticular-like structure wrapping all over PI(4,5)P_2-GUVs.

In addition, we showed that the membrane elastic properties are altered in the presence of the CHMP2B. Micropipette aspiration experiments on GUVs and HS-AFM deformation experiments on SUVs indicate that CHMP2B-covered membranes are very stiff, which is not the case when they are coated with the other CHMP proteins that we have studied. The biological consequences of this unique mechanical characteristic is not clear, but considering that CHMP2B is involved in the reparation of the plasma membrane or the nuclear envelop, but not in the formation of MVB, this high degree of rigidity is maybe required in these processes. Moreover, FRAP experiments show that once assembled the polymer forms a "static" network that blocks the diffusion of membrane-associated proteins. This ability to block the diffusion of membrane proteins might be crucial during unexpected events like plasma membrane rupture, but also during cytokinesis in complement to septins to form a diffusion barrier (Caudron and Barral 2009).

CHMP2B C-terminal truncation results in an increase of protein affinity to the membrane. We showed that CHMP2B-FL proteins has a weaker affinity for PI(4,5)P_2-containing membranes than CHMP2B- ΔC, but still almost twice higher than the other ESCRT-III proteins, as observed by FACS and spinning-disk confocal microscopy. It confirms that the C-terminal truncation of the protein results in an active protein

form as expected from previous studies (Zamborlini, Usami et al. 2006; Shim, Kimpler et al. 2007; Bajorek, Schubert et al. 2009). Yet, the C-terminal truncated protein resembles in terms of sequence to the mutant CHMP2B^{intron5}, involved in the FTD disease. CHMP2B^{intron5} causes impaired maturation of dendritic spines, a phenotype that appears to be unrelated to defect in autophagy (Belly, Bodon et al. 2010). The higher affinity for PI(4,5)P_2 due to the C-terminal mutation and the high degree of the rigidity of the assembly could relate CHMP2B to the pathology. Indeed, similarly to our observations with CHMP2B-ΔC, the mutation at the protein C-terminus is expected to result in a significant increase of the mutant protein affinity to the plasma membrane. The mutant protein in large excess on the plasma membrane as compared to the wild-type protein, could induce a stiffening of the membrane and by that contribute to the FTD onset. Moreover, CHMP2B polymerization at sites of nascent dendritic spines could block the membrane deformation process needed for dendritic spine formation and maturation. The ability of CHMP2B to block diffusion on the membrane surface would as well provide a further level of misregulation, for instance inhibiting the diffusion of receptors to dendritic spines and thus blocking their development.

- **CHMP2B and CHMP2A assemble differently and display opposite mechanical properties.** We have compared CHMP2B assembly and mechanical properties to that of CHMP2A, its closest homologue in terms of sequence. We unambiguously showed that CHMP2A requires to co-assemble with CHMP3 to bind to membranes, in contrast to CHMP2B that binds alone, in agreement with previously reported properties both *in vivo* and *in vitro* in solution (Babst, Katzmann et al. 2002; Lata, Schoehn et al. 2008; Henne, Buchkovich et al. 2012; Effantin, Dordor et al. 2013). Furthermore, CHMP2A + CHMP3 co-polymers do not exhibit an exclusive affinity to PI(4,5)P_2 lipids and assemble in a homogeneous manner on the GUV surface. Interestingly, outward-pointing membrane protrusions from the GUV surface are induced by the CHMP2A + CHMP3 co-polymer. In contrast with CHMP2B, once bound to the membrane, the CHMP2A + CHMP3 assemblies on the GUV remain dynamic and do not form any diffusion barrier to membrane-associated proteins. Eventually, the CHMP2A + CHMP3 co-polymer does not change membrane elasticity. Arguably, membrane unaltered softness is important at the very last stage of the membrane scission event carried out by ESCRT-III complex, whereas a rigid structure would oppose this process. However, a certain degree of membrane rigidity might help the constriction process prior to scission, but at this stage, it is difficult to conclude on this aspect. Moreover, at the nanometer scale, CHMP2B proteins form ring-structures whereas CHMP2A alone forms spirals *in vivo* (Lata, Roessle et al. 2008; Lata, Schoehn et al. 2008; Guizetti, Mantler et al. 2011; Guizetti, Schermelleh et al. 2011; Effantin, Dordor et al. 2013) and CHMP2A + CHMP3 form filaments or conical tubes *in vivo* and *in vitro* (Lata, Schoehn et al. 2008; Effantin, Dordor et al. 2013) and spirals around membrane tubules *in vitro* as shown with our Cryo-EM data. For all these reasons, it is difficult to argue that CHMP2B and CHMP2A are

functional homologues and play the same role in the ESCRT-III machinery. In fact, CHMP2A, CHMP3 and CHMP2B could constitute a functional module able to regulate membrane viscoelastic properties in order to accomplish scission. And, the fact that only CHMP2A has a MIM domain binding to the ATPase VPS4 might correlate with its recruitment at the final stage prior to scission and complex disassembly.

- CHMP3 works synergistically with CHMP2A but not with CHMP2B proteins. In contrast with CHMP2A and CHMP3 that work synergistically, we have shown by spinning disk confocal microscopy that the polymerization and coverage of CHMP2B on GUVs is reduced in the presence of CHMP3. FACS quantification confirmed this result and showed that CHMP2B binding to $PI(4,5)P_2$-membrane is drastically diminished when CHMP3 is added. Additionally, micropipette aspiration experiments show that CHMP2B assembly on membranes is softened in the presence of CHMP3. This moderating effect of CHMP3 proteins on CHMP2B polymerization is consistent with previously published studies showing that CHMP2B and CHMP3 do not work synergistically during HIV budding (Effantin, Dordor et al. 2013) and do not co-polymerize *in vitro* (Lata, Schoehn et al. 2008). We thus propose that CHMP3 could play a key regulation role in the sequence of recruitment of CHMP2B and CHMP2A proteins in the machinery and in their respective stoichiometry on the membranes. The ability of CHMP3 to regulate the polymerization of CHMP2A and CHMP2B suggests that this protein might also operate as a molecular switch during modulation of membrane rigidity.

- CHMP4B alone does not induce membrane deformation. A recently published study by Chiaruttini et. al (Chiaruttini, Redondo-Morata et al. 2015) analyzes the mechanical properties of Snf7, the yeast analogue of CHMP4, deduced from HS-AFM on SLBs on mica. The authors show that Snf7 proteins polymerize into spirals on flat membranes with a preferred radius of 25 nm; they propose that spirals growing beyond this preferred radius accumulate stress. They eventually develop a "Spiral Spring" model in which Snf7 should induce membrane deformation and inward buckling to release the stress. According to the authors, this model should account for the tubular exvaginations observed *in vivo* upon over expression of Snf7 (with about a 100 nm diameter) (Hanson, Roth et al. 2008). Nevertheless, not such membrane deformation or tubulation has been observed so far *in vitro* in the presence of snf7 or CHMP4 only. In our work, we studied the mechanical properties of the human protein CHMP4B on deformable membrane. We showed by FACS that CHMP4B proteins bind equally all the PIP species. Surprisingly, the assembly of CHMP4B proteins on GUVs did not induce any membrane invagination or tubulation as predicted by the "Spiral Spring" model. Moreover, we show by micropipette aspiration that CHMP4 does not stiffen the membrane like CHMP2B or as expected with the high persistence length of 260 nm calculated in (Chiaruttini, Redondo-Morata et al. 2015). Interestingly, we find a plastic behaviour of GUVs covered with CHMP4B after release of aspiration, similar to Snf7. At high resolution

by HS-AFM and Cryo-EM, we observe that CHMP4B forms spirals on membrane with similar characteristics as those published for Snf7. The most important result is that the spiral structure remains flat on the vesicles without leading to a 3D membrane budding or deformation as predicted. Moreover, on preformed deformable membrane tubes, CHMP4B proteins assemble parallel to the tube main axis when the diameter is smaller than 40 - 50 nm, inducing some spiraling of the tubes. But, interestingly, CHMP4B assembly alone does not affect the tube diameter. Moreover, on straight non-deformable Galcer tubes, CHMP4B proteins seem very weakly twisted with a large pitch. In addition of the absence of membrane deformation induced by CHMP4 polymers, our results point to a very unexpected characteristic: CHMP4 can clearly assemble on positively curved membranes, such as on the external surfaces of membrane tubes. This property was already described for another ESCRT protein, CHMP1B-IST1 (McCullough, Clippinger et al. 2015). For CHMP4B and Snf7, it was shown that, when negatively curved membrane invaginations are present (via SLBs deposited in 100 nm-deep nanofabricated concavities) polymerization is preferentially nucleated in these curved area but proceeds next towards the exterior of the cavities on the flat region (Lee, Kai et al. 2015). Note that a curved cavity has geometry similar to a sphere with a positive Gaussian curvature, different from the geometry of the necks with a negative Gaussian curvature (i.e. two curvatures of opposite signs) where the ESCRT-III complexes operate. We show with our experiments that CHMP4B can also assemble on a positively curved tube but along its main axis where curvature is minimal. Altogether, this shows that CHMP4 assemblies alone are not able to deform membranes and are rather flat on non-curved surfaces, but bind onto tubes in a way that minimizes the spontaneous curvature and preserves its twist.

- CHMP2B and CHMP2A + CHMP3 induce morphological changes on CHMP4B-bound membranes. With HS-AFM, we showed that the addition of CHMP2B induces local deformations of CHMP4B spirals previously formed on a non-deformable SLB, with locally higher interfilament spacing. Furthermore, we showed with HS-AFM that CHMP2B causes the distortion of CHMP4B-coated SUVs and budding out of the vesicle only few seconds after addition of CHMP2B. Interestingly, EM data confirm this striking effect of CHMP2B on CHMP4B-coated membrane. We showed that deformable membrane tubes covered with CHMP4B are remodelled in the presence of CHMP2B. Actually, the initially irregular tubes adopt a regular corkscrew-like morphology with CHMP4 oriented parallel to the tube axis. The mean tube diameter is slightly reduced. This implies that CHMP2B proteins not only rigidify the CHMP4 assembly as observed with our micropipette aspiration experiments, which allows for a regular helical tube morphology but also induces some spontaneous curvature that influences the tube diameter. CHMP2A+CHMP3 induce similar three-dimensional deformations on CHMP4B filaments, organizing them along the axis of regular 3D spirals with a significantly smaller tube radius (twice smaller than in the absence of the copolymer). In addition, EM data confirmed a significantly increased membrane

tubulation when CHMP2B and CHMP2A+CHMP3 are added to a membrane preparation pre-incubated with CHMP4B, as compared to the control, consistent with the CHMP2B-budding effect observed by AFM. Importantly, the regular CHMP4B 3D helices on tubes resemble in terms of size and topology the helical filaments of unknown composition observed in vivo during cytokinesis (Guizetti, Schermelleh et al. 2011; Sherman, Kirchenbuechler et al. 2016). Thus, although presenting different mechanical properties, CHMP2A (+CHMP3) and CHMP2B proteins induce similar effects on CHMP4B-bound membrane, which might explain their redundant effect in HIV egress (Morita, Sandrin et al. 2011). Most importantly, neither CHMP2B nor CHMP2A+CHMP3 alone can induce such a drastic membrane remodelling. In fact, our results clearly indicate that CHMP4B must be previously bound to the membrane, meaning that a pre-existing CHMP4B scaffold is required.

Moreover, we made the puzzling observation that CHMP2+CHMP3, and CHMP4 alone are able to assemble onto positively curved tubes, *a priori* contrary to the *in vivo* situation, with CHMP2A+CHMP3 spiraling around the tubes while CHMP4 is aligned along the tube axis that becomes helical. This implies that the CHMP2A-CHMP3 co-polymer has affinity for positively curved membranes. In the case of CHMP4B, this implies that this protein has neither affinity for highly positively curved surfaces such as tubes in contrast with CHMP2A+CHMP3 but probably nor for highly negatively curved surface since it aligns parallel to the zero-curvature line along the tube; at the same time, it imposes a twist to the tube with a curvature of the order of 1/50 nm^{-1}. Moreover, the mixed assemblies of CHMP4B with CHMP2B or CHMP2A+CHMP3 also form on positively-curved membrane tubes, keeping CHMP4B parallel to the tube axis. The strong reduction of the tube diameter in the presence of CHMP2A+CHMP3 suggests that these proteins probably constrict the tube by assembling along the positively curved area (perpendicular to the tube axis) like in the absence of CHMP4B. We cannot distinguish CHMP2B on the Cryo-EM images, thus we cannot discuss its preference for one or the other type of curvature. We also observe that the radius of the helical structure remains unchanged (about 50 nm) even when CHMP2B or CHMP2A+CHMP3 are present. This topology for CHMP4B is not in contradiction with the *in vivo* situation if we consider that the surface of the neck is locally represented by the envelope of the tube, thus with a negative curvature. It implies that CHMP4B might have affinity for negatively curved membranes, but with a low preferential curvature of the order of 1/50 nm^{-1}. If membrane curvature deviates from this value, CHMP4B polymer favors a flat conformation. Globally, it shows that 2 types of filaments operate at the neck with opposite properties: CHMP4B with affinity for weak negative curvatures (≈1/50 nm^{-1}) and CHMP2A+CHMP3 with a preference for strong positive curvatures (≈1/8 nm^{-1}). CHMP2B, due to its unique mechanical properties, might contribute to the stiffening of the assembly of the complex.

In vivo, these ECRT-III proteins operate inside neck structures, which are formed prior to their recruitment, either by other ESCRTs (in MVBs), by the acto-myosin constricting ring at the cytokinesis site, by the HIV-coated bud or hole formation upon membrane rupture. The ESCRT-III proteins are

recruited by other proteins such other ESCRTs, Alix or Gag in the case of HIV budding to a location where membrane curvature is negative. Initially, the radius of curvature is probably large enough to favor CHMP4 helical assembly. However, the shape of the membrane is not cylindrical but has a negative Gaussian curvature (a combination of negative curvature perpendicular to the neck axis and positive curvature in the normal direction), thus can also recruit CHMP2A+CHMP3 along the positively curved surface. This shows that our conclusions, based on our Cryo-EM observations, are well compatible with the actual geometry of the membranes at the site of actions of these ESCRT proteins.

- Perspectives. The first experiments that should be performed following this work would be to directly test the affinity of the CHMP proteins for positive and negative curvature. They are currently continued by N. de Franceschi in the lab. Considering the peculiar mechanical properties of CHMP2B, this protein might be left apart in a first place. Membrane nanotubes can be pulled from GUVs and the proteins either incubated or injected on the nanotube to test the affinity for positive curvature. Based on our observations, we would expect to measure a preferential binding of CHMP2A+3 to highly curved tubes. For CHMP4, large tubes (with a diameter of the order of 100 nm) have to be formed to check if the protein could assemble in this case. Studying the affinity for negative curvature is trickier because it requires developing new methods for the encapsulation of the proteins (in chapter 5.1.2). Nevertheless, it is a prerequisite to be in a position to eventually reconstitute membrane scission by the ESCRT complex.

In our experiments, we never observed membrane scission. This is certainly due to the reverted geometry of our experiments and also to the absence of Vps4. Not only Vps4 is known to depolymerize the ESCRT complex, it is also thought to play a regulatory role (Mierzwa, Chiaruttini et al. 2017). The new generation of experiments has to include Vps4 and ATP in the mix of proteins. This will obviously complicate the encapsulation protocol. To trigger the reaction, caged ATP can be used and released with UV light. Based on our hypothesis, we expect that the only place that fits the geometry of the complex is the neck of the tube, thus a very restricted zone of the tube. We envision quite challenging experiments to test existing fission models as well as the probable necessity to develop new ones.

BIBLIOGRAPHY

Abkarian, M., E. Loiseau, et al. (2011). "Continuous droplet interface crossing encapsulation (cDICE) for high throughput monodisperse vesicle design." Soft Matter **7**(10): 4610-4614.

Adell, M. A. and D. Teis (2011). "Assembly and disassembly of the ESCRT-III membrane scission complex." FEBS Lett **585**(20): 3191-3196.

Adell, M. A., G. F. Vogel, et al. (2014). "Coordinated binding of Vps4 to ESCRT-III drives membrane neck constriction during MVB vesicle formation." J Cell Biol **205**(1): 33-49.

Adell, M. A. Y., S. M. Migliano, et al. (2016). "ESCRT-III and Vps4: a dynamic multipurpose tool for membrane budding and scission." FEBS Journal: n/a-n/a.

Adell, M. A. Y., S. M. Migliano, et al. (2017). "Recruitment dynamics of ESCRT-III and Vps4 to endosomes and implications for reverse membrane budding." Elife **6**: e31652.

Agromayor, M. and J. Martin-Serrano (2013). "Knowing when to cut and run: mechanisms that control cytokinetic abscission." Trends Cell Biol **23**(9): 433-441.

Aimon, S., J. Manzi, et al. (2011). "Functional reconstitution of a voltage-gated potassium channel in giant unilamellar vesicles." PLoS One **6**(10): 6.

Alonso, Y. A. M., S. M. Migliano, et al. (2016). "ESCRT-III and Vps4: a dynamic multipurpose tool for membrane budding and scission." Febs J **283**(18): 3288-3302.

Ando, T. (2014). High-speed AFM imaging.

Ando, T. (2017). High-speed atomic force microscopy for observing protein molecules in dynamic action. 31st International Congress on High-Speed Imaging and Photonics, SPIE.

Angelova, M. I., S. Soléau, et al. (1992). Preparation of giant vesicles by external AC electric fields. Kinetics and applications. Trends in Colloid and Interface Science VI. C. Helm, M. Lösche and H. Möhwald. Darmstadt, Steinkopff**:** 127-131.

Antonny, B., C. Burd, et al. (2016). "Membrane fission by dynamin: what we know and what we need to know." The EMBO Journal **35**(21): 2270-2284.

Axelrod, D., D. E. Koppel, et al. (1976). "Mobility measurement by analysis of fluorescence photobleaching recovery kinetics." Biophys J **16**(9): 1055-1069.

Azmi, I., B. Davies, et al. (2006). "Recycling of ESCRTs by the AAA-ATPase Vps4 is regulated by a conserved VSL region in Vta1." J Cell Biol **172**(5): 705-717.

Babst, M., B. A. Davies, et al. (2011). "Regulation of Vps4 during MVB sorting and cytokinesis." Traffic **12**(10): 1298-1305.

Babst, M., D. J. Katzmann, et al. (2002). "ESCRT-III: An endosome-associated heterooligomeric protein complex required for MVB sorting." Developmental Cell **3**(2): 271-282.

Babst, M., B. Wendland, et al. (1998). "The Vps4p AAA ATPase regulates membrane association of a Vps protein complex required for normal endosome function." EMBO J **17**(11): 2982-2993.

Bajorek, M., H. L. Schubert, et al. (2009). "Structural basis for ESCRT-III protein autoinhibition." Nat Struct Mol Biol **16**(7): 754-762.

Bankaitis, V. A., L. M. Johnson, et al. (1986). "Isolation of yeast mutants defective in protein targeting to the vacuole." Proc Natl Acad Sci U S A **83**(23): 9075-9079.

Barlowe, C., L. Orci, et al. (1994). "COPII: a membrane coat formed by Sec proteins that drive vesicle budding from the endoplasmic reticulum." Cell **77**(6): 895-907.

Bashkirov, P. V., S. A. Akimov, et al. (2008). "GTPase cycle of dynamin is coupled to membrane squeeze and release, leading to spontaneous fission." Cell **135**(7): 1276-1286.

Baumgartel, V., S. Ivanchenko, et al. (2011). "Live-cell visualization of dynamics of HIV budding site interactions with an ESCRT component." Nat Cell Biol **13**(4): 469-474.

Belly, A., G. Bodon, et al. (2010). "CHMP2B mutants linked to frontotemporal dementia impair maturation of dendritic spines." J Cell Sci **123**(17): 2943-2954.

Bernard, A. L., M. A. Guedeau-Boudeville, et al. (2002). "Raspberry vesicles." Biochim Biophys Acta **23**: 1-2.

Bodon, G., R. Chassefeyre, et al. (2011). "Charged Multivesicular Body Protein 2B (CHMP2B) of the Endosomal Sorting Complex Required for Transport-III (ESCRT-III) Polymerizes into Helical Structures Deforming the Plasma Membrane." Journal of Biological Chemistry **286**(46): 40276-40286.
Bodon, G., R. Chassefeyre, et al. (2011). "Charged Multivesicular Body Protein 2B (CHMP2B) of the Endosomal Sorting Complex Required for Transport-III (ESCRT-III) Polymerizes into Helical Structures Deforming the Plasma Membrane." Journal of Biological Chemistry **286**(46): 40276-40286.
Bonifacino, J. S. and B. S. Glick (2004). "The Mechanisms of Vesicle Budding and Fusion." Cell **116**(2): 153-166.

Braga, J., J. M. Desterro, et al. (2004). "Intracellular macromolecular mobility measured by fluorescence recovery after photobleaching with confocal laser scanning microscopes." Mol Biol Cell **15**(10): 4749-4760.

Braunger, J. A., C. Kramer, et al. (2013). "Solid Supported Membranes Doped with PIP2: Influence of Ionic Strength and pH on Bilayer Formation and Membrane Organization." Langmuir **29**(46): 14204-14213.

Brewer, S. H., W. R. Glomm, et al. (2005). "Probing BSA Binding to Citrate-Coated Gold Nanoparticles and Surfaces." Langmuir **21**(20): 9303-9307.

Brochard, F. and J. F. Lennon (1975). "Frequency spectrum of the flicker phenomenon in erythrocytes." Journal de Physique **36**(11): 1035-1047.

Buchkovich, Nicholas J., William M. Henne, et al. (2013). "Essential N-Terminal Insertion Motif Anchors the ESCRT-III Filament during MVB Vesicle Formation." Developmental Cell **27**(2): 201-214.

Campelo, F. and V. Malhotra (2012). "Membrane fission: the biogenesis of transport carriers." Annu Rev Biochem **81**: 407-427.

Campelo, F., H. T. McMahon, et al. (2008). "The hydrophobic insertion mechanism of membrane curvature generation by proteins." Biophys J **95**(5): 2325-2339.

Campillo, C., P. Sens, et al. (2013). "Unexpected membrane dynamics unveiled by membrane nanotube extrusion." Biophys J **104**(6): 1248-1256.

Campsteijn, C., M. Vietri, et al. (2016). "Novel ESCRT functions in cell biology: spiraling out of control?" Curr Opin Cell Biol **41**: 1-8.

Carlton, J. G., M. Agromayor, et al. (2008). "Differential requirements for Alix and ESCRT-III in cytokinesis and HIV-1 release." Proc Natl Acad Sci U S A **105**(30): 10541-10546.

Carlton, J. G., A. Caballe, et al. (2012). "ESCRT-III governs the Aurora B-mediated abscission checkpoint through CHMP4C." Science **336**(6078): 220-225.

Carlton, J. G. and J. Martin-Serrano (2007). "Parallels between cytokinesis and retroviral budding: a role for the ESCRT machinery." Science **316**(5833): 1908-1912.

Carvalho, K., L. Ramos, et al. (2008). "Giant Unilamellar Vesicles Containing Phosphatidylinositol(4,5)bisphosphate: Characterization and Functionality." Biophysical Journal **95**(9): 4348-4360.

Cashikar, A. G., S. Shim, et al. (2014). "Structure of cellular ESCRT-III spirals and their relationship to HIV budding." Elife: e02184.

Caudron, F. and Y. Barral (2009). "Septins and the lateral compartmentalization of eukaryotic membranes." Dev Cell **16**(4): 493-506.

Chappie, J. S., J. A. Mears, et al. (2011). "A pseudoatomic model of the dynamin polymer identifies a hydrolysis-dependent powerstroke." Cell **147**(1): 209-222.

Chatellard-Causse, C., B. Blot, et al. (2002). "Alix (ALG-2-interacting protein X), a protein involved in apoptosis, binds to endophilins and induces cytoplasmic vacuolization." J Biol Chem **277**(32): 29108-29115.

Chernomordik, L. V. and M. M. Kozlov (2003). "Protein-lipid interplay in fusion and fission of biological membranes." Ann Rev Biochem **72**(1): 175-207.

Chernomordik, L. V. and M. M. Kozlov (2005). "Membrane hemifusion: crossing a chasm in two leaps." Cell **123**(3): 375-382.

Chiaruttini, N., L. Redondo-Morata, et al. (2015). "Relaxation of Loaded ESCRT-III Spiral Springs Drives Membrane Deformation." Cell **163**(4): 866-879.
Cho, N.-J., C. W. Frank, et al. (2010). "Quartz crystal microbalance with dissipation monitoring of supported lipid bilayers on various substrates." Nat. Protocols **5**(6): 1096-1106.
Christ, L., C. Raiborg, et al. (2017). "Cellular Functions and Molecular Mechanisms of the ESCRT Membrane-Scission Machinery." Trends Biochem Sci **42**(1): 42-56.
Christ, L., E. M. Wenzel, et al. (2016). "ALIX and ESCRT-I/II function as parallel ESCRT-III recruiters in cytokinetic abscission." The Journal of Cell Biology **212**(5): 499.
Cockcroft, S. and N. Carvou (2007). "Biochemical and biological functions of class I phosphatidylinositol transfer proteins." Biochim Biophys Acta **6**: 677-691.
De Craene, J.-O., D. Bertazzi, et al. (2017). "Phosphoinositides, Major Actors in Membrane Trafficking and Lipid Signaling Pathways." International Journal of Molecular Sciences **18**(3): 634.
de Pablo, P. J. (2011). "Introduction to atomic force microscopy." Methods Mol Biol **783**: 197-212.
Di Paolo, G. and P. De Camilli (2006). "Phosphoinositides in cell regulation and membrane dynamics." Nature **443**(7112): 651-657.
Di Paolo, G., H. S. Moskowitz, et al. (2004). "Impaired PtdIns(4,5)P2 synthesis in nerve terminals produces defects in synaptic vesicle trafficking." Nature **431**(7007): 415-422.
Doherty, G. J. and H. T. McMahon (2009). "Mechanisms of endocytosis." Annu Rev Biochem **78**: 857-902.
Dowlatshahi, D. P., V. Sandrin, et al. "ALIX Is a Lys63-Specific Polyubiquitin Binding Protein that Functions in Retrovirus Budding." Dev Cell **23**(6): 1247-1254.
Doyotte, A., A. Mironov, et al. (2008). "The Bro1-related protein HD-PTP/PTPN23 is required for endosomal cargo sorting and multivesicular body morphogenesis." Proc Natl Acad Sci U S A **105**(17): 6308-6313.
Drury, J. L. and M. Dembo (1999). "Hydrodynamics of micropipette aspiration." Biophys J **76**(1 Pt 1): 110-128.
Effantin, G., A. Dordor, et al. (2012). "ESCRT-III CHMP2A and CHMP3 form variable helical polymers in vitro and act synergistically during HIV-1 budding." Cellular Microbiology: in press.
Effantin, G., A. Dordor, et al. (2013). "ESCRT-III CHMP2A and CHMP3 form variable helical polymers in vitro and act synergistically during HIV-1 budding." Cell Microbiol **15**(2): 213-226.
Effantin, G., A. Dordor, et al. (2013). "ESCRT-III CHMP2A and CHMP3 form variable helical polymers in vitro and act synergistically during HIV-1 budding." Cellular Microbiology **15**(2): 213-226.
Eggert, U. S., T. J. Mitchison, et al. (2006). "Animal cytokinesis: from parts list to mechanisms." Annu Rev Biochem **75**: 543-566.
Elia, N., G. Fabrikant, et al. (2012). "Computational Model of Cytokinetic Abscission Driven by ESCRT-III Polymerization and Remodeling." Biophysical Journal **102**(10): 2309-2320.
Elia, N., C. Ott, et al. (2013). "Incisive imaging and computation for cellular mysteries: lessons from abscission." Cell **155**(6): 1220-1231.
Elia, N., R. Sougrat, et al. (2011). "Dynamics of endosomal sorting complex required for transport (ESCRT) machinery during cytokinesis and its role in abscission." Proc Natl Acad Sci U S A **108**(12): 4846-4851.
Evans, E., V. Heinrich, et al. (2003). "Dynamic tension spectroscopy and strength of biomembranes." Biophys J **85**(4): 2342-2350.
Evans, E. and D. Needham (1987). "Physical properties of surfactant bilayer membranes: thermal transitions, elasticity, rigidity, cohesion and colloidal interactions." The Journal of Physical Chemistry **91**(16): 4219-4228.
Evans, E. and W. Rawicz (1990). "Entropy-driven tension and bending elasticity in condensed-fluid membranes." Phys Rev Lett **64**(17): 2094-2097.
Fabrikant, G., S. Lata, et al. (2009). "Computational model of membrane fission catalyzed by ESCRT-III." PLoS Comput Biol **5**(11): e1000575.
Faini, M., R. Beck, et al. (2013). "Vesicle coats: structure, function, and general principles of assembly." Trends Cell Biol **23**(6): 279-288.

Falkenburger, B. H., J. B. Jensen, et al. (2010). "Phosphoinositides: lipid regulators of membrane proteins." J Physiol **588**(Pt 17): 3179-3185.
Ferguson, S. M. and P. De Camilli (2012). "Dynamin, a membrane-remodelling GTPase." Nat Rev Mol Cell Biol **13**(2): 75-88.
Fisher, R. D., H. Y. Chung, et al. (2007). "Structural and biochemical studies of ALIX/AIP1 and its role in retrovirus budding." Cell **128**(5): 841-852.
Fournier, J. B., A. Ajdari, et al. (2001). "Effective-Area Elasticity and Tension of Micromanipulated Membranes." Physical Review Letters **86**(21): 4970-4973.
Frolov, V. A., A. Y. Dunina-Barkovskaya, et al. (2003). "Membrane permeability changes at early stages of influenza hemagglutinin-mediated fusion." Biophys J **85**(3): 1725-1733.
Fujita, H., Y. Umezuki, et al. (2004). "Mammalian class E Vps proteins, SBP1 and mVps2/CHMP2A, interact with and regulate the function of an AAA-ATPase SKD1/Vps4B." J Cell Sci **117**(Pt 14): 2997-3009.
Ganser-Pornillos, B. K., M. Yeager, et al. (2008). "The structural biology of HIV assembly." Curr Opin Struct Biol **18**(2): 203-217.
Garcia-Saez, A. J. and P. Schwille (2010). "Stability of lipid domains." FEBS Lett **584**(9): 1653-1658.
Garnier-Lhomme, M., R. D. Byrne, et al. (2009). "Nuclear envelope remnants: fluid membranes enriched in sterols and polyphosphoinositides." PLoS One **4**(1): 23.
Garten, M., L. D. Mosgaard, et al. (2017). "Whole-GUV patch-clamping." Proc Natl Acad Sci U S A **114**(2): 328-333.
Ghazi-Tabatabai, S., S. Saksena, et al. (2008). "Structure and disassembly of filaments formed by the ESCRT-III subunit Vps24." Structure **16**(9): 1345-1356.
Green, R. A., E. Paluch, et al. (2012). "Cytokinesis in animal cells." Annu Rev Cell Dev Biol **28**: 29-58.
Guizetti, J. and D. W. Gerlich (2010). "Cytokinetic abscission in animal cells." Semin Cell Dev Biol **21**(9): 909-916.
Guizetti, J. and D. W. Gerlich (2012). "ESCRT-III polymers in membrane neck constriction." Trends Cell Biol **22**(3): 133-140.
Guizetti, J., J. Mantler, et al. (2011). "Correlative time-lapse imaging and electron microscopy to study abscission in HeLa cells." Methods Cell Biol **96**: 591-601.
Guizetti, J., L. Schermelleh, et al. (2011). "Cortical Constriction During Abscission Involves Helices of ESCRT-III-Dependent Filaments." Science **331(6024)**: 1616-1620.
Hanson, P. I., R. Roth, et al. (2008). "Plasma membrane deformation by circular arrays of ESCRT-III protein filaments." J Cell Biol **180**(2): 389-402.
Hanson, P. I., R. Roth, et al. (2008). "Plasma membrane deformation by circular arrays of ESCRT-III protein filaments." J Cell Biol. **180(2)**: 389-402.
Hed, G. and S. A. Safran (2004). "Attractive instability of oppositely charged membranes induced by charge density fluctuations." Phys Rev Lett **93**(13): 23.
Helfrich, W. and R.-M. Servuss (1984). "Undulations, steric interaction and cohesion of fluid membranes." Il Nuovo Cimento D **3**(1): 137-151.
Helm, C. A., J. N. Israelachvili, et al. (1992). "Role of hydrophobic forces in bilayer adhesion and fusion." Biochemistry **31**(6): 1794-1805.
Henne, W. M., N. J. Buchkovich, et al. (2011). "The ESCRT pathway." Dev Cell **21**(1): 77-91.
Henne, W. M., N. J. Buchkovich, et al. (2012). "The Endosomal Sorting Complex ESCRT-II Mediates the Assembly and Architecture of ESCRT-III Helices." Cell **151**(2): 356-371.
Henne, W. M., H. Stenmark, et al. (2013). "Molecular mechanisms of the membrane sculpting ESCRT pathway." Cold Spring Harb Perspect Biol **5**(9).
Hinshaw, J. E. and S. L. Schmid (1995). "Dynamin self-assembles into rings suggesting a mechanism for coated vesicle budding." Nature **374**(6518): 190-192.
Hochmuth, R. M. (2000). "Micropipette aspiration of living cells." J Biomech **33**(1): 15-22.
Höök, F., M. Rodahl, et al. (1998). "Energy Dissipation Kinetics for Protein and Antibody−Antigen Adsorption under Shear Oscillation on a Quartz Crystal Microbalance." Langmuir **14**(4): 729-734.

Horger, K. S., D. J. Estes, et al. (2009). "Films of agarose enable rapid formation of giant liposomes in solutions of physiologic ionic strength." J Am Chem Soc **131**(5): 1810-1819.
Hosler, B. A., T. Siddique, et al. (2000). "Linkage of familial amyotrophic lateral sclerosis with frontotemporal dementia to chromosome 9q21-q22." Jama **284**(13): 1664-1669.
Hsu, V. W., S. Y. Lee, et al. The evolving understanding of COPI vesicle formation, Nat Rev Mol Cell Biol. 2009 May;10(5):360-4. doi: 10.1038/nrm2663. Epub 2009 Mar 18.
Hurley, J. H. (2015). "ESCRTs are everywhere." Embo J **34**(19): 2398-2407.
Hurley, J. H. and P. I. Hanson (2010). "Membrane budding and scission by the ESCRT machinery: it's all in the neck." Nat Rev Mol Cell Biol **11**(8): 556-566.
Jalmar, O., A. J. García-Sáez, et al. (2010). "Giant unilamellar vesicles (GUVs) as a new tool for analysis of caspase-8/Bid-FL complex binding to cardiolipin and its functional activity." Cell Death & Disease **1**(12): e103.
Jimenez, A. J., P. Maiuri, et al. (2014). "ESCRT machinery is required for plasma membrane repair." Science **343**(6174): 30.
Jouvenet, N., P. D. Bieniasz, et al. (2008). "Imaging the biogenesis of individual HIV-1 virions in live cells." Nature **454**(7201): 236-240.
Jouvenet, N., M. Zhadina, et al. (2011). "Dynamics of ESCRT protein recruitment during retroviral assembly." Nat Cell Biol **13**(4): 394-401.
Juan, T. and M. Furthauer (2017). "Biogenesis and function of ESCRT-dependent extracellular vesicles." Semin Cell Dev Biol **12**(17): 30252-30255.
Kang, M., C. A. Day, et al. (2009). "A generalization of theory for two-dimensional fluorescence recovery after photobleaching applicable to confocal laser scanning microscopes." Biophys J **97**(5): 1501-1511.
Kang, M., C. A. Day, et al. (2012). "Simplified Equation to Extract Diffusion Coefficients from Confocal FRAP Data." Traffic **13**(12): 1589-1600.
Katoh, K., H. Shibata, et al. (2004). "CHMP4b is a major binding partner of the ALG-2-interacting protein Alix among the three CHMP4 isoforms." Arch Biochem Biophysics **421**(1): 159-165.
Katzmann, D. J., M. Babst, et al. (2001). "Ubiquitin-dependent sorting into the multivesicular body pathway requires the function of a conserved endosomal protein sorting complex, ESCRT-I." Cell **106**(2): 145-155.
Kieffer, C., J. J. Skalicky, et al. (2008). "Two distinct modes of ESCRT-III recognition are required for VPS4 functions in lysosomal protein targeting and HIV-1 budding." Dev Cell **15**(1): 62-73.
Knopman, D. S., A. R. Mastri, et al. (1990). "Dementia lacking distinctive histologic features: a common non-Alzheimer degenerative dementia." Neurology **40**(2): 251-256.
Kozlov, M. M., H. T. McMahon, et al. (2010). "Protein-driven membrane stresses in fusion and fission." Trends Biochem Sci **35**(12): 699-706.
Kozlovsky, Y. and M. M. Kozlov (2003). "Membrane fission: model for intermediate structures." Biophys J **85**(1): 85-96.
Kuhl, T. L., D. E. Leckband, et al. (1994). "Modulation of interaction forces between bilayers exposing short-chained ethylene oxide headgroups." Biophys J **66**(5): 1479-1488.
Kuzmin, P. I., J. Zimmerberg, et al. (2001). "A quantitative model for membrane fusion based on low-energy intermediates." Proc Natl Acad Sci U S A **98**(13): 7235-7240.
Kwok, R. and E. Evans (1981). "Thermoelasticity of large lecithin bilayer vesicles." Biophys J **35**(3): 637-652.
Lafaurie-Janvore, J., P. Maiuri, et al. (2013). "ESCRT-III assembly and cytokinetic abscission are induced by tension release in the intercellular bridge." Science **339**(6127): 1625-1629.
Lajoie, P., E. A. Partridge, et al. (2007). "Plasma membrane domain organization regulates EGFR signaling in tumor cells." J Cell Biol **179**(2): 341-356.
Lamblet, M., B. Delord, et al. (2008). Key role of receptor density in colloid/cell specific interaction: A quantitative biomimetic study on giant vesicles.

Landsberg, M. J., P. R. Vajjhala, et al. (2009). "Three-dimensional structure of AAA ATPase Vps4: advancing structural insights into the mechanisms of endosomal sorting and enveloped virus budding." Structure **17**(3): 427-437.
Lata, S., M. Roessle, et al. (2008). "Structural basis for autoinhibition of ESCRT-III CHMP3." J Mol Biol **378**(4): 818-827.
Lata, S., G. Schoehn, et al. (2008). "Helical structures of ESCRT-III are disassembled by VPS4." Science **321**(5894): 1354-1357.
Leckband, D. E., C. A. Helm, et al. (1993). "Role of calcium in the adhesion and fusion of bilayers." Biochemistry **32**(4): 1127-1140.
Lee, H. H., N. Elia, et al. (2008). "Midbody targeting of the ESCRT machinery by a noncanonical coiled coil in CEP55." Science **322**(5901): 576-580.
Lee, I. H., H. Kai, et al. (2015). "Negative membrane curvature catalyzes nucleation of endosomal sorting complex required for transport (ESCRT)-III assembly." Proc Natl Acad Sci U S A **112**(52): 15892-15897.
Lee, J. A., . and F. B. Gao (2008). "Roles of ESCRT in autophagy-associated neurodegeneration." Autophagy **492)**: 230-232.
Lee, J. A., A. Beigneux, et al. (2007). "ESCRT-III dysfunction causes autophagosome accumulation and neurodegeneration." Curr Biol **17**(18): 1561-1567.
Lee, J. A. and F. B. Gao (2008). "ESCRT, autophagy, and frontotemporal dementia." BMB Rep **41**(12): 827-832.
Lee, M. C., L. Orci, et al. (2005). "Sar1p N-terminal helix initiates membrane curvature and completes the fission of a COPII vesicle." Cell **122**(4): 605-617.
Lee, S., N. P. Cho, et al. (2009). "An ultra-sensitive nanoarray chip based on single-molecule sandwich immunoassay and TIRFM for protein detection in biologic fluids." Analyst **134**(5): 933-938.
Lee, S., A. Joshi, et al. (2007). "Structural basis for viral late-domain binding to Alix." Nat Struct Mol Biol **14**(3): 194-199.
Lenz, M., D. J. G. Crow, et al. (2009). "Membrane Buckling Induced by Curved Filaments." Pys Rev Lett **103**: 038101.
Leung, K. F., J. B. Dacks, et al. (2008). "Evolution of the multivesicular body ESCRT machinery; retention across the eukaryotic lineage." Traffic **9**(10): 1698-1716.
Lin, Y., L. A. Kimpler, et al. (2005). "Interaction of the mammalian endosomal sorting complex required for transport (ESCRT) III protein hSnf7-1 with itself, membranes, and the AAA+ ATPase SKD1." J Biol Chem **280**(13): 12799-12809.
Lipowsky, R. (1995). "The morphology of lipid membranes." Curr Opin Struct Biol **5**(4): 531-540.
Loncle, N., M. Agromayor, et al. (2015). "An ESCRT module is required for neuron pruning." Sci Rep **5**(8461).
Marsh, D. (2006). "Elastic curvature constants of lipid monolayers and bilayers." Chem Phys Lipids **144**(2): 146-159.
Martin-Serrano, J. and S. J. Neil (2011). "Host factors involved in retroviral budding and release." Nat Rev Microbiol **9**(7): 519-531.
Martin-Serrano, J., T. Zang, et al. (2001). "HIV-1 and Ebola virus encode small peptide motifs that recruit Tsg101 to sites of particle assembly to facilitate egress." Nat Med **7**: 1313 - 1319.
Mathivet, L., S. Cribier, et al. (1996). "Shape change and physical properties of giant phospholipid vesicles prepared in the presence of an AC electric field." Biophys J **70**(3): 1112-1121.
Matsuoka, K., L. Orci, et al. (1998). "COPII-coated vesicle formation reconstituted with purified coat proteins and chemically defined liposomes." Cell **93**(2): 263-275.
Mattila, J. P., A. V. Shnyrova, et al. (2015). "A hemi-fission intermediate links two mechanistically distinct stages of membrane fission." Nature **524**(7563): 109-113.
McCullough, J., A. K. Clippinger, et al. (2015). "Structure and membrane remodeling activity of ESCRT-III helical polymers." Science **350**(6267): 1548-1551.
McCullough, J., R. D. Fisher, et al. (2008). "ALIX-CHMP4 interactions in the human ESCRT pathway." Proc Nat Acad Sci USA **105**(22): 7687-7691.

McLaughlin, S., J. Wang, et al. (2002). "PIP2 and Proteins: Interactions, Organization, and Information Flow." Annual Review of Biophysics and Biomolecular Structure **31**(1): 151-175.
McMahon, H. T. and E. Boucrot (2011). "Molecular mechanism and physiological functions of clathrin-mediated endocytosis." Nat Rev Mol Cell Biol **12**(8): 517-533.
McMahon, H. T. and J. L. Gallop (2005). "Membrane curvature and mechanisms of dynamic cell membrane remodelling." **438**(7068): 590-596.
Mears, J. A. and J. E. Hinshaw (2008). "Visualization of Dynamins." Methods in cell biology **88**: 237-256.
Meleard, P., L. A. Bagatolli, et al. (2009). "Giant unilamellar vesicle electroformation from lipid mixtures to native membranes under physiological conditions." Methods Enzymol **465**: 161-176.
Mierzwa, B. E., N. Chiaruttini, et al. (2017). "Dynamic subunit turnover in ESCRT-III assemblies is regulated by Vps4 to mediate membrane remodelling during cytokinesis." Nat Cell Biol **19**(7): 787-798.
Miura, G. I., J. Y. Roignant, et al. (2008). "Myopic acts in the endocytic pathway to enhance signaling by the Drosophila EGF receptor." Development **135**(11): 1913-1922.
Mohandas, N. and E. Evans (1994). "Mechanical properties of the red cell membrane in relation to molecular structure and genetic defects." Annu Rev Biophys Biomol Struct **23**: 787-818.
Monroe, N., H. Han, et al. (2014). "The oligomeric state of the active Vps4 AAA ATPase." J Mol Biol **426**(3): 510-525.
Morales-Penningston, N. F., J. Wu, et al. (2010). "GUV preparation and imaging: minimizing artifacts." Biochim Biophys Acta **1798**(7): 1324-1332.
Morita, E., L. A. Colf, et al. (2010). "Human ESCRT-III and VPS4 proteins are required for centrosome and spindle maintenance." Proc Nat Acad Sci. U.S.A. **107**: 12889–12894.
Morita, E., V. Sandrin, et al. (2007). "Human ESCRT and ALIX proteins interact with proteins of the midbody and function in cytokinesis." EMBO J **26**(19): 4215-4227.
Morita, E., V. Sandrin, et al. (2011). "ESCRT-III Protein Requirements for HIV-1 Budding." Cell Host Microbe **9**(3): 235-242.
Morita, E., V. Sandrin, et al. (2011). "ESCRT-III Protein Requirements for HIV-1 Budding." Cell host & microbe **9**(3): 235-242.
Morita, E. and W. I. Sundquist (2004). "Retrovirus budding." Annu Rev Cell Dev Biol **20**(1): 395-425.
Morlot, S., V. Galli, et al. (2012). "Membrane shape at the edge of the dynamin helix sets location and duration of the fission reaction." Cell **151**(3): 619-629.
Motta, I., A. Gohlke, et al. (2015). "Formation of giant unilamellar proteo-liposomes by osmotic shock." Langmuir : the ACS journal of surfaces and colloids **31**(25): 7091-7099.
Murk, J. L. A. N., B. M. Humbel, et al. (2003). "Endosomal compartmentalization in three dimensions: Implications for membrane fusion." Proceedings of the National Academy of Sciences **100**(23): 13332.
Muziol, T., E. Pineda-Molina, et al. (2006). "Structural basis for budding by the ESCRT-III factor CHMP3." Dev Cell **10**(6): 821-830.
Neumann, S. and G. van Meer (2008). "Sphingolipid management by an orchestra of lipid transfer proteins." Biol Chem **389**(11): 1349-1360.
Obita, T., S. Saksena, et al. (2007). "Structural basis for selective recognition of ESCRT-III by the AAA ATPase Vps4." Nature **449**(7163): 735-739.
Olmos, Y. and J. G. Carlton (2016). "The ESCRT machinery: new roles at new holes." Curr Opin Cell Biol **38**: 1-11.
Olmos, Y., L. Hodgson, et al. (2015). "ESCRT-III controls nuclear envelope reformation." Nature **522**(7555): 236-239.
Palade, G. (1975). "Intracellular aspects of the process of protein synthesis." Science **189**(4206): 867.
Pautot, S., B. J. Frisken, et al. (2003). "Engineering asymmetric vesicles." Proc Natl Acad Sci U S A **100**(19): 10718-10721.
Pecreaux, J., H. G. Dobereiner, et al. (2004). "Refined contour analysis of giant unilamellar vesicles." Eur Phys J E Soft Matter **13**(3): 277-290.

Peel, S., P. Macheboeuf, et al. (2011). "Divergent pathways lead to ESCRT-III catalyzed membrane fission." Trends Biochem Sci **36**((4)): 199-210.
Piper, R. C. and D. J. Katzmann (2007). "Biogenesis and function of multivesicular bodies." Annu Rev Cell Dev Biol **23**: 519-547.
Pires, R., B. Hartlieb, et al. (2009). "A crescent-shaped ALIX dimer targets ESCRT-III CHMP4 filaments." Structure **17**(6): 843-856.
Pontani, L. L., J. van der Gucht, et al. (2009). "Reconstitution of an actin cortex inside a liposome." Biophys J **96**(1): 192-198.
Prévost, C., H. Zhao, et al. (2015). "IRSp53 senses negative membrane curvature and phase separates along membrane tubules." Nature Communications **6**: 8529.
Pucadyil, T. J. and A. Chattopadhyay (2006). "Confocal fluorescence recovery after photobleaching of green fluorescent protein in solution." J Fluoresc **16**(1): 87-94.
Rawicz, W., K. C. Olbrich, et al. (2000). "Effect of chain length and unsaturation on elasticity of lipid bilayers." Biophys J **79**(1): 328-339.
Rawicz, W., B. A. Smith, et al. (2008). "Elasticity, strength, and water permeability of bilayers that contain raft microdomain-forming lipids." Biophys J **94**(12): 4725-4736.
Raymond, C. K., I. Howald-Stevenson, et al. (1992). "Morphological classification of the yeast vacuolar protein sorting mutants: evidence for a prevacuolar compartment in class E vps mutants." Mol Biol Cell **3**(12): 1389-1402.
Reits, E. A. and J. J. Neefjes (2001). "From fixed to FRAP: measuring protein mobility and activity in living cells." Nat Cell Biol **3**(6): 35078615.
Rodriguez, N., F. Pincet, et al. (2005). "Giant vesicles formed by gentle hydration and electroformation: a comparison by fluorescence microscopy." Colloids Surf B Biointerfaces **42**(2): 125-130.
Roll-Mecak, A. and R. D. Vale (2008). "Structural basis of microtubule severing by the hereditary spastic paraplegia protein spastin." Nature **451**(7176): 363-367.
Rossetti, F. F., M. Bally, et al. (2005). "Interactions between Titanium Dioxide and Phosphatidyl Serine-Containing Liposomes: Formation and Patterning of Supported Phospholipid Bilayers on the Surface of a Medically Relevant Material." Langmuir **21**(14): 6443-6450.
Roth, M. G. (2004). "Phosphoinositides in constitutive membrane traffic." Physiol Rev **84**(3): 699-730.
Rothman, J. H., I. Howald, et al. (1989). "Characterization of genes required for protein sorting and vacuolar function in the yeast Saccharomyces cerevisiae." Embo J **8**(7): 2057-2065.
Roux, A., D. Cuvelier, et al. (2005). "Role of curvature and phase transition in lipid sorting and fission of membrane tubules." EMBO J **24**(8): 1537-1545.
Roux, A., G. Koster, et al. (2010). "Membrane curvature controls dynamin polymerization." Proc Natl Acad Sci U S A **107**(9): 4141-4146.
Ruan, Y., A. Miyagi, et al. (2017). "Direct visualization of glutamate transporter elevator mechanism by high-speed AFM." Proc Natl Acad Sci U S A **114**(7): 1584-1588.
Saksena, S. and S. D. Emr (2009). "ESCRTs and human disease." Biochem Soc Trans **37**(Pt 1): 167-172.
Saksena, S., J. Sun, et al. (2007). "ESCRTing proteins in the endocytic pathway." Trends in Biochemical Sciences **32**(12): 561-573.
Saksena, S., J. Wahlman, et al. (2009). "Functional reconstitution of ESCRT-III assembly and disassembly." Cell **136**(1): 97-109.
Salmon, E. D., R. J. Leslie, et al. (1984). "Spindle microtubule dynamics in sea urchin embryos: analysis using a fluorescein-labeled tubulin and measurements of fluorescence redistribution after laser photobleaching." J Cell Biol **99**(6): 2165-2174.
Sandre, O., L. Moreaux, et al. (1999). "Dynamics of transient pores in stretched vesicles." Proc Natl Acad Sci U S A **96**(19): 10591-10596.
Sauerbrey, Z. (1959). Z. Phys. **155**: 206-222.
Scheffer, L. L., S. C. Sreetama, et al. (2014). "Mechanism of Ca(2)(+)-triggered ESCRT assembly and regulation of cell membrane repair." Nat Commun **5**(5646).
Schmid, S. L. (2017). "Reciprocal regulation of signaling and endocytosis: Implications for the evolving cancer cell." J Cell Biol **3**(201705017): 201705017.

Schmid, S. L. and V. A. Frolov (2011). "Dynamin: functional design of a membrane fission catalyst." Annu Rev Cell Dev Biol **27**: 79-105.
Schmidt, O. and D. Teis (2012). "The ESCRT machinery." Curr Biol **22**(4): 028.
Schoneberg, J., I.-H. Lee, et al. (2017). "Reverse-topology membrane scission by the ESCRT proteins." Nat Rev Mol Cell Biol **18**(1): 5-17.
Scott, A., H. Y. Chung, et al. (2005). "Structural and mechanistic studies of VPS4 proteins." EMBO J **24(20)**: 3658-3669.
Scott, A., J. Gaspar, et al. (2005). "Structure and ESCRT-III protein interactions of the MIT domain of human VPS4A." Proc Natl Acad Sci U S A **102**(39): 13813-13818.
Shen, Q. T., A. L. Schuh, et al. (2014). "Structural analysis and modeling reveals new mechanisms governing ESCRT-III spiral filament assembly." J Cell Biol **206**(6): 763-777.
Sherman, S., D. Kirchenbuechler, et al. (2016). "Resolving new ultrastructural features of cytokinetic abscission with soft-X-ray cryo-tomography." Sci Rep **6**(27629).
Shi, Z. and T. Baumgart (2015). "Membrane tension and peripheral protein density mediate membrane shape transitions." Nat Commun **6**(5974).
Shim, S., L. A. Kimpler, et al. (2007). "Structure/Function Analysis of Four Core ESCRT-III Proteins Reveals Common Regulatory Role for Extreme C-Terminal Domain." Traffic **8**(8): 1068-1079.
Shnyrova, A. V., P. V. Bashkirov, et al. (2013). "Geometric catalysis of membrane fission driven by flexible dynamin rings." Science **339**(6126): 1433-1436.
Shpetner, H. S. and R. B. Vallee (1989). "Identification of dynamin, a novel mechanochemical enzyme that mediates interactions between microtubules." Cell **59**(3): 421-432.
Siegel, D. P. and M. M. Kozlov (2004). "The gaussian curvature elastic modulus of N-monomethylated dioleoylphosphatidylethanolamine: relevance to membrane fusion and lipid phase behavior." Biophys J **87**(1): 366-374.
Skibinski, G., N. J. Parkinson, et al. (2005). "Mutations in the endosomal ESCRTIII-complex subunit CHMP2B in frontotemporal dementia." Nat Genet **37**(8): 806-808.
Slagsvold, T., K. Pattni, et al. (2006). "Endosomal and non-endosomal functions of ESCRT proteins." Trends in Cell Biology **16**(6): 317-326.
Sorre, B., A. Callan-Jones, et al. (2012). "Nature of curvature coupling of amphiphysin with membranes depends on its bound density." Proc Natl Acad Sci U S A **109**(1): 173-178.
Soumpasis, D. M. (1983). "Theoretical analysis of fluorescence photobleaching recovery experiments." Biophys J **41**(1): 95-97.
Sprong, H., P. van der Sluijs, et al. (2001). "How proteins move lipids and lipids move proteins." Nat Rev Mol Cell Biol **2**(7): 504-513.
Stachowiak, J. C., D. L. Richmond, et al. (2008). "Unilamellar vesicle formation and encapsulation by microfluidic jetting." Proc Natl Acad Sci U S A **105**(12): 4697-4702.
Stahelin, R. V., J. L. Scott, et al. (2014). "Cellular and molecular interactions of phosphoinositides and peripheral proteins." Chem Phys Lipids **182**: 3-18.
Steigemann, P. and D. W. Gerlich (2009). "Cytokinetic abscission: cellular dynamics at the midbody." Trends Cell Biol **19**(11): 606-616.
Stuchell-Brereton, M. D., J. J. Skalicky, et al. (2007). "ESCRT-III recognition by VPS4 ATPases." Nature **449**(7163): 740-744.
Sweeney, N. T., J. E. Brenman, et al. (2006). "The coiled-coil protein shrub controls neuronal morphogenesis in Drosophila." Curr Biol **16**(10): 1006-1011.
Sweitzer, S. M. and J. E. Hinshaw (1998). "Dynamin undergoes a GTP-dependent conformational change causing vesiculation." Cell **93**(6): 1021-1029.
Takahashi, N., T. Kishimoto, et al. (2002). "Fusion pore dynamics and insulin granule exocytosis in the pancreatic islet." Science **297**(5585): 1349-1352.
Takamori, S., M. Holt, et al. (2006). "Molecular anatomy of a trafficking organelle." Cell **127**(4): 831-846.
Tang, S., W. M. Henne, et al. (2015). "Structural basis for activation, assembly and membrane binding of ESCRT-III Snf7 filaments." Elife **4**.

Teis, D., S. Saksena, et al. (2008). "Ordered Assembly of the ESCRT-III Complex on Endosomes Is Required to Sequester Cargo during MVB Formation." Developmental cell **15**(4): 578-589.
Teo, H., O. Perisic, et al. (2004). "ESCRT-II, an endosome-associated complex required for protein sorting: crystal structure and interactions with ESCRT-III and membranes." Dev Cell **7**(4): 559-569.
Urwin, H., S. Ghazi-Noori, et al. (2009). "The role of CHMP2B in frontotemporal dementia." Biochem Soc Trans **37**(Pt 1): 208-212.
van der Zee, J., H. Urwin, et al. (2008). "CHMP2B C-truncating mutations in frontotemporal lobar degeneration are associated with an aberrant endosomal phenotype in vitro." Hum Mol Genet **17**(2): 313-322.
Van Engelenburg, S. B., G. Shtengel, et al. (2014). "Distribution of ESCRT machinery at HIV assembly sites reveals virus scaffolding of ESCRT subunits." Science **343**(6171): 653-656.
van Meer, G., D. R. Voelker, et al. (2008). "Membrane lipids: where they are and how they behave." Nat Rev Mol Cell Biol **9**(2): 112-124.
Vassilieva, E. V. and A. Nusrat (2008). "Vesicular trafficking: molecular tools and targets." Methods Mol Biol **440**: 3-14.
Vietri, M., K. O. Schink, et al. (2015). "Spastin and ESCRT-III coordinate mitotic spindle disassembly and nuclear envelope sealing." Nature **522**(7555): 231-235.
von Schwedler, U. K., M. Stuchell, et al. (2003). "The protein network of HIV budding." Cell **114**(6): 701-713.
Wang, Y.-H., A. Collins, et al. (2012). "Divalent Cation-Induced Cluster Formation by Polyphosphoinositides in Model Membranes." Journal of the American Chemical Society **134**(7): 3387-3395.
Waugh, R. and E. A. Evans (1979). "Thermoelasticity of red blood cell membrane." Biophys J **26**(1): 115-131.
Weinberger, A., F. C. Tsai, et al. (2013). "Gel-assisted formation of giant unilamellar vesicles." Biophys J **105**(1): 154-164.
Weiss, M. (2004). "Challenges and artifacts in quantitative photobleaching experiments." Traffic **5**(9): 662-671.
Wilhelmsen, K. C., T. Lynch, et al. (1994). "Localization of disinhibition-dementia-parkinsonism-amyotrophy complex to 17q21-22." Am J Hum Genet **55**(6): 1159-1165.
Williams, R. L. and S. Urbe (2007). "The emerging shape of the ESCRT machinery." Nat Rev Mol Cell Biol **8**(5): 355-368.
Wollert, T. and J. H. Hurley (2010). "Molecular mechanism of multivesicular body biogenesis by ESCRT complexes." Nature **464**(7290): 864-869.
Wollert, T. and J. H. Hurley (2010). "Molecular mechanism of multivesicular body biogenesis by ESCRT complexes." Nature **464(7290)**: 864-869.
Wollert, T., C. Wunder, et al. (2009). "Membrane scission by the ESCRT-III complex." Nature **458**(7235): 172-177.
Xiao, J., X. W. Chen, et al. (2009). "Structural basis of Ist1 function and Ist1-Did2 interaction in the multivesicular body pathway and cytokinesis." Mol Biol Cell **20**(15): 3514-3524.
Yamamoto, D., N. Nagura, et al. (2009). "Streptavidin 2D Crystal Substrates for Visualizing Biomolecular Processes by Atomic Force Microscopy." Biophysical Journal **97**(8): 2358-2367.
Yang, D., N. Rismanchi, et al. (2008). "Structural basis for midbody targeting of spastin by the ESCRT-III protein CHMP1B." Nat Struct Mol Biol **15(12)**: 1278-1286.
Zamborlini, A., Y. Usami, et al. (2006). "Release of autoinhibition converts ESCRT-III components into potent inhibitors of HIV-1 budding." Proc Natl Acad Sci U S A **103**(50): 19140-19145.
Zeman, K., H. Engelhard, et al. (1990). "Bending undulations and elasticity of the erythrocyte membrane: effects of cell shape and membrane organization." Eur Biophys J **18**(4): 203-219.
Zhang, H., Y. Wang, et al. (2014). "Endocytic pathways downregulate the L1-type cell adhesion molecule neuroglian to promote dendrite pruning in Drosophila." Dev Cell **30**(4): 463-478.

Zimmerberg, J. and M. M. Kozlov (2006). "How proteins produce cellular membrane curvature." Nat Rev Mol Cell Biol **7**(1): 9-19.